國立高雄師範大學物理學系博士班

博士論文

Department of Physics

National Kaohsiung Normal University

Doctor's Thesis

在 CERN COMPASS 實驗組量測 190-GeV 的 π 介子束流所產生之 Drell－Yan 過程的非極化雙渺子角度分布

Measurements of Unpolarized Dimuon Angular Distributions of Drell–Yan Production with 190-GeV Pion beams in the COMPASS Experiment at CERN

指導教授：郭榮升博士，章文箴博士

Advisors：Dr. Guo Rurng-Sheng, Dr. Chang Wen-Chen

研究生：連昱翔 撰

Graduate：Lien Yu-Hsiang

中 華 民 國 一一〇 年 八 月

August 2021

國立高雄師範大學博士班研究生

論文口試審定書

物理學系博士班 連昱翔 所提之論文

在 CERN COMPASS 實驗組量測 190-GeV 的 π 介子束流所產生之 Drell－Yan 過程的非極化雙渺子角度分布

經下列委員口試及審議通過，特此證明：

口試委員 章文成

高崇文

郭家銘

楊毅

黃建文

郭榮升

指導教授 章文成

郭榮升

系主任 黃建文

中華民國 一一〇 年 七 月 十五 日

Acknowledgements

First of all, I would like to thank to my supervisor, Professor Rurng-Sheng Guo, for leading me to start the research in the field of high energy physics since I was an undergraduate student. His guidance and support is gratefully acknowledged.

A grateful thanks to my co-supervisor, Professor Wen-Chen Chang, who guides and advises me with his enormous patience and expertise on my research path. Because of him, I became a real scientist.

I would like to thank all the members of the COMPASS Collaboration, especially thanks to all the members of the Drell–Yan group. A special thanks to Dr. Catarina Quintans and Dr. Bakur Parsamyan for their wise advices, comments and suggestions on my thesis topic. A warm thanks to Dr. Vincent Andrieux, who gave me enormous supports and advices, not only on my analysis work but also in life when I stayed at CERN. Without his support, I would not be able to finish my thesis. Many thanks to Dr. Riccardo Longo, with whom I worked together with this thesis topic in 2015 data and successfully managed to my first ever release result. I thank to Alexandr Chumakov, with whom I have successfully done and cross-check this analysis together in this challenging year. Gratefully thanks to Moritz Benjamin Veit, for his strongest supports on the trigger efficiencies study which is the key elements on this thesis. I want to thank Dr. Marco Meyer and Dr. Charles-Joseph Naïm, for their great help on the Monte-Carlo simulation.

I want to thank all the colleagues from the COMPASS group of Academia Sinica. A special thanks to Dr. Marcia Quaresma, who gave me many advices and comments before she returned to Portugo. A warm thanks to Chia-Yu Hsieh, who guides and supports me since my early steps into this group.

Finally I express my appreciation thanks to my family, my friends, and my love. With their strongest supports and encouragement, I became an ambitious man.

摘要

Drell – Yan過程發生在當強子與強子之間互相碰撞時，藉由兩者之中的夸克與反夸克相互湮滅，透過中間態虛光子的生成後而最後產生正反輕子對（例如e^+e^-或是$\mu^+\mu^-$）。而透過Drell – Yan過程產生之正反輕子對的角度分佈將提供碰撞強子之部分子分佈函數（PDF）的重要訊息，此函數為描述強子內部結構的非微擾量子色動力學之機率分布函數。

COMPASS實驗組是位於瑞士日內瓦CERN（歐洲核子研究組織）中SPS（超質子同步加速器）的高能量固定靶實驗組。

此論文著重在分析由COMPASS實驗組在2018年取數得到的大質量Drell – Yan過程之產物，其取數期間是使用能量為190-GeV的π介子束流撞擊橫向極化氨靶材以及鎢靶材。而量測出的三個角度係數（也稱為非極化不對稱性）λ、μ和ν將會詳細呈現，此不對稱性是用來描述大質量Drell – Yan過程在非極化部分的散射截面分佈。由於非極化不對稱性關聯於Lam – Tung關係的違背，可用來測試量子色動力學理論的完備性，因此在當代吸引了人們的注意。另外，因為角度分佈非常敏感於實驗裝置的接收率計算，因此這個分析主題需要完備的模擬架構建立。在最後的非極化不對稱性結果呈現上會相依於五種物理量：核子Bjorken變量（x_N）、π介子Bjorken變量（x_π）、費曼變量（x_F）、雙渺子橫向動量（q_T）及雙渺子不變質量（$M_{\mu\mu}$）。與此同時，非極化不對稱性量測結果也會與兩個過去的π介子引導Drell – Yan實驗組NA10及E615之量測結果做互相比對，以及與微擾量子色動力學的理論計算結果比較。

在論文的第二部分則是致力於以非相對論性量子色動力學的架構來分析由固定靶能量尺度下藉由魅夸克偶素生成之強作用產物。此目標是利用計算出π介子和質子引導魅夸克偶素的數據來計算新的長距離矩陣元素（LDMEs）集合。

Abstract

The Drell–Yan process occurring in hadron-hadron collisions is the annihilation of a quark and anti-quark into a lepton pair (e^+e^- or $\mu^+\mu^-$) which goes through intermediate virtual photon production. The angular distribution of lepton pairs from the Drell–Yan process provides important information on the Parton Distribution Functions (PDFs) of colliding hadrons, which are non-perturbative QCD universal objects describing the hadron structure.

The COMPASS experiment is a high-energy fixed-target experiment at SPS (Super Proton Synchrotron) at CERN (also known as European Organization for Nuclear Research) in Geneva, Switzerland. This experiment aims to probe the structure and spectroscopy of hadrons.

This thesis is focused on the analysis of the high-mass Drell–Yan production data collected by the COMPASS experiment during the 2018 data taking, using a 190 GeV π^- beam impinging on transversely polarized ammonia (NH_3) and tungsten (W) targets. The measured angular coefficients (also known as unpolarized asymmetries) λ, μ and ν that describe the unpolarized part of the Drell–Yan cross-section in the high-mass region will be presented in detail. These unpolarized asymmetries have attracted people's attention in the recent past, being related to the Lam-Tung violation since it's one of the test ground for QCD theory. This analysis topic require an extensive study of Monto–Carlo framework since its sensitivity to the acceptance effects due to the experimental apparatus. The results will be shown as a function of nucleon Bjorken variable (x_N), pion Bjorken variable (x_π), Feynman-x (x_F), transverse momentum (q_T) and invariant mass of the muon pairs ($M_{\mu\mu}$). A comparison with results from the past pion-induced Drell–Yan experiments NA10 and E615 will also be done, as well as with the predictions from fixed-order perturbative QCD calculations.

The second part of the thesis is devoted to the analysis of hadroproduction of charmonium production at fixed-target energies in the framework of non-relativistic QCD (NRQCD). The goal is to determine the new set of color-octet long-distance matrix elements (LDMEs) by using both pion- and proton-induced charmonium data.

Contents

List of Tables

List of Figures

Introduction

The Nucleon Structure

The nucleon, such as proton and neutron, is the fundamental building blocks of this world. Exploring the structure of nucleon is an intriguing but challenge topic until nowadays, since the internal structure of nucleon is not static but have a very complex internal structure and dynamics. In 1969, Richard Feynman proposed the so-called parton model [1] which gave a first approximation of the structure of nucleon observed by the scattering experiment with the longitudinal momentum of its constituents. In this model, the constituents of nucleon are called *parton*, which nowadays have been identified as quarks and gluons, and its longitudinal momentum distribution of partons inside the nucleon are also known as Parton Distribution Functions (PDFs). By increasing energy scale in several scattering experiments, the quark and gluon structure of the nucleon through Deep-Inelastic Scattering[1] (DIS) has been revealed. The schematic representation of deep inelastic electron-proton scattering in the parton model is shown in Fig. 1.

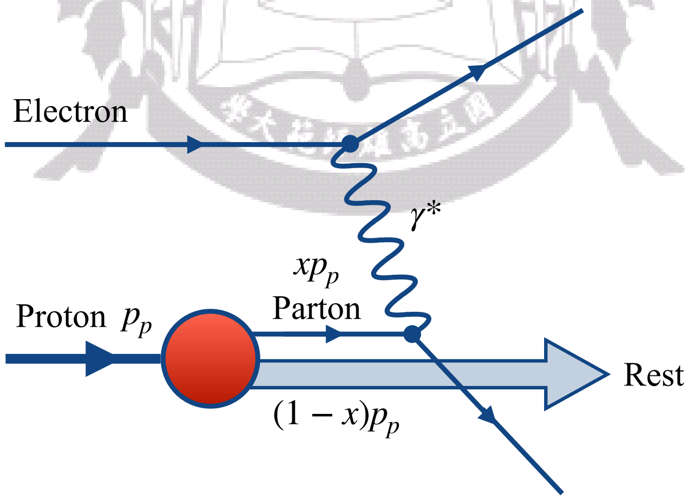

Figure 1: The schematic representation of deep inelastic electron-proton scattering in the parton model.

These discoveries from experiments have led to the development of Quantum Chromodynamics (QCD) theory, a theory of describing the mechanism of strong interaction. With

[1]the scattering of high-energy electron and muon beams off nucleon target

the information of PDFs, the structure of the nucleon can be quantitatively parameterized and described through QCD-based framework. However, the description of longitudinal momentum and the spin of parton failed to obtain a consistent observation between experimental measurement and theoretical calculation, which lead people to consider the possible contribution from the transverse motion of partons inside the nucleon for a complete description of nucleon structure. In recent years, there are significant progresses ongoing in both experiment and theory point of view, which extends the original Feynman one-dimensional parton picture to a full three-dimensional tomographic understanding of the partons inside the nucleon. The extension to the transverse motion can be either in the coordinate space (spatial tomography) or in the momentum space (momentum tomography). In the extension of the coordinate space introduced the so-called Generalised Parton Distributions (GPDs) [2], while in the extension of the momentum space introduce the so-called Transverse Momentum Dependent (TMD) parton distribution functions [3].

Because of the principle of uncertainty, the transverse momentum and the transverse coordinate cannot be measured simultaneously. However, the idea of nucleon structure picture from two different tomography can be unified within the concept of the so-called Wigner distributions. Fig. 2 shows the sketch of nucleon structure extension relation from the original Feynman one-dimensional parton picture to a full multi-dimensional tomographic understanding.

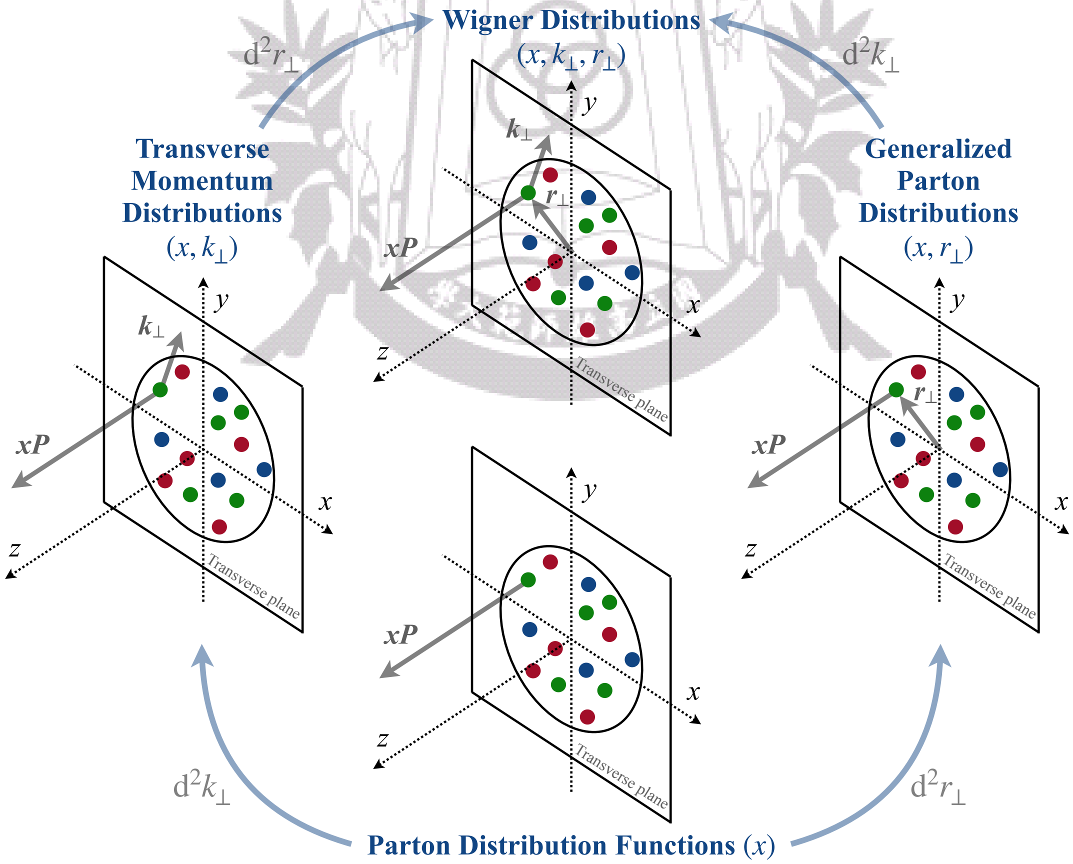

Figure 2: The sketch of nucleon structure extension relation from the original Feynman one-dimensional parton picture to a full multi-dimensional tomographic understanding.

In particular, studying the nucleon spin structure provides a unique way to understand the internal structure and parton correlations of the nucleon. Starting from the European Muon Collaboration (EMC) data [4], the results suggested that the intrinsic spin of quarks inside the proton only contributes little to the total spin of proton. Nowadays, a good understanding of the longitudinal spin structure of proton between experimental measurement and theoretical calculation is achieved, while the puzzle from the data in measurements of transverse single-spin asymmetries of proton still remains. This lead to the importance of understanding the multi-dimensional tomographic nucleon structure.

Transverse Momentum Dependent Parton Distribution

After the discovery of scaling in DIS and the partonic structures in the nucleon, only the longitudinal momentum distributions of partons have been explored. To investigate the nucleon spin structure in transverse degrees of freedom, one can access through the TMDs. There are three transverse degrees of freedom: the transverse spin of nucleon $\vec{S}_N$, the transverse spin of quark $\vec{s}_q$ and the intrinsic transverse momentum of quark $\vec{k}_T$. The transverse spin is the spin component perpendicular to the nucleon momentum direction, which is a natural vector to correlate with the transverse momentum of quark in TMDs. Base on the correlation among the transverse spin of nucleon $\vec{S}_N$ and quark $\vec{s}_q$ and also the intrinsic transverse momentum of quark $\vec{k}_T$, one could classify different TMDs. The so-called Sivers function is the correlation between intrinsic transverse momentum of quark and transverse spin of nucleon. The Boer–Mulders function is the correlation between transverse spin of quark and its transverse momentum. The transversity distribution is the correlation between the transverse spin of quark and transverse spin of nucleon. Despite there are also other TMDs, most of the recent progresses in TMDs focus on these three distributions. The correlations between different transverse spin of nucleon and quark resulting different TMDs are summarized in Fig. 3.

In the leading-twist approximation [5], there are in total eight TMDs (as shown in Fig. 3). The TMDs can be accessed via the Semi-Inclusive Deep Inelastic Scattering (SIDIS) process or the Drell–Yan process (see Section 1.1). The former process can access TMDs via using unpolarized beam and unpolarized target, unpolarized beam and polarized target, or polarized beam and polarized target, which is the convolution of TMDs of the target hadron and the fragmentation functions of the struck quark; the later one can access TMDs via using unpolarized hadron-hadron collision, single polarized hadron-hadron collision, or double polarized hadron-hadron collision, which is the convolution of TMDs of the two hadrons participating in the reaction.

Assuming factorization and universality of TMDs, the same TMDs extracted from two different processes should be the same. Despite TMDs are already accessible via SIDIS process, the are many unique informations and advantages on TMDs to extract from the Drell–Yan process. First of all, the SIDIS cross-section is a convolution of a PDF and a fragmentation function, while the Drell–Yan cross-section the convolution of two parton distributions. On the other hand, the extraction of TMDs from SIDIS process required the information of both PDF and fragmentation function and the fragmentation function is often poorly known. So that the feature of Drell–Yan process allows an independent measurement of TMDs which can provide a consistency check of extracted TMDs from SIDIS process.

Second, the TMDs of meson or anti-proton can be only accessed via the Drell–Yan process since there is no static meson or anti-proton target existed to perform the SIDIS experiment. Third, the TMDs of antiquark could be sensitively probed by the proton-induced Drell–Yan process, while it is overshadowed by the valence quark's TMDs in the SIDIS process. Finally, despite the concept of universality of TMDs, the Sivers and the Boer–Mulders functions as the time-reversal-odd TMDs are predicted to undergo a sign reversal between the space-like SIDIS process and the time-like Drell–Yan process:

$$f_{1T}^{q\perp}(x, k_T)\,|_{\text{Drell-Yan}} = -f_{1T}^{q\perp}(x, k_T)\,|_{\text{SIDIS}}$$
$$h_1^{q\perp}(x, k_T)\,|_{\text{Drell-Yan}} = -h_1^{q\perp}(x, k_T)\,|_{\text{SIDIS}}$$

This fundamental prediction is a direct consequence of QCD gauge invariance, which is an important subject to verify for TMDs physics.

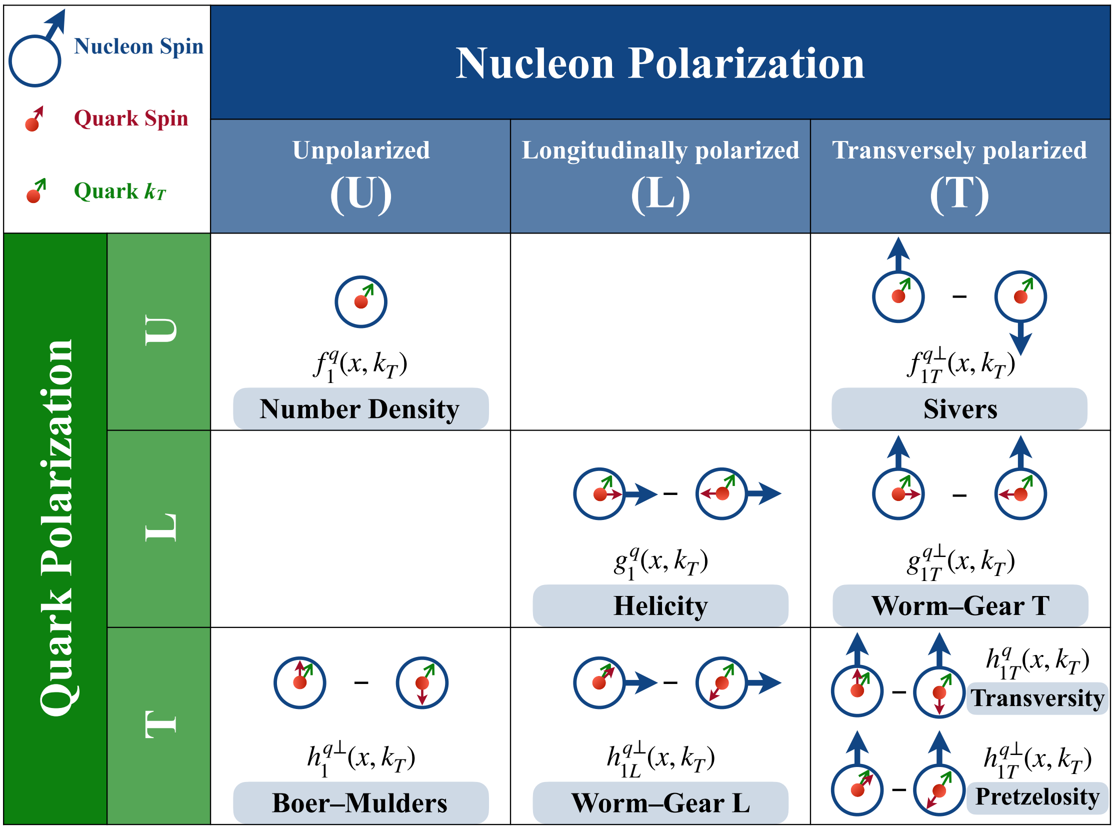

Figure 3: The leading-twist transverse-momentum-dependent parton distributions classified according to the polarization of the quark and nucleon. The U, L and T represent the Unpolarized, Longitudinally polarized and Transversely polarized direction, respectively.

Outline of the Thesis

The thesis is organized as follows: in Chapter 1 the Drell–Yan process will be reviewed and highlighted, especially from the perspectives of decay angular distribution and the related experimental results in the last decades. In Chapter 2 the COMPASS experimental apparatus is described in detail, with particular attention on the set-up in the years of 2015 and 2018 for the Drell–Yan data taking. In particular, a comprehensive study on the efficiency of trigger system for the COMPASS apparatus during the 2018 run is given in Chapter 3, which is the key component of the whole angular analysis framework. In Chapter 4 the Monte–Carlo (MC) framework in the COMPASS experiment is demonstrated, especially the agreement of kinematics distributions between Data and MC sample will be highlighted which ensures the correction of the angular acceptance estimation. Chapter 5 is devoted to the data analysis taken by the COMPASS experiment for the data of 2018, regarding the data taking condition, event selection criteria and background estimation. The results of high-mass Drell–Yan unpolarized asymmetries will be shown in Chapter 6. Additionally, Chapter 7 presents the work of a phenomenological study for the charmonium production. Finally, a summary of highlights of the present work are given in Chapter 8.

CHAPTER 1

The Drell–Yan Process

1.1 The History of Drell–Yan Process

In 1970, Christenson *et al.* [6] reported on the first measurement of high-mass muon pair $\mu^+\mu^-$ production produced in hadron-hadron collisions. The differential cross-section of this $\mu^+\mu^-$ production as a function of invariant mass is continuum but dropping rapidly with increasing dimuon mass. Sid Drell and Tung-Mow Yan interpreted the dimuon continuum as resulted from the decay of virtual photons formed by the process of annihilation of quark and antiquark during the hadron-hadron collision. This proposed reaction is named as Drell–Yan process [7]. Fig. 1.1 depicts the Drell–Yan process.

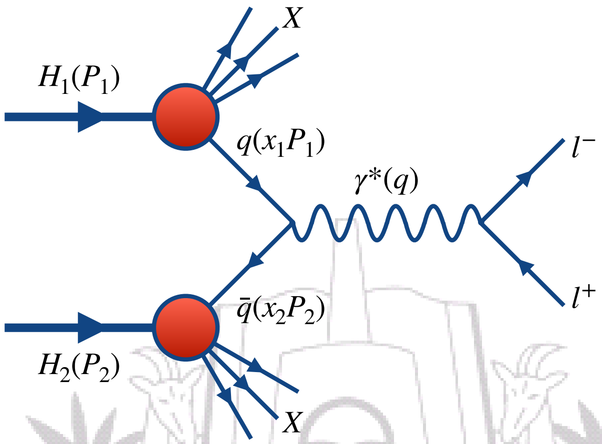

Figure 1.1: The diagram of Drell–Yan process, as originally proposed by Drell and Yan.

As introduced above, the Drell–Yan process occurring in hadron-hadron collisions is the annihilation of a quark and anti-quark into a lepton pair (e^+e^- or $\mu^+\mu^-$) which goes through intermediate virtual photon production. When a quark q with momentum fraction x_1 from one hadron H_1 with momentum P_1 and polarization S_1 annihilates with an anti-quark $\bar{q}$ with momentum fraction x_2 from the other hadron H_2 with momentum P_2 and polarization S_2, it could produce a virtual photon γ^* of momentum q with an invariant mass $Q = \sqrt{q^2}$ which then decays into a lepton pairs l^+l^-. The general Drell–Yan reaction can be written as following:

$$H_1(P_1, S_1) + H_2(P_2, S_2) \longrightarrow \gamma^*(q) + X \longrightarrow l^+(l') + l^-(l) + X \tag{1.1}$$

In principle the hadronic cross-section to produce the lepton pair is exactly calculable as long as parton distribution functions (PDFs) are known, which provide the information of probability distributions to find a parton with momentum fraction x in a colliding hadron with momentum P. Since the Drell–Yan process is via electromagnetic interaction, the cross-section from annihilation of quark and antiquark into the lepton-pair is predicable. The Drell–Yan process is also an important tool to access the parton distribution functions of the colliding hadrons, other than DIS.

There were several predictions given by Drell and Yan for the massive lepton pair production [7] confirmed by the experiments [8], such as the angular distribution of the decay lepton pair, the linear dependence of the cross-section on the mass number of the target nucleus and so on. However, there were some results found to deviate from the Drell–Yan model:

one is a factor of two (the so-called K-factor) larger cross-section with respect to the calculation by using the naive parton model PDFs, another is the larger mean value of transverse momentum with respect to the model. Fortunately, the explanation from the Quantum Chromodynamics (QCD) have been made later. Base on the QCD-improved Drell–Yan process by considering not only the pure electromagnetic quark-antiquark annihilation but also the gluon emission and absorption contribution, such as gluon-gluon fusion or quark-gluon scattering sub-processes, the new calculation leads to a factor of two enhancement of cross-section, matching the observation. The involvement of gluon provided the correct mechanisms of large transverse momentum of the lepton pair. On the other hand, the Drell–Yan process also play an important role in validating QCD theory as the correct theory of strong interaction.

By considering the simple quark-antiquark annihilation and the first order partonic process in QCD to a lepton pair with large momentum transfer $Q \gg \Lambda_{\mathrm{QCD}}$, the Drell–Yan process successfully describes the hadronic cross-section despite there are still missing a lot of contributions from the gluon radiations and interactions from higher-order QCD dynamics. This success indicates that the Drell–Yan process captures the very important contribution to the cross-section when the momentum transfer is much larger than the hadronic scale.

A set of variables related to the Drell–Yan process is summarized in Tab. 1.1.

Variable(s)	Description
P_π, P_N	4-momenta of the pion, and of the target nucleon
$l, l', q = l + l'$	4-momenta of the leptons and the virtual photon
S_T	transverse component of the target polarization in Target Rest Frame
$Q^2 = q^2$	photon virtuality
$M_{\mu\mu} \sim \sqrt{Q^2}$	invariant mass of the dimuon
q_T	transverse component of the virtual photon momentum
$x_\pi = q^2/(2P_\pi \cdot q)$	pion Bjorken variable (often referred to as x_1)
$x_N = q^2/(2P_N \cdot q)$	nucleon Bjorken variable (often referred to as x_2)
$x_F = x_\pi - x_N$	Feynman variable

Table 1.1: Kinematic variables of Drell–Yan process.

1.2 The Drell–Yan Cross-Section

In the Drell–Yan process, the cross-section for the massive lepton pair production in hadronic collision can be factorized into the convolution of three terms: one is the partonic hard part cross-section which evaluated at the hard scale Q, the others are two non-perturbative and universal PDFs of two colliding hadrons.

In case of the large momentum transfer Q, the differential cross-section of the Drell–Yan process can be expressed as the leading-order (LO) contribution and a power series of higher-order QCD corrections:

$$\frac{\mathrm{d}\sigma}{\mathrm{d}Q^2} = \sum_n \frac{\mathrm{d}\sigma^{\mathrm{LO}}}{\mathrm{d}Q^2} \left[1 + O\left(1/Q^n\right)\right] \tag{1.2}$$

The leading-order contribution refers to the naive Drell–Yan process by simple quark-antiquark annihilation (as shown in Fig. 1.1), while the higher-order QCD corrections include processes with gluon. The higher-order terms can be approximated at the large momentum transfer Q region [9]. In this case the first term of $1/Q$ power expansion can be factorized into a convolution of the partonic hard part cross-section which is evaluated at the hard scale Q and two non-perturbative and universal PDFs of two colliding hadrons, as mentioned above.

Furthermore, the first subleading term of power expansion $(1/Q^2)$ for the massive lepton pair production in hadronic collisions can be factorized into the convolution of three probabilities: first is the partonic hard part cross-section which evaluated at the hard scale Q, second is a non-perturbative and universal PDF of one colliding hadron, and third is a non-perturbative and universal multiparton correlation functions [10].

It has been shown that the power expansion of the Drell–Yan cross-section beyond the first subleading term are not factorizable [11]. On the other hand, it is important to make sure that the higher-order corrections are sufficiently small when comparing the cross-section of Drell–Yan process between experimental data and theoretical predictions based on the factorized formalism.

1.2.1 Decay Angular Distribution

In the following, the discussion is made about the COMPASS experiment configurations (see Chapter 2), where is the reaction between an unpolarized negative pion beam H_π and a transversely polarized target H_N, while detecting muon-antimuon pair $\mu^+\mu^-$ in the final state. The Drell–Yan reaction from Eq. (1.1) can be re-written as following:

$$H_\pi(P_\pi) + H_N(P_N, S) \longrightarrow \gamma^*(q) + X \longrightarrow \mu^+(l') + \mu^-(l) + X \tag{1.3}$$

The Drell–Yan cross-section expressed in terms of the target spin S_T and the polar and azimuthal angles (θ_{CS} and φ_{CS}) of the decay muon pair are commonly defined using two coordinate systems: the target rest frame (TF) and the Collins–Soper (CS) virtual-photon rest frame [12, 13]. (The detailed definition of CS frame is shown in Section 6.1.) The frame definitions are sketched in Fig. 1.2.

When the polarizations of the produced leptons are summed over, the leading-order differential cross-section of pion-induced Drell–Yan production off a transversely polarized nucleon can be expressed as [12, 13]:

$$\begin{aligned}
\frac{\mathrm{d}\sigma}{\mathrm{d}q^4\mathrm{d}\Omega} &\propto \hat{\sigma}_U \\
&\times\Bigg\{1 + A_U^1\cos^2\theta_{\mathrm{CS}} + \sin 2\theta_{\mathrm{CS}} A_U^{\cos\varphi_{\mathrm{CS}}}\cos\varphi_{\mathrm{CS}} + \sin^2\theta_{\mathrm{CS}} A_U^{\cos 2\varphi_{\mathrm{CS}}}\cos 2\varphi_{\mathrm{CS}} \\
&\quad + S_T\Big[(A_T^{\sin\varphi_S} + \cos^2\theta_{\mathrm{CS}}\tilde{A}_T^{\sin\varphi_S})\sin\varphi_S \\
&\quad + \sin 2\theta_{\mathrm{CS}}\left(A_T^{\sin(\varphi_{\mathrm{CS}}+\varphi_S)}\sin(\varphi_{\mathrm{CS}}+\varphi_S) + A_T^{\sin(\varphi_{\mathrm{CS}}-\varphi_S)}\sin(\varphi_{\mathrm{CS}}-\varphi_S)\right) \\
&\quad + \sin^2\theta_{\mathrm{CS}}\left(A_T^{\sin(2\varphi_{\mathrm{CS}}+\varphi_S)}\sin(2\varphi_{\mathrm{CS}}+\varphi_S) + A_T^{\sin(2\varphi_{\mathrm{CS}}-\varphi_S)}\sin(2\varphi_{\mathrm{CS}}-\varphi_S)\right)\Big]\Bigg\}
\end{aligned} \tag{1.4}$$

Here $\hat{\sigma}_U = (F_U^1 + F_U^2)$, with F_U^1 and F_U^2 represent the polarization and azimuth-independent structure functions. The label U and T represent the unpolarized and the transverse polariza-

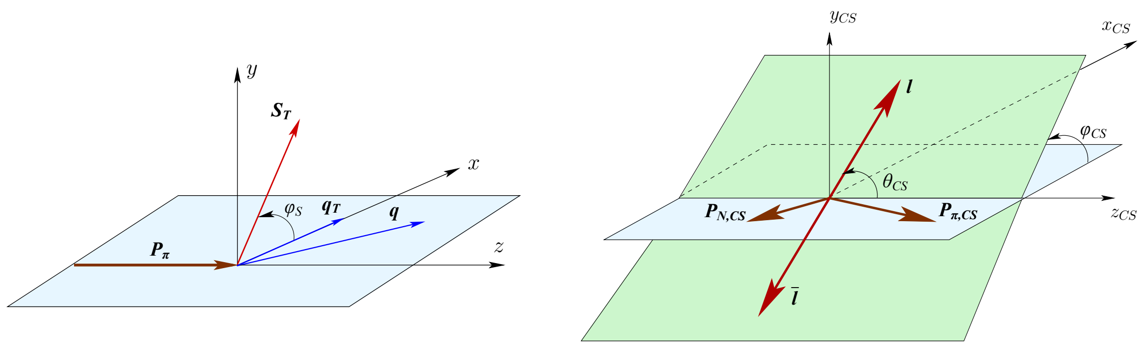

Figure 1.2: Reference systems. Left panel: target rest frame. Note that z-axis (x-axis) is chosen along the beam momentum (along q_T). Right panel: the Collins–Soper frame. The Collins–Soper frame is the rest frame of the virtual photon obtained from the target rest frame by boosting first along the z-axis and then along the x-axis so that both longitudinal and transverse components of the momentum of the virtual photon vanish.

tion dependence of the corresponding asymmetries, respectively. In Eq. (1.4), the leading-order differential cross-section of the Drell–Yan process contains five target Transverse-Spin-dependent Asymmetries (TSAs) and three Unpolarized Asymmetries (UAs), which will be discussed in more detail in Section 1.3 and Section 1.4, respectively. The definition of asymmetries A_U and A_T are the ratio of corresponding structure functions to the sum of the unpolarized ones ($\hat{\sigma}_U$). It is given as the amplitude of the respective modulations in the polar and azimuthal angle of the lepton momentum in the CS frame, which is θ_{CS} and φ_{CS} and also the azimuthal angle of the target spin vector in the target rest frame φ_{S} [12, 13].

1.3 The Transverse-Spin-Dependent Asymmetries

Considering the terms in the leading-order QCD parton model framework, Eq. (1.4) can be written as follows:

$$\begin{aligned}\frac{d\sigma}{dq^4 d\Omega} \propto \hat{\sigma}'_U \times \Big\{ 1 + D_{\sin^2\theta_{\text{CS}}} A_U^{\cos 2\varphi_{\text{CS}}} \cos 2\varphi_{\text{CS}} + S_T \Big[D_{1+\cos^2\theta_{\text{CS}}} A_T^{\sin\varphi_{\text{S}}} \sin\varphi_{\text{S}} \\ + D_{\sin^2\theta_{\text{CS}}} \sin^2\theta_{\text{CS}} \Big(A_T^{\sin(2\varphi_{\text{CS}}+\varphi_{\text{S}})} \sin(2\varphi_{\text{CS}}+\varphi_{\text{S}}) + A_T^{\sin(2\varphi_{\text{CS}}-\varphi_{\text{S}})} \sin(2\varphi_{\text{CS}}-\varphi_{\text{S}}) \Big) \Big] \Big\}\end{aligned} \tag{1.5}$$

where

$$\hat{\sigma}'_U = (F_U^1 + F_U^2)(1 + A_U^1 \cos^2\theta_{\text{CS}}) \tag{1.6}$$

At the leading-order perturbative QCD within the leading-twist approximation, $F_U^2 = 0$ therefore $A_U^1 = 1$. Here the depolarisation factor $D_{f(\theta_{\text{CS}})}$ depends only on the lepton polar angle, which is defined as follows:

$$D_{f(\theta_{\text{CS}})} = \frac{f(\theta_{\text{CS}})}{1 + A_U^1 \cos^2\theta_{\text{CS}}} \tag{1.7}$$

In the Eq. (1.5), only one unpolarized asymmetry term $A_U^{\cos 2\varphi_{CS}}$ and three TSAs terms $A_T^{\sin\varphi_S}$, $A_T^{\sin(2\varphi_{CS}+\varphi_S)}$ and $A_T^{\sin(2\varphi_{CS}-\varphi_S)}$ can be described by contributions from only leading-twist TMDs. The term $A_U^{\cos 2\varphi_{CS}}$ related to the Boer–Mulders TMD of the nucleon ($h_1^{q\perp}$), while $A_T^{\sin\varphi_S}$, $A_T^{\sin(2\varphi_{CS}+\varphi_S)}$ and $A_T^{\sin(2\varphi_{CS}-\varphi_S)}$ referred to the nucleon's Sivers TMD ($f_{1T}^{q\perp}$), Pretzelosity TMD ($h_1^{q\perp}$) and Transversity TMD (h_1^q), respectively. In greater detail, the connection of the measurement of those asymmetries to the TMDs are:

- $A_U^{\cos 2\varphi_{CS}}$ gives access to the Boer–Mulders functions of the incoming pion $h_{1,\pi}^{q\perp}$.
- $A_T^{\sin\varphi_S}$ gives access to the Sivers function of the target nucleon $f_{1T}^{q\perp}$.
- $A_T^{\sin(2\varphi_{CS}+\varphi_S)}$ gives access to the Boer–Mulders function of the beam pion $h_{1,\pi}^{q\perp}$ and the Pretzelosity function of the target nucleon $h_1^{q\perp}$.
- $A_T^{\sin(2\varphi_{CS}-\varphi_S)}$ gives access to the Boer–Mulders function of the beam pion $h_{1,\pi}^{q\perp}$ and the Transversity function of the target nucleon h_1^q.

1.3.1 Sivers Function

A measurement of the Sivers function plays an important role to understand the nature of the TMDs and the spin of the nucleons. The Sivers function is the correlation between the transverse momentum of quark and the transverse spin of proton, which was suggested by Sivers [14]. Because of the gauge link requirement in a gauge-invariant definition of the TMD and the time-reversal-odd object for the Sivers function, it requires a soft gluon during the initial- or final-state interactions. The Sivers function is connected to the angular momentum of the quark because it is related to the forward scattering amplitude, where the helicity of the nucleon is flipped so that the orbital angular momentum of the struck quark must be involved.

Several measurements of the Sivers $\sin(\varphi_h - \varphi_s)$ angular modulation in the SIDIS experiment with a transversely polarized target have been performed by HERMES [15], COMPASS [16, 17, 18, 19], and the JLab Hall-A [20] Collaborations. There are also some global fits have been performed and extracted the quark and antiquark Sivers functions from those measurements [21, 22]. The global analysis confirms the theoretical expectations for the sign of the u and d quarks Sivers functions, and also the non-zero $\bar{d}$ sea-quark Sivers function is obtained in order to explain the large Sivers moment observed for SIDIS production of K^+.

Because of the invariance of QCD under parity and time-reversal, the time-reversal-odd Sivers TMD $f_{p\uparrow}^q(x, k_T, \vec{S})$ for finding an unpolarized quark inside a transversely polarized proton from SIDIS and the Drell–Yan process satisfied:

$$f_{p\uparrow}^q(x, k_T, \pm\vec{S})\ |_{\text{Drell-Yan}} = f_{p\uparrow}^q(x, k_T, \mp\vec{S})\ |_{\text{SIDIS}} \tag{1.8}$$

Since the Sivers function $f_{1T}^{q\perp}(x, k_T)$ is proportional to the difference of TMD in two opposite orientation of polarized nucleons:

$$f_{1T}^{q\perp}(x, k_T) \propto \frac{f_{p\uparrow}^q(x, k_T, \pm\vec{S}) - f_{p\uparrow}^q(x, k_T, \mp\vec{S})}{2} \tag{1.9}$$

Base on the definition of Eq. (1.8), the Sivers function changes sign from SIDIS to the Drell–Yan process:

$$f_{1T}^{q\perp}(x, k_T)\ |_{\text{Drell-Yan}} = -f_{1T}^{q\perp}(x, k_T)\ |_{\text{SIDIS}} \tag{1.10}$$

As a consequence of factorization of TMD in QCD, the prediction and experimental test of sign-change of Sivers function have bring people's attention. As mentioned before, the signs of valence-quark Sivers function have already been measured from several SIDIS experiments, the missing puzzle for the test of sign change is the measurements of valence-quark Sivers functions in the single polarized Drell–Yan experiments. The first measurement of the Sivers effect in the Drell–Yan like process (W- and Z-boson production) in collisions of transversely polarized protons at Relativistic Heavy Ion Collider (RHIC) was reported by the STAR Collaboration [23]. However, the hard scales Q of these measurements from the STAR experiment are about 80 GeV/c and 90 GeV/c, which is quite different from the one explored in fixed-target experiments where Q ranges approximately between 1-9 GeV/c. Such high energy region is not excluded that TMD evolution effects may be sizeable when using Sivers TMD results extracted from fixed-target SIDIS experiments to describe the result from the STAR experiment. A dedicated Drell–Yan experiment at COMPASS (see Chapter 2) using 190 GeV/c pion beam off transversely polarized target have carried out the first measurement of the Sivers effect in the Drell–Yan process [24].

The asymmetries are reported in one-dimensional kinematic bins of x_N, x_π, x_F and q_T. Fig. 1.3 shows the result of TSAs $A_T^{\sin\varphi_S}$, $A_T^{\sin(2\varphi_{CS}+\varphi_S)}$ and $A_T^{\sin(2\varphi_{CS}-\varphi_S)}$ in the pion-induced Drell–Yan process as a function of x_N, x_π, x_F and q_T. The last column in Fig. 1.3 shows the TSAs results integrated over the entire kinematic range. Due to the relatively large statistical uncertainties, there is no clear trend observed for any of these TSAs.

The average Sivers asymmetry $A_T^{\sin\varphi_S} = 0.060 \pm 0.057(\text{stat.}) \pm 0.040(\text{syst.})$ is found to be positive at around one standard deviation of the total uncertainty. Fig. 1.4 highlights the extracted average Sivers asymmetry and the comparison with several theoretical predictions [22, 25, 26]. The sign-change hypothesis for the Sivers TMD in the Drell–Yan process with respect to the SIDIS process corresponding to the positive sign of Sivers asymmetry $A_T^{\sin\varphi_S}$. The first measurement of the Sivers asymmetry in Drell–Yan process from the COMPASS experiment is consistent with the predicted change of sign for the Sivers function [22, 25, 26].

1.3.2 Boer–Mulders Function

The Boer–Mulders function is the correlation between transverse spin of quark and its intrinsic transverse momentum in an unpolarized nucleon, which was proposed by Boer and Mulders [27]. Similar to Sivers function, the Boer–Mulders function is another time-reversal-odd TMD, which requires a soft gluon during the initial- or final-state interactions as well. For the time-reversal-odd TMD with a tensor spin projection $f_{p\uparrow}^{h_{1q}}(x, k_T, \vec{S})$ case, as in Eq 1.8 the measurement from SIDIS and Drell–Yan process satisfied:

$$f_{p\uparrow}^{h_{1q}}(x, k_T, \pm\vec{S})\ |_{\text{Drell-Yan}} = -f_{p\uparrow}^{h_{1q}}(x, k_T, \mp\vec{S})\ |_{\text{SIDIS}} \tag{1.11}$$

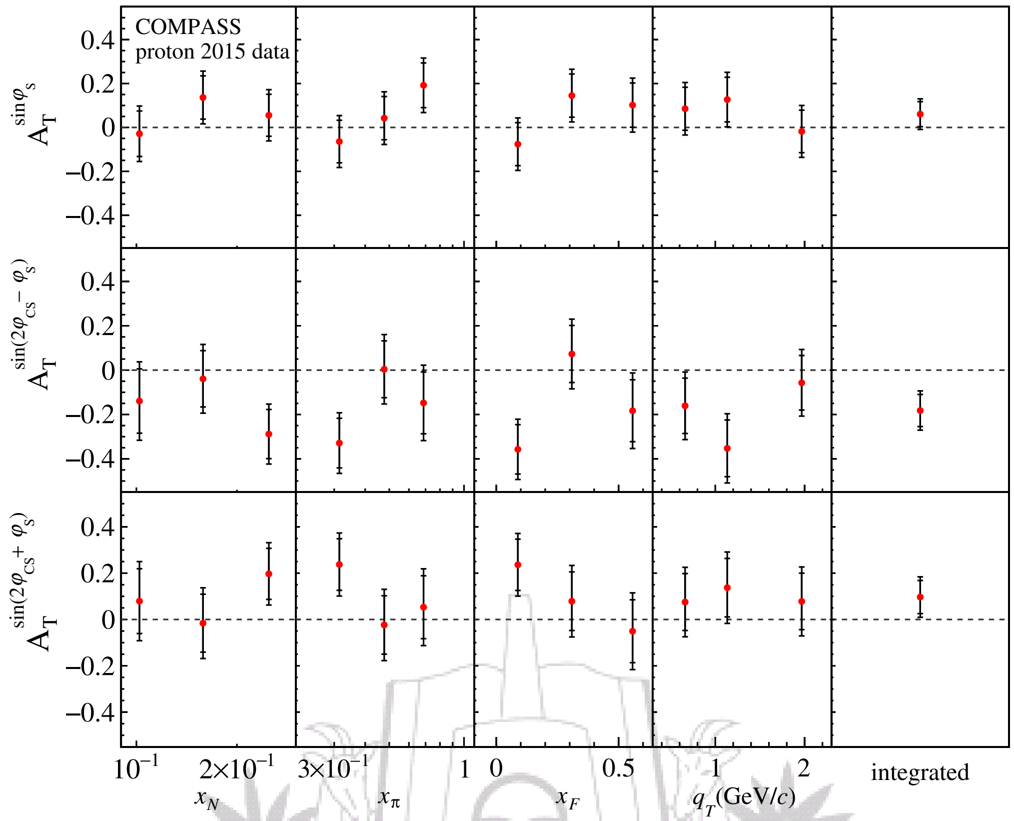

Figure 1.3: The extracted TSAs $A_T^{\sin\varphi_S}$, $A_T^{\sin(2\varphi_{CS}+\varphi_S)}$ and $A_T^{\sin(2\varphi_{CS}-\varphi_S)}$ in the pion-induced Drell–Yan process as a function of x_N, x_π, x_F and q_T by the COMPASS experiment. The inner (outer) error bars represent statistical (total experimental) uncertainties.(Adopted from [24])

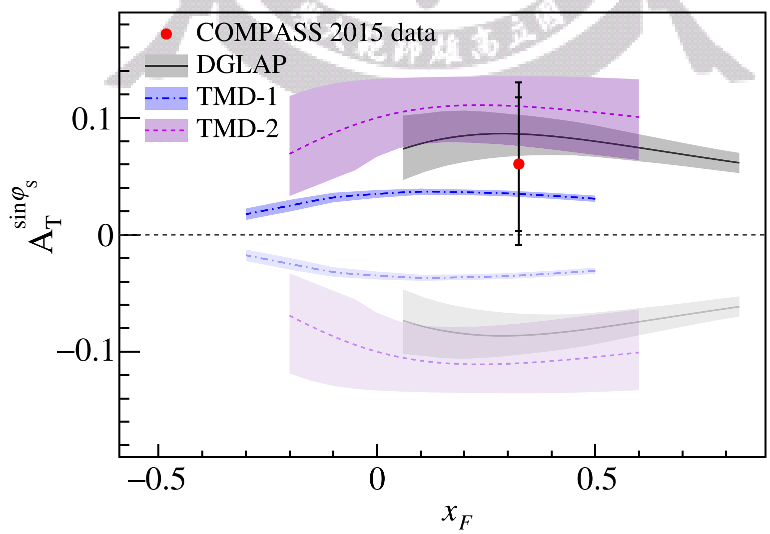

Figure 1.4: The extracted average Sivers asymmetry, compared with several theoretical predictions [22, 25, 26]. The dark-shaded (light-shaded) predictions are evaluated with (without) the sign-change hypothesis. (Adopted from [24])

Since the Boer–Mulders function $h_1^{q\perp}(x, k_T)$ is proportional to the difference of TMD in two opposite orientation of polarized quarks:

$$h_1^{q\perp}(x, k_T) \propto \frac{f_{p\uparrow}^{h_{1q}}(x, k_T \pm \vec{S}) + f_{p\uparrow}^{h_{1q}}(x, k_T, \mp\vec{S})}{2} \tag{1.12}$$

Base on the definition of Eq. (1.11), the Boer–Mulders function also changes sign from SIDIS to Drell–Yan process:

$$h_1^{q\perp}(x, k_T)\ |_{\text{Drell–Yan}} = -h_1^{q\perp}(x, k_T)\ |_{\text{SIDIS}} \tag{1.13}$$

Several models have calculated the flavour and x dependencies of the Boer–Mulders functions. Such as the quark-diquark model [28], the relativistic constituent quark model [29], and also the lattice QCD [30]. All models predicted that the u and d valence-quark Boer–Mulders functions are negative from the SIDIS process.

While the Sivers functions do not exist for spin-zero hadrons, the Boer–Mulders functions can be non-zero for pions. There are several model predictions for the pion's valence-quark Boer–Mulders functions, such as quark-spectator-antiquark model [31] and bag model [32]. All models give a consistent prediction that the valence-quark Boer–Mulders functions for nucleons and mesons are of the same signs and also similar magnitude. This universal behavior of the valence-quark Boer–Mulders functions from pions and nucleons is to be confirmed by the experiment in the future. For the nucleon's antiquark Boer–Mulders functions are calculated by the meson cloud model [33], which is an important source for sea quarks in the nucleons. Base on this model, the nucleon's antiquark Boer–Mulders functions can be contributed by the valence-quark Boer–Mulders functions in the pion cloud, which give the prediction that the nucleon's antiquark Boer–Mulders functions are of the same signs (negative) as the valence-quark Boer–Mulders functions for pion.

Tab. 1.2 summarized the theoretical prediction to the signs of the Boer–Mulders functions from the SIDIS and Drell–Yan processes. All the theoretical predictions give the consistent results that the sign of Boer–Mulders functions for u, d valence-quark and $\bar{u}$, $\bar{d}$ antiquark in the nucleon, and also the valence-quark in the pion are of negative sign. Furthermore, the signs of these Boer–Mulders functions will reverse and become positive for the Drell–Yan process with respect to the SIDIS process.

Table 1.2: The summary of theoretical prediction to the signs of the Boer–Mulders functions from the SIDIS and Drell–Yan processes.

	u_N	d_N	$\bar{u}_N$	$\bar{d}_N$	V_π
SIDIS	-	-	-	-	-
Drell–Yan	+	+	+	+	+

1.4 The Unpolarized Asymmetries

In the literature the three unpolarized asymmetries in Eq. (1.4) are often expressed by:

$$\lambda = A_U^1, \quad \mu = A_U^{\cos\varphi_{\text{CS}}}, \quad \nu = 2A_U^{\cos 2\varphi_{\text{CS}}} \tag{1.14}$$

These terms attracted particular attention on both theoretical and experimental side in the last decades. The unpolarized part of the differential cross-section in d^4q and $d\Omega = d\cos\theta_{CS}\, d\varphi_{CS}$ can be written as follows [34]:

$$\frac{d\sigma}{dq d\Omega} = \frac{\alpha^2}{2\pi N_c Q^2 s^2}\Big[F_U^1(1+\cos^2\theta_{CS}) + F_U^2(1-\cos^2\theta_{CS}) + F_U^{\cos\varphi_{CS}}\sin 2\theta_{CS}\cos\varphi_{CS} + F_U^{\cos 2\varphi_{CS}}\sin^2\theta_{CS}\cos 2\varphi_{CS}\Big] \tag{1.15}$$

where $N_c = 3$ is the number of colours in QCD, s represents the center of mass squared energy of the reaction and F_U^1, F_U^2, $F_U^{\cos\varphi_{CS}}$ and $F_U^{\cos 2\varphi_{CS}}$ are the structure functions depending on q. From Eq. (1.15) one can derive the expression for the normalized decay angular distribution:

$$\frac{dN}{d\Omega} = \frac{3}{8\pi}\left[\frac{F_U^1(1+\cos^2\theta_{CS}) + F_U^2(1-\cos^2\theta_{CS})}{2F_U^1 + F_U^2} + \frac{F_U^{\cos\varphi_{CS}}\sin 2\theta_{CS}\cos\varphi_{CS} + F_U^{\cos 2\varphi_{CS}}\sin^2\theta_{CS}\cos 2\varphi_{CS}}{2F_U^1 + F_U^2}\right] \tag{1.16}$$

By introducing λ, μ and ν, which defined as following:

$$\lambda = \frac{F_U^1 - F_U^2}{F_U^1 + F_U^2}, \quad \mu = \frac{F_U^{\cos\varphi_{CS}}}{F_U^1 + F_U^2}, \quad \nu = 2\frac{F_U^{\cos 2\varphi_{CS}}}{F_U^1 + F_U^2} \tag{1.17}$$

In conclusion, one can re-write Eq. (1.16) by three unpolarized asymmetries λ, μ and ν as following:

$$\frac{dN}{d\Omega} \propto \frac{3}{4\pi}\frac{1}{\lambda+3}\left(1 + \lambda\cos^2\theta_{CS} + \mu\sin 2\theta_{CS}\cos\varphi_{CS} + \frac{\nu}{2}\sin^2\theta_{CS}\cos 2\varphi_{CS}\right) \tag{1.18}$$

1.5 Lam–Tung Relation

In the naive Drell–Yan model, or at leading-order, the virtual photon formed by annihilation of quark and anti-quark ($q\bar{q} \to \gamma^*$) is transversely polarized, which means that the lepton angular distribution varies as $1 + \cos^2\theta_{CS}$ (i.e. $\lambda = 1$, $\mu = 0$, $\nu = 0$) because of the helicity conservation. This is one of the successes of the naive Drell–Yan model whose prediction was soon confirmed by the experimental measurement.

Beyond the electromagnetic leading-order Drell–Yan model, the higher-order QCD effects in $O(\alpha_s)$ (such as gluon emission $q\bar{q} \to \gamma^* g$ and quark-gluon Compton scattering $qg \to \gamma^* q$), the intrinsic transverse momentum of partons k_T contribution should be included. The virtual photon is not required to be fully transversely polarized and the azimuthal-related unpolarized asymmetries μ and ν are no longer zero. Nevertheless, the so-called Lam–Tung relation [35] is expected to hold for the next-leading-order Drell–Yan process:

$$1 - \lambda = 2\nu \tag{1.19}$$

where a non-zero ν generates non-zero dependence on $\cos 2\varphi_{CS}$.

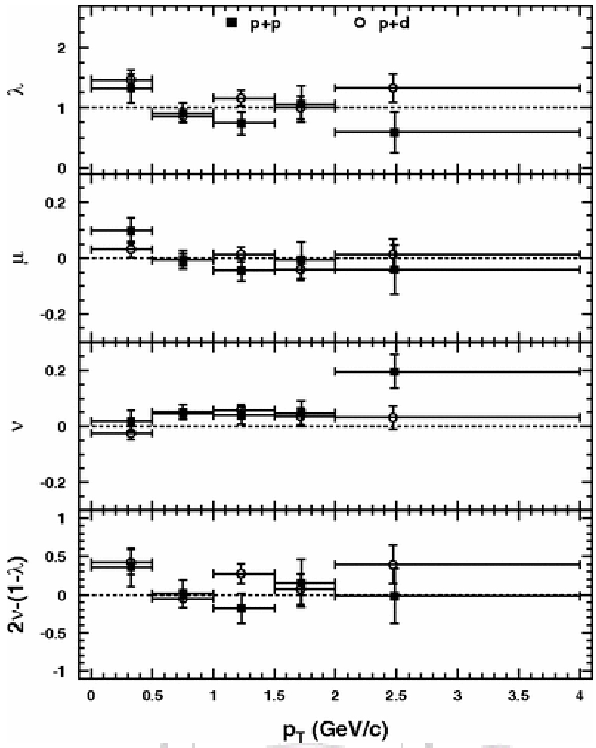

Figure 1.5: The unpolarized asymmetries result λ, μ, ν and also $1 - \lambda - 2\nu$ relation as a function of q_T from E866 measurement (Adopted from [36])

The Lam–Tung relation was found to be satisfied in the proton-induced Drell–Yan production by E866 experiment [36]. Fig. 1.5 shows the unpolarized asymmetries result λ, μ, ν and also $1 - \lambda - 2\nu$ relation as a function of q_T from E866 measurement.

However, if one take into account the contribution from the next-to-next-leading-order (NNLO) Drell–Yan process ($O(\alpha_s^2)$), such as $q\bar{q} \to \gamma^* gg$, $qg \to \gamma^* qg$ and $gg \to \gamma^* g$, the Lam–Tung relation is expected to be violated base on perturbative QCD calculation [37].

The violation of Lam–Tung relation have been tested in both proton- and pion-induced Drell–Yan experiments at CERN and Fermilab. In case of proton-induced Drell–Yan experiments, one of the measurement for the lepton pair angular distribution of Z-boson production in proton-proton collision at $\sqrt{s}$ = 8 TeV at the Large Hadron Collider (LHC) is carried out by the CMS collaboration [38], which shows a clear Lam–Tung violation at large transverse momentum region (q_T up to 300 GeV). Similar measurement also carried out by the CDF collaboration in proton-antiproton collision at $\sqrt{s}$ = 1.96 TeV at Fermilab [39], which shows no Lam–Tung violation at large transverse momentum region (q_T up to 90 GeV). Fig. 1.6 shows the extracted λ and ν as a function of transverse momentum by CMS measurement and compare with perturbative calculation [34]. Fig. 1.7 shows the extracted λ and ν as a function of transverse momentum by CDF measurement and compare with perturbative calculation [34].

In case of the pion-induced Drell–Yan experiments, the unpolarized asymmetries were studied by two fixed-target experiments in the past [41, 44]. During the '80s, NA10 [41, 42, 43] at CERN was one of the pioneering Drell–Yan experiments. The experiment performed a series of pion-induced Drell–Yan measurements using different beam energies (140, 194 and 286 GeV). A large sample of 152,000 Drell–Yan events for dimuon masses $M_{\mu\mu} > 4.05$

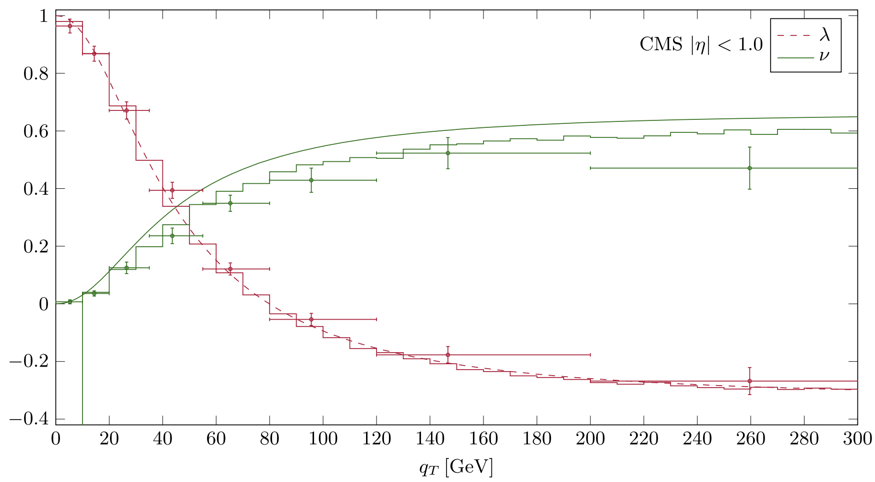

Figure 1.6: The unpolarized asymmetries result λ and ν as a function of q_T from CMS measurement, which comparing with LO (line) and NLO (histogram) fixed-order perturbative QCD calculations. (Adopted from [34])

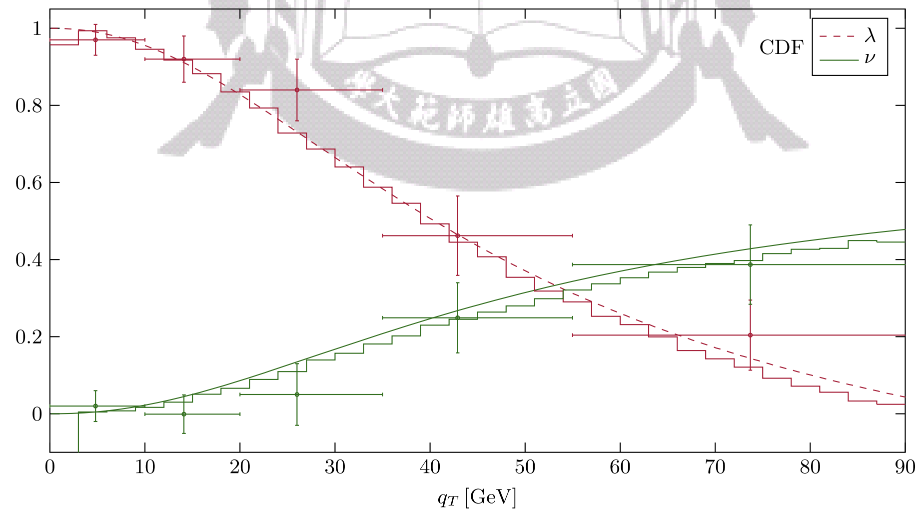

Figure 1.7: The unpolarized asymmetries result λ and ν as a function of q_T from CDF measurement, which comparing with LO (line) and NLO (histogram) fixed-order perturbative QCD calculations. (Adopted from [34])

GeV/c^2, was collected using the 194 GeV beam and a tungsten target.

In the meantime during the ’80s, the unpolarized Drell–Yan measurements were also performed by the E615 collaboration at Fermilab, using 252 GeV π^- beam scattering off a tungsten (W) target. The results, presented in Ref. [44], were obtained from the analysis of ~36,000 Drell–Yan events with $M_{\mu\mu} > 4.05$ GeV/c^2. A summary of the unpolarized asymmetries result from three fixed-target experiments (NA10, E615 and E866) is shown in Tab. 1.3.

Table 1.3: The summary of the unpolarized asymmetries result from two fixed-target pion-induced Drell–Yan and one proton-induced Drell–Yan experiments [41, 44].

Experiment Interaction Beam Energy	**NA10** $\pi^- + W$ 194 GeV/c	**E615** $\pi^- + W$ 252 GeV/c	**E866** $p + d$ 800 GeV/c
$\langle\lambda\rangle$	0.83 ± 0.04	1.17 ± 0.06	1.07 ± 0.07
$\langle\mu\rangle$	0.008 ± 0.010	0.09 ± 0.02	0.003 ± 0.013
$\langle\nu\rangle$	0.091 ± 0.009	0.169 ± 0.019	0.027 ± 0.010
$\langle 2\nu - (1-\lambda)\rangle$	0.01 ± 0.04	0.51 ± 0.07	0.12 ± 0.07
x_1 range	$0.2 \to 1.0$	$0.2 \to 1.0$	$0.15 \to 0.85$
x_2 range	$0.1 \to 0.4$	$0.04 \to 0.38$	$0.02 \to 0.24$

The Lam–Tung relation was found to be strongly violated in E615 and NA10 measurements, which is also significantly deviated from the perturbative QCD calculations. Fig. 1.8a-1.8b shows the comparison of unpolarized asymmetries result λ, μ, ν and also $1 - \lambda - 2\nu$ relation as function of q_T with NLO and NNLO fixed-order perturbative QCD calculations from NA10 and E615 measurement, respectively.

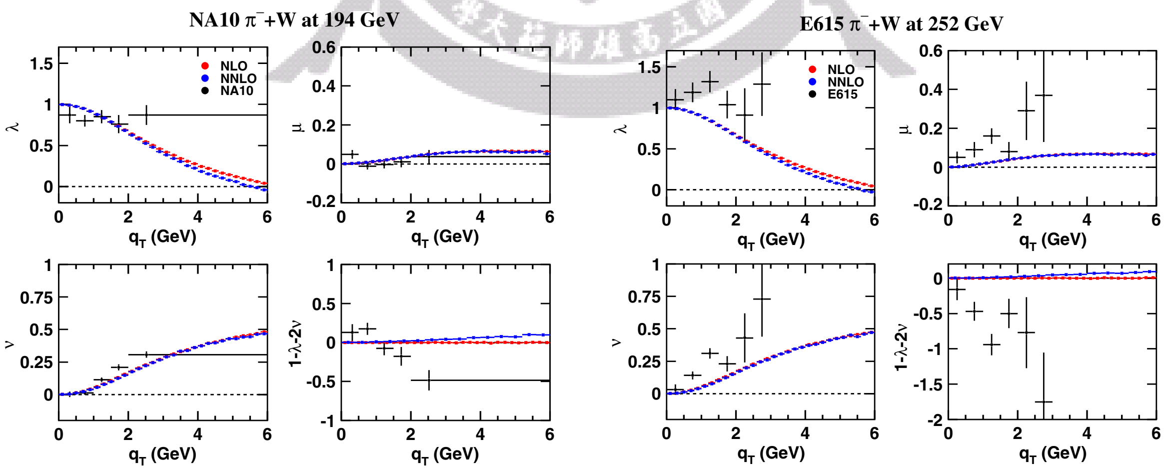

(a) NA10 (b) E615

Figure 1.8: The unpolarized asymmetries result λ, μ, ν and also $1-\lambda-2\nu$ relation as function of q_T from NA10 and E615 measurement, which comparing with NLO (red point) and NNLO (blue point) fixed-order perturbative QCD calculations. (Adopted from [40])

1.6 The Boer–Mulders functions in the Drell–Yan Process

An explanation of the $\cos 2\varphi_{CS}$ dependence beyond the Lam–Tung relation observed in the Drell–Yan process was meanwhile proposed, by introducing a non-perturbative TMD Boer–Mulders function [45] at small transverse momentum of the lepton pair.

The Boer–Mulders asymmetry can be accessed by not only from the leading-twist differential cross-section in Eq. (1.4) ($A_U^{\cos 2\varphi_{CS}}$) but also from the unpolarized differential cross-section in Eq. (1.18) (ν).

The Boer–Mulders function $h_1^{q\perp}$ represents a correlation between quark's intrinsic transverse momentum and transverse spin (transversely polarized quark) in an unpolarized hadron. In case of the pion-induced Drell–Yan production, the contribution of the Boer–Mulders effect in ν is proportional to the convolution of the nucleon's valence-quark Boer–Mulders functions $h_{1,N}^{q\perp}$ and the pion's valence-antiquark Boer–Mulders functions $h_{1,\pi}^{\bar{q}\perp}$:

$$A_U^{\cos 2\varphi_{CS}} = \frac{\nu}{2} \propto h_{1,N}^{q\perp} h_{1,\pi}^{\bar{q}\perp} \tag{1.20}$$

The $\cos 2\varphi_{CS}$ angular dependence can be qualitatively understood as caused by the correlation of transverse spins of the annihilating quark and antiquark through the Boer–Mulders functions. The $\cos 2\varphi_{CS}$ dependence observed in the NA10 and E615 pion-induced Drell–Yan experiments and also in the E866 proton-induced Drell–Yan experiment, can be quantitatively described by the calculations with the Boer–Mulders function.

By comparing the measurement of ν as a function of q_T from proton-induced Drell–Yan production (Fig. 1.5) and pion-induced Drell–Yan production (Fig. 1.8a-1.8b), one can noticed the overestimation/underestimation of asymmetry ν with respect to the perturbative QCD calculation. On the other hand, the measurement suggests a negative contribution from the Boer–Mulders effect in the proton-induced Drell–Yan production, while a positive contribution from the Boer–Mulders effect in the pion-induced Drell–Yan production, which is consistent with the theoretical prediction (see Tab. 1.2). This sign changed result imply that the proton's sea-quark Boer–Mulders function has a sign opposite to the proton's valence-quark Boer–Mulders function, while the pion's valence-quark Boer–Mulders function has a same sign to the proton's valence-quark Boer–Mulders function [46].

Boer [45] assumed that $h_1^{q\perp}$ is proportional to the spin-averaged PDF $f_1(x)$:

$$h_1^{q\perp}(x, k_T) = C_H \frac{\alpha_T}{\pi} \frac{M_c M_H}{k_T^2 + M_c^2} e^{-\alpha_T k_T^2} f_1(x) \tag{1.21}$$

where M_H is the mass of hadron, M_C and C_H are both constant fitting parameters, α_T is a fixed fitting parameter which assumed to be 1 $(GeV/\mathrm{c})^{-2}$. Base on this parametrization, the asymmetry ν is given as following:

$$\nu = 16\kappa_1 \frac{q_T^2 M_c^2}{(q_T^2 + 4M_c^2)^2} \tag{1.22}$$

where $\kappa_1 = C_{H_1} C_{H_2}/2$ for the incoming two hadrons H_1 and H_2. The large value of κ_1 fitting result represent a sizeable Boer–Mulders function for the valence antiquark in the pion and for the valence quarks in the nucleon. However, this empirical parametrization (Eq. (1.22)) somehow depending on the beam energy, which contradicts with the universality of TMD Boer–Mulders function.

Fig. 1.9 shows the ν extraction from both the pion- and proton-induced Drell–Yan experiments and fitted by Eq. (1.22). It's clear to see that the asymmetry ν measured from

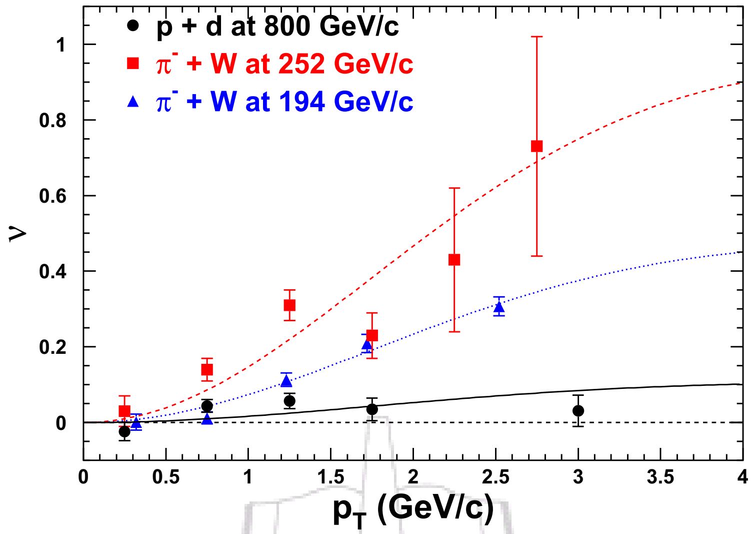

Figure 1.9: The ν extraction as a function of q_T from both pion- (NA10 in blue, E615 in red) and proton-induced (E866 in black) Drell–Yan experiments. Curves are fits to the data using an empirical parametrization. (Adopted from [47])

the proton-induced Drell–Yan experiment is significantly smaller than the pion-induced Drell–Yan experiment. Since the pion-induced Drell–Yan cross-section is dominated by the annihilation between a valence antiquark in the pion and a valence quark in the nucleon, while a sea antiquark in the nucleon is contributed during the annihilation for the proton-induced Drell–Yan cross-section. On the other hand, the result from the proton-induced Drell–Yan experiment suggest that the proton's sea-quark Boer–Mulders functions are smaller than valence quarks.

There are several theoretical prediction for the Boer–Mulders functions of proton from proton-induced Drell–Yan data ($p+p$ and $p+d$ interaction). Fig. 1.10 shows the calculation of asymmetry ν as function of q_T for the proton-induced Drell–Yan process and compare with both $p+p$ and $p+d$ Drell–Yan data, which obtained by Ref. [48]. Despite the statistical uncertainties of the data still not precise enough to accurately extract the Boer–Mulders functions of proton, it clearly shows that the proton's sea-quark Boer–Mulders functions can be extracted from the Drell–Yan data.

Recently, there are also some theoretical predictions for the Boer–Mulders functions of pion from pion-induced Drell–Yan process. Fig. 1.11 and Fig. 1.12 show the prediction of $A_U^{\cos 2\varphi_{CS}}(\nu)$ asymmetry contribution from the Boer–Mulders effect for COMPASS kinematics [49, 50]. The ongoing unpolarized pion-induced Drell-Yan experiments at COMPASS are expected to provide new information on the pion's Boer–Mulders functions.

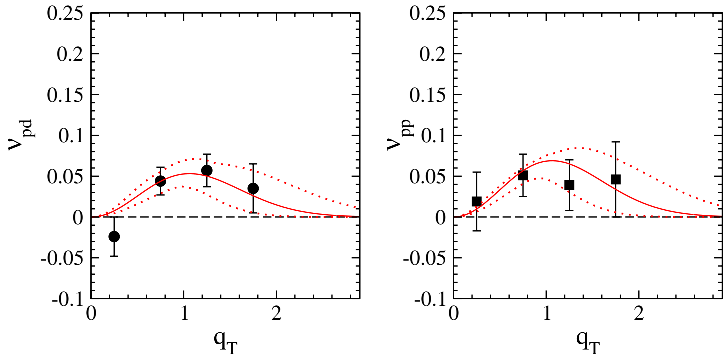

Figure 1.10: The ν extraction as a function of q_T from proton-induced ($p + p$ in the right panel and $p + d$ in the left panel) Drell–Yan experiments. Curves are the fitted result which described in Ref. [48] (Adopted from [48])

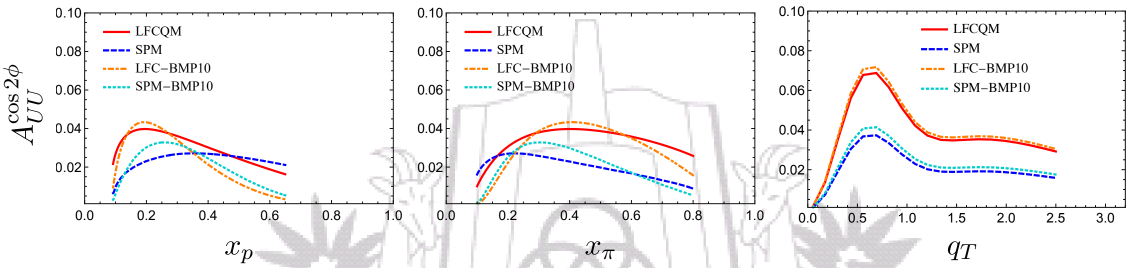

Figure 1.11: $A_U^{\cos 2\varphi_{CS}}$ as s function of x_N (left), x_π (middle) and q_T (right) in the COMPASS kinematics. (Adopted from [49])

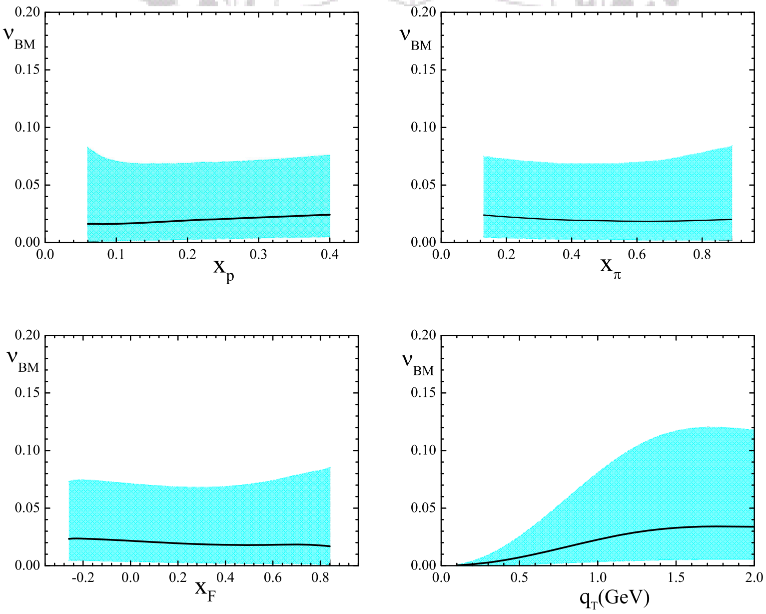

Figure 1.12: $A_U^{\cos 2\varphi_{CS}}$ as s function of x_p (top-left), x_π (top-right), x_F (bottom-left) and q_T (bottom-right) in the COMPASS kinematics. (Adopted from [50])

CHAPTER 2

The COMPASS Experiment

The COMPASS (COmmon Muon Proton Apparatus for Structure and Spectroscopy) experiment is a high-energy fixed-target experiment at SPS (Super Proton Synchrotron) at CERN (also known as European Organization for Nuclear Research) in Geneva, Switzerland. This experiment aims to probe the structure and spectroscopy of hadrons. This chapter will mainly focus on the introduction of beam line, target, spectrometers and trigger system which dedicate for the Drell–Yan measurement.

2.1 Overview of the COMPASS Experiment

In February 1997, the COMPASS experiment was approved by CERN Research Board. This single experiment was actually unified by two different physics projects from two distinct groups: one is to probe the spin structure of the nucleon by using a muon beam, the other is to probe the hadron spectroscopy by using hadron beam. Building on that, many efforts have been done by COMPASS collaborators and resulting a highly flexible and multi-purpose set-up experiment. The spectrometers were built and installed during the years 1999 and 2000, then the first technical run started in 2001. The first physics data taking with a muon beam and either longitudinally or transversely polarised proton and deuteron targets started in 2002, which was a muon run for probing the quark-gluon structure of nucleon through SIDIS. After a year of shut-down in 2005, the muon run was continued in the years 2006, 2007, 2010 and 2011 with a new large-aperture target magnet. The physics data taking with hadron beams scattering off a liquid hydrogen target and nuclear targets started in 2008 and extended to 2009, which was a hadron run for the hadron spectroscopy programme. The physics measurements approved in the beginning of COMPASS were finished in 2011.

A second-phase of COMPASS (also known as COMPASS-II) have been proposed [13] and approved by CERN in 2010. The continuation of the COMPASS experiment include three physics programs: The Primakoff measurement, the polarized Drell–Yan measurement, and the Deeply Virtual Compton Scattering (DVCS) measurement. The first physics data taking was dedicated to the Primakoff measurement and started in 2012. The physics data taking for the polarized Drell–Yan measurement with a beam of negative pions and a polarized proton target was performed in the years 2015 and 2018. The years 2016 and 2017 were dedicated to DVCS measurement with a muon beam.

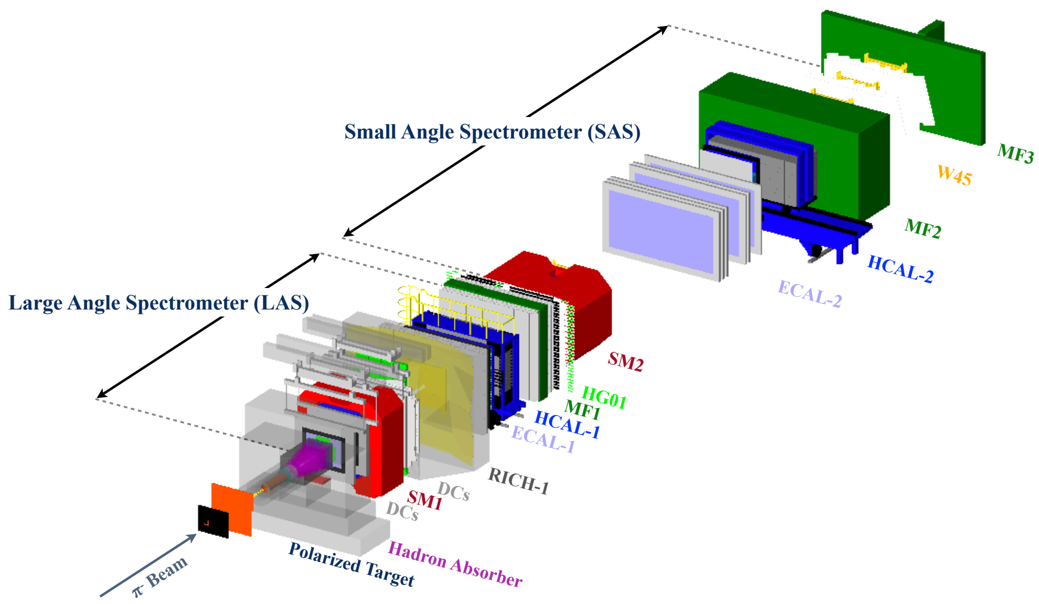

Figure 2.1: The sketch of two-staged spectrometers set-up during the COMPASS Drell–Yan measurement in the year 2018.

The spectrometers behind the target in the COMPASS experiment are about 50-m long two-staged spectrometers which consist of two dipole magnets. Fig. 2.1 shows a sketch of two-staged spectrometers set-up during the COMPASS Drell–Yan measurement in the year 2018. The first stage of spectrometer, namely Large Angle Spectrometer (LAS), contains the first dipole magnet (SM1) with a field integral of 1.0 Tm which is located at right after the target. This spectrometer is mainly used to measure small momentum particles travelled with a large angle. The second stage of spectrometer, namely Small Angle Spectrometer (SAS), contains the second dipole magnet (SM2) with a field integral of 4.4 Tm. This spectrometer is mainly used to measure high-momentum particles within a small angle.

The convention of experimental coordinate in the COMPASS experiment is defined as follows: a z-axis is defined as the direction of beam line, a y-axis is defined as the direction from the ground surface to the sky, and a x-axis definition is constrained by right-hand rule ($\hat{x} \equiv \hat{y} \times \hat{z}$). For the x coordinate, in particularly, the left (right) hand side is referred to the Jura (Saleve) side[1] when the one looking down the beam line, respectively.

2.2 Beam Line

The hadron or muon beam used in the COMPASS experiment is produced by the CERN SPS M2 beam line. The CERN SPS M2 beam line was rebuilt from originally delivered only a high-intensity muon beam to now also provide a high-intensity hadron beam. A hadron and muon beams can be either a negative or a positive charge. Switching between different type of beams usually takes about 30 minutes. The hadron beam is a secondary product which is generated by using a 400 GeV/c proton beam from the CERN SPS impinging a primary beryllium (Be) production target (T6) at the entrance of M2 beam line. In order to achieve variation of beam intensity, four different thickness (40, 100, 200 or 500 mm) of Be targets or empty target is adjustable. For instance, a hadron beam with 190 GeV/c central momentum and intensity up to 10^8 hadrons per second is achieved by using 500 mm thick Be target. The length of beam line from T6 target to the COMPASS target is 1131.8 m. The schematic view of M2 beam line is shown in Fig. 2.2.

During the Drell–Yan measurement, a negative hadron beam with 190 GeV/c central momentum was used, which the pion (π^-) is the dominate component (96.8%). Since the π^- beam is just one of secondary hadron product ($\pi^\pm$, $K^\pm$, p and $\bar{p}$) from T6 target, the selection and isolation of π^- beam is achieved by an array of quadrupoles and dipoles distributed downstream of T6 target along the M2 beam line. However, K^- and $\bar{p}$ may be still present in the outcome of beam at a level of a few percent (2.4% of K^- and 0.8% of $\bar{p}$). A summary of relative composition of the hadron beam for typical momenta available at the M2 beam line is shown in Tab. 2.1.

The most upstream part of the COMPASS apparatus, Beam Momentum Station (BMS), is located at about 100 m upstream of the COMPASS target region. This station consists of four scintillator hodoscopes (BM01-BM04), two scintillating fibres (BM05 and BM06), an array of quadrupoles for selecting beam momentum and three consecutive dipole magnets (B6) for bending the beam horizontally which is deflected upwards to the surface level. The schematic view of BMS is shown in Fig. 2.3. The BMS is mainly used to measure the incident beam

[1]This was referred to the name of neighboring mountains.

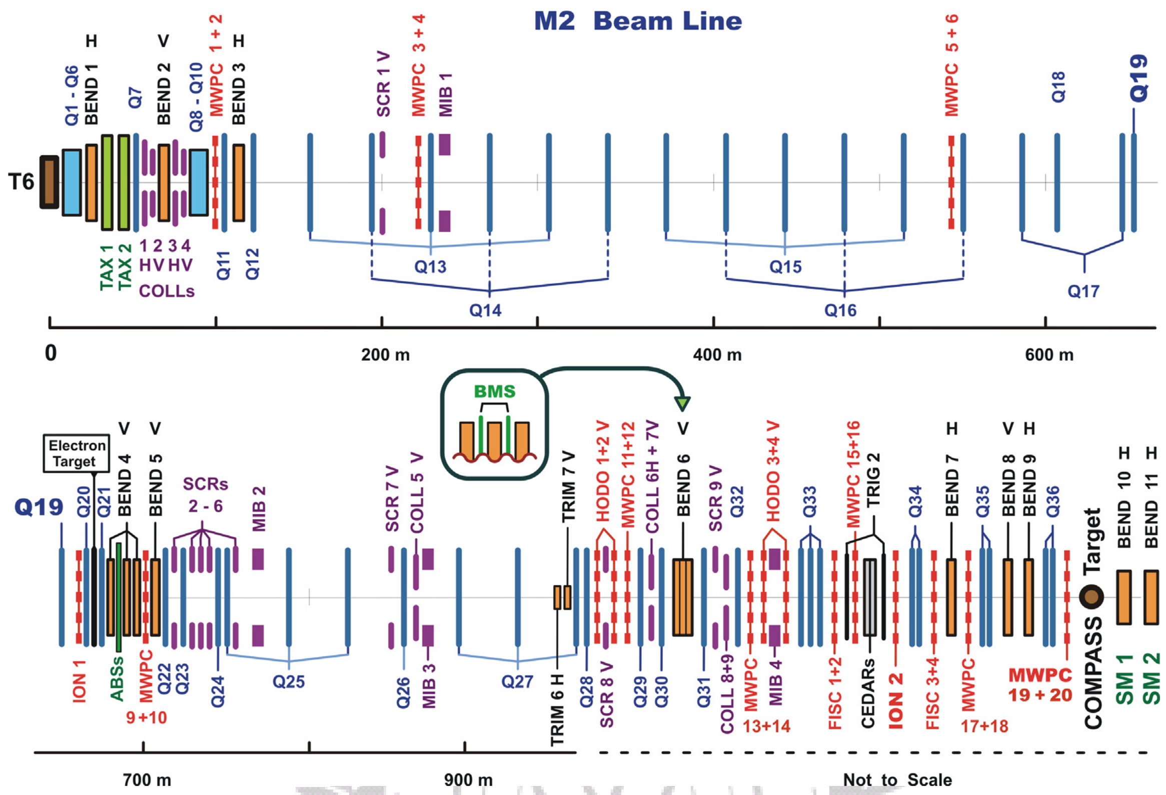

Figure 2.2: The CERN SPS M2 beam line. (Adopted from [51])

Momentum	**Positive beams**			**Negative beams**		
(GeV/c)	π^+	K^+	p	π^-	K^-	$\bar{p}$
100	61.8%	1.5%	36.7%	95.8%	1.8%	19.1%
160	36.0%	1.7%	62.3%	96.6%	2.3%	31.9%
190	24.0%	1.4%	74.6%	96.8%	2.4%	0.8%
200	20.5%	1.2%	78.3%	96.9%	2.4%	0.7%

Table 2.1: The relative composition of the hadron beam at the COMPASS experiment for some typical momenta, which is calculated from measured values [52]. The relative uncertainties for pions and protons is around 1%, while for kaons and anti-protons is 2-3%.

momentum for muon beam, while it is moved out of the M2 beam line during the hadron beam setting in order to minimise the material budget along the beam path.

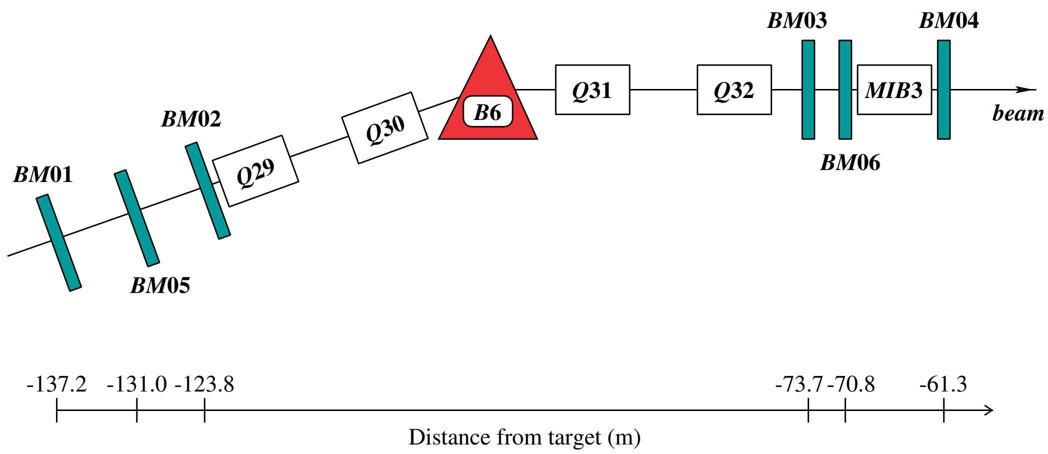

Figure 2.3: The schematic view of Beam Momentum Station. (Adopted from [53])

2.3 Polarised Target and Hadron Absorber

In the COMPASS Drell–Yan measurement, two of most important components: a polarized target and a hadron absorber, which are both located at upstream of spectrometers. The polarized target station is the most complex and important set-up in the COMPASS experiment which bring the possibility for the measurement of transverse spin asymmetries. And the hadron absorber station is a protector of spectrometers which possess a strong stopping power on hadron showers from the beam-target interaction to prevent the damage on detectors.

A sketch of the polarized target station is shown in Fig. 2.4. The polarized target station consists two cells of polarizable solid-state ammonia (NH_3) in a liquid helium (mixture of 10% ^{3}He and 90% ^{4}He) cooling bath, which are packed inside two separated cylindrical PCTFE (PolyChloroTriFluoroEthylene[2]) made containers. The target cells are placed in the dilution refrigerator (so-called polarized target cryostat) in order to stabilize the polarization of solid-state NH_3 cells with a low temperature (around 60 mK), which only the hydrogen protons are polarizable. The polarization is achieved using the Dynamic Nucleon Polarization (DNP) technique [55], The DNP technique transfers the polarization of electrons to the polarization of nucleons since the electron possess higher magnetic moment and make it easier to polarize than the nucleon.

The transferring of polarization from electron to nucleon is achieved by using high intensity microwaves (about 70 GHz) to irradiate on the polarizable material in conditions of low temperature and high homogeneous magnetic field (typically in several Tesla), so that the proton spin will get parallel or anti-parallel to the magnetic field. This technique is possible to polarize the hydrogen protons up to 90% polarization. The measurement of the polarization

[2]A special material with excellent resistance at low temperature which can minimized perturbation of the polarization

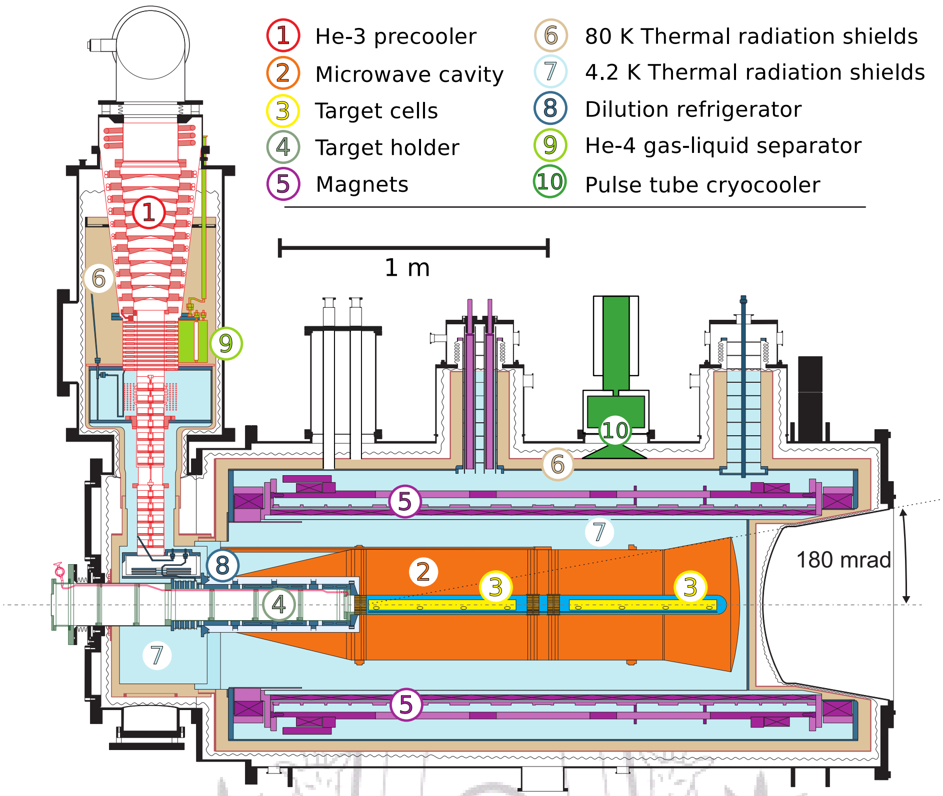

Figure 2.4: The sketch of the polarized target station. (Adopted from [54])

is done by using ten coils of Nuclear Magnetic Resonance (NMR) which were attached on both of two PCTFE containers separately. A sketch of PCTFE containers and NMR coils is shown in Fig. 2.5.

The COMPASS polarized target system consists of two magnetic field: One is a superconducting solenoid magnet with a high homogeneous magnetic field of 2.5 T, and another is a superconducting dipole magnet with a 0.63 T filed in the transverse direction. The solenoid magnet generates a longitudinal (parallel to the beam axis) field which is used for DNP procedure. The dipole magnet generates a transverse (perpendicular to the beam axis) direction field which is used for polarization rotation. During the polarization procedure, the longitudinal polarization is achieved first with applying the solenoid magnet. The solenoid magnet will be switched off and the target materials will be rapidly cooled in order to go in the frozen-spin regime after reaching a desired polarization value. After the longitudinal polarization is done, the transverse polarization is achieved by applying the dipole magnet to rotate the polarization of target materials in the frozen-spin regime from longitudinal to transverse direction. In order to hold the polarization in transverse direction, the dipole magnet keeps turning on during the physics data taking. On the other hand, the incident angle of beam line is adjusted in order to compensate the deviation from magnetic field. During the Drell–Yan measurement in years 2015 and 2018, two ammonia target cells with both 55 cm long with a diameter 4 cm and a 20 cm gap between two cells were installed.

The hadron absorber is placed downstream of the polarized target region. It is mainly used to reduce the high-rate secondary particle flux produced by the interaction of the pion

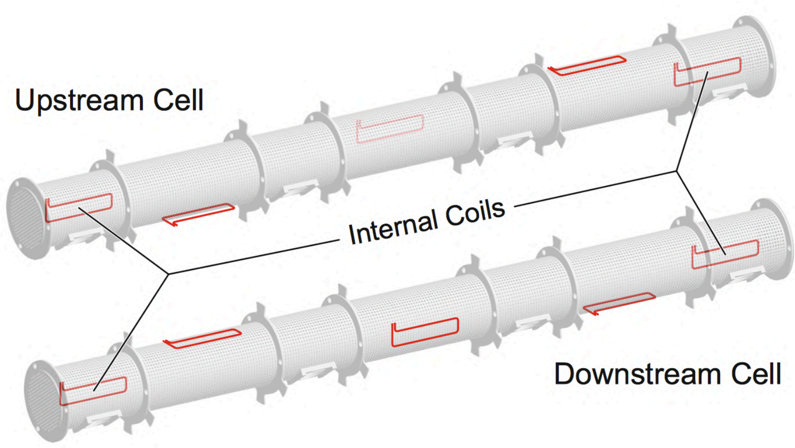

Figure 2.5: PCTFE containers and NMR coils. (Adopted from [54])

beam in the target to access spectrometers in downstream. In the mean time, it also makes possible a higher acceptable intensity of the incident pion beam. Consequently, a worse vertex resolution suffering from the multiple scattering of produced muons with the heavy materials in the hadron absorber..

The hadron absorber consists of one alumina (Al_2O_3) end-cap cone plug, one scintillator plane and one stainless steel frame. The scintillator plane (also known as vertex detector) was placed between end-cap cone plug and stainless steel frame. It was installed during the year 2015 but removed in the year 2018. More details about vertex detector are available in Section 2.4.1. Inside the stainless steel frame, a cylindrical aluminum (Al) block, six cylindrical tungsten (W) plugs and several alumina blocks were installed. The cylindrical aluminum block is 7 cm long with a diameter of 10 cm, placed along the beam line and around 100 cm downstream of the NH_3 target. The six cylindrical tungsten plugs are all 20 cm long but in varied diameters, which are 9.5, 9.5, 9.5, 9.5, 9 and 8.5 cm from upstream to downstream, respectively. All of aluminum block and tungsten plugs are placed inside the alumina blocks. A photo of the placement of polarized target and hadron absorber is shown in Fig. 2.6.

2.4 Tracking Detectors

The COMPASS tracking system consists of many kinds of tracking stations extending the entire spectrometers region. The tracking system has the wide acceptance from extremely small polar angle to 165 mrad. Furthermore, the main stations can be divided into three groups, base on different angular acceptance coverage: the very small area trackers, the small area trackers and the large area trackers.

Each tracker usually consists at least two projection of wires (or scintillators) perpendicular to the beam axis in order to reduce ambiguity. In the COMPASS detector convention, the terms X-plane and Y-plane refer to the coordinate of wires in horizontal and vertical, respectively. While the majority of detectors consist of more then two projections of wires, the terms U-plane and V-plane are adopted for representing the coordinate of wires rotated clockwise and anticlockwise, respectively, with respect to the x-axis.

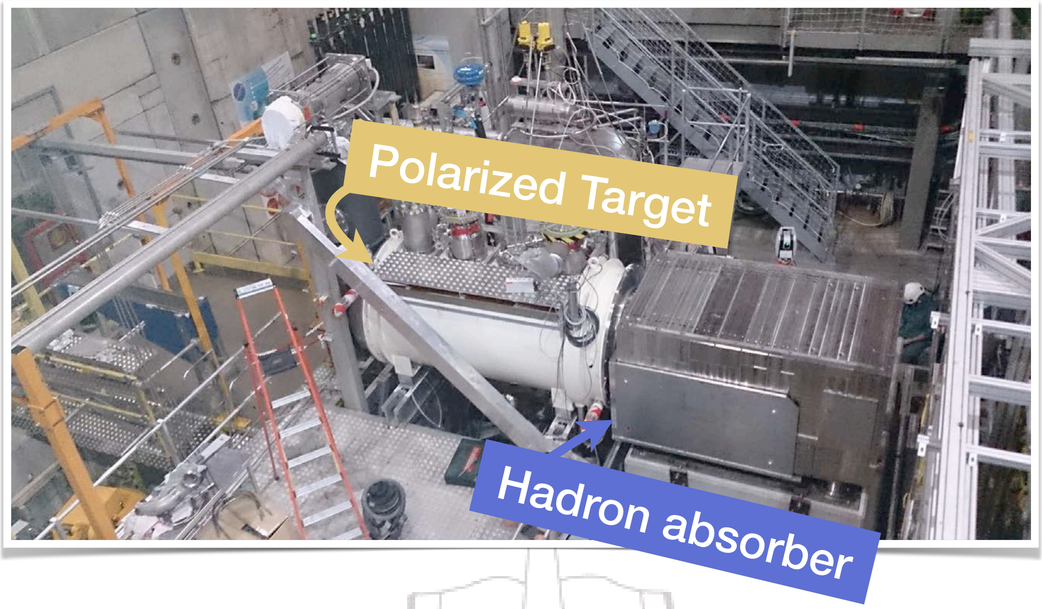

Figure 2.6: The photo of the placement of polarized target and hadron absorber.

2.4.1 Very Small Area Trackers

The very small area trackers are used to measure the particle's trajectories which are extremely close to the beam axis (e.g. beam). These trackers consist two kinds of detectors: the Scintillating Fibre (SciFi) detectors and Silicon Microstrip detectors. The detectors in this area requires an excellent time resolution or spatial resolution in order to make a good association[3] between hits and tracks from the very high rate of incident beam particles.

The SciFi detectors consist five stations: FI01, FI15, FI04, FI03 and FI35 (in the order of upstream to downstream). The size of the active area for each stations vary from 3.9×3.9 cm^2 to 5.4×5.4 cm^2. A single station contains at least two or up to six projection of planes depending on the station. Each projection of plane is made of the superposition of multiple[4] staggered fibre layers. The diameter of the fibre is 0.5 mm, which lead to the spatial resolution in 130 μm for all of SciFi detectors. The advantage of the SciFi detectors is the excellent time resolution, which is 400 ps. A schematic view of fibre configuration of a SciFi coordinate plane is shown in Fig. 2.7.

Among them, FI01, FI15, FI04 and FI03 detectors (so-called the Beam Telescopes) are composed of two (X,Y), three (U,X,Y), three (X,Y, U) and three (X,Y, U)[5] planes, respectively. The beam telescopes are all located in front of the target region for the purpose of beam measurement.

Additionally, one more SciFi detector FI35, namely vertex detector, is composed of six

[3] To identify hits belonging to the same track or not.
[4] 14 layers
[5] in the order of upstream to downstream

planes of (U2, U1, Y2, Y1, X2, X1) projection. The vertex detector was placed between the downstream of polarized target and the upstream of the hadron absorber. It was used to improve the vertex resolution since the spatial resolution of track passing through the hadron absorber is compromised[6]. Unfortunately, this detector suffered from huge occupancy of background signal due to significant radiations from the hadron absorber. Consequently, the information of the FI35 is not used for tracking reconstruction in 2015 Drell–Yan data production, and also been removed from spectrometers during the 2018 Drell–Yan data taking.

The silicon detectors consist of three stations. The size of the active area for each stations is 5×7 cm^2. The silicon detectors bring a fine time resolution of 2.5 ns but a excellent spatial resolution of 10 μm. However, these detectors could not support long term radiation exposure from a high-rate hadron beam. All of silicon detectors have been removed from the Drell–Yan measurement.

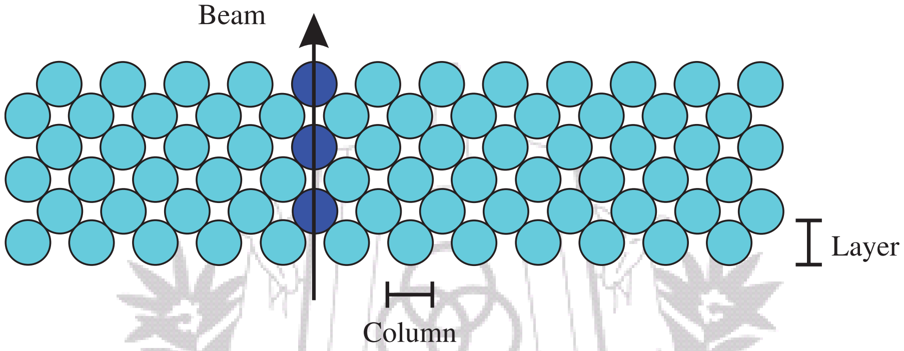

Figure 2.7: Schematic of fibre configuration of a SciFi plane. (Adopted from [51])

2.4.2 Small Area Trackers

The small area trackers are used to measure the particle's trajectories at small angle. These trackers consist of two kinds of detectors: the Micro-mesh Gaseous Structure (MicroMegas) detectors and Gas Electron Multipliers (GEMs) detectors, which are all gaseous detectors. The detectors in this area cover a tracking region from 8 mrad to 45 mrad.

The MicroMegas detectors consist of three stations: MP01, MP02 and MP03 (in the order of upstream to downstream). Each stations is composed of four (V, U, X,Y) planes,which are all located in between the downstream of hadron absorber and the first dipole magnet (SM1). The MicroMegas detector's volume can be decomposed into a conversion gap and an amplification gap separated by a metallic micro-mesh. The resulting primary electrons from the process of ionization drift to the mesh when a particle passing through the conversion gap, and a huge number of electron/ion pairs from an avalanche are produced after the primary electrons drift to the amplification gap possessing a higher field. The principle of operation of the MicroMegas detectors is demonstrated in Fig. 2.8.

Electron/ion can drift over a maximum distance of 100 μm the spatial resolution of MicroMegas detectors is around 100 μm. A good time resolution is achieved in 9 ns

[6]Due to the multiple scattering effect.

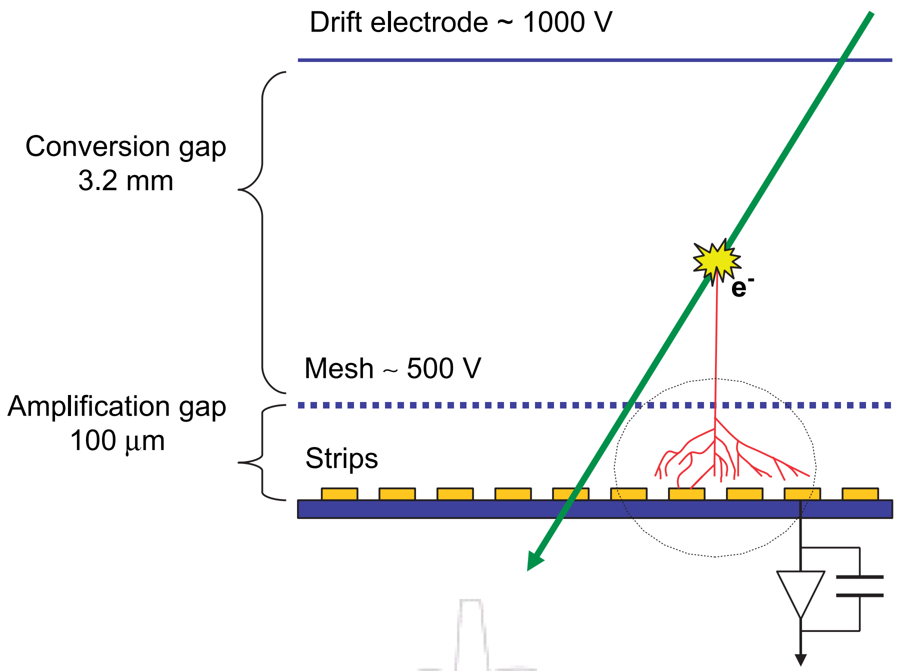

Figure 2.8: Operation principle of the MicroMegas detectors. (Adopted from [53])

by the optimised gas mixture: Ne(80%)/C_2H_6(10%)/CF_4(10%). The size of the active area for each stations is 40×40 cm^2, with a central dead zone of 5 cm in diameter. In the Drell–Yan measurement, all the MicroMegas detectors were upgraded by installing the pixelized MicroMegas detector in central dead zone (Fig. 2.9). However, these pixelized MicroMegas detectors are not important for the Drell–Yan measurement because of too small angle coverage.

The GEMs detectors consist of eleven stations: from GM01 to GM11 (in the order of upstream to downstream). Each stations are composed of four (U, V, Y, X) planes. The GEMs detectors are widely distributed from the end of SM1 magnet until the end of the spectrometers. A single GEM detector's volume can be decomposed into three of 50μm thin Polyimide foils distributed by a large number of micro-holes (about 10^4/cm^2) with applying a potential difference of several 100 V across the foil. Similar to the MicroMegas detector, when a particle passes through the GEMs detectors volume, avalanche multiplication of primary electrons drifts into the holes and then goes to the next foil up to the readout electronic. The principle of operation of the GEMs detectors is demonstrated in Fig. 2.10. The size of the active area for each stations is 31×31 cm^2, with a central deactivated area of 5 cm in diameter. The central area is deactivated during the normal high-intensity physics run in order to avoid too high rate of muon with small angle[7]. This area can be activated during the alignment run in order to increase the statistics by using beam track. The average time resolution is 12 ns and the average spatial resolution is about 70 μm for the GEMs detectors. Additionally, there are two more pixelized GEMs detectors: GP02 and GP03 in the spectrometers. But they are not important for the Drell–Yan measurement because of too small angle coverage.

[7]Usually the beam decay muon

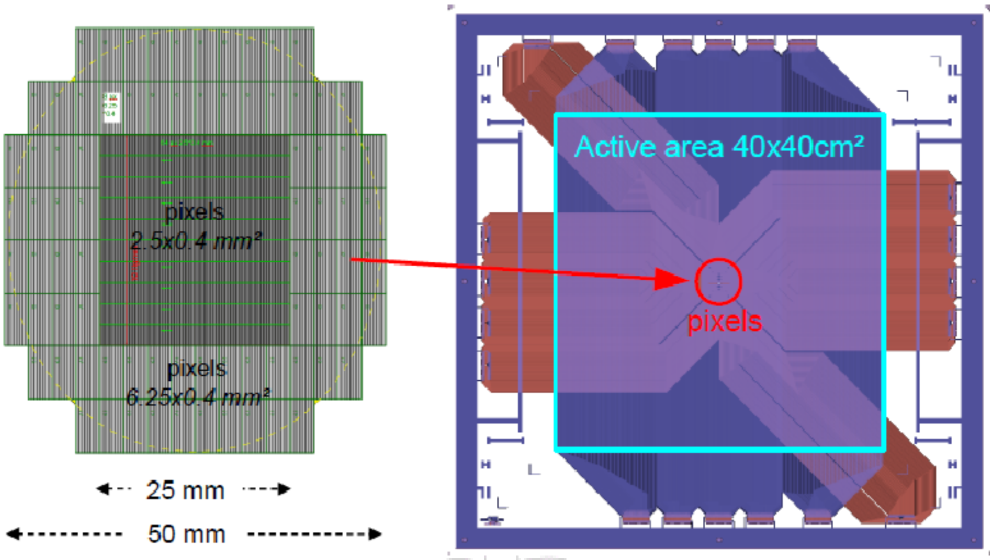

Figure 2.9: The board design of the pixelized MicroMegas. (Adopted from [57])

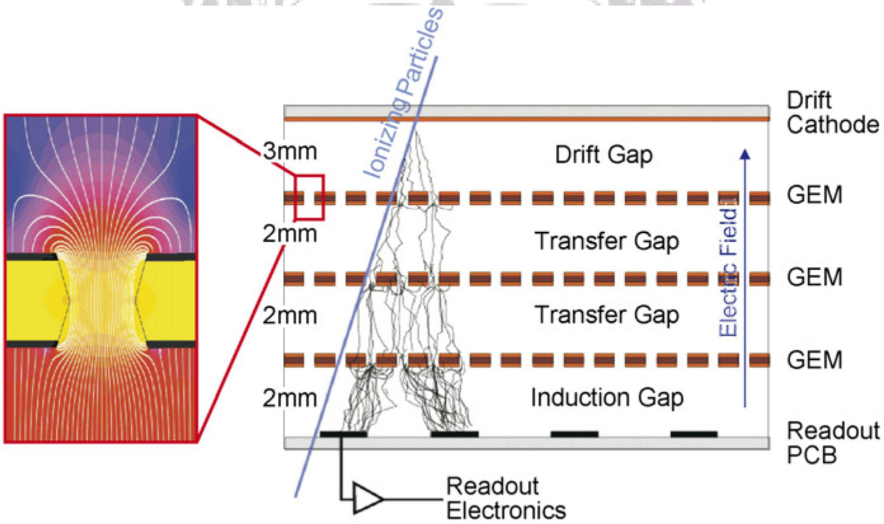

Figure 2.10: The principle of operation of the GEMs detectors. (Adopted from [53])

2.4.3 Large Area Trackers

The large area trackers are used to measure the particle's trajectories at large angle. The central part of each detectors in this area has been deactivated (dead zone) which is covered by the small area trackers. The advantage of detectors in large area is the largest active area covering a track region up to 180 mrad. Consequently, the worse time and spatial resolution are for these detectors compared to the small area trackers. These trackers consist five kinds of detectors: the Drift Chambers (DCs), the Straw Tube Chambers (Straws), the Multi-Wire Proportional Chambers (MWPCs), the large area drift chambers (W45) and the RichWall (RW), which are all gaseous detectors.

The DCs consist of four stations: DC00, DC01, DC04 and DC05 (in the order of upstream to downstream). DC00 and DC01 are located at upstream of SM1 magnet while DC04 and DC05 are located at downstream of SM1 magnet. The size of the active area for DC01 and DC01 is 180×127 cm^2, which compose of four pairs (Y1, Y2, X1, X2, U1, U2, V1, V2) of projection planes, respectively. The larger active area 248×208 cm^2 for DC04 and DC05 has achieved, which compose of four pairs (U2, U1, V2, V1, X2, X1, Y2, Y1) of projection planes, respectively. The purpose of the double planes for each projection is to avoid tracking ambiguities. These DCs hold a 30 cm in diameter large dead zone (so-called beam killer) in the central region which are deactivated during the normal physics runs and activated only during the alignment runs, since DCs cannot sustain high rate of charged particles which are usually distributed in small angle region. Each plane is decomposed with a set of 20 μm radius sensitive wires and 100 μm radius potential wires, which equally and alternately distributed in space. Those wires are enclosed in between two cathode foils with a gas gap of 8 mm. The principle of operation of the DCs detectors is demonstrated in Fig. 2.11. The spatial resolution of DCs is around 300 μm. The DCs are the very important detectors (with high resolution and efficiency) for tracking particles in the upstream of SM1 magnet since the total particle flux in this region is much higher compared to the downstream side of SM1 magnet due to the low energy background which is bent away by the magnet.

The Straws detectors are made of tubes where a gold plated tungsten anode wire is located in the center of tube and attracts the electrons from ionization. The Straws detectors consist of two stations: ST03 and ST05, which are located in the SAS region. The ST05 detectors was not used for the tracking purpose but remained in the spectrometers during 2015 Drell–Yan data taking, finally was removed during 2015 Drell–Yan data taking. The ST03 detector is composed of six (X1, Y1, U, V, Y2, X2) planes, here U and V projection are rotated by $-10°$ and $+10°$ with respect to x axis, respectively. The size of the active area for Y-, U- and V-projection planes is 323×272 cm^2, while for X-projection plane is 350×243 cm^2. Each plane includes a dead zone in the central region with a size of 20×20 cm^2. The schematic view of the Straw detector is shown in Fig. 2.12. The spatial resolution of Straws detectors is around 450 μm. The Straws detectors are mainly used for tracking of charged particles produced at large scattering angles downstream of the SM1 magnet.

The MWPCs detectors consist of fourteen stations: PA (7 stations), PS (1 station) and PB (6 stations), distributed along the spectrometers in both LAS and SAS region. There are three different type of MWPCs detectors are used: type-A (PA), type-A* (PS) and type-B (PB). The size of the active area for type-A and type-A* stations is 520×260 cm^2, while for type-B stations with the smaller size of the active area 178×90 cm^2. The type-A station is composed of three (U, X, V) projection planes, here U and V projection are rotated by $+10°$ and $-10°$

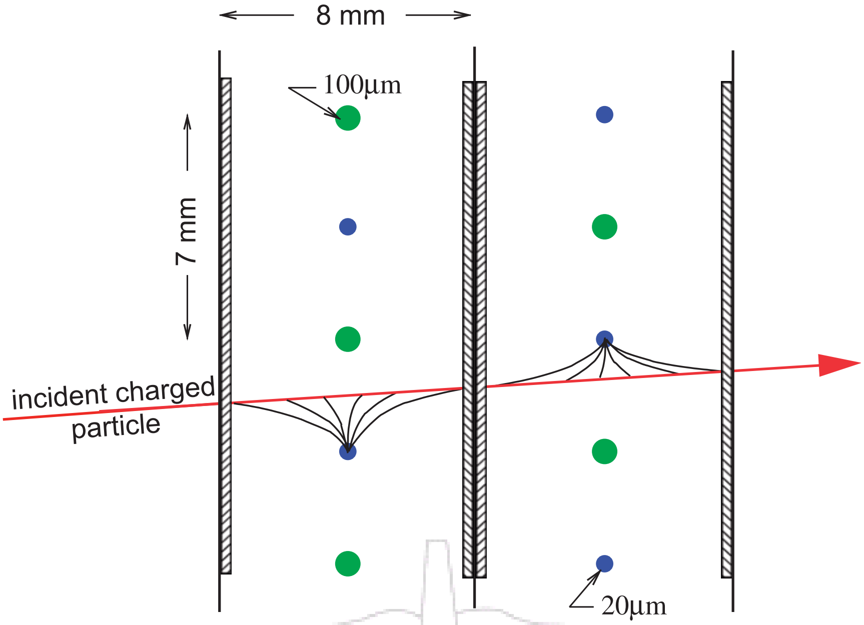

Figure 2.11: The principle of operation of the Drift Chamber. (Adopted from [53])

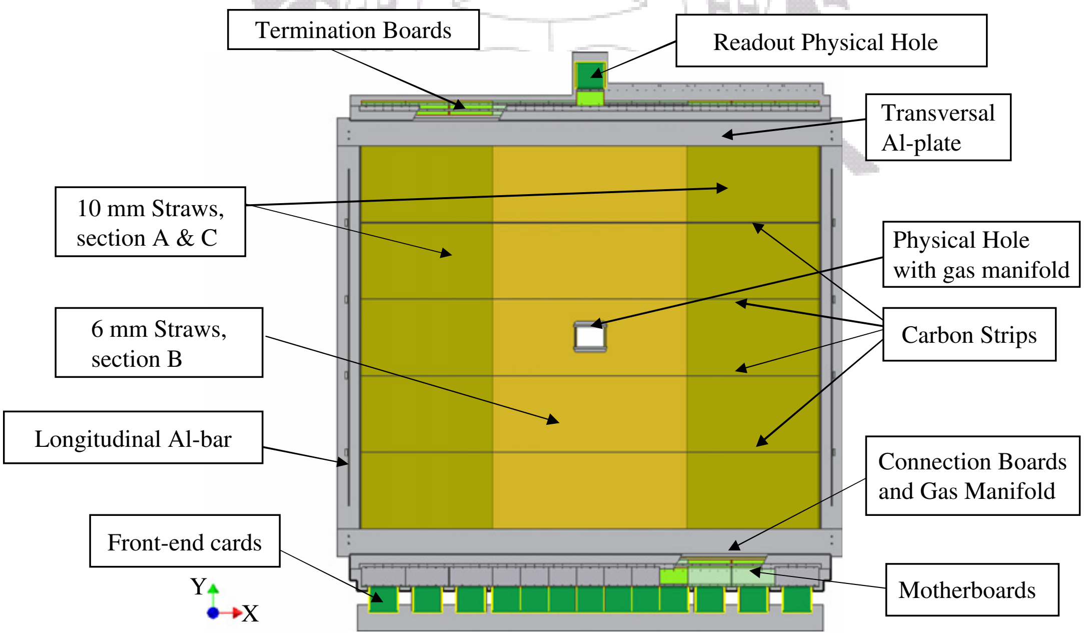

Figure 2.12: The schematic view of the Straw detector. (Adopted from [53])

with respect to x axis, respectively. A dead zone of 16-22 mm in diameter at central region is also introduced in each station, depending on the position of the MWPCs detectors along the beam axis. The type-A* station is composed of four (Y, U, X, V) projection planes, which are similar to type-A but added with an extra Y-projection plane in the upstream. Finally, the type-B station is composed of either two (X, U) or one (V) projection plane. The spatial resolution of MWPCs detectors is around 600 μm. The MWPCs detectors are mainly used for tracking of charged particles at large radial distances to the beam axis.

The W45 detectors consist of six stations: from DW01 to DW06 (in the order of upstream to downstream), which are all located in the SAS region. Each stations are composed of two pairs of projection planes, which the direction of projection planes depending on the station: XY-type (X1, X2, Y1, Y2), XY-type (X1, X2, Y1, Y2), VY-type (V1, V2, Y1, Y2), YU-type (Y1, Y2, U1, U2), XV-type (X1, X2, V1, V2) and UX-type (U1, U2, X1, X2), respectively. The size of the active area for each W45 detectors is 178×120 cm^2, with a central dead zone of 50 cm or 100 cm in diameter. The spatial resolution of W45 detectors is around 1500 μm. The W45 detectors are mainly used for tracking of charged particles deflected by a large angle in the SAS region.

The RW consists of two stations: DR01 and DR02, which are located at the downstream of RICH detector (described in Section 2.5.1). Each stations are composed of four (X1, X2, Y1,Y2) projection planes. The size of the active area for each RW detectors is 527×391 cm^2, with a central dead zone of 102×51 cm^2. Each plane is made by Mini Drift Tubes (MDT) modules, which is composed of an eight-cell aluminium comb made with a wall thickness of 0.44 mm and covered by a 0.15 mm thick stainless steel foil on the top. A sketch of a single MDT module is shown in Fig. 2.13. The RW detectors are mainly used to improve the tracking accuracy at downstream of RICH detector.

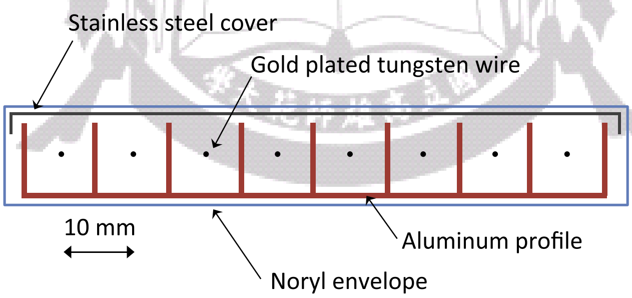

Figure 2.13: The sketch of a single Mini Drift Tube module. (Adopted from [51])

2.5 Particle Identification

For the purpose of identifying different type of particles passing through spectrometers region, the COMPASS particle identification (PID) system includes three kinds of detectors: The Ring Imaging Cherenkov (RICH) detector, the calorimeters and the muon identification detector systems. A detailed description of these detectors is referred to Ref. [53].

2.5.1 Ring Imaging Cherenkov Detector

The Ring Imaging Cherenkov detector is used to identify different outgoing hadrons (e.g. pions, kaons and protons) in certain momentum range[8] which base on the Cherenkov effect: a particle in the medium emits photons if particle travels faster then the speed of the light in that medium. The emitted photons are reflected by two spherical mirrors to the photon detectors sitting outside of the LAS geometrical acceptance. The principle of the RICH detector and its schematic view are shown in Fig. 2.14.

In the Drell–Yan measurement, the usage of RICH detector is limited because the muon is the dominate particle in the spectrometers. So the RICH detector only provides additional time information for the track reconstruction.

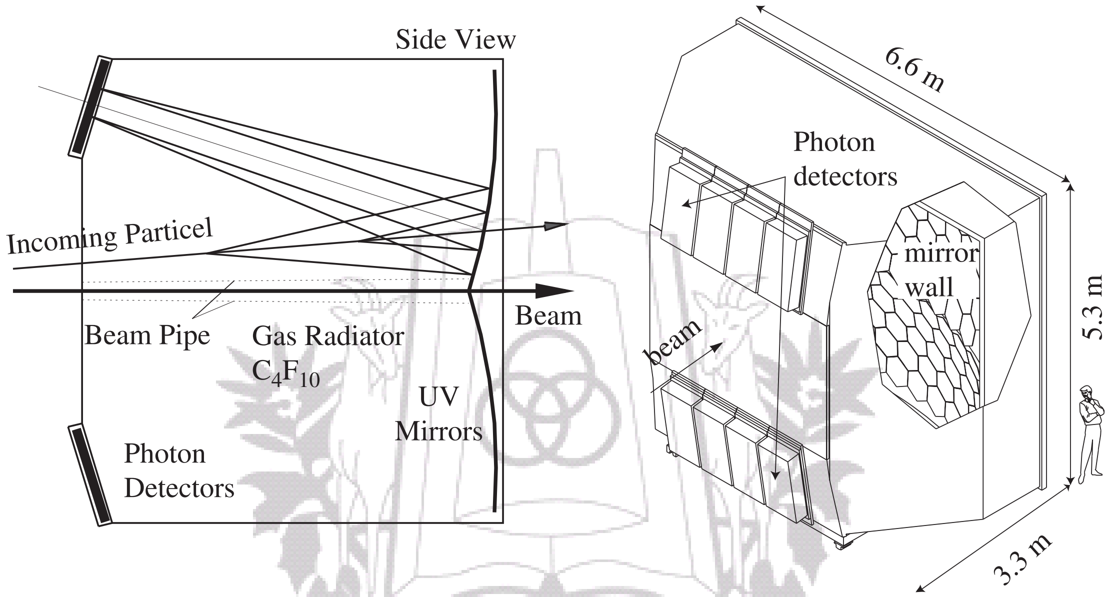

Figure 2.14: The principle and schematic view of the RICH detector. (Adopted from [53])

2.5.2 Calorimeters

The calorimeters are mainly used to measure the energy of particles. There are two kinds of calorimeters: electromagnetic calorimeters (ECALs) and hadronic calorimeters (HCALs). Individually, the electromagnetic calorimeters are mainly for measuring the energy of electromagnetic showers and the hadronic calorimeters are for measuring hadrons. There are two electromagnetic calorimeters (ECAL1 and ECAL2) and two hadronic calorimeters (HCAL1 and HCAL2) in the spectrometers.

ECAL1 and HCAL1 are located in the LAS region and ECAL2 and HCAL2 are located in the SAS region, respectively. The ECALs are made of lead glass modules which produce electromagnetic showers when photons or electrons passing through. The intensity of light signal emitted by electromagnetic showers is proportional to the energy of particle.

[8]From 5 to 50 GeV/c

HCALs are of modular structure: each module is made of alternating iron layers and scintillator plates. A shower of secondary particles is generated in iron layer when a hadron passes through. Furthermore, a light signal will be produced in the scintillator plate proportional to the deposited energy. The hadrons with energy in the range 10-100 GeV/c will be almost absorbed in HCALs.

2.5.3 Muon Identification

The muon identification is based on the measurement of track which passes through significant amount of materials. There are two muon identification detector systems (so-called muon filtering system) covering the LAS and the SAS region in the spectrometers, respectively. Each system consists of one hadron absorber wall (so-called muon filter) and two sets of tracking stations: The muon filtering system in the LAS region consists a 60 cm thick iron absorber wall (Muon Filter 1) between two separated muon wall stations (MW1). The muon filtering system in the SAS region consists a 2.4 m thick concrete absorber wall (Muon Filter 2) followed by two muon wall stations (MW2). The muon filters are used to filter out hadrons and particles and the muon walls are used for tracking purpose. A segmented side view of MW1 is shown in Fig. 2.15.

In addition, a third muon filter (Muon Filter 3) made of 60 cm iron absorber is used and located near the end of the spectrometers. Muon Filter 3 covers the central part where there are holes in both the previous muon filters, corresponding to very small angle of muon scattering.

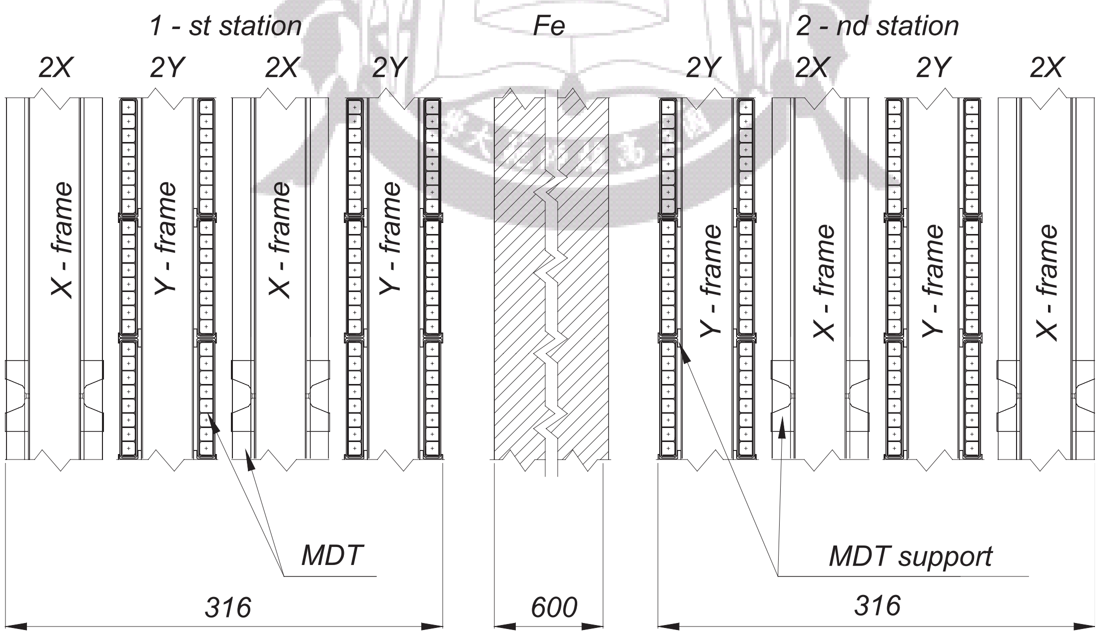

Figure 2.15: The segmented side view of Muon Filter 1. All dimensions are given in millimeters. (Adopted from [53])

2.6 Trigger System

The COMPASS trigger system mainly consists of pairs of scintillator hodoscopes connected via a coincidence matrix (trigger matrix pattern) and is to be fired by the muons coming from the target (target pointing trigger). The physics trigger used during the COMPASS 2015/2018 Drell-Yan runs includes single muon triggers and muon pair triggers.

There are three kinds of single muon trigger systems which are all the target pointing triggers: Large Angle Spectrometers Trigger (LAST), Outer Trigger (OT) and Middle Trigger (MT). LAST covers the muon pass through Large Angle Spectrometers (LAS) region, while OT and MT cover the Small Angle Spectrometers (SAS) region. The dimuon triggers are constructed by two coincident single muon triggers in a pre-set time window[9]. There are three kinds of dimuon triggers recorded during 2015/2018 Drell-Yan runs, where at least one muon falling into large angle spectrometers region is required: Both muons are in LAS region (LAST–LAST) or one muon is in LAS region and another in SAS region (OT–LAST, MT–LAST).

2.6.1 Coincidence Matrix

Each single muon trigger is given by the coincidence of two signals from the pair of hodoscopes (one located in upstream and another in downstream) scintillator strips (so-called slabs) which fulfills a trigger matrix pattern (so-called coincidence matrix) within the time window[10].

Depending on the trigger principle and geometry, the shape of the coincidence matrix is adjusted. For the purpose of target pointing, the triggering is done in the non-bending hodoscope of horizontal slabs. In order to set a trigger on the outgoing muon track from the volumn of target, the trigger matrix is usually set along the diagonal region. This is illustrated in Fig. 2.16. The coincidence matrices used for the 2015/2018 runs are shown in Fig. 2.17.

2.6.2 Large Angle Spectrometers Trigger

The LAST system consists of three horizontal hodoscopes: HG01Y1 (H1), HG02Y1 and HG02Y2 (H2) with two coincidence matrices: H1⊗HG02Y1 and H1⊗HG02Y2. Both of coincidence matrices are identical and shown in Fig. 2.17a and Fig. 2.17b. H1 is situated in upstream and HG02Y1 (HG02Y2) is situated in downstream at Jura (Saleve) side, respectively. Each hodoscopes contains 32 slabs. As for the size of slab in H1, the width (along y axis) is 6 cm, and the length (along x axis) is 230 cm. As for the size of slab in H2, the width is 13.6 cm, and the length is 252.5 cm. The geometry of H1 and H2 is illustrated in Fig. 2.18 and Fig. 2.19.

The LAST trigger covers the range of angle θ larger than 20 mrad, up to the end of the acceptance of the large angle spectrometers.

[9]Time window for the coincidence between two single muon triggers is 5 ns.

[10]Time window for the coincidence between two planes in LAST (OT, MT) is 10 ns (6 ns, 4 ns), respectively.

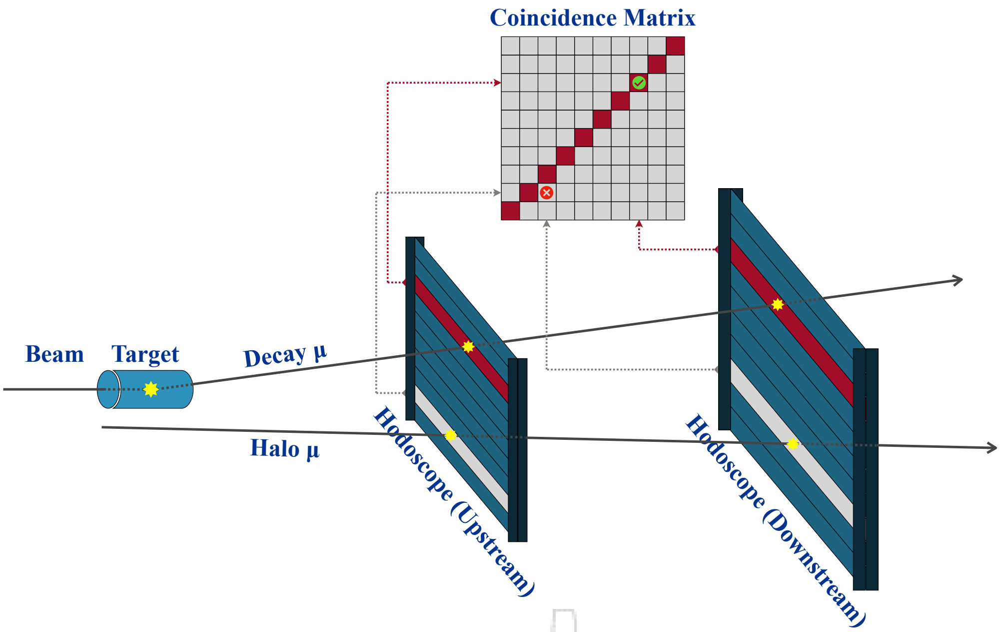

Figure 2.16: The principle of target pointing triggers.

2.6.3 Outer Trigger

The OT system consists of three horizontal hodoscopes: HO03Y1 (HO03), HO04Y1 and HO04Y2 (HO04) with one coincidence matrix: HO03⊗HO04. The coincidence matrix is shown in Fig. 2.17c. HO03 is situated directly behind SM2 magnet and HO04Y1 (HO04Y2) is situated behind the Muon Filter 2 at Jura (Saleve) side, respectively. HO03 contains 18 slabs, and both HO04Y1 and HO04Y2 contain 16 slabs. As for the size of slab in HO03 (HO04), the width is 7 (15) cm and the length is 250 cm, respectively. The geometry of HO03 and HO04 is illustrated in Fig. 2.20 and Fig. 2.21.

The OT trigger covers the range of angle θ larger than 5 mrad, up to the end of the acceptance of the small angle spectrometers.

2.6.4 Middle Trigger

The MT system consists of two subsystems: HM04 and HM05 with one coincidence matrix: HM04⊗HM05. Each of subsystems is composed of two vertical (HM0∗X1dn, HM0∗X1up) and two horizontal hodoscpes (HM0∗Y1dn, HM0∗Y1up). The subsystem HM04 is located behind the HO04 and the subsystem HM05 is behind the Muon Wall 2. For the Drell–Yan data taking, only the horizontal hodoscopes are used. The coincidence matrix is shown in Fig. 2.17d. Each horizontal hodoscope contains 16 slabs, the size of slab is different between the first 8 slabs and the last 8 ones. The sizes of slabs in MT are summarized in Tab. 2.2. The detailed geometry of HM03 and HM04 are illustrated in Fig. 2.22 and Fig. 2.23.

The MT trigger covers the range of angle θ from 0.5 mrad to 5 mrad, the most forward direction of muon tracks. The most energetic muon from the π^- beam decay will be detected by this trigger.

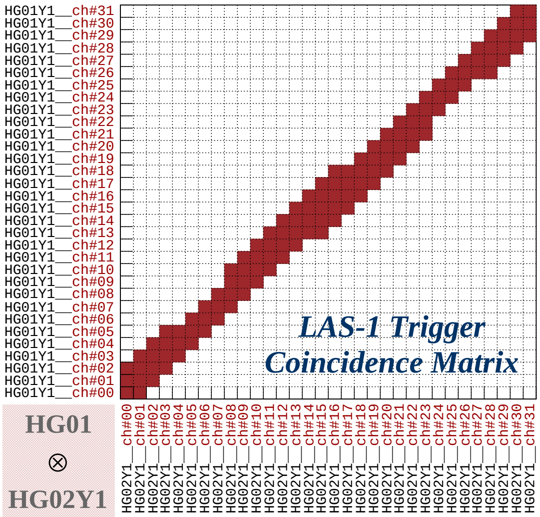

(a) LAS Trigger 1

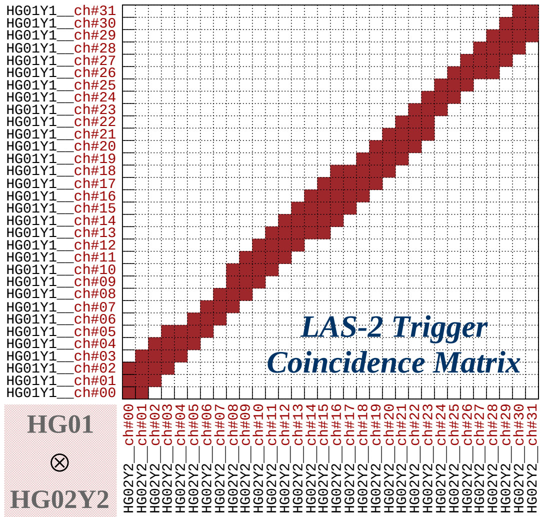

(b) LAS Trigger 2

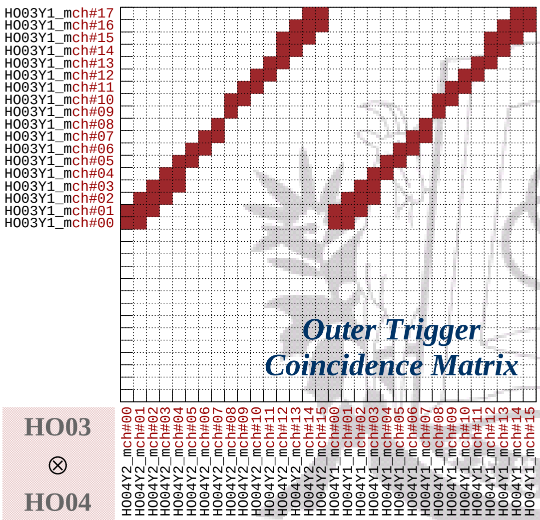

(c) Outer Trigger

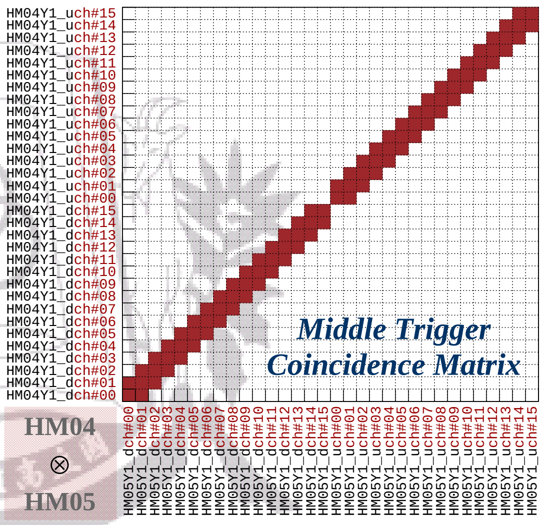

(d) Middle Trigger

Figure 2.17: The digit pattern of coincidence matrices. For each matrix, the x axis corresponds to the slab number of downstream hodoscope of each hodoscopes pair, and the y axis corresponds to the slab number of upstream hodoscope. Each pixel corresponds to the combination of signal pair from two slabs.

Hodoscope	No. of slabs	Length (cm)	Width (cm)
HM04Y1dn	16	120	25-21
HM04Y1up	16	120	21-25
HM05Y1dn	16	150	30-25
HM05Y1up	16	150	25-30

Table 2.2: The geometrical dimensions of Middle trigger hodoscope.

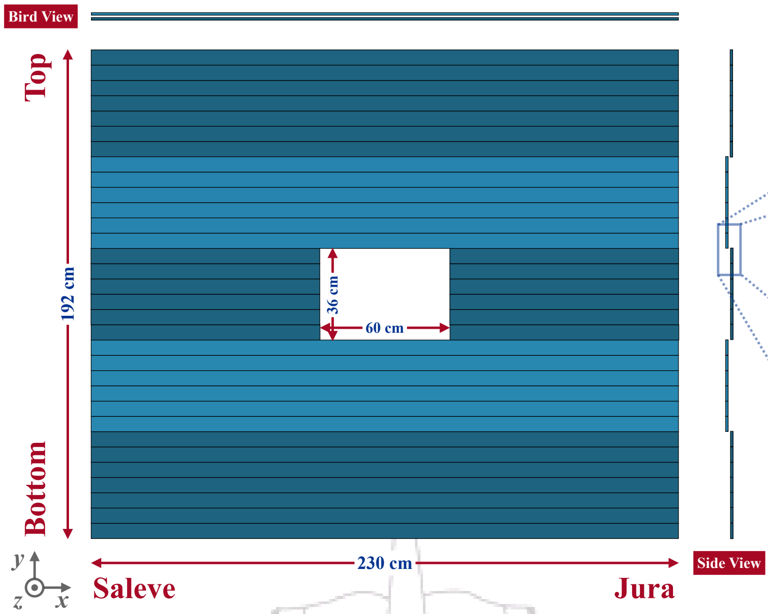

Figure 2.18: The geometry of H1 hodoscope.

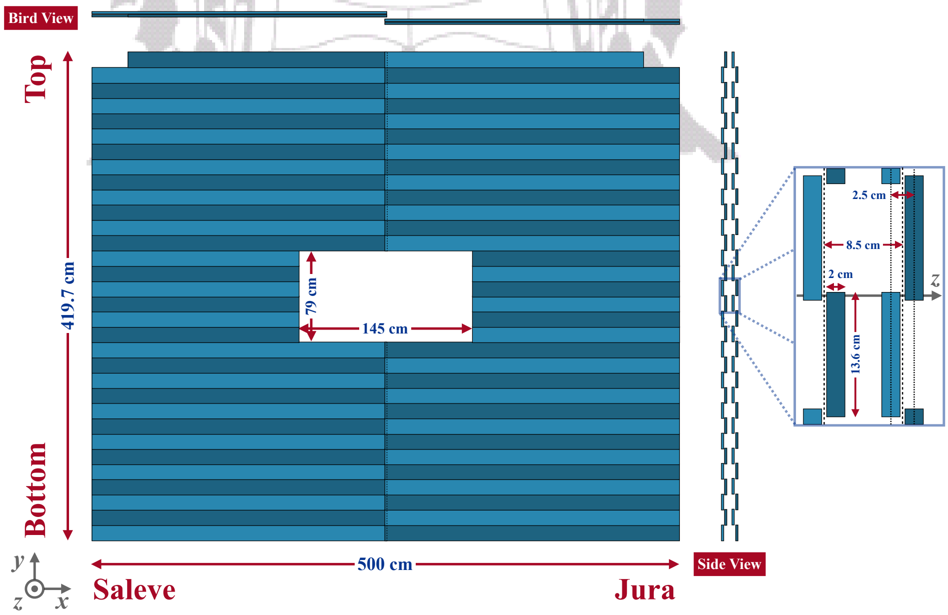

Figure 2.19: The geometry of H2 hodoscope.

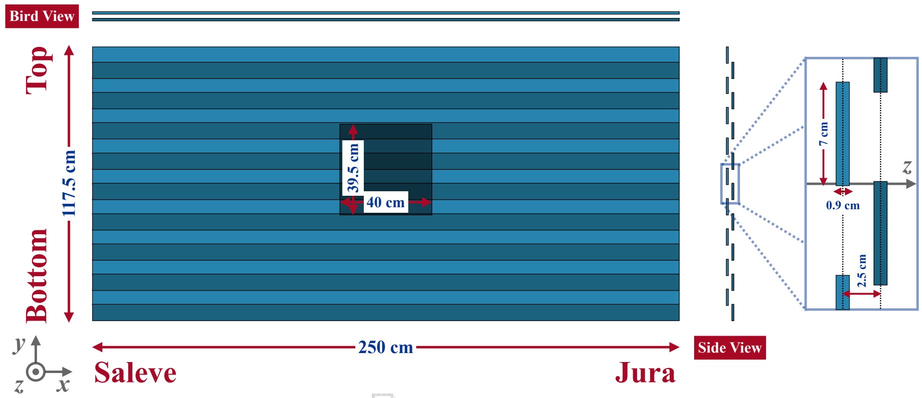

Figure 2.20: The geometry of HO03 hodoscope.

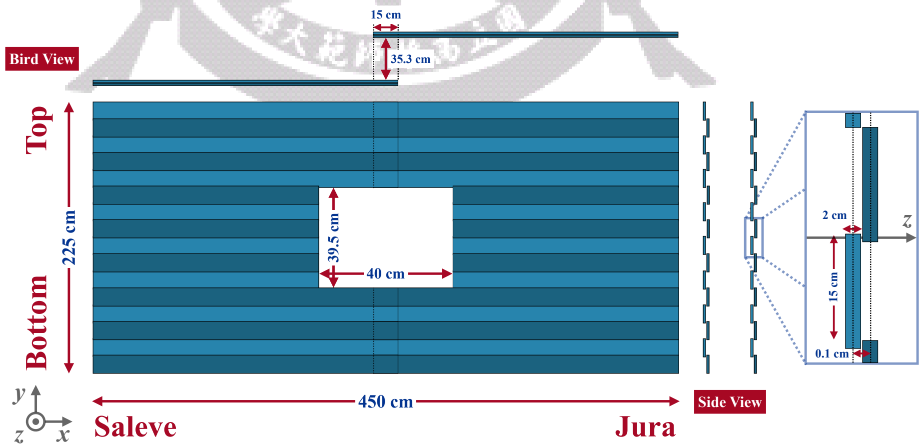

Figure 2.21: The geometry of HO04 hodoscope.

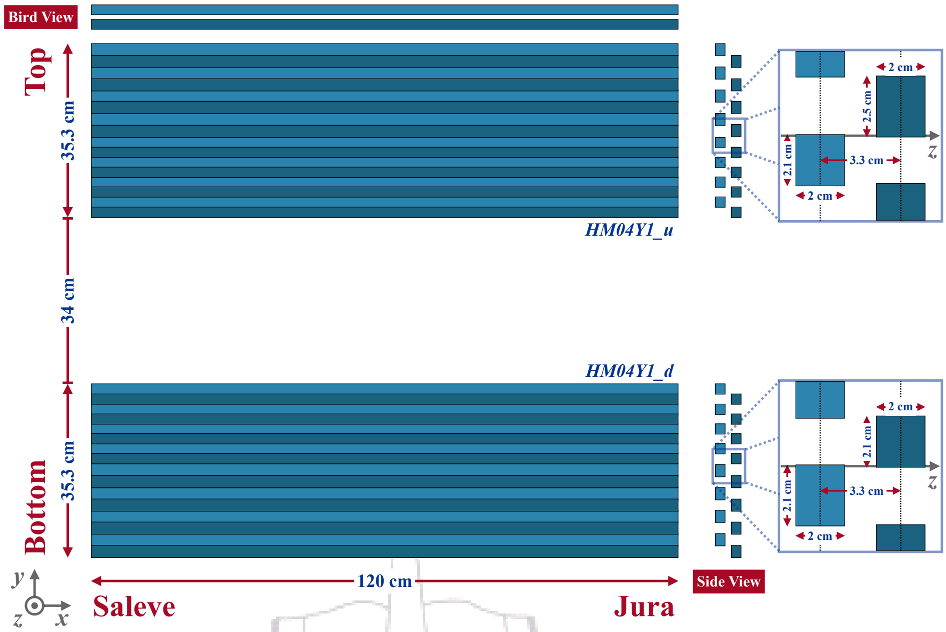

Figure 2.22: The geometry of HM04 hodoscope.

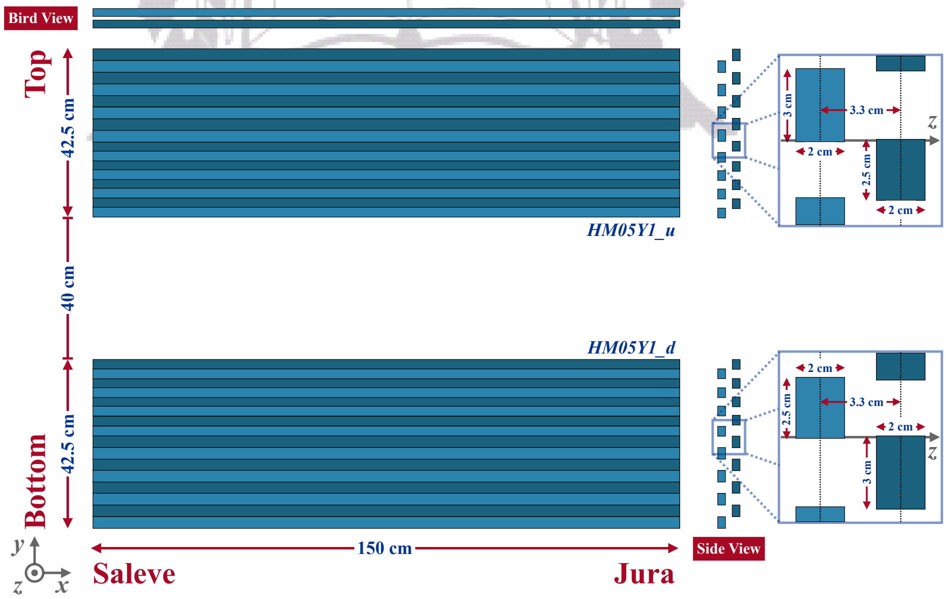

Figure 2.23: The geometry of HM05 hodoscope.

2.7 Data Acquisition and Production

Data Acquisition (DAQ) system is one of the most important parts for an experiment and it is a fully automatic procedure to read, process and store a large amount and high trigger rate of data flow from a significant amount of detector channels. The COMPASS DAQ system deals with approximately 0.25 millions of detector channels with a trigger rate around 30 kHz during a typical 9.6 s long SPS spill time. The average event size is 40 kB, which lead to an acquired data rate up to 1.2 GB/s during a spill time. An overview of the data flow is shown in Fig. 2.24.

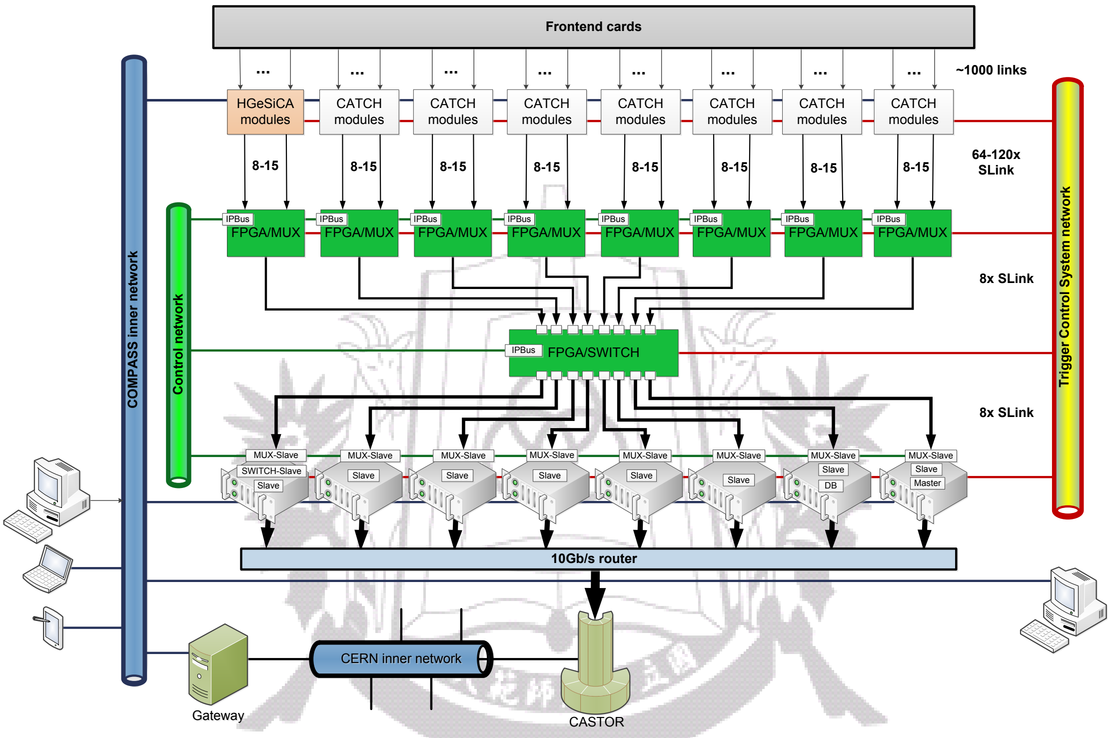

Figure 2.24: Schematic readout and data acquisition flow at the COMPASS experiment since 2015. (Adopted from [58])

The analog signals from each detector are readout and collected by front-end cards, and then digitized via either ADC[11] or TDC[12] which are placed on the front-end card, or other read-out cards at the next stage, such as GANDALF[13], GeSiCA[14] or CATCH[15]. The digitized data is sent to FPGA[16] multiplexing cards via optical fibres (SLink[17]) and then distributed to multiplexer slaves via a FPGA switch [59]. In the end the final raw data will be built by the

[11]Analog-to-Digital Converter.

[12]Time-to-Digital Component.

[13]Generic Advanced Numerical Device for Analog and Logic Functions.

[14]GEM and Silicon Control and Acquisition.

[15]COMPASS Accumulate, Transfer and Control Hardware.

[16]Field Programmable Gate Array

[17]The Simple Link Interface.

online computers (slaves) and transferred to CASTOR[18] magnetic tape.

Data production is to transform the recorded raw data into a suitable data format for data analysis (also known as event reconstruction). In the COMPASS experiment, a standard procedure to perform data production is using the COMPASS reconstruction software: CORAL[19], which receives the raw data files from CASTOR and produce the so-called mini Data Summary Trees (mDSTs) with the reconstructed events. The output mDSTs can be analyzed with a C++ based software package: PHAST[20], which allows to access all informations saved in the mDSTs and perform the data analysis with the C++ codes.

The procedure of data production can be divided into three steps: clustering, track reconstruction and vertexing. In the first step, the clustering (also known as decoding process) is read and translated the raw data in binary format into calibrated digits and hits by taking into account the detectors geometries. In the second step, the track reconstruction is done with hits information from the first step with a Kalman Filter algorithm [60] to build tracks. Initially the spectrometer is divided into several regions, where the reconstruct track segments in each of these regions. Then these segment tracks will be bridged together by taking into account the magnetic field and the materials present in the connection of the region. In the end of the outcome of the Kalman procedure, each track will be fitted with the information of charged, momentum and χ^2. In the final step, the vertexing is using all the previous reconstructed tracks to do the extrapolation into the target region for reconstructing the vertices. An example of event reconstruction with the COMPASS 2018 setup is shown in Fig. 2.25.

[18]CERN Advanced STORage.
[19]COMPASS Reconstruction and AnaLysis Program.
[20]PHysics Analysis Software and Tool; ROOT-based software.

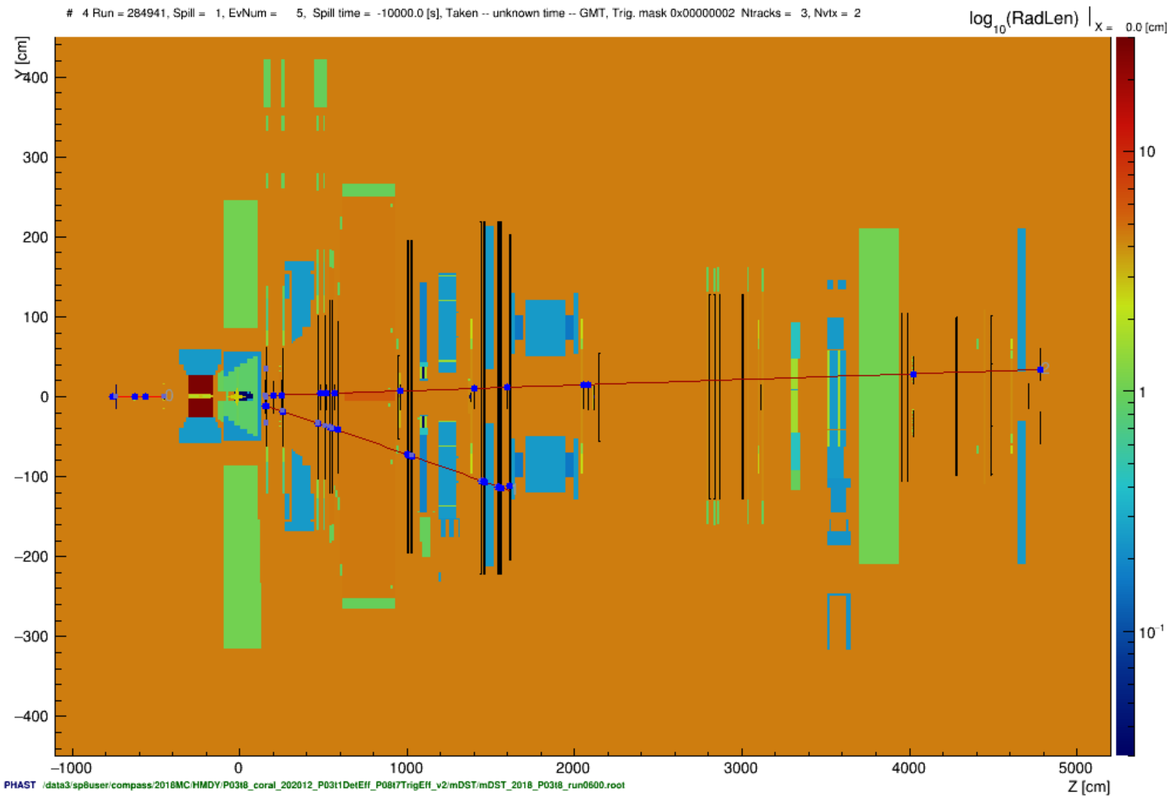

Figure 2.25: An example of event reconstruction with the COMPASS 2018 setup. The blue point represent the hits from detectors, red line represent the reconstructed trajectory, yellow star represent the reconstructed vertex which inside the W target region.

CHAPTER 3

Efficiency of Trigger System

The physics trigger used during the 2015/2018 Drell-Yan data taking has been illustrated in Section 2.6

In this chapter the method of extracting hodoscopes efficiencies and coincidence matrices efficiencies will be described. The efficiencies of trigger system play an important role in the angular analysis, since the acceptance of muon pairs highly correlate with them.

3.1 Efficiencies of Trigger System

The overall trigger efficiency is a convolution of the geometrical acceptance of hodoscopes ($\Omega_{\text{Hodoscope}}$), the hodoscopes efficiency ($\epsilon_{\text{Hodoscope}}$), the geometrical acceptance of the coincidence matrix (Ω_{Matrix}) and the coincidence matrix efficiency (ϵ_{Matrix}). The final goal is to extract $\epsilon_{\text{Hodoscope}}$ for each hodoscopes (ϵ_{HG01Y1}, ϵ_{HO03Y1}...) and ϵ_{Matrix} for each single muon trigger (ϵ_{LAST1}, ϵ_{LAST2}, ϵ_{OT}, ϵ_{MT}) so that the efficiencies information can be applied in the CORAL level of Monte–Carlo chain. The efficiency is extracted from 2018 test-7 production data. Since the geometrical acceptances of the hodoscopes are already taken into account in TGEANT there is no need of considering them in this study.

The single muon trigger efficiency can be defined as:

$$\epsilon_{\text{MuonTrigger}} = \epsilon_{\text{Hodoscope;upstream}} \times \epsilon_{\text{Hodoscope;downstream}} \times \epsilon_{\text{Matrix}} \tag{3.1}$$

where the muon trigger corresponds to LAST, OT or MT. After convoluting two single muon triggers, one can get a dimuon trigger efficiency as following:

$$\epsilon_{\text{DimuonTrigger}} = \epsilon_{\text{MuonTrigger1}} \times \epsilon_{\text{MuonTrigger2}} \tag{3.2}$$

where the dimuon trigger corresponds to LAST–LAST, OT–LAST or MT–LAST.

The best way to evaluate the hodoscope efficiencies and coincidence matrix efficiencies is using the Calorimeter Trigger (CT) events. The CT event was triggered by clusters coming from muon in a calorimeter which is independent of the muon trigger flags.

In the hodoscope efficiencies extraction, the CT events from dedicated CaloDump production are as data sample dumped from physics run in 2018. As for the coincidence matrix efficiencies extraction, CT events from dedicated trigger run are used because the information of single muon trigger flags are needed but these flags were not stored during the physics runs.

The final goal is to extract the period dependence of hodoscope efficiencies and coincidence matrix efficiencies, because the impact of trigger efficiencies is significant for the angular analysis and also the strong time dependence of trigger efficiencies is observed.

The requirement of event selection and parameters between the extraction of hodoscope efficiencies and coincidence matrix efficiencies are not identical. More details on the selection conditions and extraction method will be described in the next two subsections.

3.2 Hodoscopes Efficiencies

In the hodoscopes efficiency extraction, it is important to select good muon track rigorously due to the requirement of track extrapolation. A series of selection cuts are applied in order to select the good muon candidates from CT events:

1. **One charged muon candidates from best primary vertex**:
   Check if each track has crossed more than 30 radiation length ($X/X0 \geq 30$) for selecting the muon candidates. Furthermore, select the vertex among the smallest χ^2_{vertex}.

2. **Checking the quality of tracks**:
   Check the quality of the track by requiring χ^2_{track} smaller than 10 times the number of degrees of freedom: $\chi^2_{\text{track}}/n.d.f. \leq 10$.

3. **Rejection of fake muon track**:
   Require the total momentum of the track p_μ should greater than 10 GeV/c. (20 GeV/c in case of OT and MT region) in order to suppress the possibility of fake muon tracks.

4. **Number of hits from muon wall**:
   Require the total number of hits from muon wall A (for LAST) should more then 6 hits. Require the total number of hits from muon wall B and MWPCs (for OT and MT) should more then 6 hits.

5. **Tracks with proper first or last measured point**:
   Require that the first measured point of the track for LAST event sample is upstream of HG01 hodoscope ($Z_{\mathrm{First}} \leq 300$ cm), and that the last measured point of the track for OT and MT event samples are downstream of HM04 hodoscopes ($Z_{\mathrm{Last}} \geq 4200$ cm).

6. **Trigger pointing (LAST or OT or MT)**:
   This criterion requires that the extrapolated tracks pass through the active area of the hodoscopes. For the purpose of trigger efficiency study, the corresponding trigger bit on is not required where in the standard analysis trigger pointing is required. Additionally, in terms of active area of the hodoscopes, cut out 2.5 cm around all edges of hodoscopes including the dead zone and also cut out 20% of slab size (width in y direction) around all edges of each slabs to get rid of border effect. An example of track distribution on HG01Y1 and HO03Y1 hodoscopes after requiring trigger pointing cut is shown in Fig. 3.1.

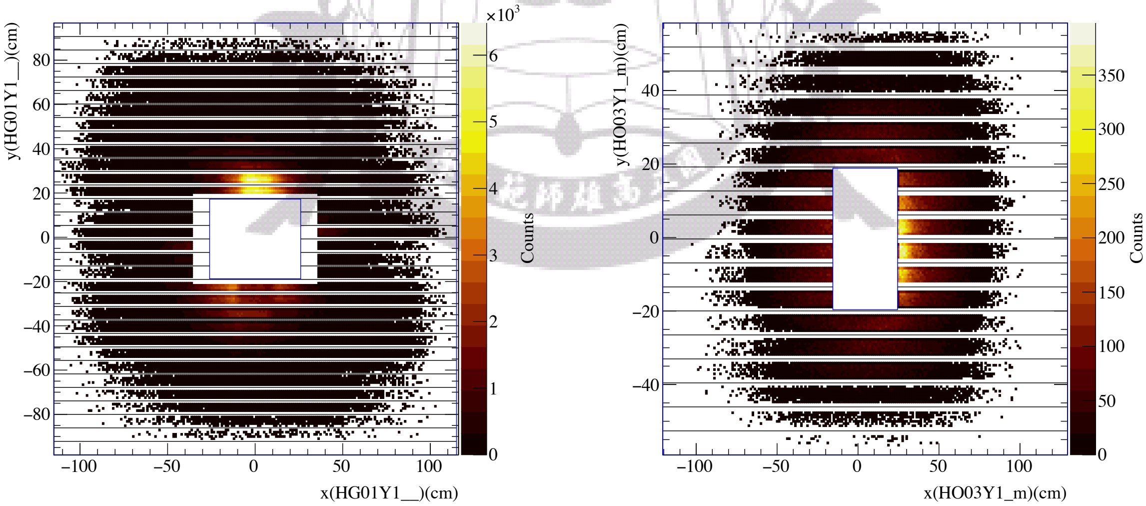

(a) HG01Y1 (b) HO03Y1

Figure 3.1: The track distribution on HG01Y1 and HO03Y1 hodoscopes after requiring trigger pointing cut.

After selecting all of good muon candidates from CT event, the slab number calculation from extrapolation procedure is done in order to infer which slab was supposed to be fired by muon track on each hodoscopes. The hodoscope efficiencies can be obtained by the ratio with requiring the existence of hit from the corresponding slab or the neighboring slabs (slab# ± 1):

$$\epsilon_{\text{Hodoscope}} = \frac{N_{\text{Track}} \otimes (f_{\text{HitInSlab\#}} || f_{\text{HitInSlab\#+1}} || f_{\text{HitInSlab\#-1}})}{N_{\text{Track}}} \quad (3.3)$$

where $f_{\text{HitInSlab\#}}$ represents the flag of hit in the corresponding slab channel, $f_{\text{HitInSlab\#}\pm 1}$ correspond to the neighboring slab channels.

Due to the lack of statistics on the edge of hodoscopes, the extracted efficiencies on the edge fluctuate a lot and a smoothing method is performed which is to parametrize efficiencies with polynomial or exponential functions along x direction slab by slab. An example of one-dimensional slab-by-slab efficiency parametrization is shown in Fig. 3.2.

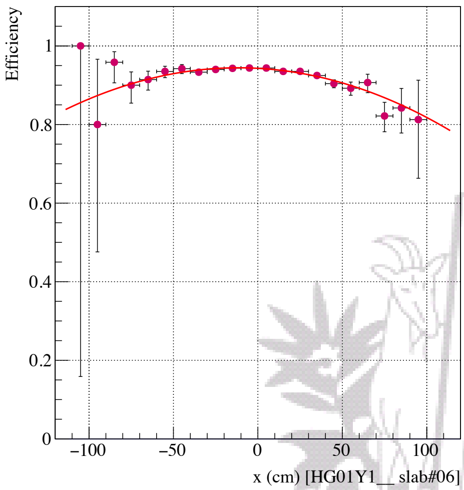

(a)

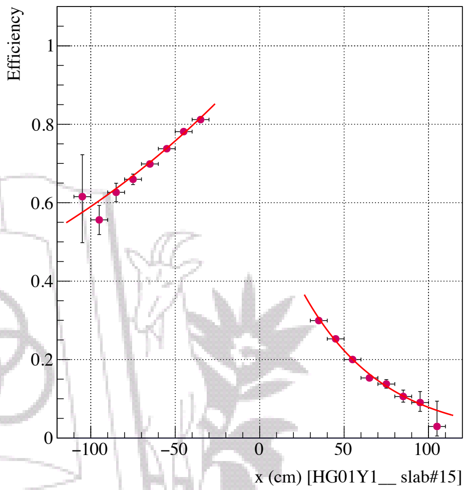

(b)

Figure 3.2: The example of one-dimensional slab efficiencies parametrization from fitting procedure.

An example of two-dimensional HG01Y1 efficiency from P03 period in 2018 data taking before and after smoothing procedure are shown in Fig. 3.3

The final smoothed two-dimensional hodoscope efficiencies from one of the periods in 2018 (P03) are shown in Fig. 3.4. The smoothed two-dimensional hodoscope efficiencies from all of periods in 2018 are shown Appendix A.

3.3 Coincidence Matrices Efficiencies

It is more straightforward to extract coincidence matrix efficiencies since the track information in this analysis is not needed (no tracking involved). The idea is to use just the hit information from each event, and check for two conditions:

1. Checking for the corresponding hits from hodoscope pairs in the time window of corresponding trigger. The time window setting during 2018 data taking is listed in Tab. 3.1.

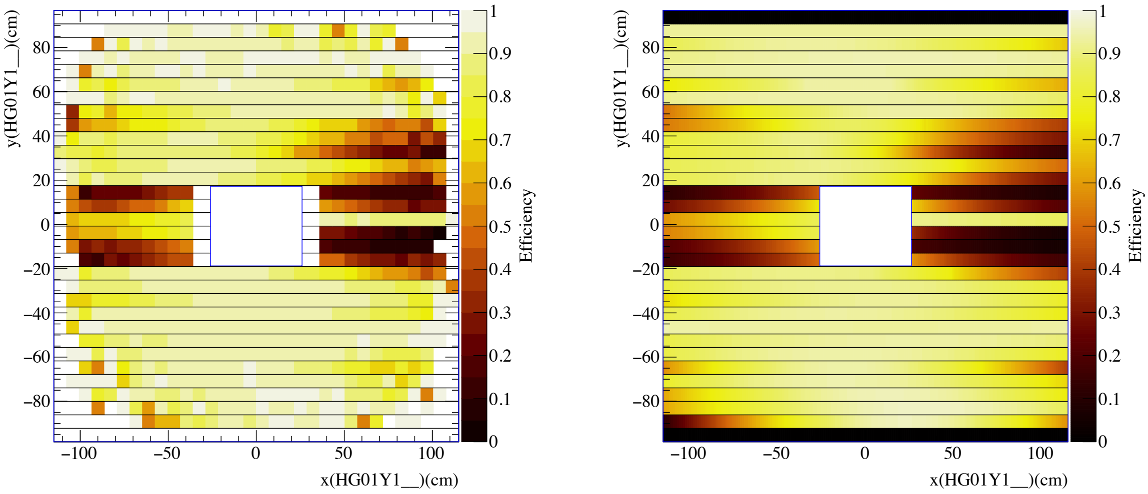

(a) Non-smoothing efficiency

(b) Smoothing efficiency

Figure 3.3: The example of two-dimensional HG01Y1 efficiency before/after parametrization from fitting procedure.

2. Checking for the coincidence matrix pattern compatibility, where the matrix pattern is shown in Fig. 2.17. The hit pairs from upstream and downstream of hodoscopes channels should be fulfilled with the matrix pattern of corresponding trigger.

Trigger	Time window (ns)
LAST	10
Outer (OT)	6
Middle (MT)	4

Table 3.1: The time windows of hits from upstream/downstream hodoscope pair.

After selecting the hit pairs (N_{HitPairs}) from these two conditions, one can obtain the coincidence matrix efficiencies by the ratio of requiring single muon trigger bit. In the case more than one pairs of hits satisfy the pixel condition, the event will be discarded from the candidate sample in order to get rid of possible ambiguity:

$$\epsilon_{\text{Matrix}} = \frac{N_{\text{HitPairs}} \otimes f_{\text{MuonTriggerBit}}}{N_{\text{HitPairs}}} \tag{3.4}$$

where $f_{\text{MuonTriggerBit}}$ represents the flag of single muon trigger bit.

The final coincidence matrix efficiencies from P03 period during the 2018 data taking are shown in Fig. 3.5. The coincidence matrix efficiencies from all of periods during the 2018 data taking are shown in Appendix B.

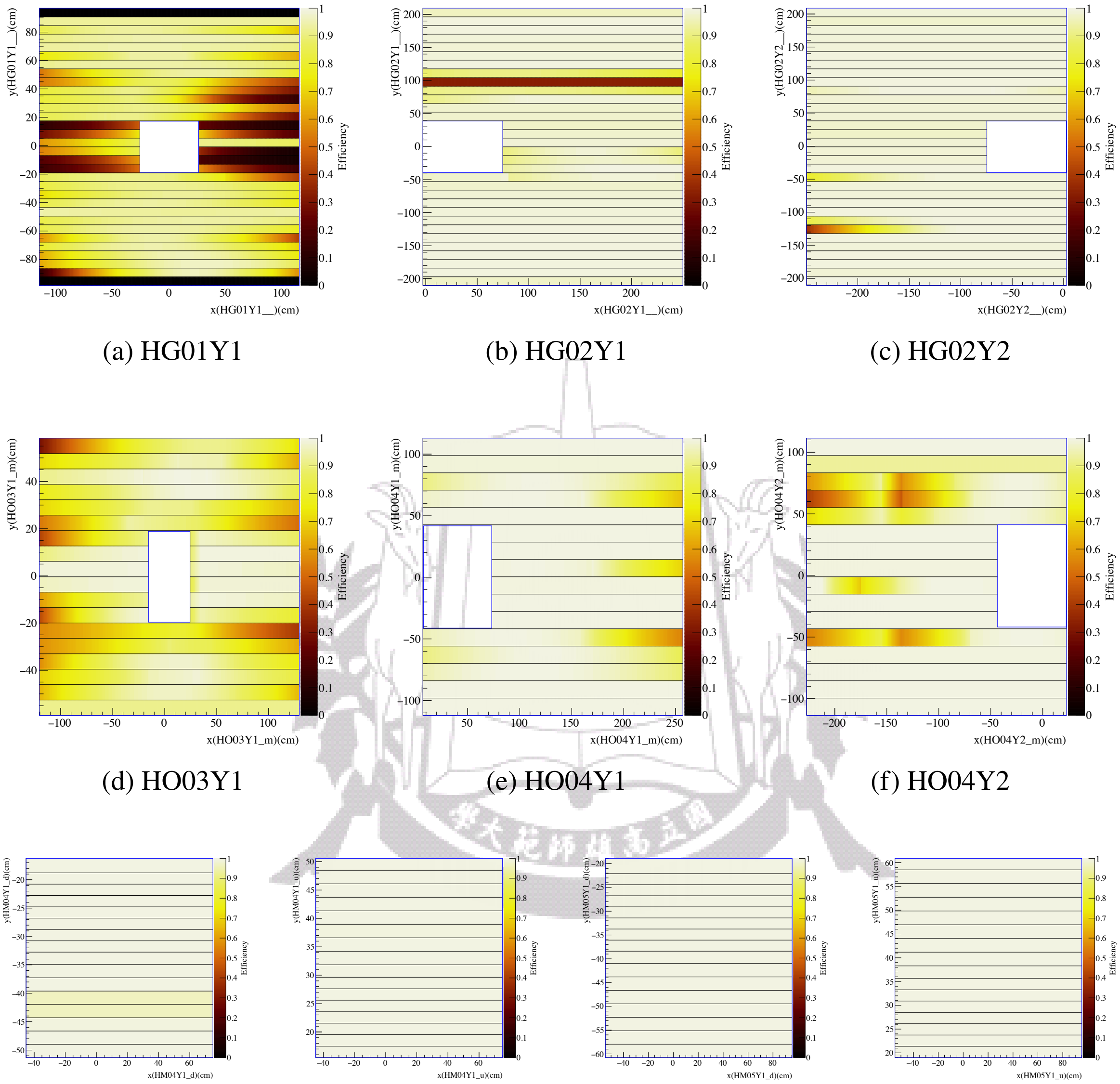

(a) HG01Y1 (b) HG02Y1 (c) HG02Y2

(d) HO03Y1 (e) HO04Y1 (f) HO04Y2

(g) HM04Yd (h) HM04Yu (i) HM05Yd (j) HM05Yu

Figure 3.4: The hodoscope efficiencies during the 2018 P03 time interval. For each hodoscope, the x axis corresponds to the x position in laboratory frame, and the y axis corresponds to the y position in laboratory frame.

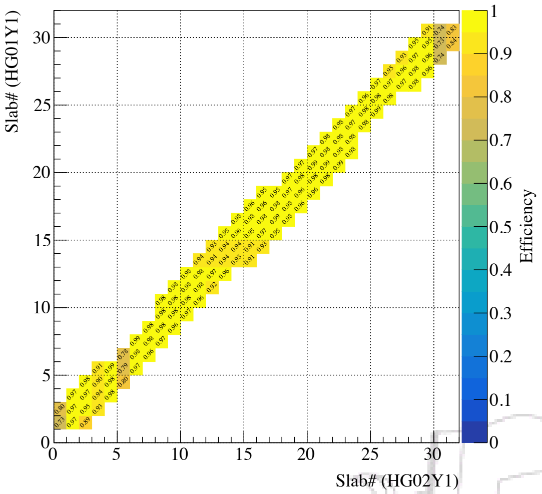

(a) LAST1

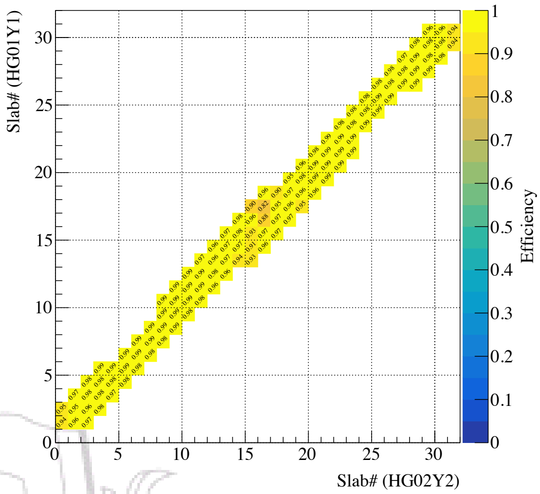

(b) LAST2

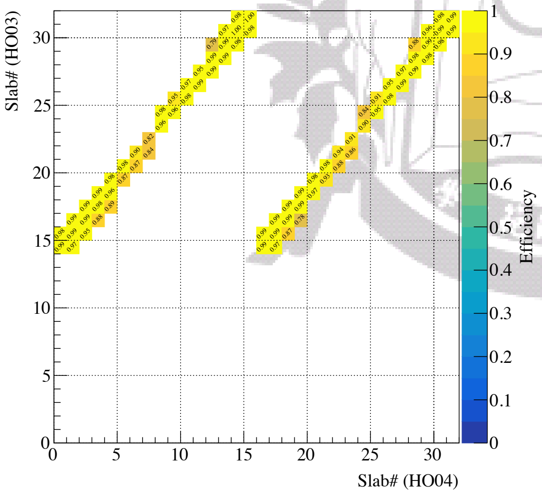

(c) OT

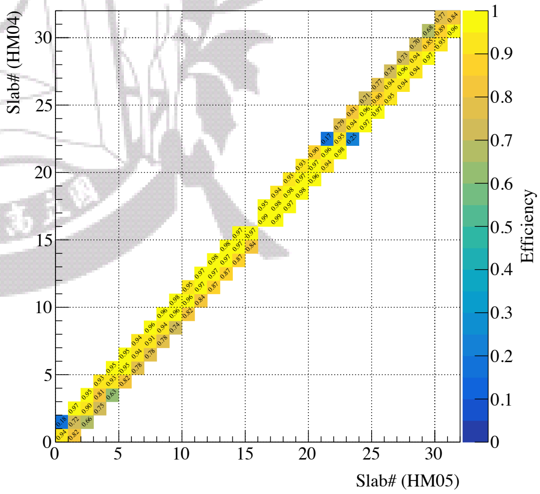

(d) MT

Figure 3.5: The efficiencies of coincidence matrices extracted from P03-t6 trigger run samples.

CHAPTER 4

Monte–Carlo Simulation

4.1 Monte–Carlo Framework in the COMPASS experiment

The Monte-Carlo framework in the COMPASS experiment is composed of four parts as shown in Fig. 4.1: PYTHIA, TGEANT, CORAL and PHAST. The well-known PYTHIA event generator [61] [62] provides the input kinematic information of dimuon pairs or single muons from a specific interaction, for example, Drell–Yan or J/ψ process, as the start of simulation process. These kinematic conditions of generated events are sampled based on the calculated differential cross sections of the interaction. The PYTHIA 8.244 is used in this study.

The TGEANT [63] is an updated detector simulation work for the COMPASS experiment based on GEANT4 package [64]. The descriptions of the beam condition, trigger setting and detector setup are improved, compared to the previous framework of COMGeant. The packages of track reconstruction CORAL and physics analysis PHAST are the common modules used for both real data and MC-simulated one. In the analysis of these two data sets, the same parameters and analysis selection criteria are imposed to ensure the validity of acceptance correction.

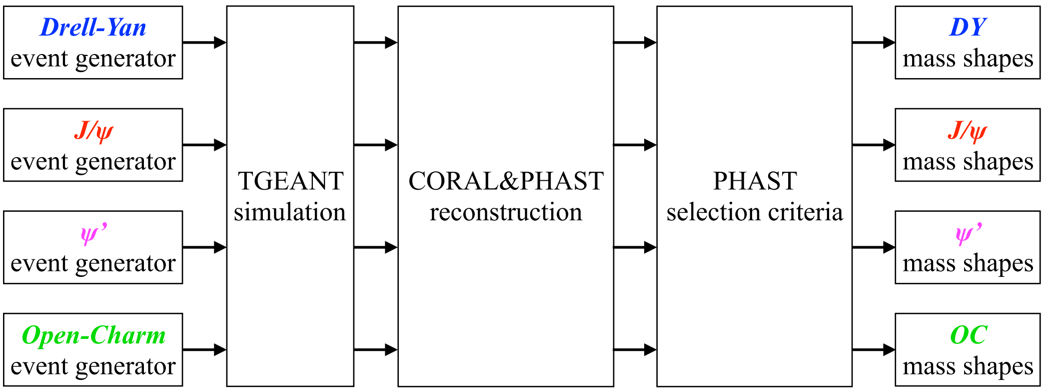

Figure 4.1: Schematic of Monte-Carlo simulation work flow.

4.2 Event Simulation and Reconstruction

For the study of angular acceptance in high-mass region, it's enough to generate the Drell–Yan events. In order to perform the background estimation study (see Section 5.4) from data sample in the dimuon mass region between 2 to 10 GeV/c^2, the other events from other physics processes (low-mass Drell–Yan process, J/ψ, ψ' and open-charm) should be prepared as well.

In general, the basic settings of PYTHIA event generator, e.g. beam energy, hadron PDFs, primordial k_T etc, are identical for the simulation of each process, except for some specific switches as described below. Since the observed events are triggered by muon tracks, the appearance of muons in the final state is required in the settings of PHYTIA.

Because the cross section of Drell–Yan process decreases rapidly with the mass, it is difficult to get a reasonably good statistic of MC events across a wide mass region. To enhance the statistics of the Drell–Yan MC events in high mass region, we generated two sets of Drell–Yan MC events in separated mass regions: low-mass Drell–Yan (0.5−3.5 GeV/c^2) and high-mass Drell–Yan (3.5−11 GeV/c^2). A combination of them leads to a smooth distribution over the whole mass range. The way of obtaining their relative weights in merging them will be described below:

Drell–Yan process: use the ”Weak boson processes” where only the production of single virtual photon is involved.

J/ψ **meson**: use the ”Onia processes” where only the charmonium states are involved. In this setting, the excited charmonium states could contribute to the production of J/ψ.

ψ' **meson**: use the ”Onia processes” and turn on ψ' production only.

Open-Charm: use the ”Hard QCD processes” with heavy-flavor subset where only the charm quark production is involved.

Fig. 4.2 shows the invariant-mass spectra of the generated and reconstructed events for each physics process in the MC simulation. The reconstructed efficiency in the high mass region (>3.5 GeV/c^2) is roughly about 18% and the mass resolution is about 160 MeV/c^2.

In TGEANT simulation, the amount of proton and neutron inside the nucleon have been considered in different materials. During the event generation, the interaction of beam particle with proton or neutron is randomly generated event by event. But the cross-section ratio of physics process between proton and neutron should be given in PYTHIA setting file. The ratio of high-mass Drell–Yan cross-section $\sigma_p^{DY}/\sigma_n^{DY}$ are about 1.83, obtained from PYTHIA8 event generator with the COMPASS kinematics setting.

4.3 Acceptance Estimation

The extraction of UAs and the evaluation of related systematic uncertainties requires extensive full-chain Monte-Carlo simulations. In particular, a careful Monte-Carlo description of the experimental apparatus and detector responses is mandatory to disentangle the physics asymmetries from those induced by the acceptance of the setup. In the analysis of UAs of the pion-induced Drell–Yan, the simulations are done using TGEANT configuration for hadronic beams [65]. The description of the beam-tracks in MC is based on a parametrization extracted from the experimental data collected with random-triggers. For each simulated event, a pile-up with a rate of $7 \cdot 10^7$ π^-/s is included in a time window of $\Delta T = \pm 20$ ns.

The definition of acceptance $A(x)$, where x represent kinematic or angular variable, is the reconstructed MC sample $N_{\mathrm{MC}}^{\mathrm{Rec.}}$ divided by the generated MC sample $N_{\mathrm{MC}}^{\mathrm{Gen.}}$:

$$A(x) = \frac{N_{\mathrm{MC}}^{\mathrm{Rec.}}}{N_{\mathrm{MC}}^{\mathrm{Gen.}}} \tag{4.1}$$

An example of generated, reconstructed and acceptance distributions of $\cos\theta_{CS}$ are shown in Fig. 4.3. Here the reconstructed MC events are obtained by the same event reconstruction procedure in CORAL and the same selection criteria as real data sample are applied. The TGEANT framework takes into account not only geometrical acceptances of spectrometers (e.g. detectors, hodoscopes...) but also detectors' efficiencies with two-dimensional efficiency maps (channel by channel variation) and so on.

The final acceptance includes the following elements:

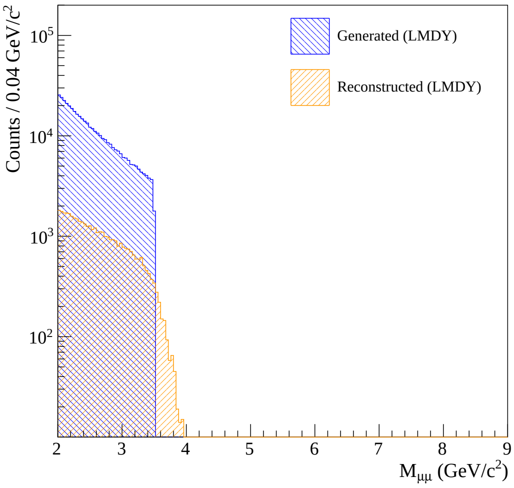

(a) Low-mass-range Drell–Yan

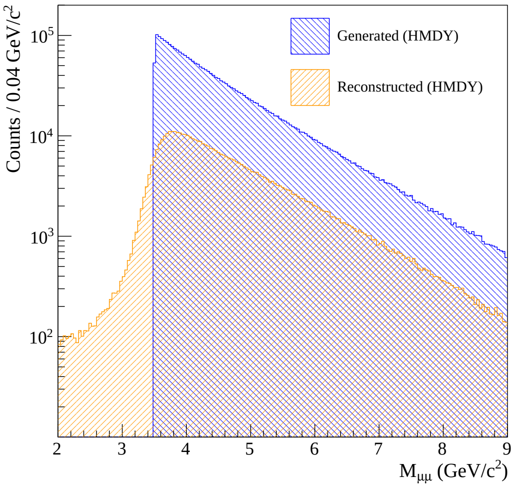

(b) High-mass-range Drell–Yan

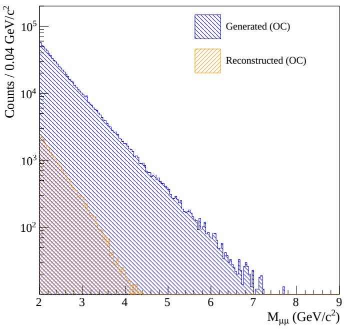

(c) open-charm

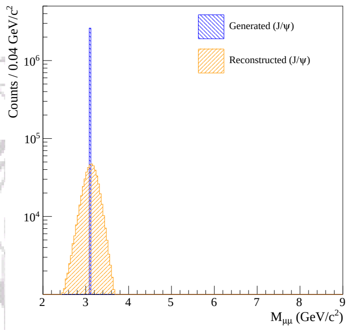

(d) J/ψ

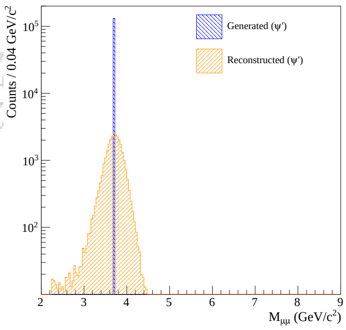

(e) ψ'

Figure 4.2: The invariant-mass spectrum of the generated and reconstructed events for (a) low-mass Drell-Yan (b) high-mass Drell-Yan (c) open charm (d) J/ψ (e) ψ'.

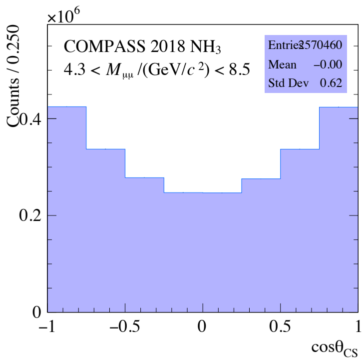

(a) $N_{\mathrm{MC}}^{\mathrm{Gen.}}$

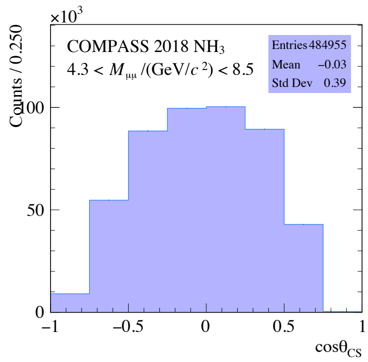

(b) $N_{\mathrm{MC}}^{\mathrm{Rec.}}$

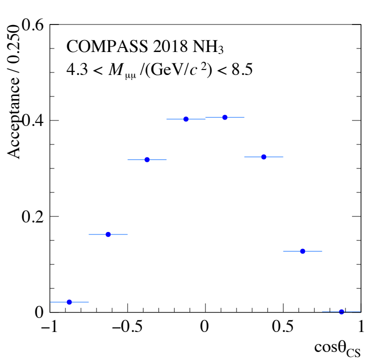

(c) $A(\cos\theta_{CS})$

Figure 4.3: Example of one-dimensional $\cos\theta_{CS}$ acceptance ingredients and computation.

1. Geometrical acceptance of spectrometers.
2. Geometrical acceptance of trigger matrix.
3. Efficiencies of detectors.
4. Efficiencies of hodoscopes.
5. Efficiencies of coincidence matrices.
6. Efficiencies of analysis cuts.
7. Resolution effect from spectrometers.

The one-dimensional kinematics acceptance in NH_3 and W targets after applying the same selection criteria (see Section 5.3) as real data sample are shown in Fig. 4.4-4.5, respectively. The overall acceptance in NH_3 target is around 20%, while it is only 10% in W target. This was due to the geometrical acceptance of coincidence matrix in the COMPASS trigger system for the target pointing effect (see Subsection 2.6.1) which was adjusted to the polarized NH_3 target. This also accounts for the lower statistics from W target (heavier material) than NH_3 target.

4.4 MC Production in different Period Configuration

Based on the study of trigger efficiencies (see Chapter 3) and the sensitivity of angular acceptance from trigger, a strong period dependence of trigger efficiencies has been observed. One the other hand, the generation of period-by-period high-mass Drell–Yan MC samples is necessary for Drell–Yan angular analysis in order to estimate the proper angular acceptance.

The period-by-period MC samples differ in the trigger and hodoscopes efficiencies which are extracted from different periods during 2018 data taking at CORAL reconstruction level. They are obtained by the same generated event sample but reconstructed in different efficiencies conditions since the implementation of detectors and hodoscopes efficiencies are implemented at event reconstruction level in the COMPASS MC chain. In the newest high-mass Drell–Yan MC production, the same event reconstruction condition as real data in the test-8 production is used. The alignment setting from P03 period and the beam file extracted from P02 period data are used in the general TGEANT production. The final reconstructed dimuon statistics in each periods of MC sample are achieved by about 100 times higher statistics with respect to each of period in real data sample. A summary of period-by-period high-mass Drell–Yan MC samples conditions and statistics is given in Tab. 4.1.

4.5 Kinematics Comparison between Data and MC

To validate the MC simulation in the angular acceptance, the agreement of kinematics distributions between read data and MC in periods, targets and triggers basis have been checked carefully. The detailed information of real data is demonstrated in Chapter 5. The comparison of the mean value of each kinematic variable in different triggers and targets from one of the periods (P03) between real data and MC are shown in Fig. 4.6. The mean

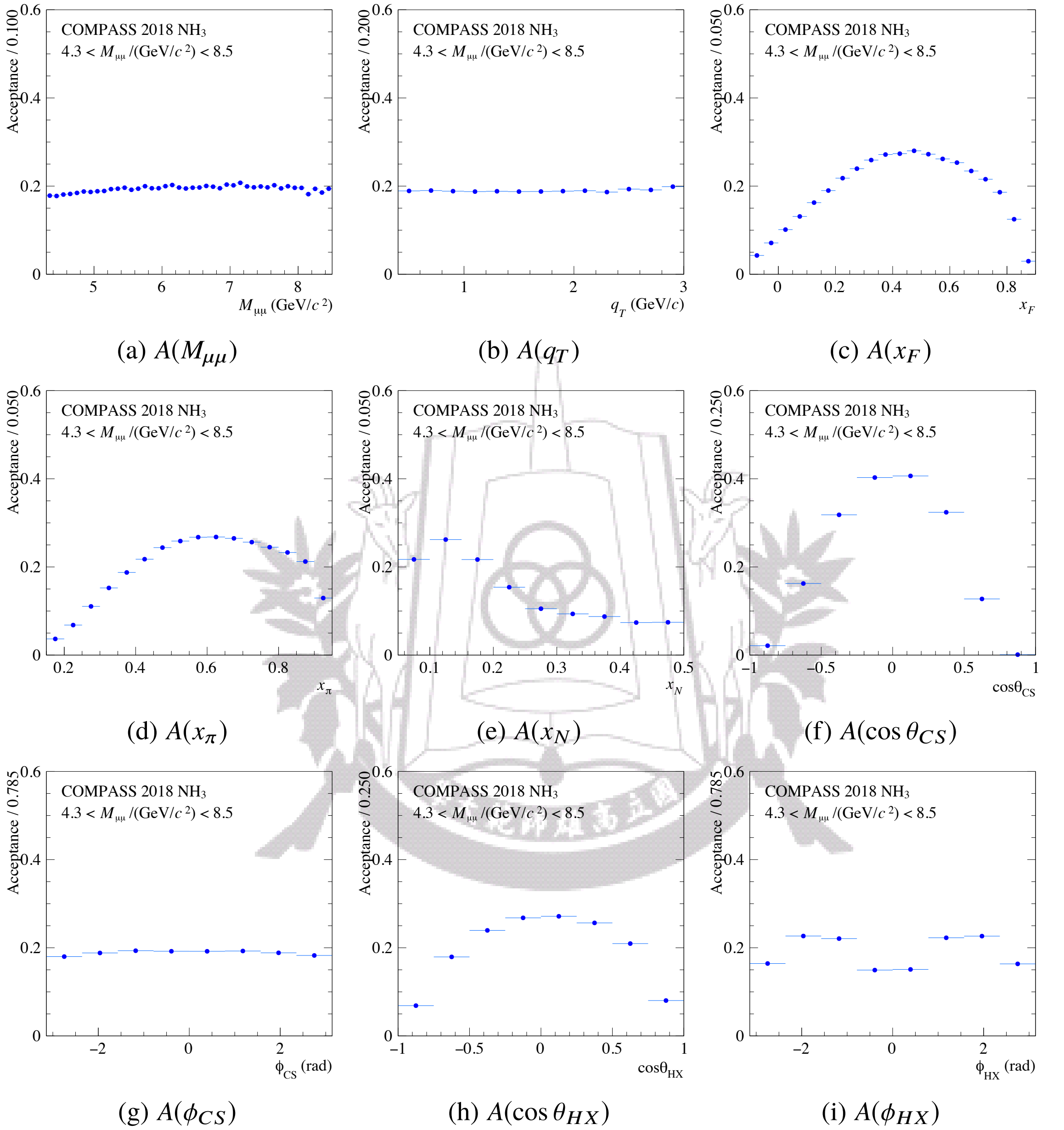

(a) $A(M_{\mu\mu})$ (b) $A(q_T)$ (c) $A(x_F)$

(d) $A(x_\pi)$ (e) $A(x_N)$ (f) $A(\cos\theta_{CS})$

(g) $A(\phi_{CS})$ (h) $A(\cos\theta_{HX})$ (i) $A(\phi_{HX})$

Figure 4.4: The one-dimensional acceptances of the NH_3 target for COMPASS 2018 setup estimated from MC sample in the P03 condition.

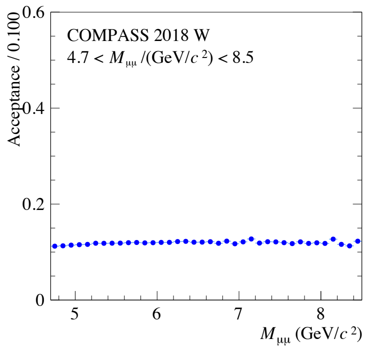

(a) $A(M_{\mu\mu})$

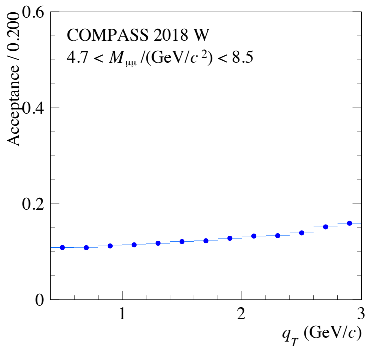

(b) $A(q_T)$

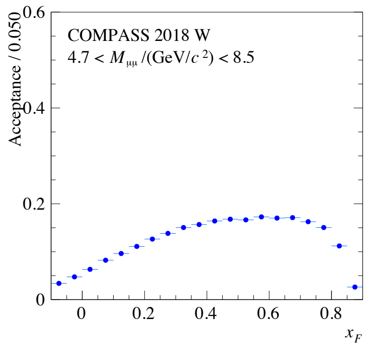

(c) $A(x_F)$

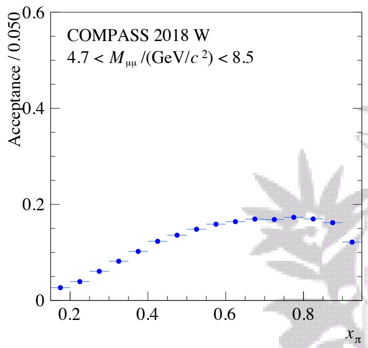

(d) $A(x_\pi)$

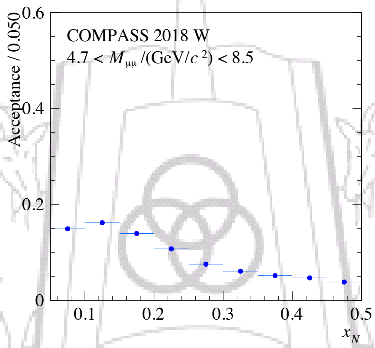

(e) $A(x_N)$

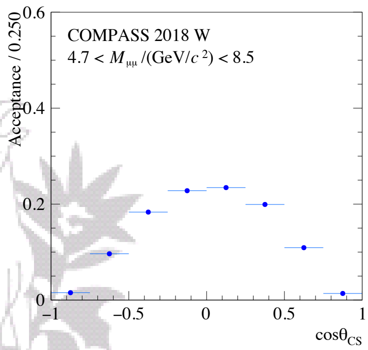

(f) $A(\cos\theta_{CS})$

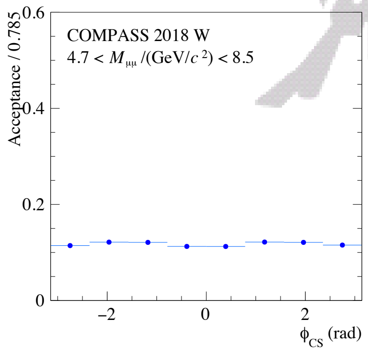

(g) $A(\phi_{CS})$

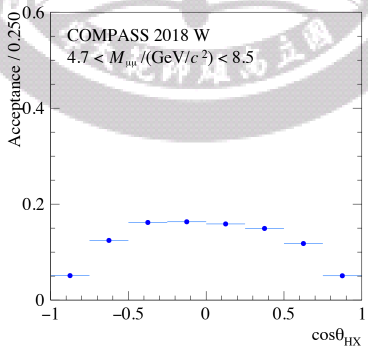

(h) $A(\cos\theta_{HX})$

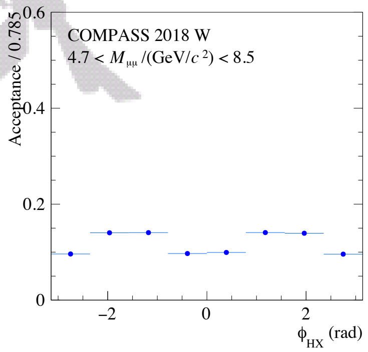

(i) $A(\phi_{HX})$

Figure 4.5: The one-dimensional acceptances of the W target for COMPASS 2018 setup estimated from MC sample in the P03 condition.

Table 4.1: Summary of period-by-period high-mass Drell–Yan MC samples conditions and statistics.

Period	#Generated Events	#Reconstructed Events
P01	25,000,000	3,108,100
P02		3,500,437
P03		3,349,314
P04		2,953,705
P05		2,894,945
P06		3,070,522
P07		2,974,206
P08		2,905,912

values of x_N, x_π, x_F, q_T and $M_{\mu\mu}$ as a function of each kinematic variable (same binning as for extracting unpolarized asymmetries which is shown in Tab. 5.8) are shown. In these comparison plots, the different colors represent the different trigger regions (red for inclusive LAST-LAST, blue for inclusive OT-LAST), while the different styles of point represent the real data and MC (close circles for real data, open circles for MC). Both real data and MC have been applied with the same selection criteria listed in Section 5.3. In general the agreement between real data and MC in terms of kinematics mean value is nice in each kinematics bin for both NH_3 and W target.

Furthermore, the agreement of the shape of each kinematics variables is also checked on a basis of period, target and trigger. The comparison of the shape of each kinematics variables in different triggers and targets between real data and MC from the full 2018 data samples are shown in Fig. 4.7, Fig. 4.8, Fig. 4.9 and Fig. 4.10, respectively. The agreement of kinematics distributions is also good in both triggers and targets. The deviation between real data and MC are kept below 20%, where deviations show up only at the edges of the kinematic phase-spaces.

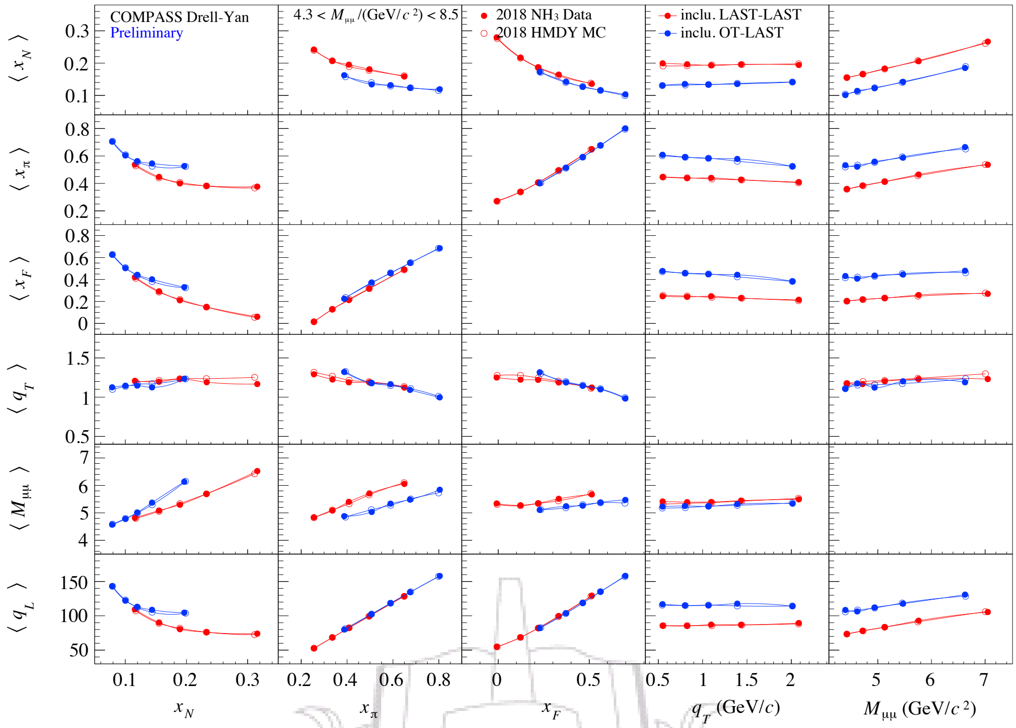

(a) NH_3 target

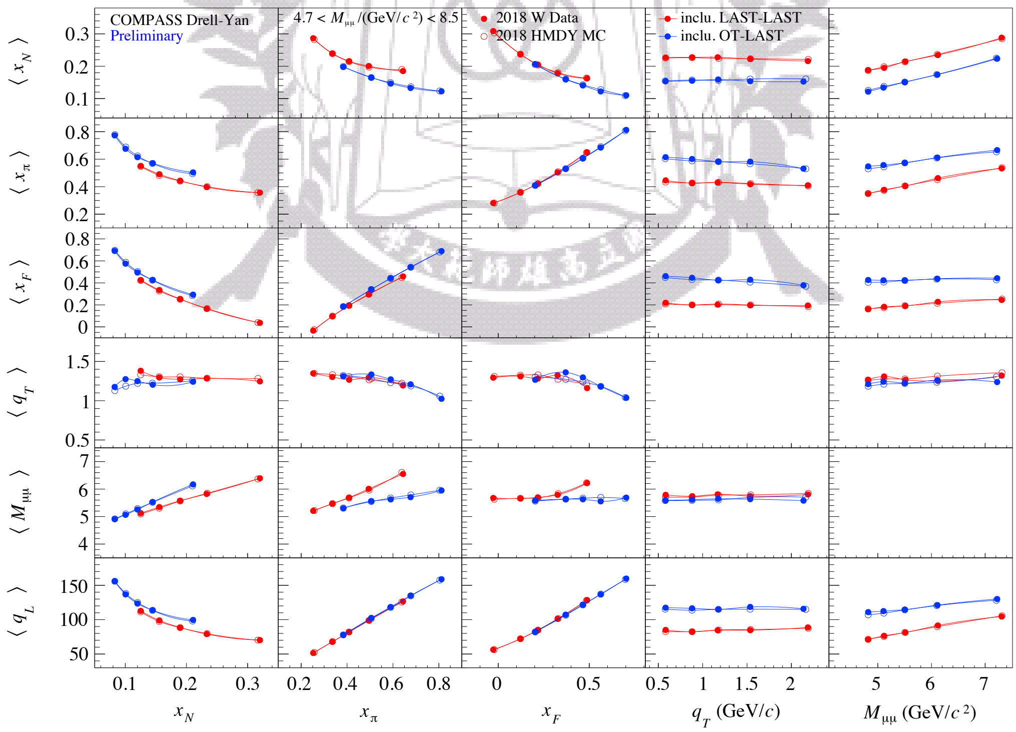

(b) W target

Figure 4.6: The comparison of the mean value of kinematics variables between real data and MC.

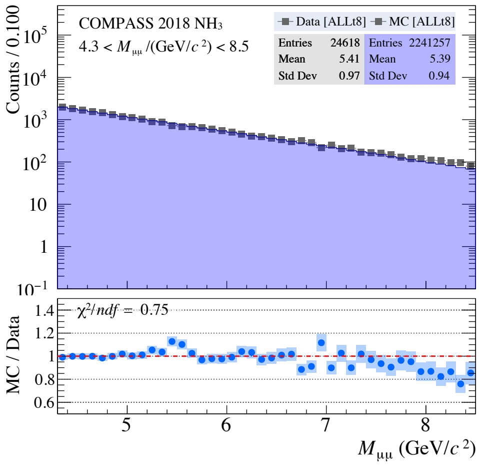

(a) $A(M_{\mu\mu})$

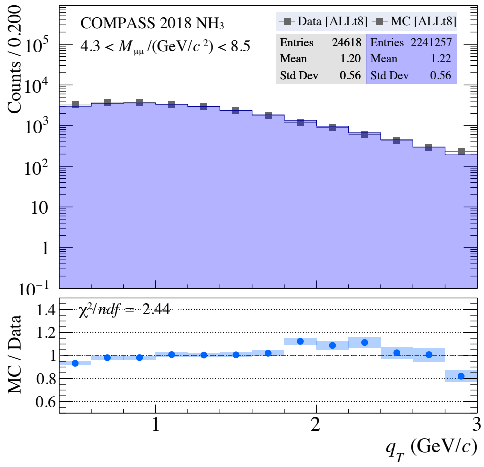

(b) $A(q_T)$

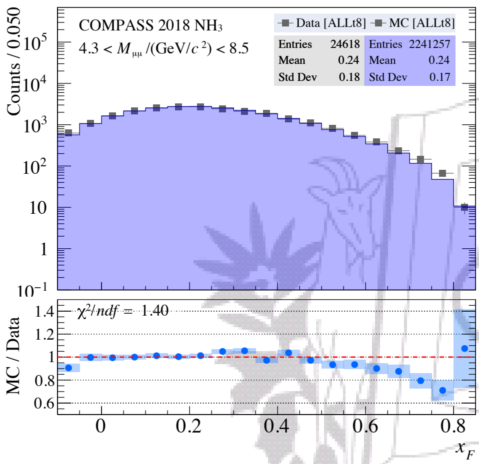

(c) $A(x_F)$

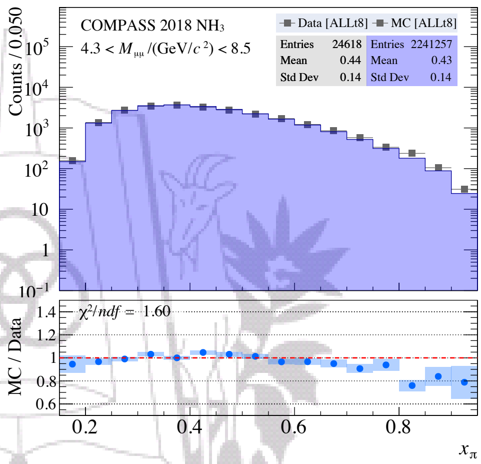

(d) $A(x_\pi)$

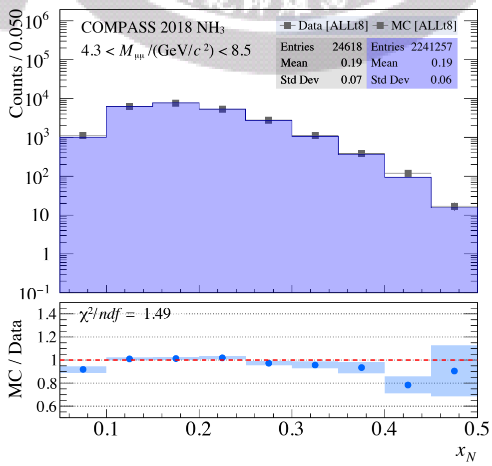

(e) $A(x_N)$

Figure 4.7: The real data and MC comparison of the shape of each kinematics variables in the LAST–LAST trigger from the NH_3 targets.

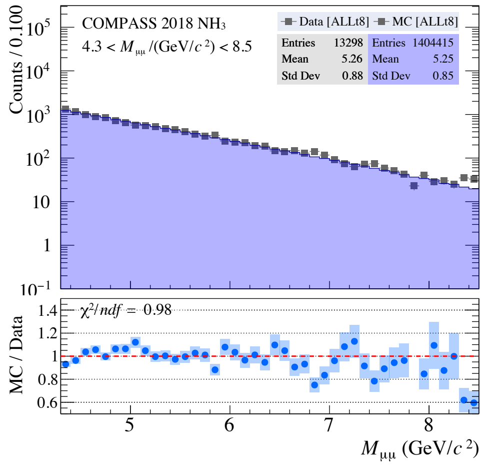

(a) $A(M_{\mu\mu})$

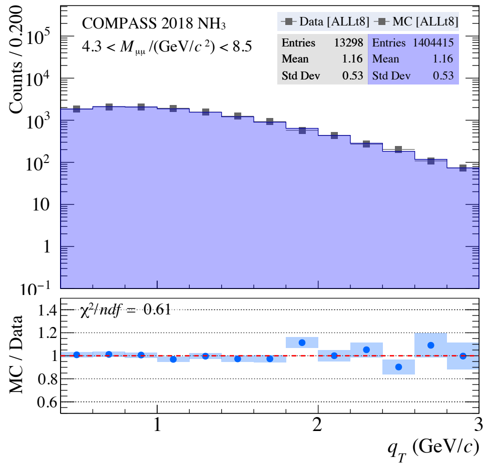

(b) $A(q_T)$

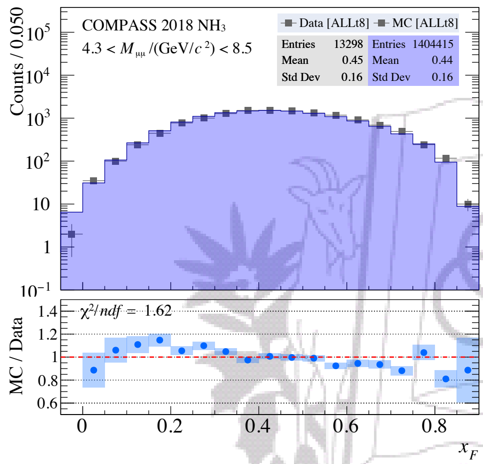

(c) $A(x_F)$

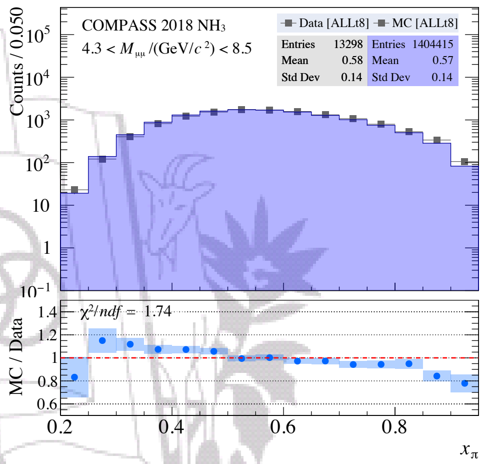

(d) $A(x_\pi)$

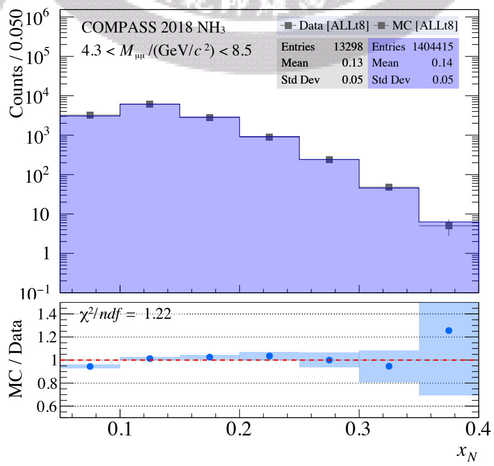

(e) $A(x_N)$

Figure 4.8: The real data and MC comparison of the shape of each kinematics variables in the OT–LAST trigger from the NH_3 targets.

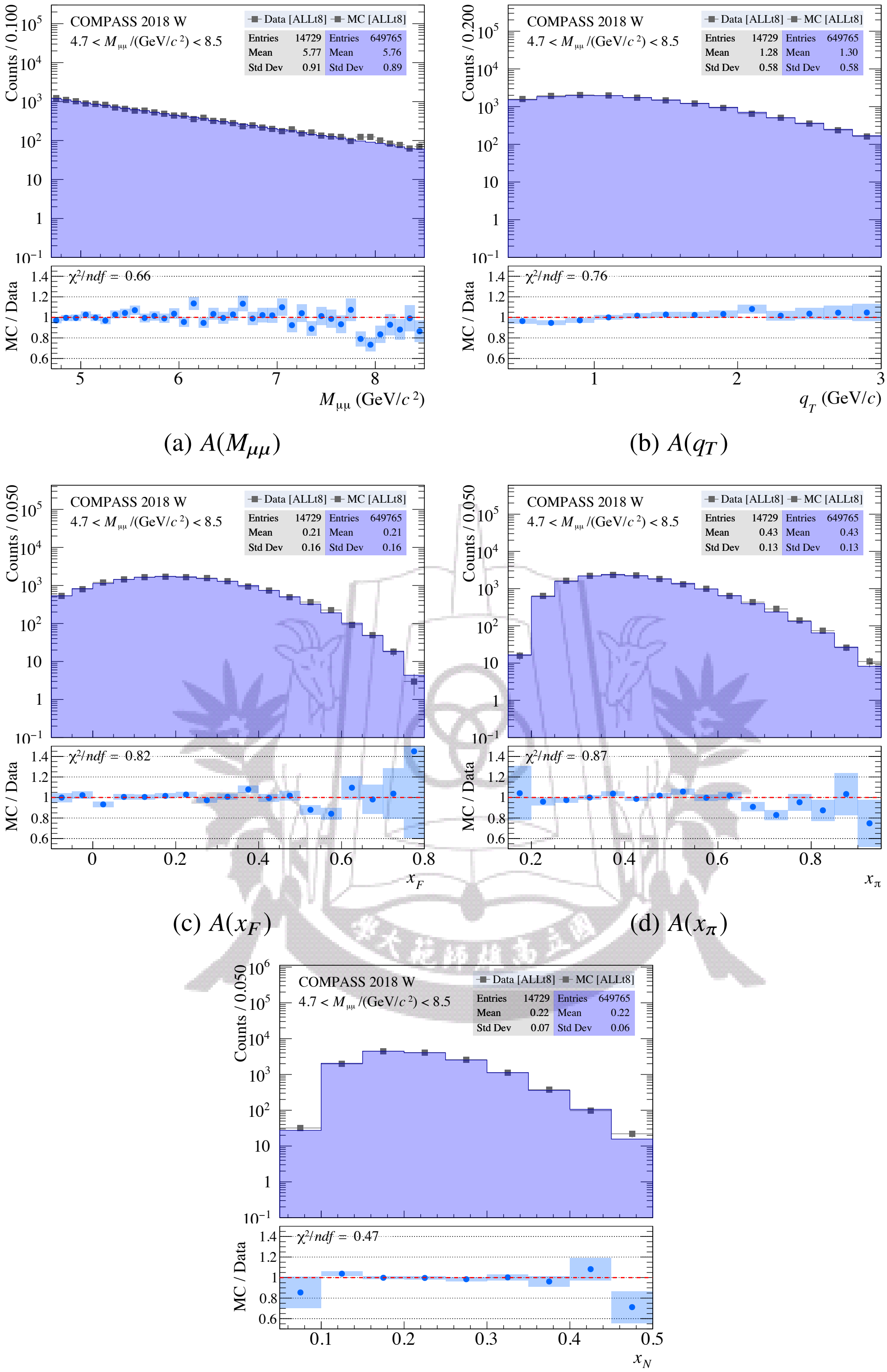

(a) $A(M_{\mu\mu})$ (b) $A(q_T)$

(c) $A(x_F)$ (d) $A(x_\pi)$

(e) $A(x_N)$

Figure 4.9: The real data and MC comparison of the shape of each kinematics variables in the LAST–LAST trigger from the W targets.

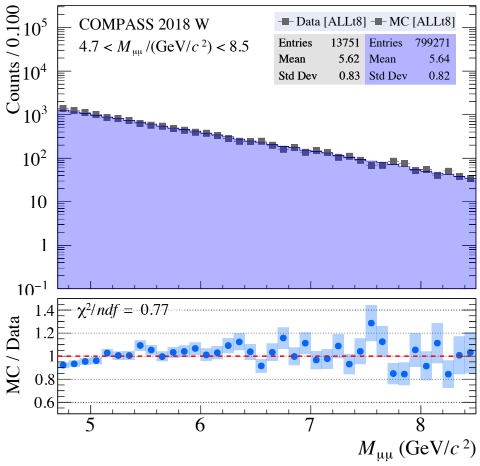

(a) $A(M_{\mu\mu})$

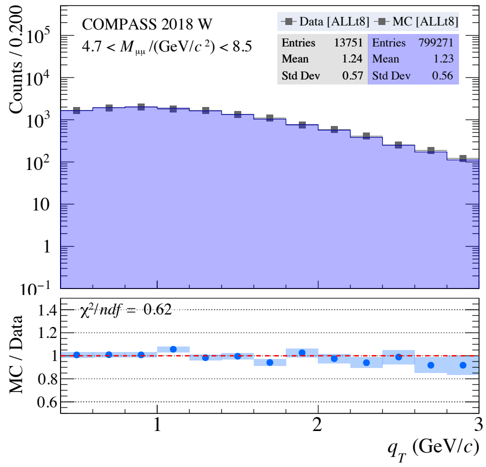

(b) $A(q_T)$

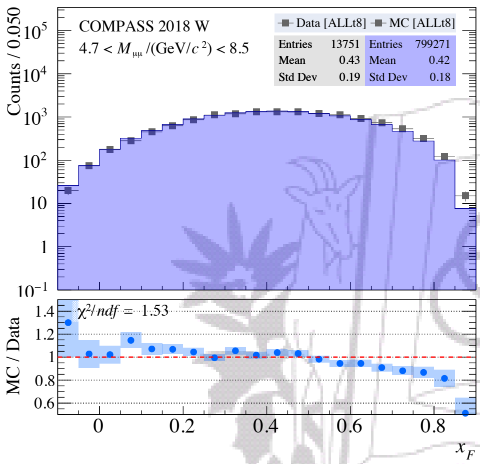

(c) $A(x_F)$

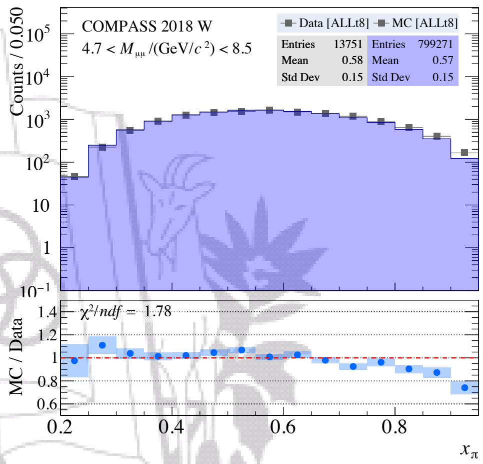

(d) $A(x_\pi)$

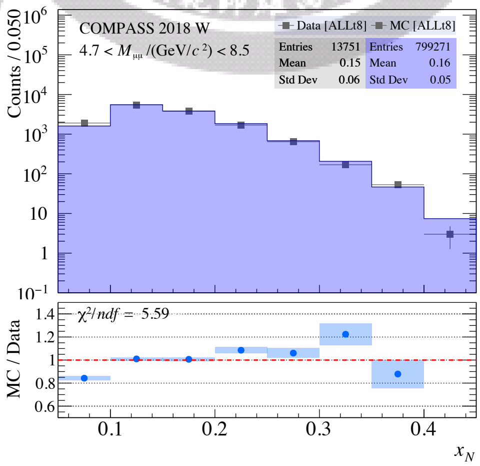

(e) $A(x_N)$

Figure 4.10: The real data and MC comparison of the shape of each kinematics variables in the OT–LAST trigger from the W targets.

CHAPTER 5

Data Analysis

In this Thesis, the data used to perform Drell–Yan angular analysis was collected during COMPASS Drell–Yan run data taking in the year of 2018 and split into 9 periods (approximated 2 weeks per period) labelled as P00-P08. The analysed data were using **test-8** production data where the raw binary data and reconstructed into ROOT-tree files were processed with the up-to-date version of CORAL software.

In this chapter, the data sample selection, background estimation, kinematics distribution and one-dimensional kinematics binning will be demonstrated. This improved data analysis framework is dedicated to the Drell–Yan unpolarized asymmetries analysis.

5.1 Data Sample

The data collected between May 16th and November 12th ($\sim$ 24 weeks) in the year of 2018. The data sample from each week is labelled as sub-period where the target polarization was fixed. Furthermore, the data from 24 sub-periods were merged into 9 periods to include data of opposite target polarization. The details about data-periods including run number and target polarization states are summarized in Tab. 5.1. In the table, the target polarization indicated the polarization direction for the upstream and downstream cells, respectively. The vertical arrows $\uparrow$ and $\downarrow$ represent the orientation of the proton spin polarization. Here the sign of the transverse polarization $(+,-)$ is defined with respect to the dipole field. The polarisation effects are cancelled out after combining data of opposite polarisation orientations, and thus it is possible to use these data sample for extracting the Drell–Yan unpolarized asymmetries.

The data sample from the first period P00 is excluded because of the absence of trigger efficiencies and corresponding MC sample in P00 condition.

Table 5.1: The summary of 2018 data taking information.

Period	Sub-period	Polarization	Run numbers	#Spills	Date
P00	SP-1	$\uparrow\downarrow$ $(-+)$	283117-283285	23600	May 16 - May 23
	SP-2	$\downarrow\uparrow$ $(+-)$	283338-283464	14263	May 25 - May 30
	SP-3	$\downarrow\uparrow$ $(+-)$	283588-283705	13560	Jun 08 - Jun 13
P01	SP-1	$\uparrow\downarrow$ $(-+)$	283849-284003	15462	Jun 21 - Jun 26
	SP-2	$\downarrow\uparrow$ $(+-)$	284022-284233	15695	Jun 27 - Jul 03
P02	SP-1	$\downarrow\uparrow$ $(+-)$	284348-284469	12069	Jul 06 - Jul 11
	SP-2	$\downarrow\uparrow$ $(+-)$	284471-284623	17569	Jul 11 - Jul 17
	SP-3	$\uparrow\downarrow$ $(-+)$	284642-284802	18690	Jul 18 - Jul 25
	SP-4	$\uparrow\downarrow$ $(-+)$	284815-284935	13871	Jul 26 - Jul 31
P03	SP-1	$\uparrow\downarrow$ $(-+)$	284941-285141	27344	Aug 01 - Aug 08
	SP-2	$\downarrow\uparrow$ $(+-)$	285149-285333	19195	Aug 09 - Aug 15
P04	SP-1	$\downarrow\uparrow$ $(+-)$	285359-285512	13143	Aug 16 - Aug 21
	SP-2	$\downarrow\uparrow$ $(+-)$	285517-285646	12796	Aug 22 - Aug 27
	SP-3	$\uparrow\downarrow$ $(-+)$	285707-285844	19614	Aug 31 - Sep 05
P05	SP-1	$\uparrow\downarrow$ $(-+)$	285865-285994	15376	Sep 05 - Sep 11
	SP-2	$\downarrow\uparrow$ $(+-)$	286019-286103	12529	Sep 12 - Sep 17
P06	SP-1	$\downarrow\uparrow$ $(+-)$	286170-286324	16734	Sep 20 - Sep 26
	SP-2	$\uparrow\downarrow$ $(-+)$	286330-286462	16924	Sep 26 - Oct 01
P07	SP-1	$\uparrow\downarrow$ $(-+)$	286481-286742	11496	Oct 03 - Oct 10
	SP-2	$\uparrow\downarrow$ $(-+)$	286749-286929	21428	Oct 11 - Oct 17
	SP-3	$\downarrow\uparrow$ $(+-)$	286941-287096	13732	Oct 17 - Oct 24
	SP-4	$\downarrow\uparrow$ $(+-)$	287107-287256	13212	Oct 25 - Oct 30
P08	SP-1	$\uparrow\downarrow$ $(-+)$	287296-287404	14686	Nov 01 - Nov 06
	SP-2	$\downarrow\uparrow$ $(+-)$	287458-287537	7435	Nov 09 - Nov 12

5.2 Stability Checks

Before performing the further data analysis, data quality on the basis of spills and runs was checked in order to minimize systematic uncertainties. The spill or run identified with a bad condition is tagged and summarized into a list, which is used in the event selection.

The quality of spills was determined by monitoring several macro-variables. These variables are assumed to indicate the goodness of working condition of spectrometer in certain time interval. The list of macro-variables used for Drell–Yan run in the spill stability analysis is shown below:

- Number of beam particles divided by number of events.
- Number of beam particles divide by number of primary vertices
- Number of hits per beam track divided by number of beam particles
- Number of primary vertices divided by number of events
- Number of outgoing tracks divided by number of events
- Number of outgoing particles divided by number of events
- Number of outgoing particles from primary vertex divided by number of primary vertices
- Number of outgoing particles from primary vertex divided by number of events
- Number of hits in outgoing particles divided by number of events
- Number of μ^+ tracks divided by number of events
- Number of μ^+ tracks from primary vertex divided by number of events
- Number of μ^- tracks divided by number of events
- Number of μ^- tracks from primary vertex divided by number of events
- Sum of χ^2 of outgoing particles divided by number of outgoing particles
- Sum of χ^2 of all vertices divided by number of all vertices
- Trigger rates (LAST–LAST,OT–LAST,MT–LAST)

The quality of runs was determined by a set of relevant kinematic variables: x_F, x_π, x_N, q_T, $M_{\mu\mu}$, P_{μ^+}, P_{μ^-}, P_{γ^*}, X_{vertex}, Y_{vertex} and Z_{vertex}. The stability of these variables was monitored run-by-run by checking their means and shapes. The runs will be labelled as a bad one once the shapes of variables are incompatible in the given period or the mean value of variables in this run id more than 5 standard deviations away from the overall mean for the given period. The rejection rates of spills and runs stability check for 9 periods of 2018 data are summarized in Tab. 5.2.

Table 5.2: The summary of rejection rates from spills and run stability check.

Period	**Bad spills+runs rejection**
P01	10.9%
P02	11.0%
P03	8.6%
P04	12.0%
P05	5.0%
P06	7.0%
P07	8.6%
P08	13.4%

5.3 Event Selection

The list of cuts applied to select the final sample of Drell–Yan events produced in NH_3 and W targets is presented in the following. In particular, the dimuon invariant-mass range between 4.3 GeV/c^2 and 8.5 GeV/c^2 is chosen to select the Drell–Yan events produced in NH_3 target, which ensures a purity of Drell–Yan events above 96%. More details about the study of the background estimation will be described later (see Section 5.4).

In order to ensure a similar level of purity for the events produced in the tungsten beam plug, stricter selections are needed. The muon pairs produced in W are characterized by a worse mass resolution[1], which leads to a higher background contamination in the high mass region. In addition, the pion beam hitting the tungsten plug produces a large amount of secondary hadrons, which increase the probability of Drell–Yan pair production from re-interactions. Building on that, a proposal with further improved mass range selection criteria: $4.7 < M_{\mu\mu}/(\mathrm{GeV}/c^2) < 8.5$ is adopted for W target in the region $-30 < Z_{\mathrm{vertex}}/(\mathrm{cm}) < -10$.

The impact of each selection criterion on the number of dimuon pairs collected in 2018 is listed in Tab. 5.3, while the period-by-period cut-flow is shown in Tab. 5.4. Here the cut-flow table are splited into two parts from cut-11 since the criteria for two targets (NH_3 and W) are different from that point on. The impact of the cuts specific for W target is reported at the bottom of each tables. Below the final list of cuts for Drell–Yan angular analysis is reviewed:

1. **Two oppositely charged muon candidates from primary vertex**:
   The tracks crossing along the spectrometer more than 30 radiation lengths ($x/X0 \geq 30$) are considered to be muon. From the sample of muon track of a given event, one first select the combinations of oppositely charged tracks and then check if they originate from a common primary vertex. In case more than one primary vertex are associated with this muon pair, the "best primary vertex" tagged by CORAL is selected if existed. Otherwise the common primary vertex with the smallest vertex-χ^2 is adopted.

2. **Dimuon trigger fired**:
   Require the LAST–LAST[2] or OT–LAST[3] trigger bits to be fired. Events from Middle

[1] muons crossing tungsten material are a subject of considerable energy loss and multiple scattering
[2] Large Angle Spectrometer Trigger.
[3] Outer Trigger.

trigger are abandon since this trigger covering the very small angles $\theta_\mu < 10$ mrad is highly contaminated by the beam decay muons.

3. **Tracks with the first and the last measured point**:
   Require the first measured point of the muon tracks to be upstream of SM1 dipole magnet ($Z_{\text{First}} \leq 300$ cm) in order to ensure the momentum measurement. And also require the last measured point to be downstream of the Muon Wall 1 ($Z_{\text{Last}} \geq 1500$ cm) to guarantee the track was not stopped into Muon Filter 1.

4. **Time of muon track defined**:
   Make sure the muon tracks have a meaningful time $t_{\mu\pm}$ with respect to the trigger time.

5. **Difference between the times of two muon tracks**:
   Require that the absolute time difference between the two muon tracks is less than 5 ns ($|t_{\mu+} - t_{\mu-}| \leq 5$ ns), rejecting mainly uncorrelated muon pairs which picking up from beam decay muon (Fig. 5.1a). After the beam decay muons were filtered by the trigger selection requirement (Cut. 2), this additional cut only bring a small impact ($< 1\%$).

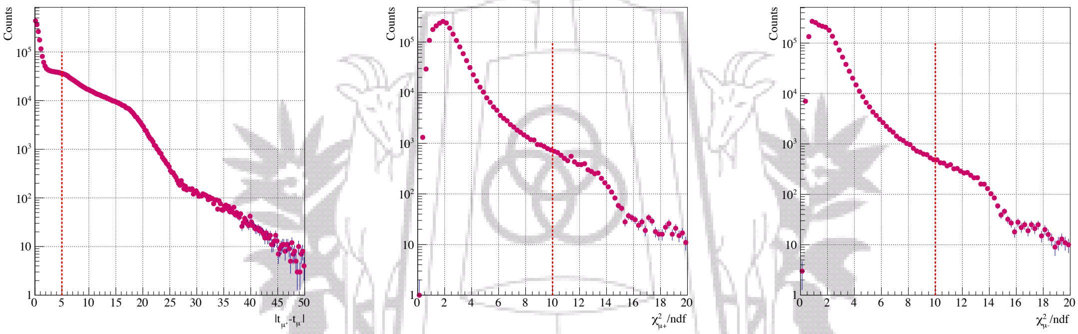

(a) $|t_{\mu+} - t_{\mu-}|$ (b) $\chi 2_{\mu+}/ndf$ (c) $\chi 2_{\mu-}/ndf$

Figure 5.1: Right Panel: the distribution of absolute time difference between the two muon tracks from P08 data sample. Middle and left panels: the distributions of $\chi^2_{\text{track}}/ndf$ of the muon tracks normalized to the number of degrees of freedom from P08 data sample.

6. **Muon track quality cut**:
   To reject badly reconstructed muon tracks, the $\chi^2_{\text{track}}/ndf$ of the muon tracks normalized to the number of degrees of freedom (Fig. 5.1b-5.1c) is required to be smaller than 10: $\chi 2_{\mu\pm} \leq 10$.

7. **Hodoscope-pointing cut (so-called trigger validation)**:
   This criterion requires that both muon tracks, extrapolated to the position of the hodoscopes corresponding to the fired trigger (LAST–LAST or OT–LAST), fall into active area of corresponding hodoscopes. This cut ensures that the two selected muons could fire the trigger.

8. **Good spills/runs selection**:
   Rejection of spills and runs marked as bad by the data quality analyses. The quality of the data was checked on spill-by-spill and run-by-run basis to identify the data recorded

in unstable conditions. The detailed information of good spills/runs selection have been demonstrated in Section 5.2.

9. **Physical limits cut**:
   This cut requires that the Bjorken variables x_π, x_N and Feynman variable x_F are within their physical limits: $-1 < x_F < 1$, $0 < x_\pi < 1$ and $0 < x_N < 1$.

10. **Dimuon transverse momentum cut**:
    Require the transverse momentum of the virtual photon to be in the range of 0.4 < q_T/(GeV/c) < 3.0. The lower limit is set to ensure a reasonably good resolution for the azimuthal angles. The upper limit is set to reject the high q_T region where the agreement between data and MC rapidly becomes bad. Fig. 5.2 shows the agreement of q_T distribution between real data and MC becomes bad after 3 GeV/c.

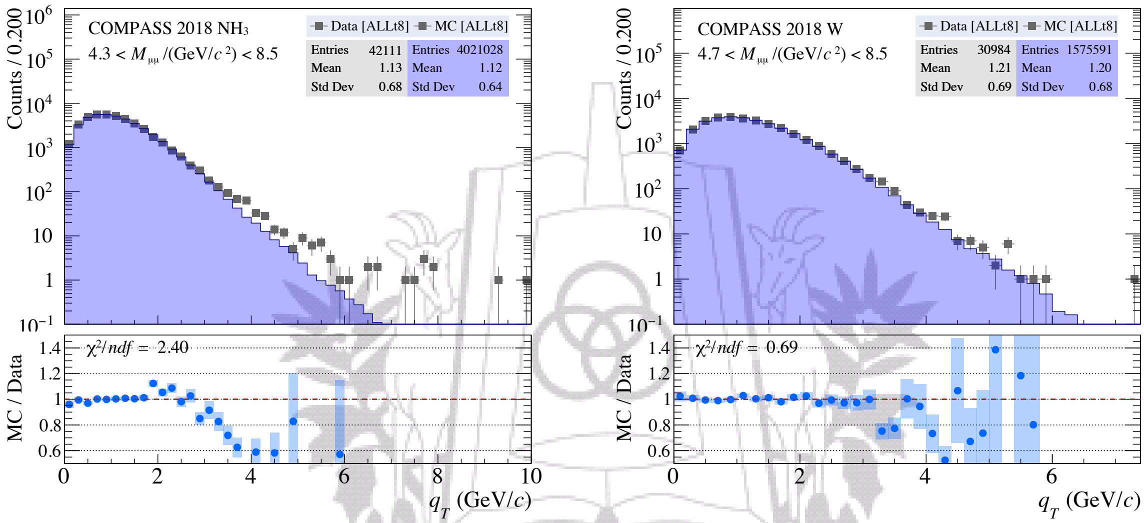

(a) NH_3 target (b) W target

Figure 5.2: The comparison of q_T distribution between real data (black point) and MC (blue histogram), bottom figure represent the ratio of MC/data. The deviation of q_T distribution above 3 GeV/c is larger then 20% in NH_3 target.

11. **Primary vertex z-position cut**:
    Require the reconstructed primary vertices along z axis to be located in the NH_3 target cells (in the upstream cell: -294.5 < Z_{vertex}/(cm) < -239.4 or in the downstream cell: -219.1 < Z_{vertex}/(cm) < -163.9) or in the first W target cell (-30.0 < Z_{vertex}/(cm) < -10.0).

12. **Primary vertex radial cut**:
    Ensure that the primary vertices in the xy-plane (both in NH_3 and in W) are located within the geometry of target cells: an elliptical cut instead of a circle cut (see Fig. 5.3) is applied in order to get rid of the shadow from veto trigger which was not introduced in MC simulation: $\frac{X^2_{\text{vertex}}/(\text{cm})}{1.9^2} + \frac{(Y_{\text{vertex}}/(\text{cm})-0.15)^2}{1.3^2} < 1.0$

13. **Invariant-mass cut for W**:
    Due to the worse mass resolution in tungsten target, the contamination from the other

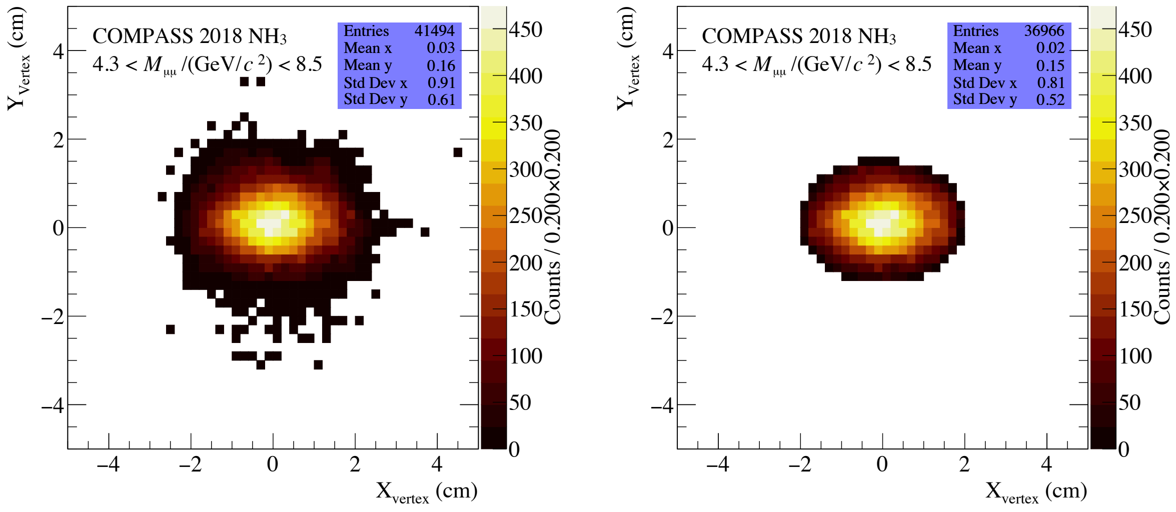

(a) No elliptical cut (b) With elliptical cut

Figure 5.3: The reconstructed primary vertices distribution on the xy-plane in NH_3 target.

processes (J/ψ, ψ' etc.) increases in the same mass region. To ensure the consistent Drell–Yan signal/background separation as in NH_3 target, a tighter mass cut for tungsten target is needed. The muon pairs produced in W target are required to be in the mass range of $4.7 < M_{\mu\mu}/(\mathrm{GeV}/c^2) < 8.5$.

14. **Dead zone of hodoscopes cut**:
Due to the non-smooth edge of slabs around the dead zone of each hodoscope in reality, which is too hard to describe properly in MC simulation, it is necessary to make a cut to enlarge the dead zone size. The idea is to perform the hodoscope pointing again, but considering a new (smaller) active area of each hodoscope plane. This removes the cases in which the fired trigger was caused by the muon track passing through the area near the dead zone. A cut by extending the size of dead zone with 2.5 cm in both sides and both x-, y-direction for six of hodoscopes planes (HG01Y1, HG02Y1, HG02Y2, HO03Y1, HO04Y1 and HO04Y2) is applied.

15. **Muon momentum cut**:
The agreement between data and MC rapidly worsens in very small momentum region (see Fig. 5.4). In order to keep a good data/MC agreement, a low momentum cut for each sign of muon is required: $p_{\mu^\pm} > 7$ GeV$/c$. Additionally, in order to minimise the possible remaining background from beam decay muon, an upper cut on the total dimuon momentum is also required: $p_{\mu^+} + p_{\mu^-} < 180$ GeV$/c$.

16. **Muon track's polar angle cut**:
Due to the observation of inconsistency between real data and MC in terms of small polar angle of μ^- in LAB frame for the NH_3 target case, A cut: $\theta_{\mu^-,\mathrm{LAB}} > 0.02$ rad is applied in order to minimize the bias of acceptance estimation in this region.

17. **Lower limit of Feynman-x cut**:
Due to very low acceptance in the negative x_F region, it's difficult to ensure the

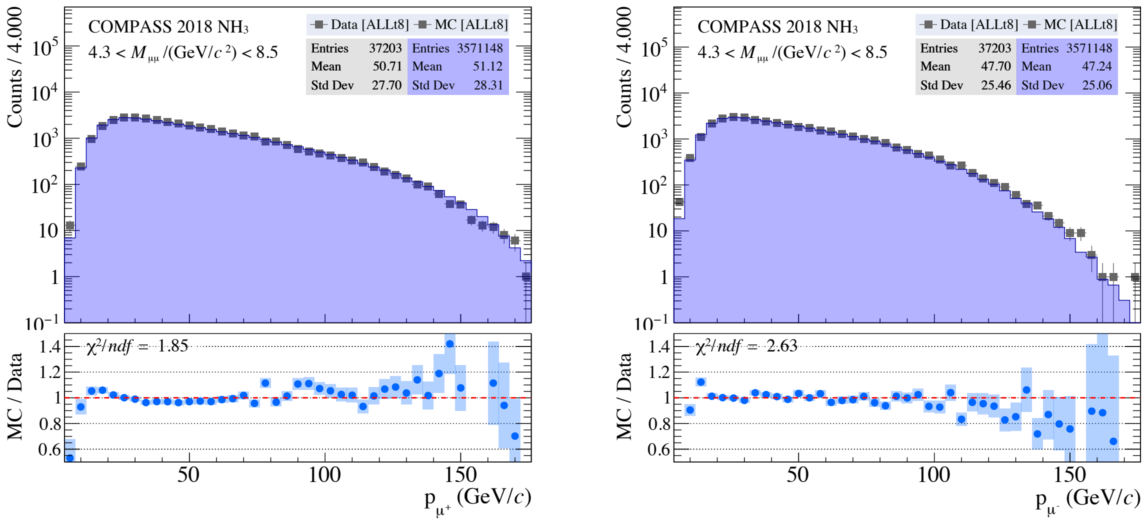

(a) NH_3 target

(b) W target

Figure 5.4: Comparison of muon momentum distribution between real data (black point) and MC (blue histogram) in NH_3 target, bottom figure represent the ratio of MC/data. The deviation of muon momentum distribution at low p_μ is larger then 20% in NH_3 target.

reliability of acceptance estimation in this region by checking data/MC agreement. To remove this bias, we make a low limit x_F cut: x_F > -0.1.

5.4 Background Estimation

The background estimation in COMPASS Drell–Yan data is done by studying the dimuon invariant-mass ($M_{\mu\mu}$) spectrum, which is one of the best quantities to separate the contribution of different processes (Drell–Yan, J/ψ, ψ', open-charm and combinatorial background). The invariant-mass spectrum in the range of 2−9 GeV/c^2 could be understood by using full-chain MC-simulated physics contributions. Therefore this method bring a possibility to set the proper mass region for studying the purity of Drell-Yan process accordingly. More details about the MC simulation framework are provided in Chapter 4.

5.4.1 Physics Processes

The physics events are selected out by requiring a muon pair with a large invariant-mass in the final state. In the dimuon mass range of 2−9 GeV/c^2, there are five kinds of physics processes to be considered: Drell–Yan process, J/ψ, ψ', open-charm and combinatorial background. The kinematic distributions of the first four sources are simulated by the MC framework while those for the combinatorial background, originated from random combination of two uncorrelated muons in the same event, are estimated by the like-sign muon pairs in real data.

Table 5.3: The cut-flow for events in the mass range $4.3 < M_{\mu\mu}/(\mathrm{GeV}/c^2) < 8.5$.

Selection criteria	**#dimuons**	**Statistics(%)**
Oppositely charged muon candidates from primary vertex	1,472,524	100.0
dimuon trigger bit (LAST–LAST, OT–LAST)	1,035,938	70.2
$Z_{First} \leq 300$ cm and $Z_{Last} \geq 1500$ cm	1,020,639	69.2
$t_{\mu\pm}$ defined	1,012,767	68.6
$\lvert t_{\mu+} - t_{\mu-} \rvert \leq 5$ ns	564,087	38.3
$\chi^2_{track}/n.d.f. \leq 10$	559,089	37.9
Hodoscope pointing (LAST–LAST, OT–LAST)	215,312	14.7
Good spills/runs	194,634	13.2
$-1 < x_F < 1$, $0 < x_\pi < 1$ and $0 < x_N < 1$	194,409	13.2
$0.4 < q_T/(\mathrm{GeV}/c) < 3.0$	171,630	11.6
Vertex z-position cut for NH_3	47,431	3.2
Vertex radial cut	42,188	2.9
$\cancel{4.7 < M_{\mu\mu}/(\mathrm{GeV}/c^2) < 8.5}$	42,188	2.9
Dead zone of hodoscopes cut (LAST–LAST, OT–LAST)	40,295	2.7
$\mu^\pm$ momentum cut	39,915	2.7
$\theta_{\mu^-,\mathrm{LAB}}/(\mathrm{rad}) < 0.02$	37,331	2.5
$-0.1 < x_F < 1$	36,966	2.5
Vertex z-position cut for W	57,509	3.9
Vertex radial cut	50,979	3.5
$4.7 < M_{\mu\mu}/(\mathrm{GeV}/c^2) < 8.5$	31,837	2.2
Dead zone of hodoscopes cut (LAST–LAST, OT–LAST)	28,788	2.0
$\mu^\pm$ momentum cut	28,283	1.9
$\cancel{\theta_{\mu^-,\mathrm{LAB}}/(\mathrm{rad}) < 0.02}$	28,283	1.9
$-0.1 < x_F < 1$	27,654	1.9

Table 5.4: The event cut-flow for each period. Enumeration of the cuts is the same as in Tab. 5.3.

	P01	**P02**	**P03**	**P04**	**P05**	**P06**	**P07**	**P08**
1.	158978	288558	221313	210520	124529	135931	244166	88529
2.	114406	204144	156558	147640	86827	94571	170248	61544
3.	113050	201177	154346	145484	85468	93140	167603	60371
4.	112191	199668	153187	144396	84775	92425	166275	59850
5.	60938	110725	86170	80625	46683	52474	92756	33716
6.	60412	109719	85441	79902	46222	52042	91952	33399
7.	21390	42223	31865	30490	17961	21216	36709	13458
8.	19058	37579	29122	26879	17065	19723	33550	11658
9.	19038	37536	29092	26847	17048	19702	33504	11642
10.	16817	33149	25723	23665	14972	17380	29656	10268
11.	4653	9204	7183	6636	4213	4687	8074	2781
12.	4129	8199	6374	5922	3727	4195	7170	2472
13.	4129	8199	6374	5922	3727	4195	7170	2472
14.	3931	7827	6096	5660	3562	4015	6854	2350
15.	3892	7759	6031	5601	3540	3975	6795	2322
16.	3616	7240	5645	5233	3315	3713	6393	2176
17.	3579	7166	5585	5202	3279	3671	6335	2149
11.	5509	11081	8576	7909	4947	5853	10133	3501
12.	4865	9779	7598	7030	4409	5206	8992	3100
13.	3039	6052	4752	4418	2765	3238	5650	1923
14.	2729	5475	4322	4015	2501	2886	5129	1731
15.	2697	5381	4249	3933	2451	2828	5041	1703
16.	2697	5381	4249	3933	2451	2828	5041	1703
17.	2631	5250	4158	3853	2403	2756	4935	1668

5.4.2 Combinatorial background

Other than the above physics processes originated from one single hard interaction, the so-called combinatorial background from individual muons from uncorrelated productions, e.g. decays of pions and kaons. To evaluate the total combinatorial background, the so-called like-sign method is used which calculated from like-sign muon pair samples from real data ($\mu^+\mu^+$ and $\mu^-\mu^-$). The uncorrelated opposite-sign muon pairs can be evaluated by the relation:

$$N_{\mu^+\mu^-} = 2\sqrt{N_{\mu^+\mu^+}N_{\mu^-\mu^-}}. \tag{5.1}$$

where $N_{\mu^+\mu^+}$ and $N_{\mu^-\mu^-}$ represents the total number of positive and negative like-sign pairs, respectively. However this relation holds only if the acceptance of muon tracks is charged symmetric, i.e. the acceptance of μ^+ and μ^- have to be identical. Since the acceptance of muons has minor asymmetry with respect to the charge of tracks in the COMPASS spectrometers, an **image cut** is applied in the offline analysis to reject the muon pairs if either one of the muons with a reverse of its charge is found to be outside the spectrometer and trigger acceptance. After this cut, a charge-symmetric acceptance is ensured. The invariant-mass spectrum for like-sign muon pairs and the constructed combinatorial background are shown in Fig. 5.5.

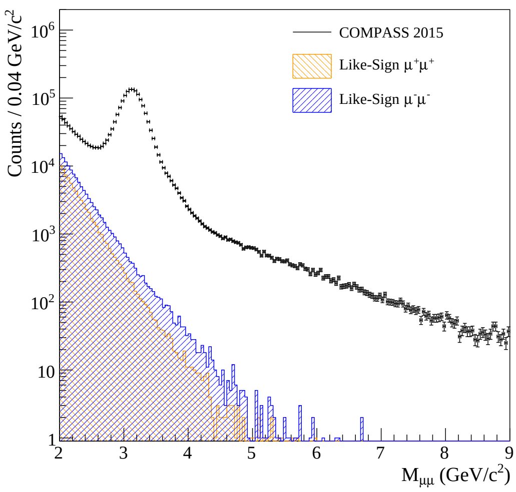

(a) Like-sign muon pairs

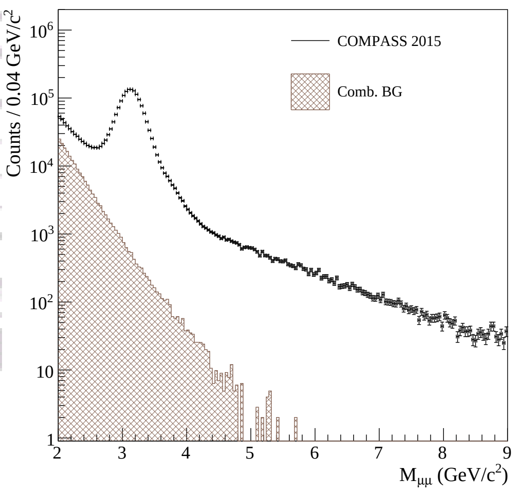

(b) Combinatorial background

Figure 5.5: Mass spectrum of like-sign muon pairs and combinatorial background.

5.4.3 Dimuon Invariant-Mass Spectrum and Background Fraction

As mentioned above, there are two sets of MC Drell–Yan events with different masses. First the invariant-mass distribution of MC-simulated Drell–Yan process is constructed by merging these two sets of low-mass and high-mass MC Drell–Yan samples with the relative weights determined by a best fit of the mass spectrum from a full-range Drell–Yan MC as shown in Fig. 5.6a. Then we perform a fit to the dimuon invariant-mass spectrum of real data by the contributions of MC-simulated Drell–Yan, J/ψ, ψ' and open charm production as well as the constructed combinatorial background. The normalization of combinatorial background is fixed while those for the other MC-simulated components are determined from the fit.

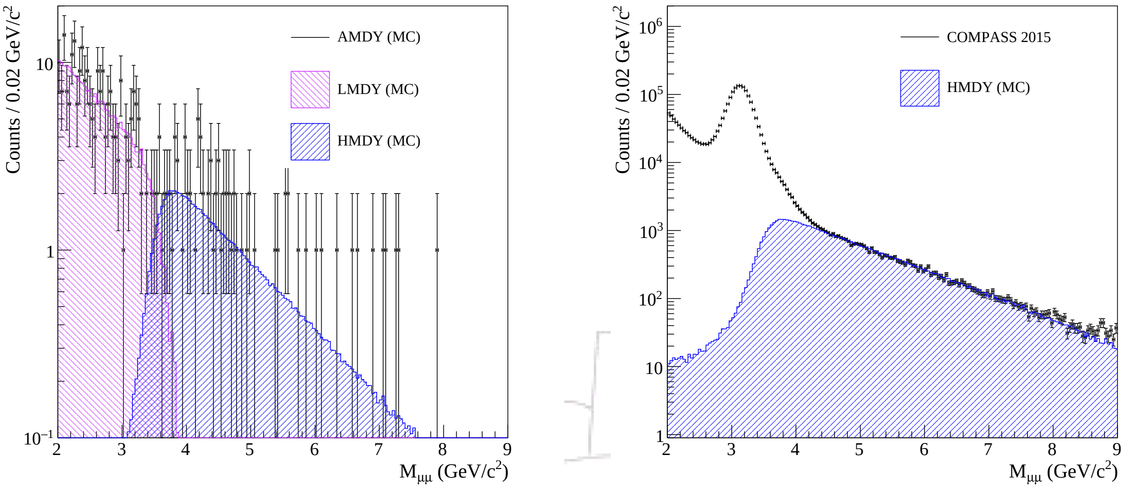

(a) (b)

Figure 5.6: (a) Determination of the relative weights of low-mass and high-mass MC Drell–Yan. (b) Determination of the normalization for Drell–Yan process on high-mass region of 5−9 GeV/c^2.

Assuming Drell–Yan process is the sole physics process contributing in the very large mass region, a fit on the high-mass region of 5−9 GeV/c^2 to determine the normalization of Drell–Yan as shown in Fig. 5.6b. The next step is to fit the invariant-mass of real data in the whole selected mass region(2−9 GeV/c^2) by all components (combinatorial background, Drell–Yan, J/ψ, ψ' and open-charm) where the normalizations is fixed for combinatorial background and Drell–Yan.

Fig. 5.7 shows the results of fitting and the individual contributions determined accordingly. It is clear that the observed dimuon invariant-mass spectrum could be nicely described by the MC-simulation. The results of fit strongly support the validity of our Monte-Carlo work since a reliable estimation of the relative strength of each physics process and the detection efficiency could be done.

Based on the invariant-mass spectrum fit, the contributions of J/ψ, ψ', open-charm and combinatorial background are disentangled from the Drell–Yan process. It is straightforward to evaluate the background fraction in a defined region of Drell–Yan process. Tab. 5.5-5.6 shows the fraction of events form various physics processes for the different mass selection of dimuon events in NH_3 and W targets. The fraction of Drell–Yan process is used in setting the invariant-mass region of 4.3(4.7)-8.5 GeV/$c^2$for the study of Drell–Yan process in NH_3 (W) target. The background fraction is estimated to be below 5.0%.

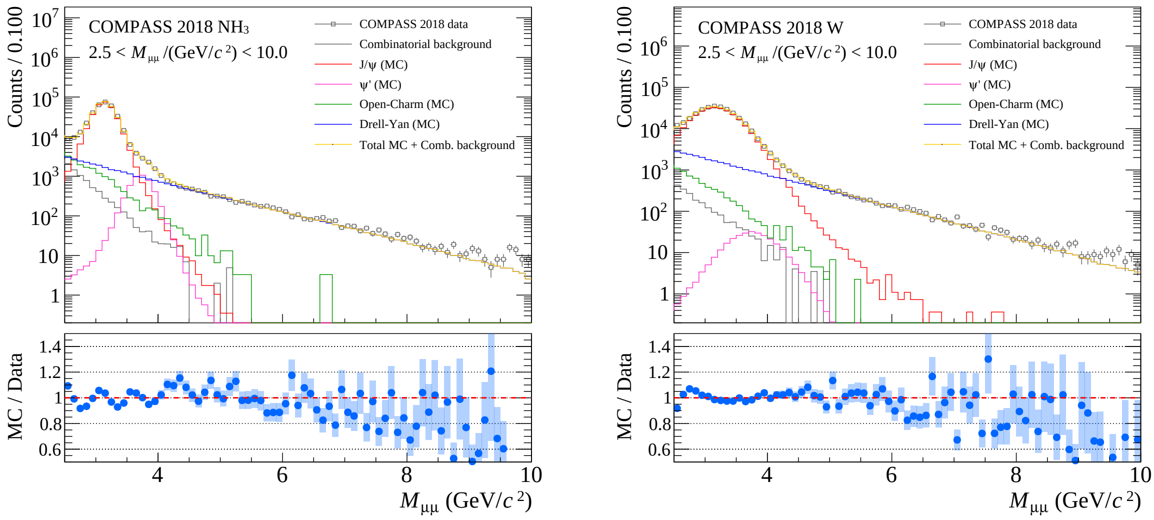

(a) NH_3 target

(b) W target

Figure 5.7: COMPASS 2018 mass spectrum.

Table 5.5: Fraction of events form various physics processes for the different mass selection of dimuon events in NH_3 target.

Mass (GeV/c^2)	Drell–Yan	J/ψ	ψ'	open-charm	Comb. Background
4.0 - 8.5	89.07%	2.11%	3.06%	4.82%	0.94%
4.1 - 8.5	92.12%	1.39%	1.31%	4.36%	0.82%
4.2 - 8.5	94.11%	0.97%	0.58%	3.69%	0.65%
4.3 - 8.5	95.35%	0.67%	0.26%	3.24%	0.47%
4.4 - 8.5	96.45%	0.44%	0.13%	2.75%	0.24%
4.5 - 8.5	97.07%	0.31%	0.08%	2.41%	0.13%
4.6 - 8.5	97.51%	0.19%	0.05%	2.11%	0.14%
4.7 - 8.5	97.59%	0.13%	0.03%	2.08%	0.16%
4.8 - 8.5	98.22%	0.10%	0.02%	1.48%	0.17%
4.9 - 8.5	98.38%	0.07%	0.01%	1.35%	0.19%
5.0 - 8.5	98.52%	0.04%	0.01%	1.28%	0.15%

5.5 Kinematic Distributions

The one-dimensional kinematics distribution of Bjorken scaling variables x_π and x_N, Feynman x_F, invariant mass $M_{\mu\mu}$, transverse momentum q_T and two-dimensional kinematics distribution of Bjorken scaling variables x_π verses x_N in NH_3 and W targets are presented in Fig. 5.8 and Fig. 5.9, respectively. The corresponding mean values of the kinematic variables in both NH_3 and W targets are listed in Tab. 5.7.

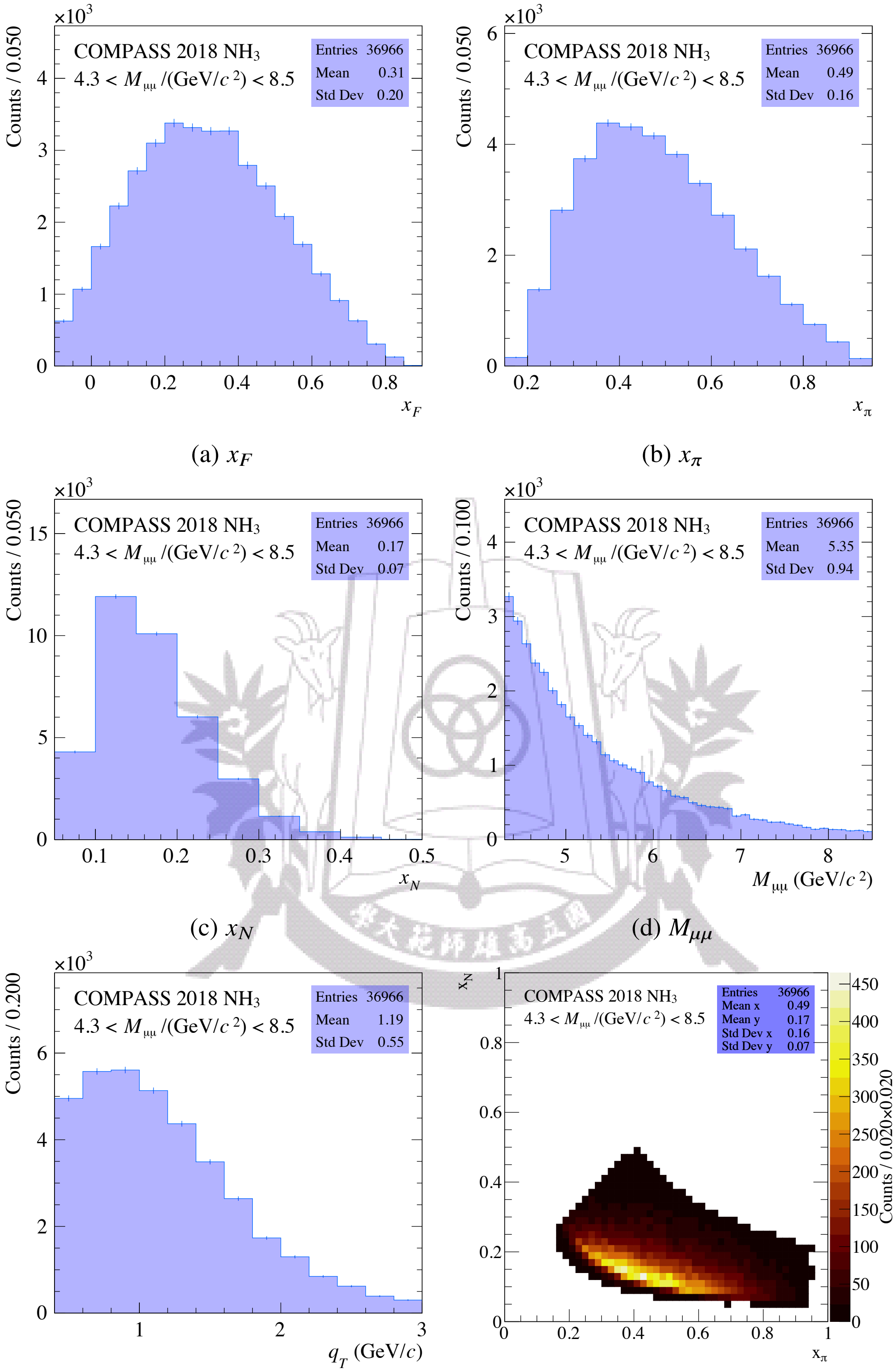

(a) x_F (b) x_π

(c) x_N (d) $M_{\mu\mu}$

(e) q_T (f) x_π v.s. x_N

Figure 5.8: The kinematics distribution in NH_3 target passing all analysis selection cut.

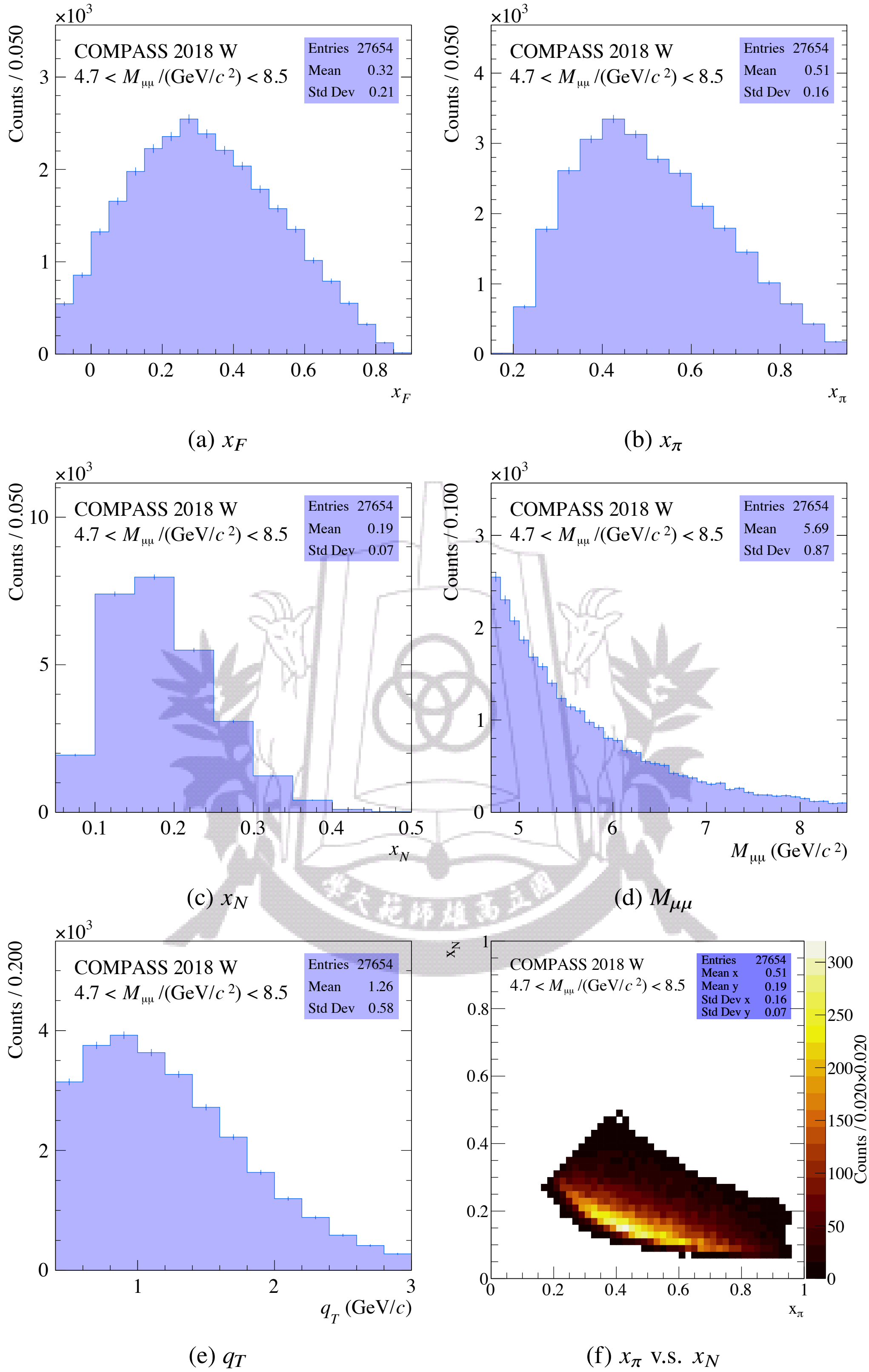

(a) x_F (b) x_π

(c) x_N (d) $M_{\mu\mu}$

(e) q_T (f) x_π v.s. x_N

Figure 5.9: The kinematics distribution in W target passing all analysis selection cut.

Table 5.6: Fraction of events form various physics processes for the different mass selection of dimuon events in W target.

Mass (GeV/c^2)	Drell–Yan	J/ψ	ψ'	open-charm	Comb. Background
4.0 - 8.5	63.41%	34.29%	0.53%	1.42%	0.35%
4.1 - 8.5	72.06%	25.63%	0.46%	1.55%	0.29%
4.2 - 8.5	79.18%	18.81%	0.37%	1.35%	0.28%
4.3 - 8.5	84.49%	13.77%	0.28%	1.32%	0.15%
4.4 - 8.5	88.75%	10.01%	0.20%	0.86%	0.17%
4.5 - 8.5	91.64%	7.32%	0.14%	0.78%	0.12%
4.6 - 8.5	93.54%	5.62%	0.09%	0.61%	0.14%
4.7 - 8.5	94.98%	4.37%	0.06%	0.44%	0.15%
4.8 - 8.5	96.06%	3.44%	0.04%	0.38%	0.08%
4.9 - 8.5	96.83%	2.75%	0.02%	0.30%	0.09%
5.0 - 8.5	97.46%	2.26%	0.02%	0.26%	0.00%

Table 5.7: The kinematics mean value in NH_3 and W target passing all analysis selection cut.

Target	$\langle x_N \rangle$	$\langle x_\pi \rangle$	$\langle x_F \rangle$	$\langle q_T \rangle$/(GeV/c)	$\langle M_{\mu\mu} \rangle$/(GeV/$c^2$)
NH_3	0.17	0.49	0.31	1.19	5.35
W	0.19	0.51	0.32	1.26	5.69

5.6 One-Dimensional Kinematics Binning

The λ, μ and ν asymmetries in the high mass range are extracted in bins of kinematic variables x_N, x_π, x_F, q_T and $M_{\mu\mu}$ (one at a time) after averaging over all other kinematic dependencies. The bin limits defined for each variable are reported for both NH_3 and W targets in Tab. 5.8. The bin-by-bin mean values of each kinematic variable are listed in Tab. 5.9. The number of dimuon pairs in each kinematic bin can be found in Tab. 5.10. The correlations between different kinematic variables base on one-dimensional kinematics binning for different target region are shown in Fig. 5.10

Table 5.8: The kinematic bin limits used for NH_3 (top) and W (bottom) data analysis.

NH_3	Bin-1	Bin-2	Bin-3	Bin-4	Bin-5
x_N	0.00-0.11	0.11-0.14	0.14-0.18	0.18-0.23	0.23-1.00
x_π	0.00-0.34	0.34-0.44	0.44-0.53	0.53-0.65	0.65-1.00
x_F	-0.10-0.13	0.13-0.26	0.26-0.38	0.38-0.53	0.53-1.00
q_T/(GeV/c)	0.40-0.68	0.68-0.95	0.95-1.25	1.25-1.70	1.70-3.00
$M_{\mu\mu}$/(GeV/c^2)	4.30-4.53	4.53-4.87	4.87-5.35	5.35-6.15	6.15-8.50
W	Bin-1	Bin-2	Bin-3	Bin-4	Bin-5
x_N	0.00-0.13	0.13-0.17	0.17-0.21	0.21-0.27	0.27-1.00
x_π	0.00-0.34	0.34-0.43	0.43-0.53	0.53-0.65	0.65-1.00
x_F	-0.10-0.10	0.10-0.23	0.23-0.35	0.35-0.50	0.50-1.00
q_T/(GeV/c)	0.40-0.74	0.74-1.02	1.02-1.34	1.34-1.77	1.77-3.00
$M_{\mu\mu}$/(GeV/c^2)	4.70-4.95	4.95-5.29	5.29-5.75	5.75-6.55	6.55-8.50

Table 5.9: The mean values of kinematic variables in each bin for NH_3 (top) and W (bottom).

NH_3	Bin-1	Bin-2	Bin-3	Bin-4	Bin-5
$\langle x_N \rangle$	0.09	0.13	0.16	0.20	0.28
$\langle x_\pi \rangle$	0.28	0.39	0.48	0.59	0.74
$\langle x_F \rangle$	0.05	0.20	0.32	0.45	0.63
$\langle q_T \rangle$/(GeV/c)	0.54	0.81	1.09	1.45	2.11
$\langle M_{\mu\mu} \rangle$/(GeV/$c^2$)	4.41	4.69	5.10	5.71	6.98
W	Bin-1	Bin-2	Bin-3	Bin-4	Bin-5
$\langle x_N \rangle$	0.11	0.15	0.19	0.24	0.31
$\langle x_\pi \rangle$	0.29	0.39	0.48	0.59	0.75
$\langle x_F \rangle$	0.02	0.17	0.29	0.42	0.62
$\langle q_T \rangle$/(GeV/c)	0.58	0.88	1.18	1.54	2.18
$\langle M_{\mu\mu} \rangle$/(GeV/$c^2$)	4.82	5.11	5.50	6.10	7.27

Table 5.10: The 2018 statistics in each kinematic bin.

NH_3	Bin-1	Bin-2	Bin-3	Bin-4	Bin-5
x_N	6458	7365	8930	7573	6640
x_π	7279	8650	7389	7470	6178
x_F	7160	8245	7937	7880	5744
q_T	7115	7646	7669	8125	6411
$M_{\mu\mu}$	7034	7885	7658	7501	6888
W	Bin-1	Bin-2	Bin-3	Bin-4	Bin-5
x_N	6007	6719	5888	5665	3375
x_π	4516	5609	6172	5771	5586
$x_F.$	4383	5620	5873	6030	5748
q_T	5760	5424	5603	5563	5304
$M_{\mu\mu}$	5919	5984	5501	5650	4600

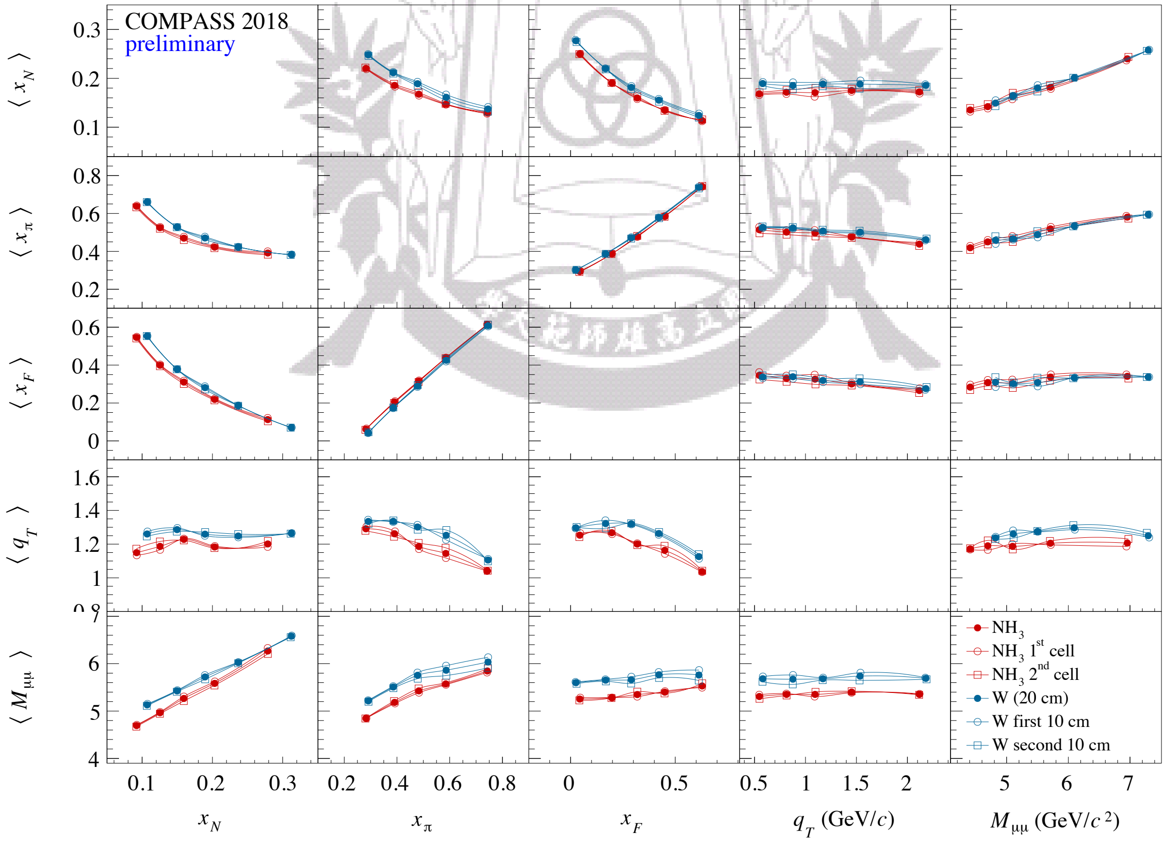

Figure 5.10: Kinematic map: correlations between kinematic variables in different target region.

CHAPTER 6

Result of Unpolarized Asymmetries

In this chapter, the results on Drell–Yan unpolarized asymmetries (UAs) λ, μ, ν and Lam–Tung relation in three reference frames (Collins–Soper, Gottfried–Jackson and Helicity) are presented, which extracted from the eight periods of 2018 COMPASS data in both NH_3 and W targets. Study of the unpolarised asymmetries requires the acceptance which extracted from a detail MC simulation (see Section 4.3).

6.1 Reference Frame

In the Eq. (1.15), the expression of Drell–Yan cross-section in terms of dimuon angular distribution should refer to a reference frame in terms of $\cos\theta$ and φ. The Collins–Soper frame, as shown in Fig. 1.2, is one of reference frame that is commonly used by most of experiments. The reference frame can be specified by the direction of z-axis in the plane containing the combination of the momentum vectors of the colliding hadrons (π^- beam $\vec{p}_\pi$ and nucleon target $\vec{p}_N$ in case of the COMPASS experiment) in the virtual photon rest frame. If one define the y-axis of reference frame at first as following:

$$\hat{y} = \frac{\vec{p}_N \times \vec{p}_\pi}{|\vec{p}_N \cdot \vec{p}_\pi|} \tag{6.1}$$

There are several choices for the z-axis used in this Thesis (see Fig. 6.1):

1. **Collins–Spoer axis**: the direction of the difference between the velocity vectors of the colliding π^- beam and nucleon target.

2. **Gottfried–Jackson axis**: the direction of the momentum of π^- beam.

3. **Helicity axis**: the direction of the sum of the velocity vectors of the colliding π^- beam and nucleon target.

After defining the y- and z-axis, the x-axis can be carried out by:

$$\hat{x} = \hat{y} \times \hat{z} \tag{6.2}$$

Now the expression of Drell–Yan cross-section in terms of dimuon angular distribution can be presented in three different reference frames: Collins–Soper frame (CS), Gottfried–Jackson frame (GJ) and Helicity frame (HX).

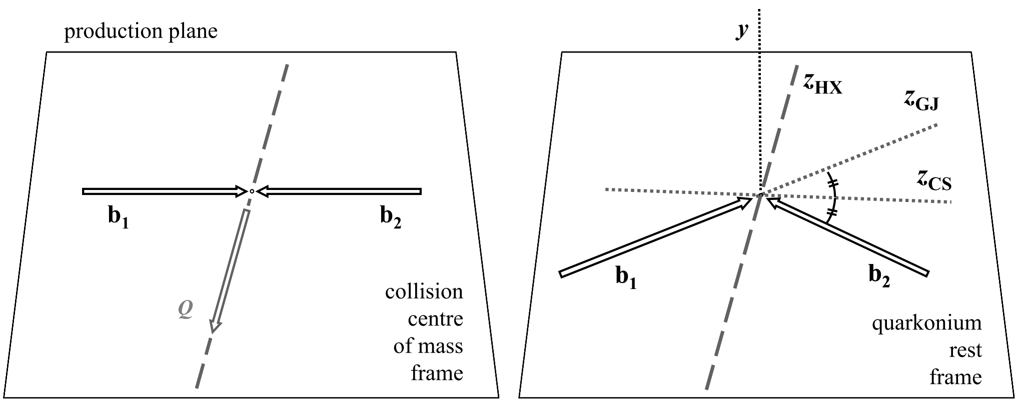

Figure 6.1: Schematic view of three different definitions of the z-axis. (Adopted from [66].)

6.2 Angular Resolutions

In the experiment, the measured kinematics variables are affected by several experimental conditions (such as resolution of detectors, tracking algorithms and so on.) so that the value of measurement are smeared with respect to it's true value. A resolution of quantity represents the smearing effect from the experimental measurement. In order to study the angular resolution in the COMPASS experiment, one of the way is using a full chain MC simulation framework (see Chapter 4). By comparing the reconstructed observable ($x^{\text{Rec.}}$) and generated true value ($x^{\text{Gen.}}$) with certain amount of MC samples, one can get the distribution of difference of observable:

$$\Delta x = x^{\text{Rec.}} - x^{\text{Gen.}} \tag{6.3}$$

To evaluate the resolution for each observable, the standard deviation of Δx distribution has been chosen as an estimator. The resolution of $\cos\theta$ and φ in three reference frames have been estimated in both NH_3 and W target. The $\Delta\cos\theta$ and $\Delta\varphi$ distributions in three reference frames and in NH_3 and W target are shown in Fig. 6.2 and Fig. 6.3, respectively.

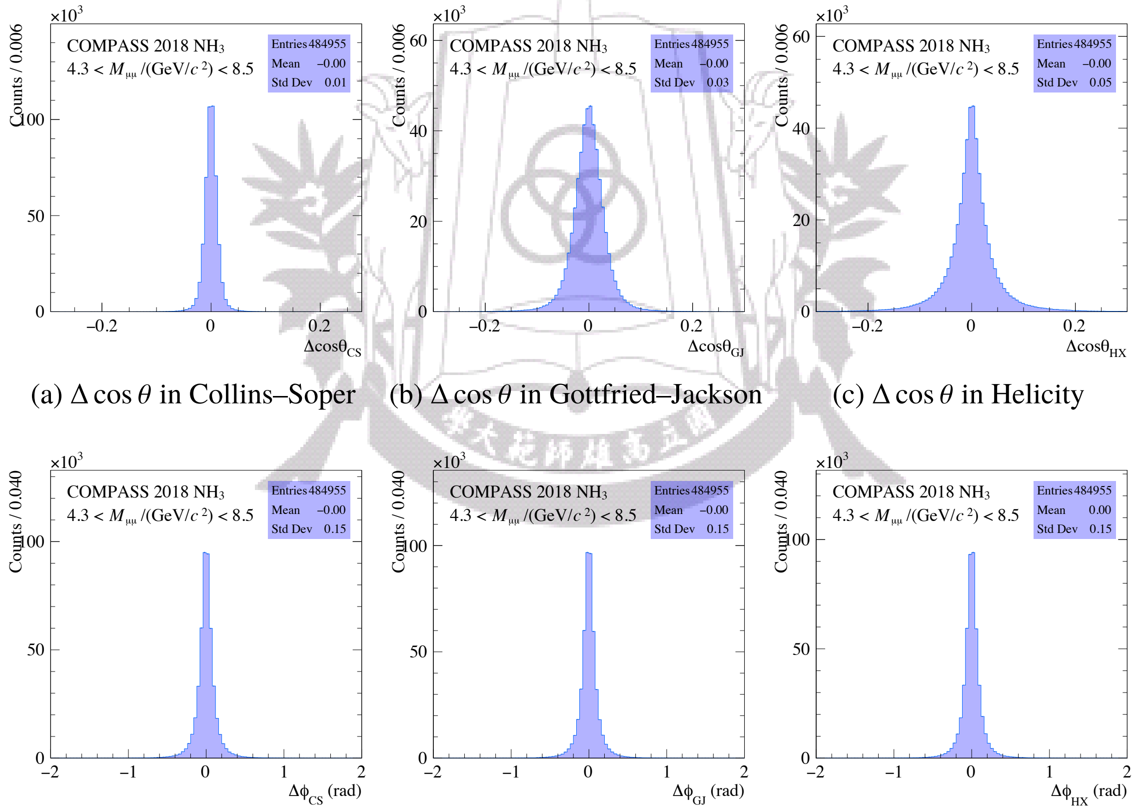

(a) $\Delta\cos\theta$ in Collins–Soper (b) $\Delta\cos\theta$ in Gottfried–Jackson (c) $\Delta\cos\theta$ in Helicity

(d) $\Delta\varphi$ in Collins–Soper (e) $\Delta\varphi$ in Gottfried–Jackson (f) $\Delta\varphi$ in Helicity

Figure 6.2: The $\Delta\cos\theta$ and $\Delta\varphi$ distributions in three reference frames and in NH_3 target estimated from high-mass Drell–Yan MC sample in P03 period condition.

The summary table of the standard deviation of $\Delta\cos\theta$ and $\Delta\varphi$ distributions in different reference frames and different targets are shown in Tab. 6.1. In general the resolution of $\cos\theta$ and φ are systematic worse in W target with respect to NH_3 target. This is expected

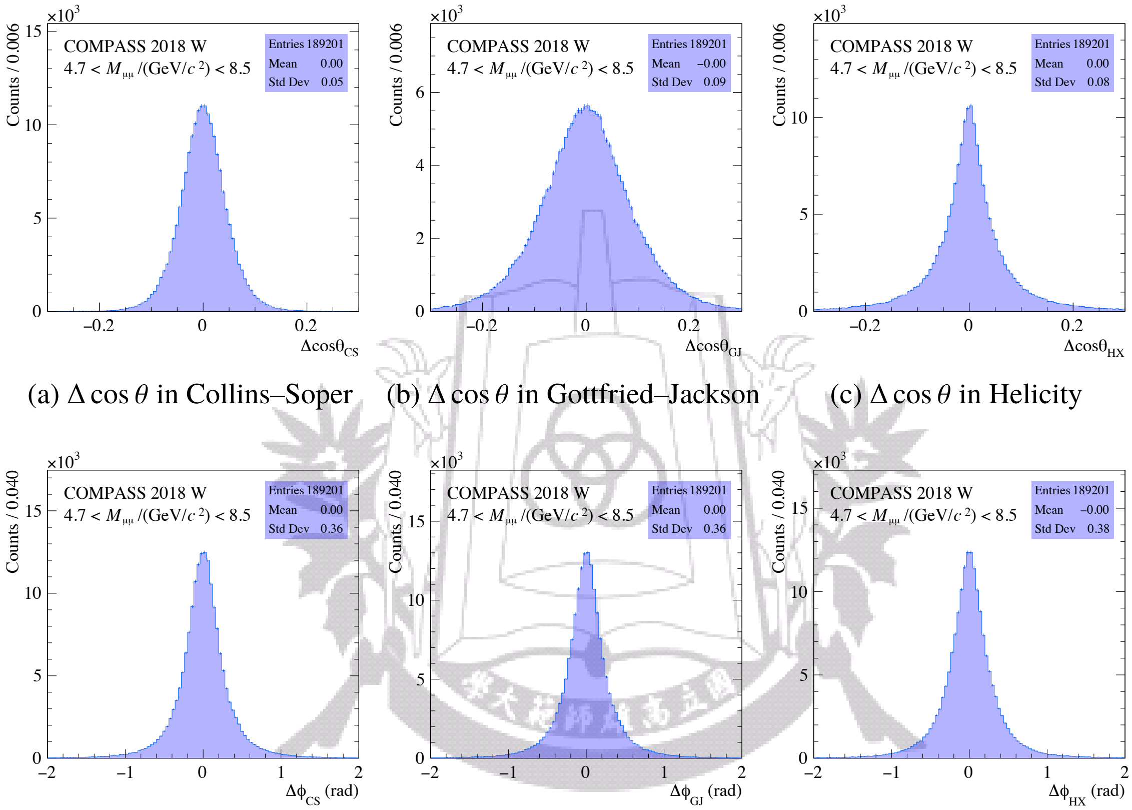

(a) $\Delta\cos\theta$ in Collins–Soper (b) $\Delta\cos\theta$ in Gottfried–Jackson (c) $\Delta\cos\theta$ in Helicity

(d) $\Delta\varphi$ in Collins–Soper (e) $\Delta\varphi$ in Gottfried–Jackson (f) $\Delta\varphi$ in Helicity

Figure 6.3: The $\Delta\cos\theta$ and $\Delta\varphi$ distributions in three reference frames and in W target estimated from high-mass Drell–Yan MC sample in P03 period condition.

due to the multiple scattering effect in W target is more pronounced in NH_3 target. The resolution of φ is rather stable among three different reference frames in both targets because of a good coverage at azimuthal angle direction in the COMPASS apparatus. The inconsistent resolution of $\cos\theta_{\mathrm{CS}}$, $\cos\theta_{\mathrm{GJ}}$ and $\cos\theta_{\mathrm{HX}}$ indicate the non-smooth acceptance coverage along polar angle direction, which has been confirmed by the hodoscopes efficiencies study (see Section 3.2).

Table 6.1: Summary of the standard deviation of $\Delta\cos\theta$ and $\Delta\varphi$ distributions.

Target	$\Delta\cos\theta_{CS}$	$\Delta\cos\theta_{GJ}$	$\Delta\cos\theta_{HX}$	$\Delta\varphi_{CS}$	$\Delta\varphi_{GJ}$	$\Delta\varphi_{HX}$
NH_3	0.01	0.03	0.05	0.15 (rad)	0.15 (rad)	0.15 (rad)
W	0.05	0.09	0.08	0.36 (rad)	0.36 (rad)	0.38 (rad)

6.3 Angular Acceptance

The detailed information of acceptance have been provided in Section 4.3. By preparing the full chain high-mass Drell–Yan MC simulation samples for the eight periods condition from 2018 data taking, the period-by-period angular acceptances are estimated and used for the extraction of Drell–Yan unpolarized asymmetries. Practically the two-dimensional angular ($\cos\theta$-φ) distribution histogram is presented in a form of 16×8-binned histogram ranging between [-1,3] for $\cos\theta$ and $[-\pi,\pi]$ for φ. Here the non-physical range of $\cos\theta$ between [1,3] is an extended region due to the implementation of the simultaneous fitting from both LAST–LAST and OT–LAST triggers (see Section 6.4 for more detail information), which is equivalent to a 8-binned histogram ranging between [-1,1] for $\cos\theta$. It is noted that the resulting bin widths for both $\cos\theta$ and φ are sufficiently larger than the experimental resolutions which estimated from MC simulation (see Tab. 6.1). This is a compromise due to the fact that the extraction of Drell–Yan unpolarized asymmetries will be done in both period basis and one-dimensional kinematics basis where statistics are significant limited (~ 1000 events per histogram). The same binning for each reference frame is adopted.

An example of two-dimensional angular acceptance histogram (integrated with all phase-space) in each reference frames and targets estimated from MC sample in P03 condition are shown in Fig. 6.4.

The two-dimensional angular acceptance histogram in each reference frames and different kinematics bins in NH_3 and W targets estimated from MC sample in P03 condition are shown in Fig. 6.5-6.10, respectively.

6.4 Extraction Methods

Two different methods have been considered and tested to extract the unpolarized asymmetries: one is the Two-Dimensional Ratio method (2DR), another is the Histogram Binned Likelihood method (HBL).

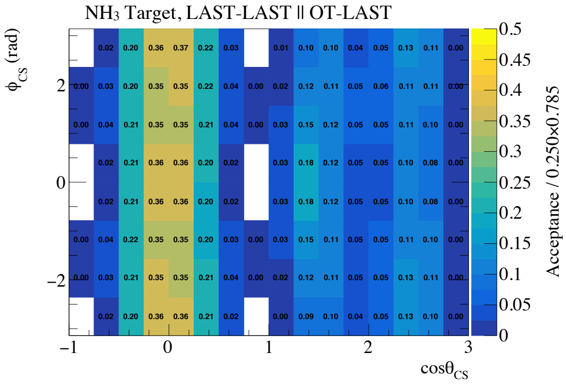

(a) Collins-Soper frame in NH_3 target

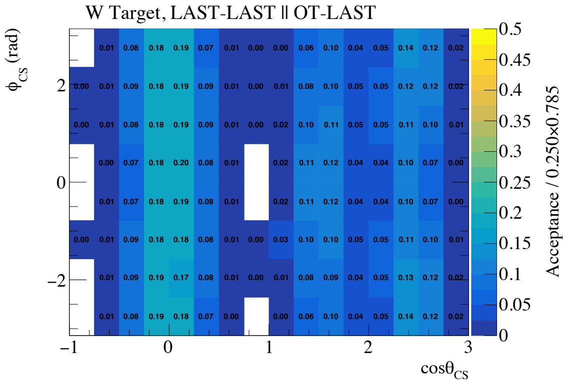

(b) Collins-Soper frame in W target

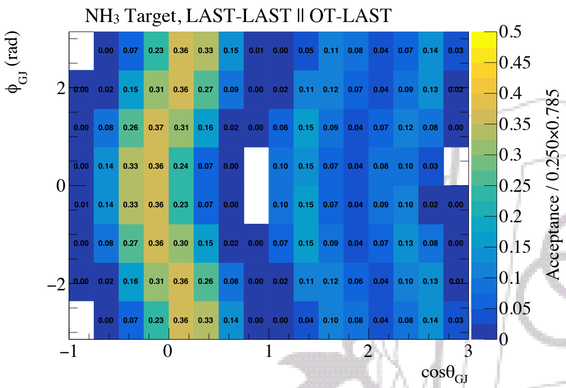

(c) Gottfried-Jackson frame in NH_3 target

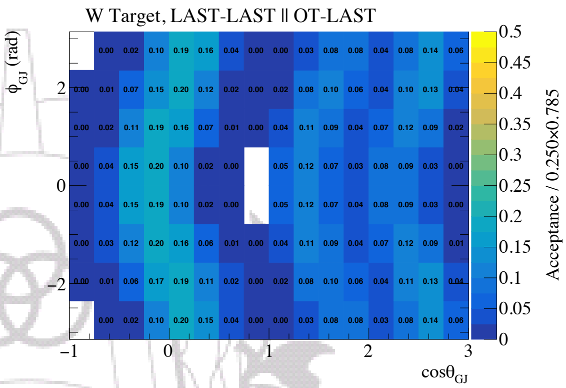

(d) Gottfried-Jackson frame in W target

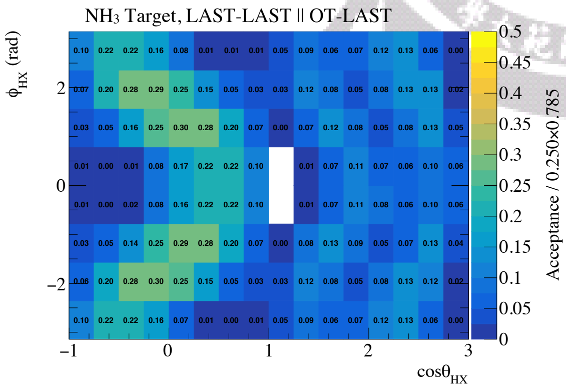

(e) Helicity frame in NH_3 target

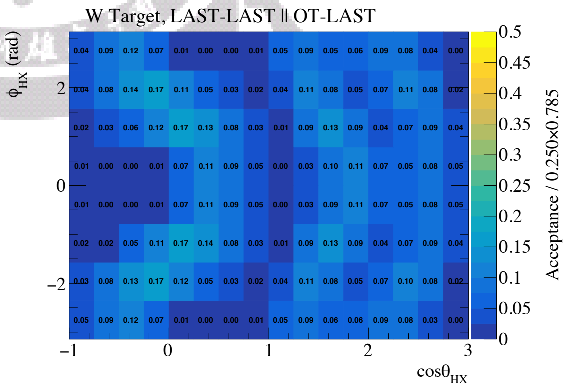

(f) Helicity frame in W target

Figure 6.4: The two-dimensional $\cos\theta$-φ acceptance (integrated with all phase-space) estimated from MC sample in P03 condition. the range of $\cos\theta$ between [-1,1] were filled by events from LAST–LAST trigger, while the range of $\cos\theta$ between [1,3] were filled by events from OT–LAST trigger

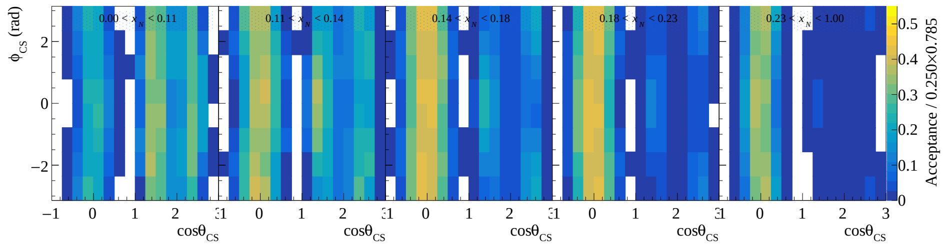

(a) x_N bin

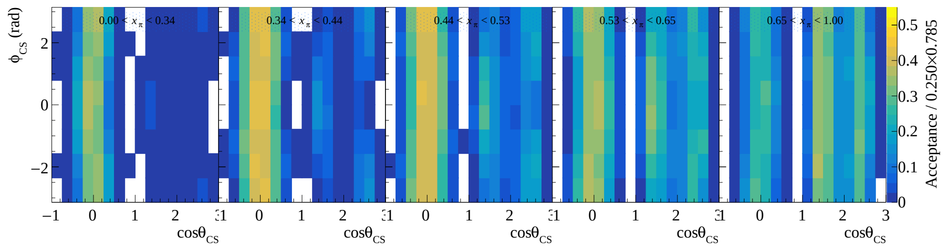

(b) x_π bin

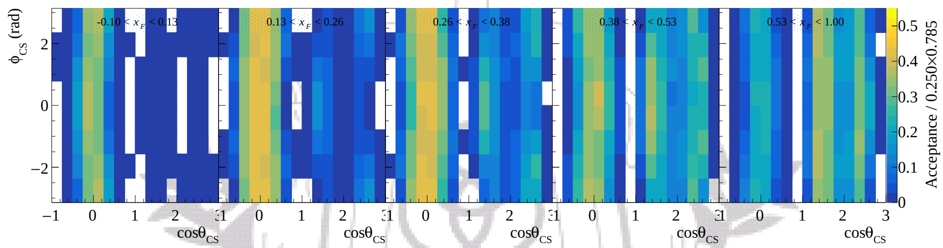

(c) x_F bin

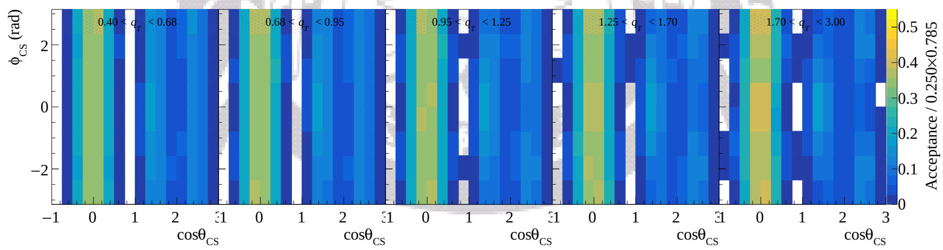

(d) q_T bin

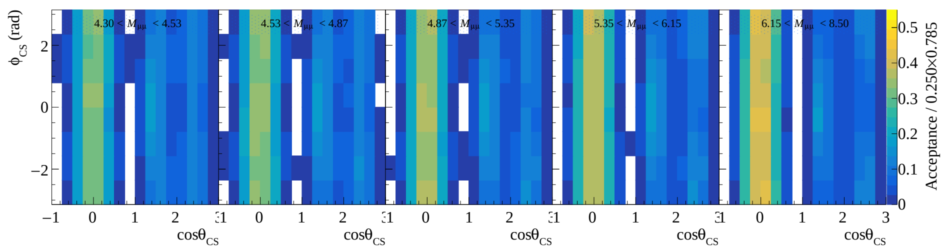

(e) $M_{\mu\mu}$ bin

Figure 6.5: The two-dimensional angular acceptance histogram as function of different kinematics variables in Collins–Spoer frame and in NH_3 target estimated from MC sample in P03 condition.

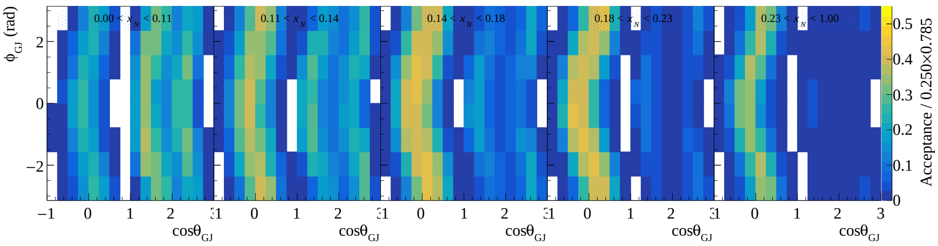

(a) x_N bin

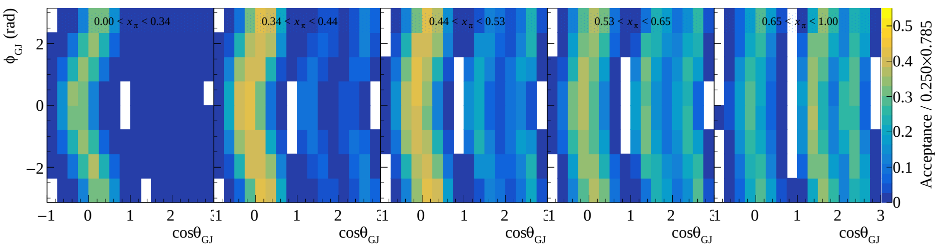

(b) x_π bin

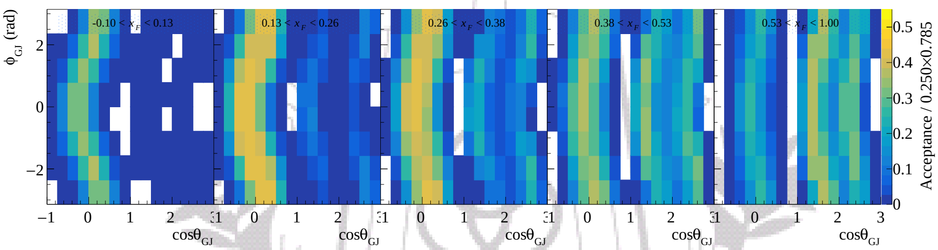

(c) x_F bin

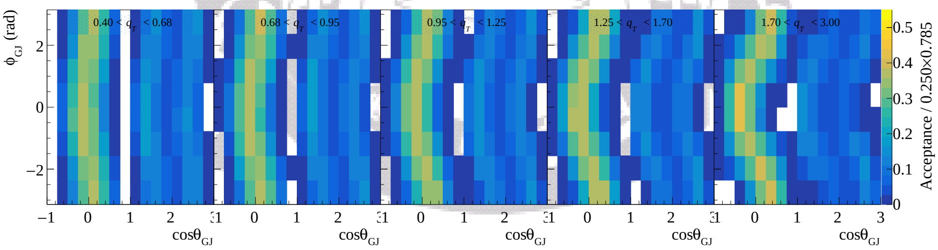

(d) q_T bin

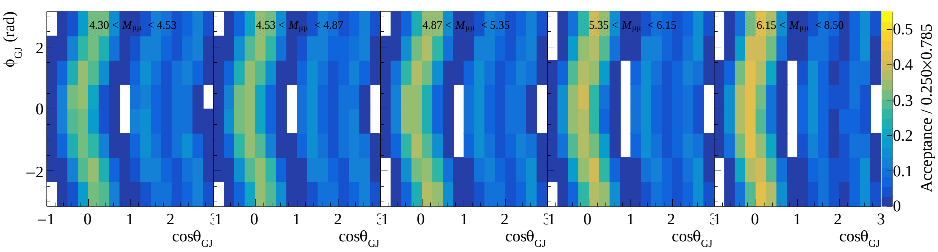

(e) $M_{\mu\mu}$ bin

Figure 6.6: The two-dimensional angular acceptance histogram as function of different kinematics variables in Gottfried–Jackson frame and in NH_3 target estimated from MC sample in P03 condition.

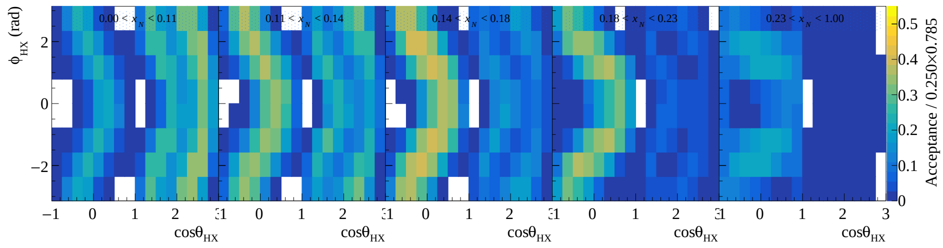

(a) x_N bin

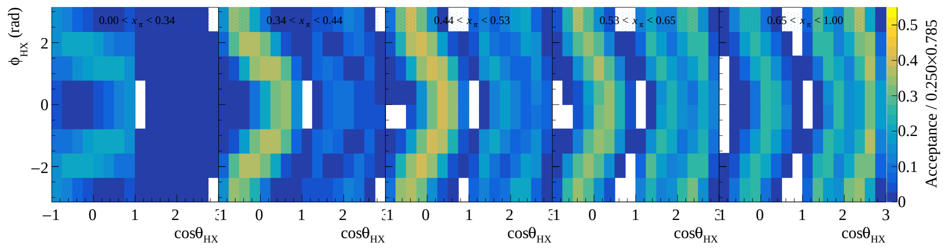

(b) x_π bin

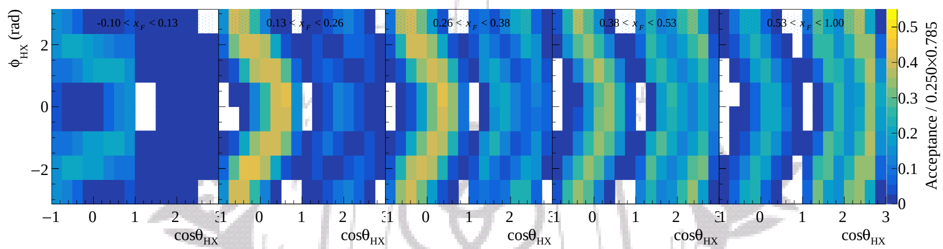

(c) x_F bin

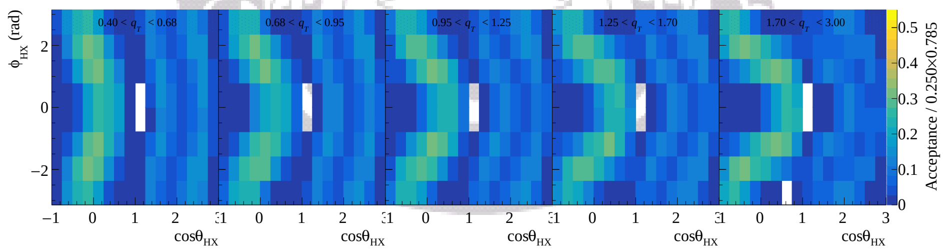

(d) q_T bin

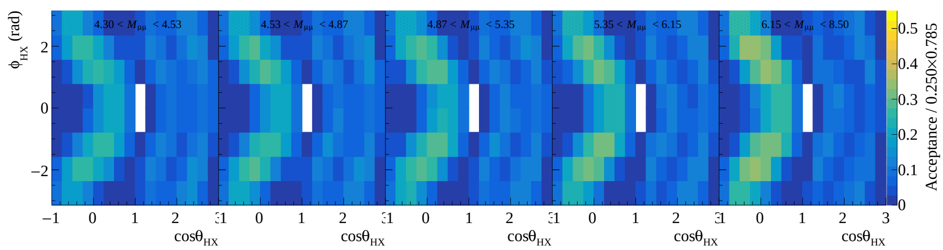

(e) $M_{\mu\mu}$ bin

Figure 6.7: The two-dimensional angular acceptance histogram as function of different kinematics variables in Helicity frame and in NH_3 target estimated from MC sample in P03 condition.

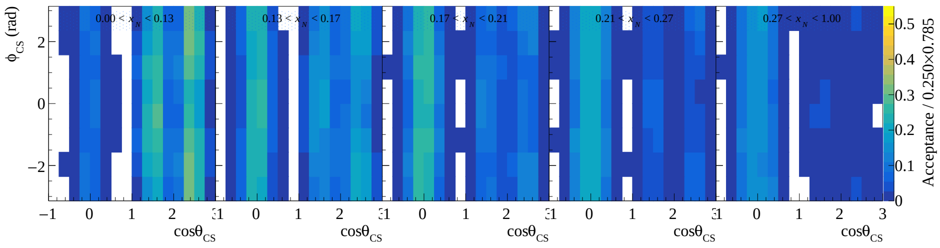

(a) x_N bin

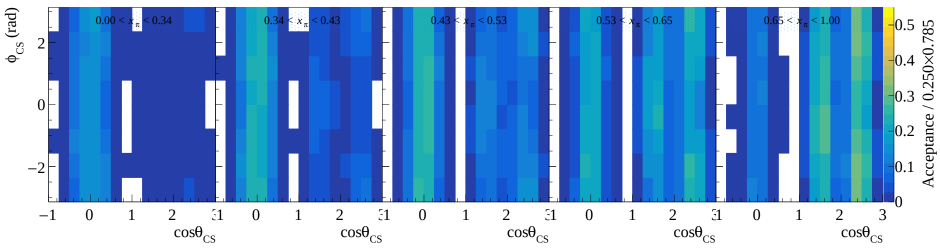

(b) x_π bin

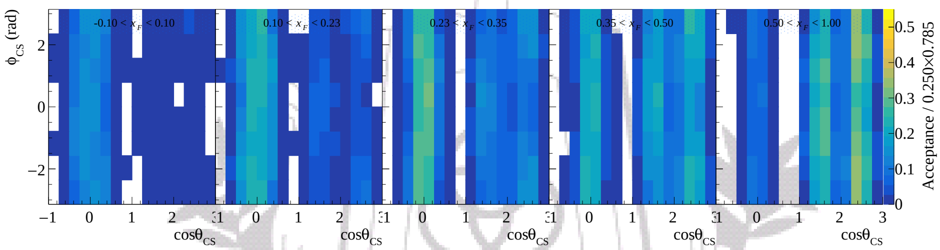

(c) x_F bin

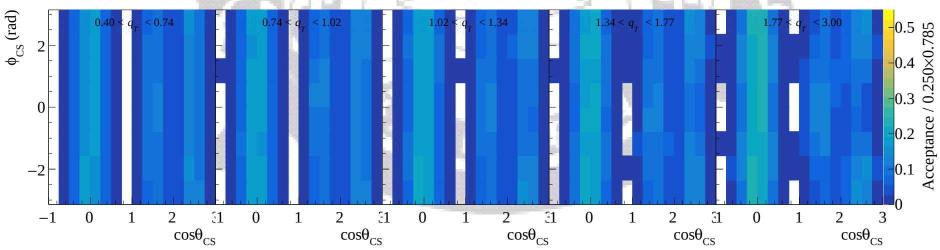

(d) q_T bin

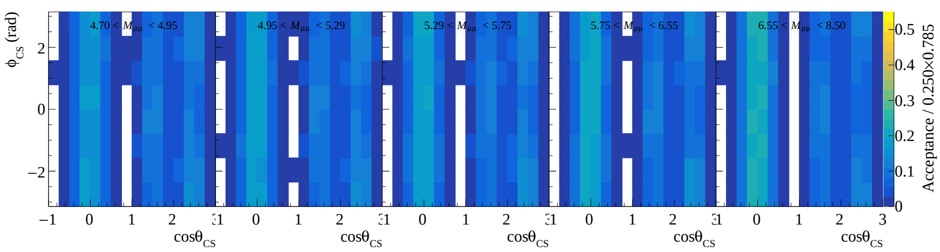

(e) $M_{\mu\mu}$ bin

Figure 6.8: The two-dimensional angular acceptance histogram as function of different kinematics variables in Collins–Spoer frame and in W target estimated from MC sample in P03 condition.

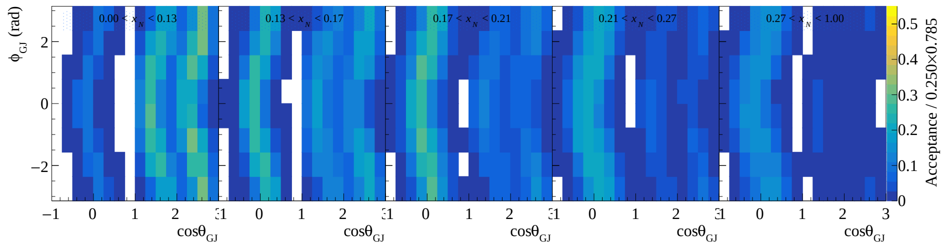

(a) x_N bin

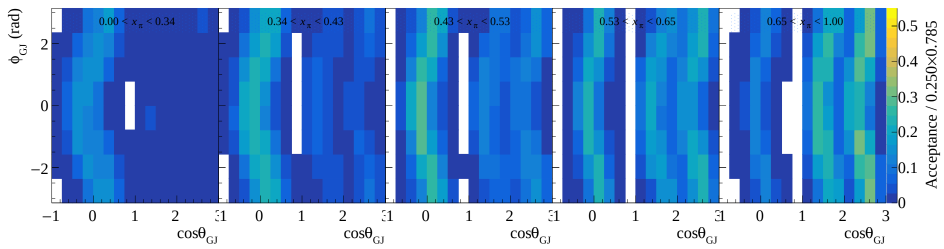

(b) x_π bin

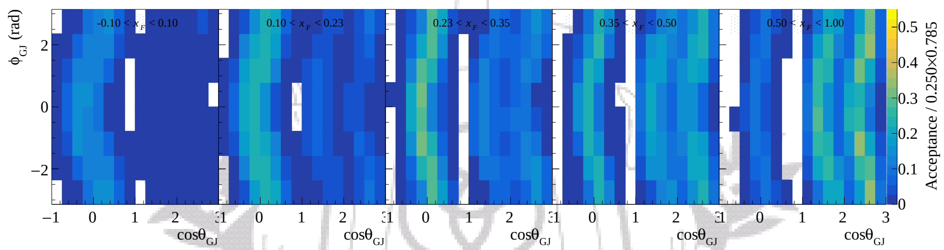

(c) x_F bin

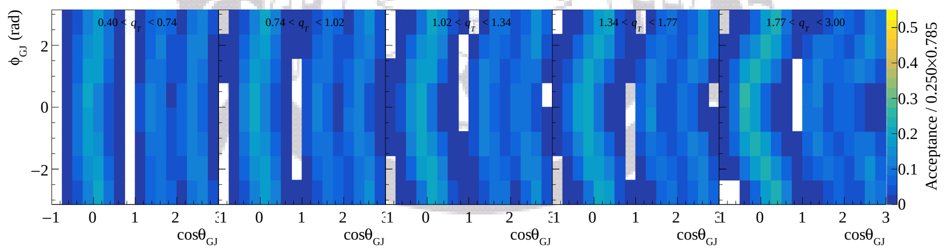

(d) q_T bin

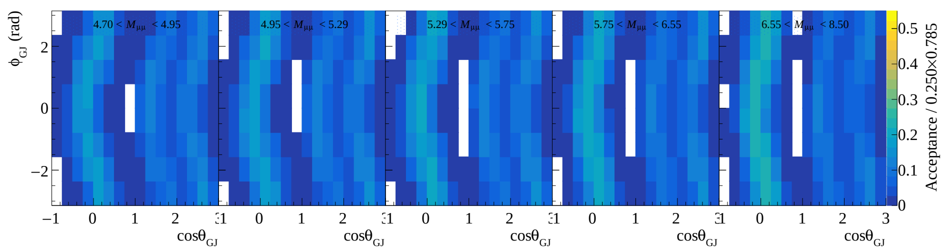

(e) $M_{\mu\mu}$ bin

Figure 6.9: The two-dimensional angular acceptance histogram as function of different kinematics variables in Gottfried–Jackson frame and in W target estimated from MC sample in P03 condition.

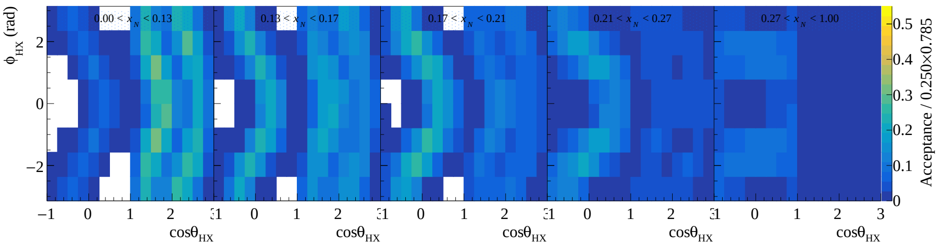

(a) x_N bin

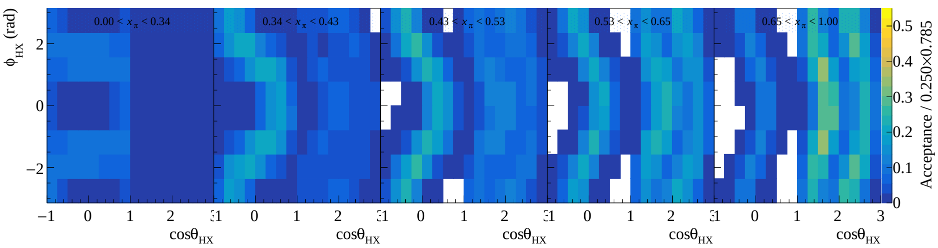

(b) x_π bin

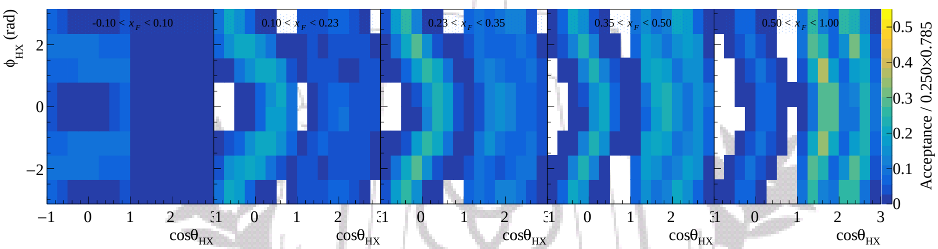

(c) x_F bin

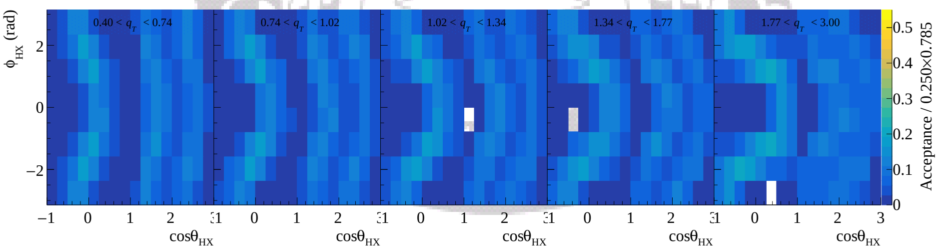

(d) q_T bin

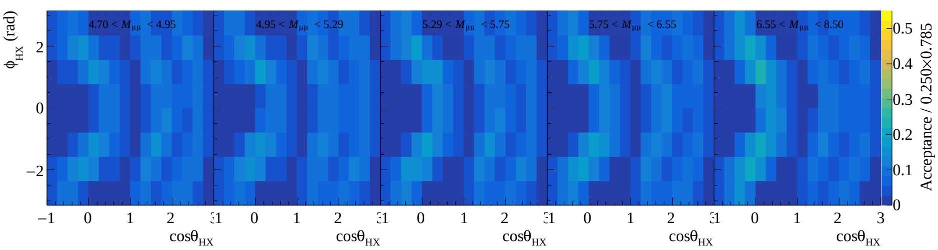

(e) $M_{\mu\mu}$ bin

Figure 6.10: The two-dimensional angular acceptance histogram as function of different kinematics variables in Helicity frame and in W target estimated from MC sample in P03 condition.

6.4.1 Two-Dimensional Ratio Method

The two-dimensional ratio method is to fill the real data (RD) into a two-dimensional $(\cos\theta, \varphi)$ histogram $N_{\text{RD}(\cos\theta,\varphi)}$, which is later on corrected for acceptance dividing by the acceptance-histogram $A(\cos\theta, \varphi)$ extracted from MC simulation.

$$N_{\text{RD}}^{\text{Corr.}}(\cos\theta, \varphi) = \frac{N_{\text{RD}(\cos\theta,\varphi)}}{A(\cos\theta, \varphi)} \tag{6.4}$$

The obtained ratio-histogram $N_{\text{RD}}^{\text{Corr.}}(\cos\theta, \varphi)$ is then fitted using the χ^2 minimization. While taking the ratio, the uncertainties on both data and acceptances are propagated assuming Gaussian uncertainties:

$$\sigma_{\text{RD}}^{\text{Corr.}}(\cos\theta, \varphi) = N_{\text{RD}}^{\text{Corr.}}(\cos\theta, \varphi)\sqrt{\left(\frac{\sigma_{\text{stst.}}(\cos\theta, \varphi)}{N_{\text{RD}}^{\text{Corr.}}(\cos\theta, \varphi)}\right)^2 + \left(\frac{\sigma_A(\cos\theta, \varphi)}{A(\cos\theta, \varphi)}\right)^2} \tag{6.5}$$

The Gaussian assumption requires considerable statistics in each given bin. This requirement is hardly satisfied at the edges of $\cos\theta$ distribution, where the smallness of the spectrometer-acceptance leads to a very low statistical population. The application of Poissonian uncertainties is more appropriate in this case. For this reason, a modified 2DR method, the so-called Histogram Binned Likelihood (HBL) method, was proposed.

6.4.2 Histogram Binned Likelihood Method

Similarly to the 2DR method, in the HBL method the angular distributions in each kinematic bin are presented in a form of two-dimensional histograms (eight by eight bins over [-1,1] for $\cos\theta$ and [-π, π] for φ angular ranges). In case of HBL method the errors assigned to each $(\cos\theta, \varphi)$-bin content (N_{RD}) are Poissonian. The acceptance is also computed on 8×8 $(\cos\theta, \varphi)$ grids using a sufficiently large amount of MC sample. In this way, the acceptance uncertainties ($\sigma_A(\cos\theta, \varphi)$), estimated using the binomial formula

$$\sigma_A(\cos\theta, \varphi) = \frac{\sqrt{N_{\text{MC}}^{\text{Gen.}}(\cos\theta, \varphi) \cdot A(\cos\theta, \varphi) \cdot [1 - A(\cos\theta, \varphi)]}}{N_{\text{MC}}^{\text{Gen.}}(\cos\theta, \varphi)} \tag{6.6}$$

where $N_{\text{MC}}^{\text{Gen.}}(\cos\theta, \varphi)$ represents the number of generated events in the considered region of phase space, can be neglected in each bin. The real data histogram is then fitted using the function $f(\cos\theta, \varphi)$:

$$f(\cos\theta, \varphi) = A(\cos\theta, \varphi) \cdot N \cdot (1 + \lambda\cos^2\theta + \mu\sin 2\theta\cos\varphi + \frac{\nu}{2}\sin^2\theta\cos 2\varphi) \tag{6.7}$$

with the acceptance entering as a scale-factor without any uncertainties assigned. The minimization is done using the MINUIT-likelihood option and allows to extract all the three unpolarized asymmetries (λ, μ, ν) simultaneously.

6.4.3 Extended Histogram Binned Likelihood Method

The extended HBL method is base on HBL method but extended into three-dimensional simultaneous fit, which is done by adding one more dimension: dimuon trigger. Due to the different angular acceptance between LAST–LAST and OT–LAST triggers, and also the missing input of simulated veto-life-time of two triggers in MC simulation, it's not proper to perform an acceptance correction by mixing both triggers together. One of the ways to get rid of this bias is to extract unpolarized asymmetries trigger-by-trigger individually, but in this way it will be difficult to combine the results from two triggers in the end, because of their different coverage of phase-space. Another way which adopted is to perform a simultaneous fit with both triggers together.

Similar to HBL method, only the definition of angular histogram is modified. The two-dimensional angular histogram in x-axis ($\cos\theta$) is extended from eight bins over [-1,1] to sixteen bins over [-1,3], where the original range [-1,1] will be filled by inclusive LAST–LAST trigger events, while the extended range [1,3] will be filled by OT–LAST trigger events (no LAST–LAST trigger fired). This modification of angular histogram is applied for both RD and MC for acceptance. Furthermore, the fitting function $f(\cos\theta, \varphi)$ has to be modified as follows:

$$f(\cos\theta, \phi) = \begin{cases} \text{if } -1 < \cos\theta \leq 1: \\ A(\cos\theta, \phi) \cdot N_0 \cdot (1 + \lambda\cos^2\theta + \mu\sin 2\theta\cos\phi + \frac{\nu}{2}\sin^2\theta\cos 2\phi), \\ \text{if } 1 < \cos\theta \leq 3: \\ A(\cos\theta, \phi) \cdot N_1 \cdot (1 + \lambda\cos^2\theta' + \mu\sin 2\theta'\cos\phi + \frac{\nu}{2}\sin^2\theta'\cos 2\phi), \end{cases}$$

where $\cos\theta' = \cos\theta - 2$.

There are five free parameters (N_0, N_1, λ, μ and ν) in the new fitting function, the two additional normalization parameters N_0 and N_1 are not limited to be identical in order to compensate the inconsistency of veto-life-time of two triggers.

After modifying these two parts in HBL method, one is able to extract unpolarized asymmetries from two triggers simultaneously in each kinematics bin. The example of two-dimensional histogram before and after extension of $\cos\theta$ are shown in Fig. 6.11.

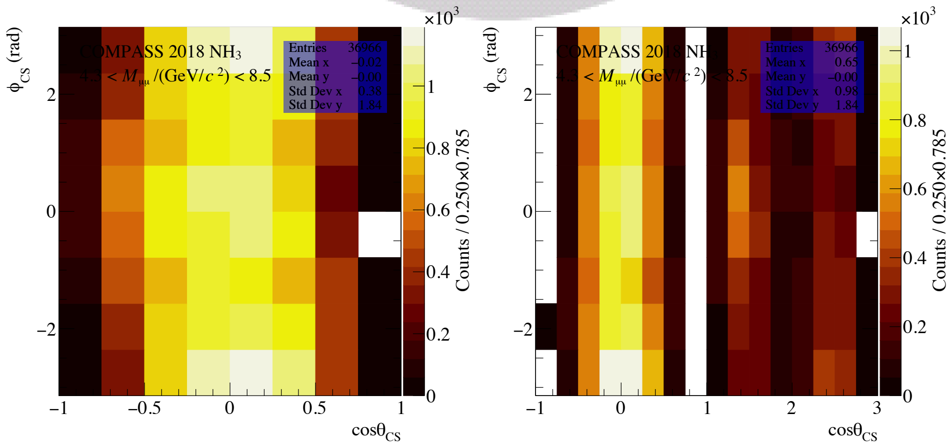

(a) Original histogram (b) Extended histogram

Figure 6.11: The example of two-dimensional histogram before and after extension of $\cos\theta$.

6.5 Extraction of Drell–Yan Unpolarized Asymmetries

The extraction of high-mass Drell–Yan unpolarized asymmetries from both NH_3 and W targets and three of reference frames is done in each periods and kinematics bins separately. There are 8 of periods and 5 kinds of kinematics variables which divided into 5 bins for extracting unpolarized asymmetries:

$$N_{\text{Fit}} = 8(\text{period}) \times 5(\text{variable}) \times 5(\text{bin}) = 200 \tag{6.8}$$

In total there are 200 fits for each target and each reference frames. The fitting χ^2/ndf in each target and each reference frame are shown in Fig. 6.12. In general the fitting quality are reasonable and stable without any failure fit.

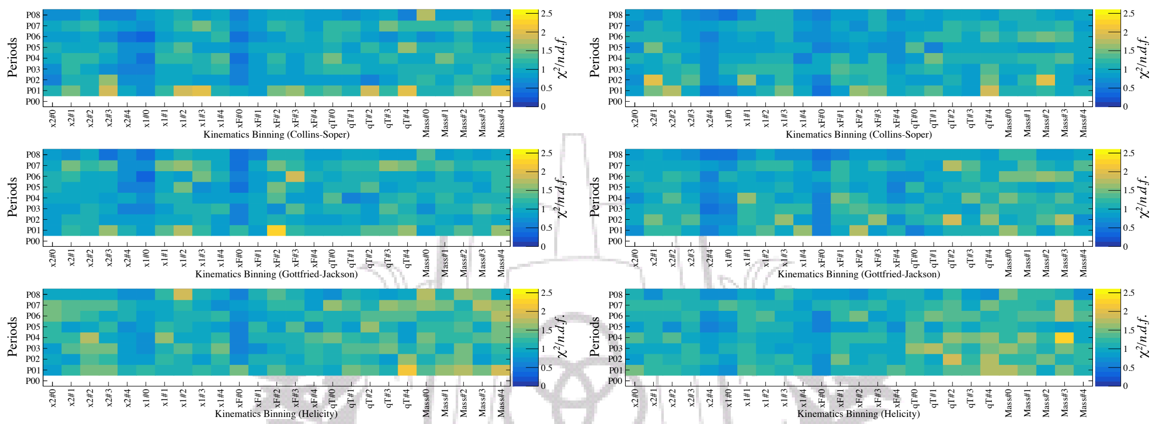

(a) NH_3 target (b) W target

Figure 6.12: The fitting χ^2/ndf during UAs extraction. x-axis represent different kinematics variables bins, y-axis represent different periods.

After obtaining 200 fitting results from each targets and reference frames, each result from 8 periods will be merged by the weighting averaged method:

$$\bar{A} = \frac{\sum_{i=1}^{8} A_i w_i}{\sum_{i=1}^{8} w_i} \quad , w_i = \frac{1}{\sigma_i^2} \tag{6.9}$$

where $\bar{A}$ is the average result (λ, μ, ν) from 8 periods, index i represent each period, A_i and σ_i represent fitting result's mean value and uncertainty from each periods, respectively.

The ratios of two normalization parameters N_1/N_0 are shown in Fig. 6.13. This ratio is expected to reflect that the veto-live-time is not identical for the two dimuon triggers, and this factor was not taken into account in the MC simulation. The deadtime of veto system entering the physics triggers was studied in a dedicated analysis, to be around 0.24 for LAST–LAST trigger, and around 0.3 for OT–LAST trigger. A ratio of $N_1/N_0 \approx 0.9$ is thus expected. The figure further illustrates that there is also a small kinematic dependence observed for this ratio.

The extracted Drell–Yan UAs and Lam–Tung relation (λ, μ, ν and $2\nu - (1 - \lambda)$) as function of different kinematics dependence (x_N, x_π, x_F, q_T and $M_{\mu\mu}$) from both NH_3 and W target in Collins-Soper, Gottfried-Jackson and Helicity frame are shown in Fig. 6.14- 6.16,

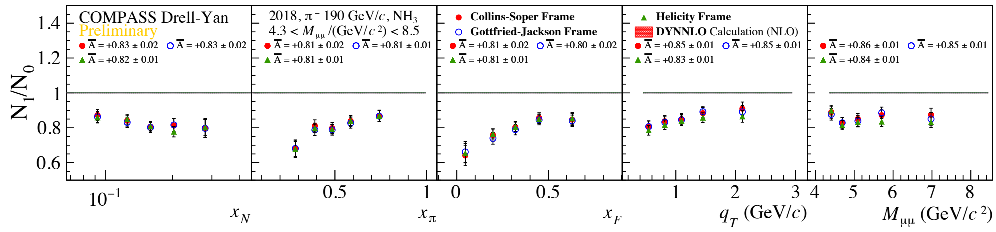

(a) NH_3 target

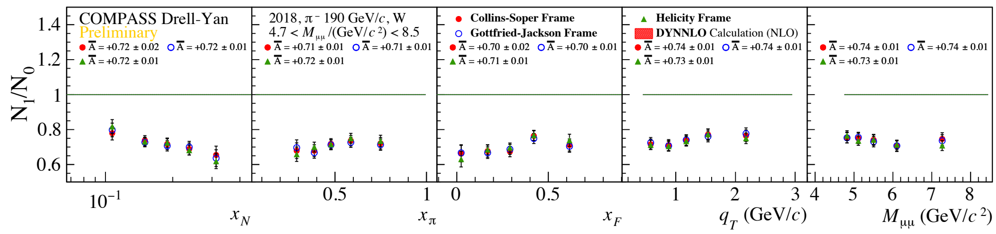

(b) W target

Figure 6.13: The ratio of N_1/N_0 parameter during UAs extraction.

respectively. In general the λ and μ results are consistent between NH_3 and W target, while the average of ν result in NH_3 target are a factor of two higher than the result from W target.

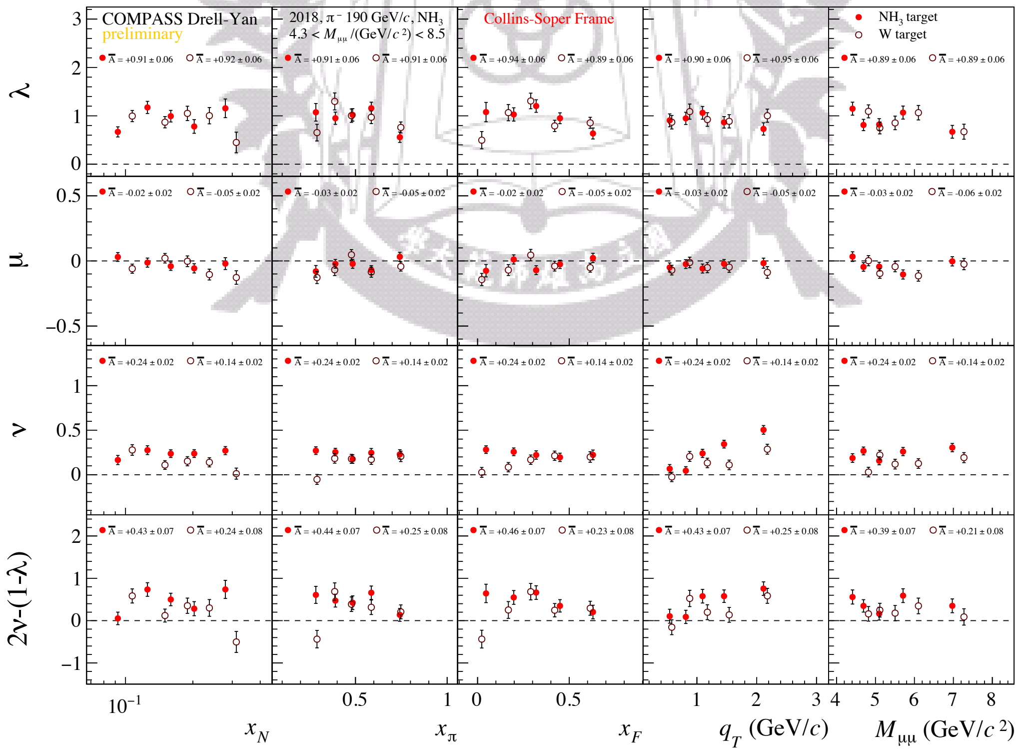

Figure 6.14: The extracted high-mass Drell–Yan unpolarized asymmetries in Collins-Soper frame.

The same extracted Drell–Yan unpolarized asymmetries and Lam–Tung relation (λ, μ, ν

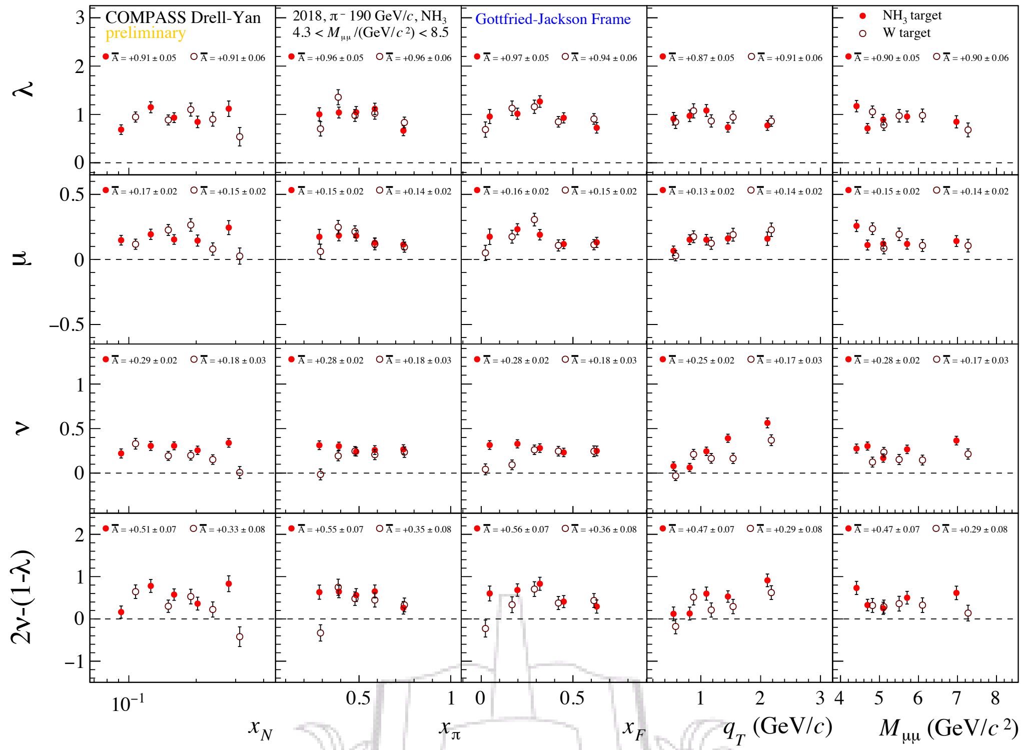

Figure 6.15: The extracted high-mass Drell–Yan unpolarized asymmetries in Gottfried-Jackson frame.

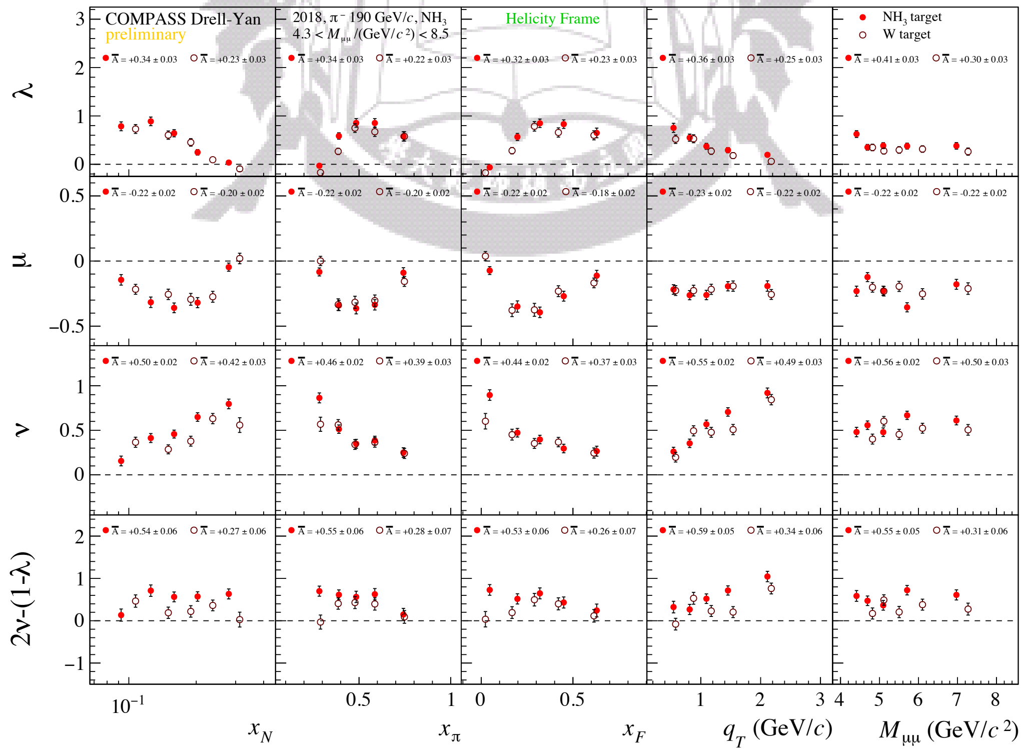

Figure 6.16: The extracted high-mass Drell–Yan unpolarized asymmetries in Helicity frame.

and $2\nu - (1-\lambda)$) as function of different kinematics dependence (x_N, x_π, x_F, q_T and $M_{\mu\mu}$) from W target are also compared with the result from NA10 [43], E615 [44] collaborations and also the NLO pQCD calculation from DYNNLO. The results from NH3 are shown in Fig. 6.17-6.19, and those from W target are shown in Fig. 6.20-6.22. In general the average of λ and ν from COMPASS measurement is consistent with the two past measurements, while the average of μ result from COMPASS measurement is in different sign with respect of two past measurement. The sign change of μ result is due to the definition of y-axis [66] in the reference frame (see Section 6.1 for the definition from the COMPASS experiment). The ν result in large q_T region from COMPASS measurement are also found to be deviated from NLO pQCD calculation similar to two past measurements, which could indicated the effect of non-perturbative TMD Boer–Mulders function.

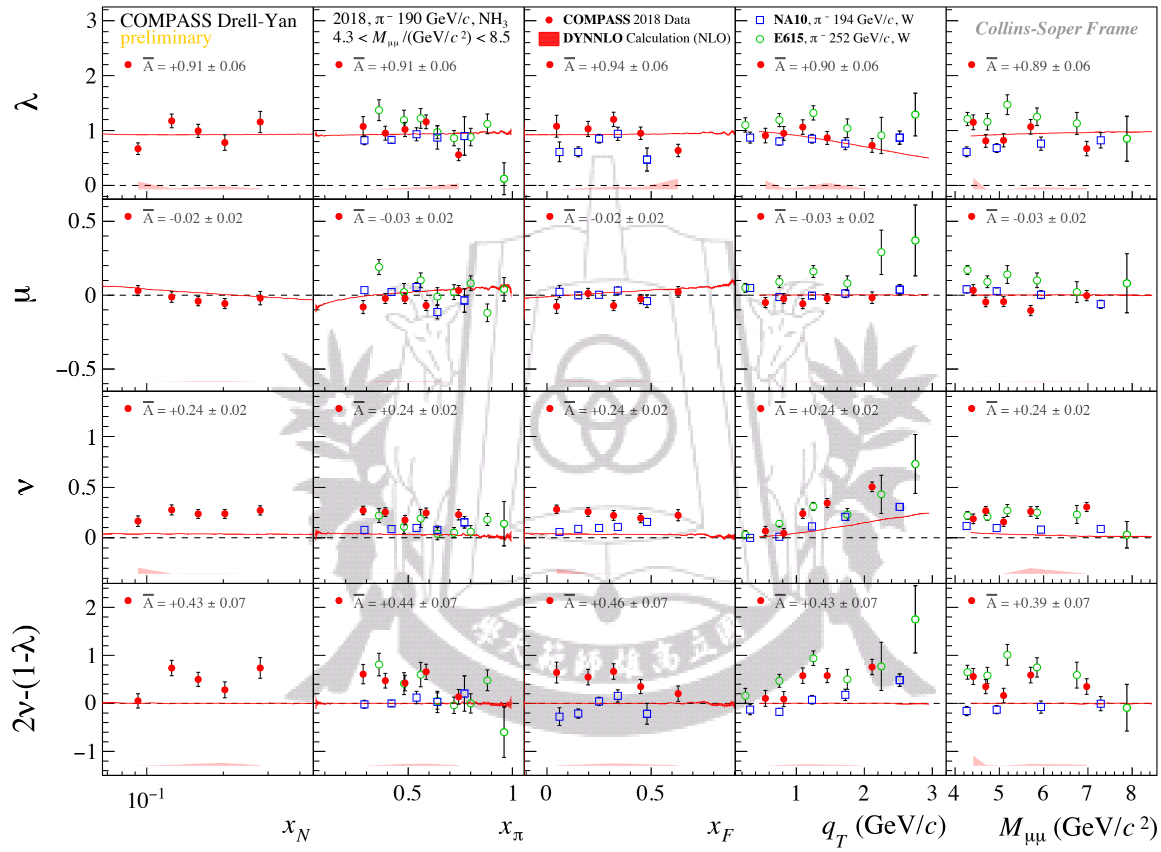

Figure 6.17: The comparison of extracted high-mass Drell–Yan unpolarized asymmetries from NH_3 target in Collins–Soper frame from COMPASS measurement (red close circle) with NA10 (blue open square), E615 (green open circle) experiments and also DYNNLO calculation (red line).

6.6 Discussion

The Drell–Yan unpolarized asymmetries have been studied by two fixed-target experiments in the past. During the ’80s, NA10 at CERN was one of the pioneering Drell–Yan experiments. The experiment performed a series of pion-induced Drell–Yan measurements

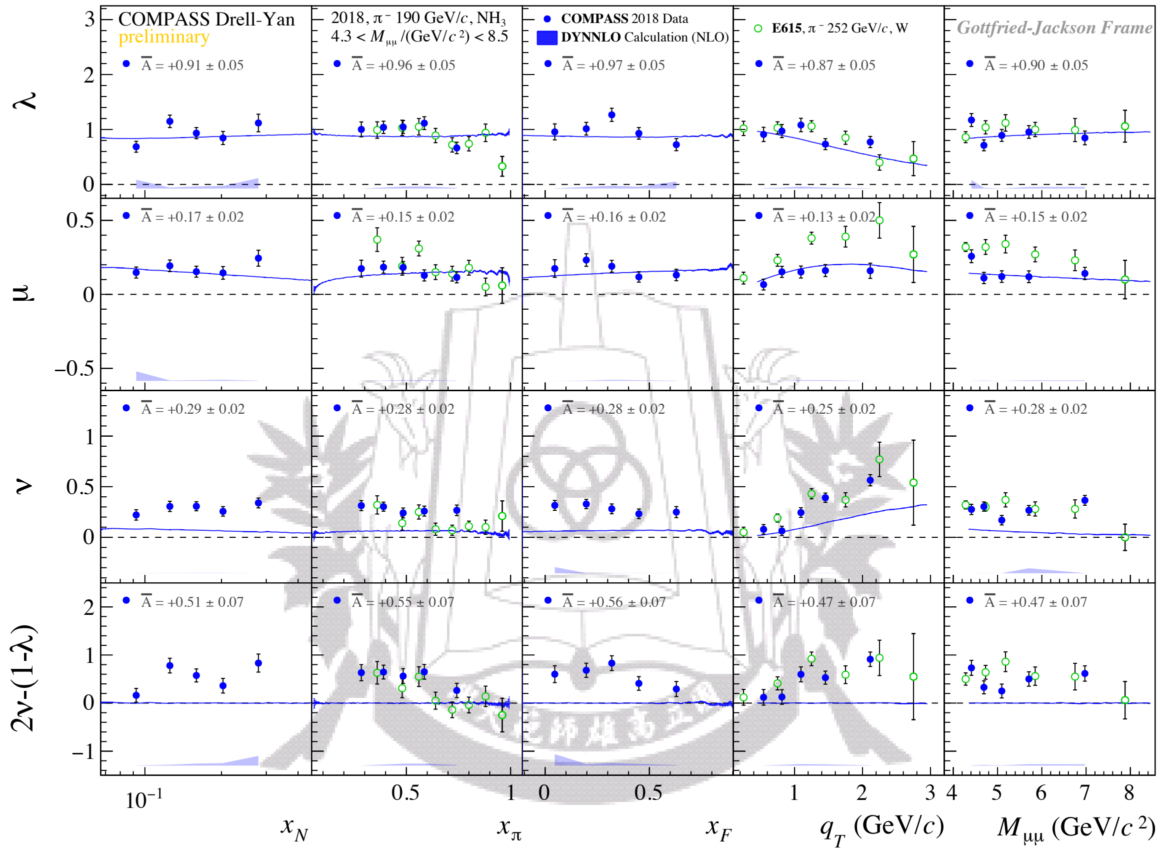

Figure 6.18: The comparison of extracted high-mass Drell–Yan unpolarized asymmetries from NH_3 target in Gottfried–Jackson frame from COMPASS measurement (blue close circle) with E615 (green open circle) experiments and also DYNNLO calculation (blue line).

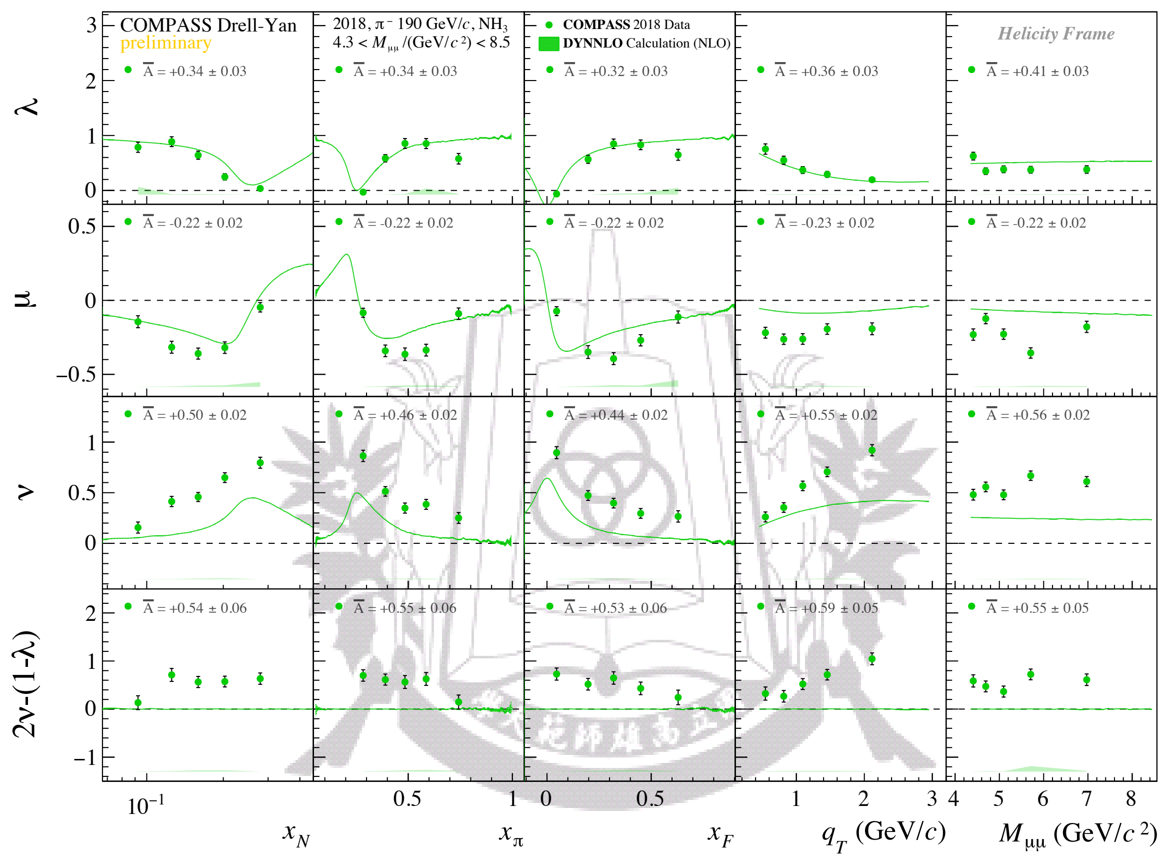

Figure 6.19: The comparison of extracted high-mass Drell–Yan unpolarized asymmetries from NH_3 target in Helicity frame from COMPASS measurement (green close circle) with DYNNLO calculation (green line).

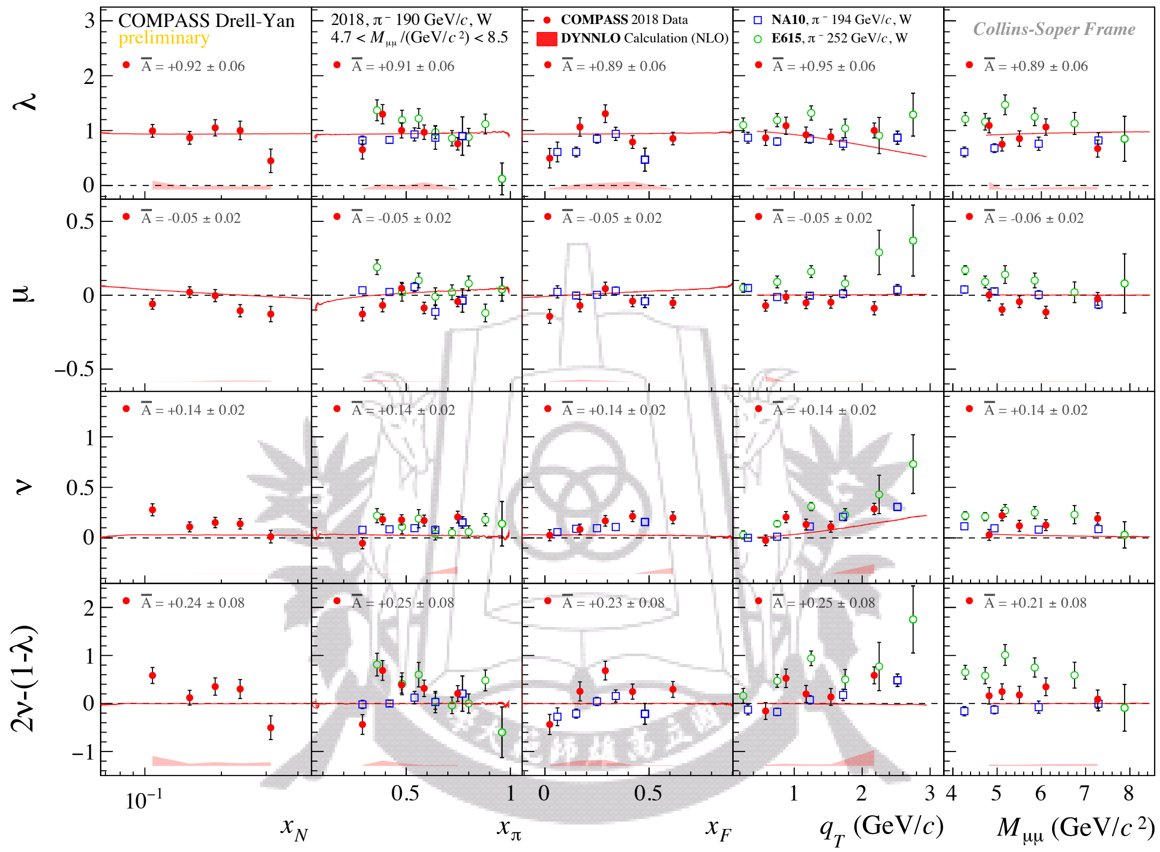

Figure 6.20: The comparison of extracted high-mass Drell–Yan unpolarized asymmetries from W target in Collins–Soper frame from COMPASS measurement (red close circle) with NA10 (blue open square), E615 (green open circle) experiments and also DYNNLO calculation (red line).

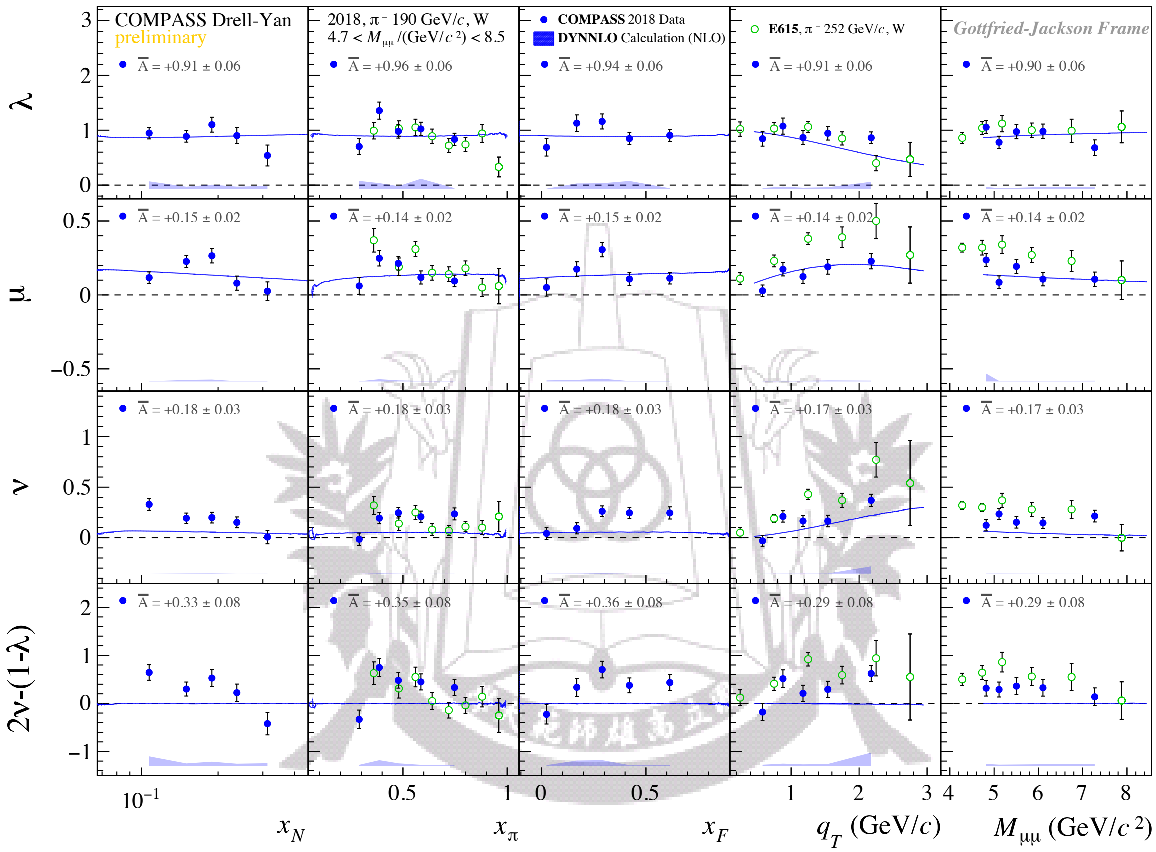

Figure 6.21: The comparison of extracted high-mass Drell–Yan unpolarized asymmetries from W target in Gottfried–Jackson frame from COMPASS measurement (blue close circle) with E615 (green open circle) experiments and also DYNNLO calculation (blue line).

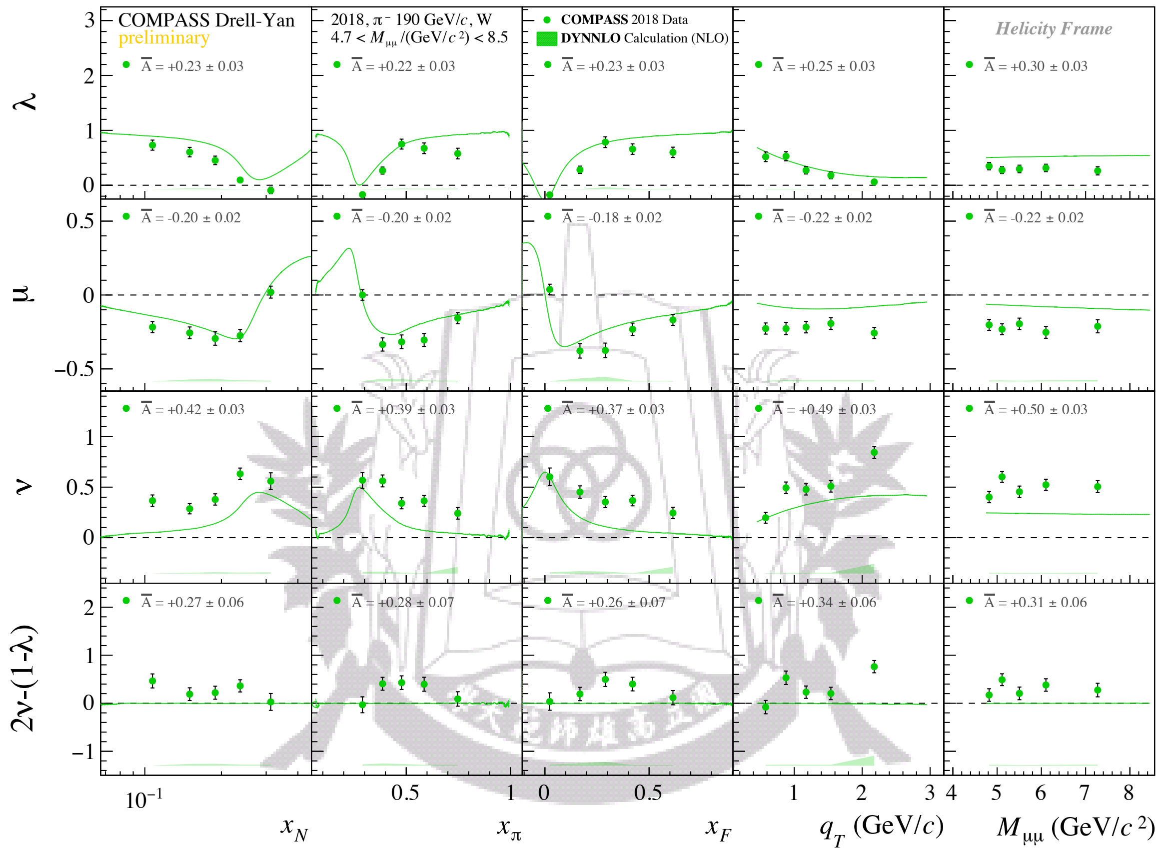

Figure 6.22: The comparison of extracted high-mass Drell–Yan unpolarized asymmetries from W target in Helicity frame from COMPASS measurement (green close circle) with DYNNLO calculation (green line).

using different beam energies (140, 194 and 286 GeV). A large sample of 152,000 DY events for dimuon masses $M_{\mu\mu} > 4.05$ GeV/c^2, was collected using the 194 GeV beam and a tungsten target. In the meantime during the '80s, unpolarized Drell–Yan measurements were also performed by the E615 collaboration at Fermilab, using 252 GeV π^- beam scattering off a tungsten target. The E615 results were obtained from the analysis of 36,000 DY events with $M_{\mu\mu} > 4.05$ GeV/c^2.

The study of Drell–Yan unpolarized asymmetries from COMPASS measurement by using data from 2018 data taking is done in this Thesis. By comparing the COMPASS preliminary result from W target with E615 and NA10 measurement and also NLO perturbative QCD calculation, the consistency of COMPASS results with two past measurement is confirmed. Tab. 6.2 summarized the unpolarized asymmetries result from two fixed-target pion-induced Drell–Yan experiments (NA10, E615) with COMPASS preliminary result. The result of λ

Table 6.2: The summary of the unpolarized asymmetries result from fixed-target pion-induced Drell–Yan experiments and also COMPASS preliminary result.

Experiment Interaction Beam Energy	**COMPASS** $\pi^- + NH_3$ 190 GeV/c	**COMPASS** $\pi^- + W$ 190 GeV/c	**NA10** $\pi^- + W$ 194 GeV/c	**E615** $\pi^- + W$ 252 GeV/c
$\langle\lambda\rangle$	0.89 ± 0.06	0.89 ± 0.06	0.83 ± 0.04	1.17 ± 0.06
$\langle\mu\rangle$	-0.03 ± 0.02	-0.06 ± 0.02	0.008 ± 0.010	0.09 ± 0.02
$\langle\nu\rangle$	0.24 ± 0.02	0.14 ± 0.02	0.091 ± 0.009	0.169 ± 0.019
$\langle 2\nu - (1-\lambda)\rangle$	0.39 ± 0.07	0.21 ± 0.08	0.01 ± 0.04	0.51 ± 0.07
x_1 range	$0.2 \to 0.9$	$0.2 \to 0.9$	$0.2 \to 1.0$	$0.2 \to 1.0$
x_2 range	$0.05 \to 0.5$	$0.05 \to 0.5$	$0.1 \to 0.4$	$0.04 \to 0.38$

asymmetries are consistent between past experiments and COMPASS experiment, while the average of μ asymmetries are in opposite sign between past experiments and COMPASS experiment. The different sign of μ is possible since it depend on the definition of y-axis in the reference frame. In this Thesis, the definition of y-axis in the reference frame follows the COMPASS convention, defined in the COMPASS proposal [13] (see Section 6.1). Fig. 6.23 shows the impact of reverse y-axis definition on the extracted unpolarized asymmetries:

$$\hat{y} \equiv \frac{\vec{p}_\pi \times \vec{p}_N}{|\vec{p}_N \cdot \vec{p}_\pi|} \tag{6.10}$$

The example shows that reversing the direction of y-axis brings a sign change for μ asymmetries, while having no impact for λ and ν asymmetries.

For the ν asymmetries, not only a deviation of ν as function of q_T with respect to pQCD calculation, but also the strong violation of Lam–Tung relation is observed as E615 and NA10 measurement. Since the measurement of all experiments are much larger than the perturbative QCD calculation, this suggests a room of positive sign of non-perturbative TMD Boer–Mulders function contribution. Fig. 6.24 and Fig. 6.25 highlight the ν asymmetries and Lam–Tung violation as a function of q_T from three pion-induced Drell–Yan experiments, respectively.

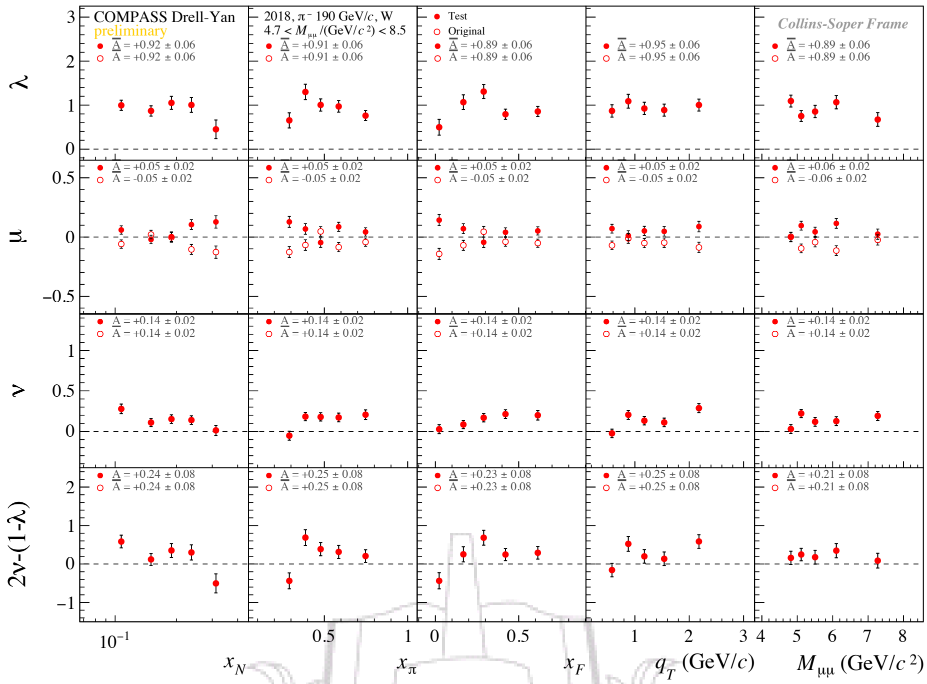

Figure 6.23: An example of the impact of reverse y-axis definition in Collins–Soper frame on the extracted unpolarized asymmetries. The result with the original y-axis definition are labelled as "Original", while the result with the reverse y-axis definition are labelled as "Test".

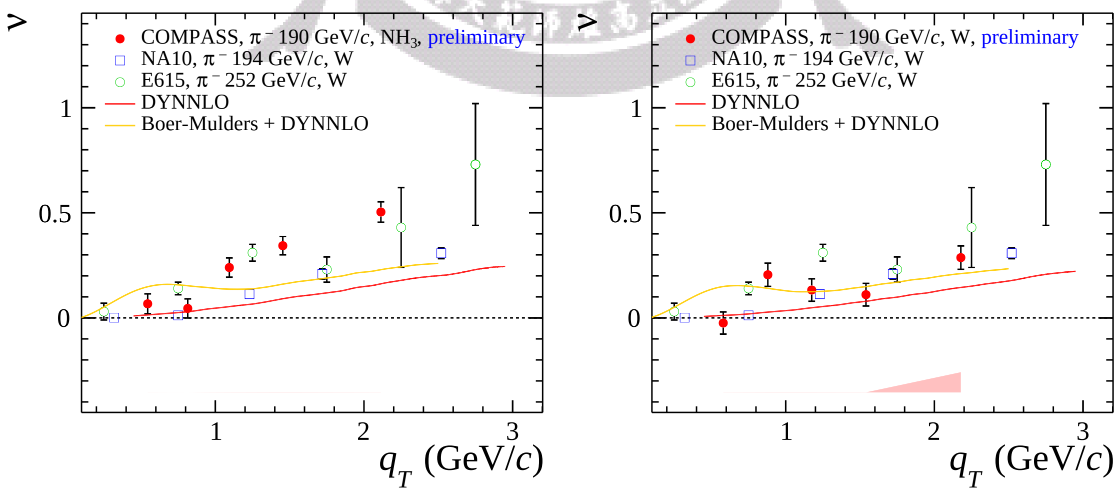

Figure 6.24: The ν asymmetries as a function of q_T from three pion-induced Drell–Yan experiments. Left panel: COMPASS NH_3 data, right panel: COMPASS W data.

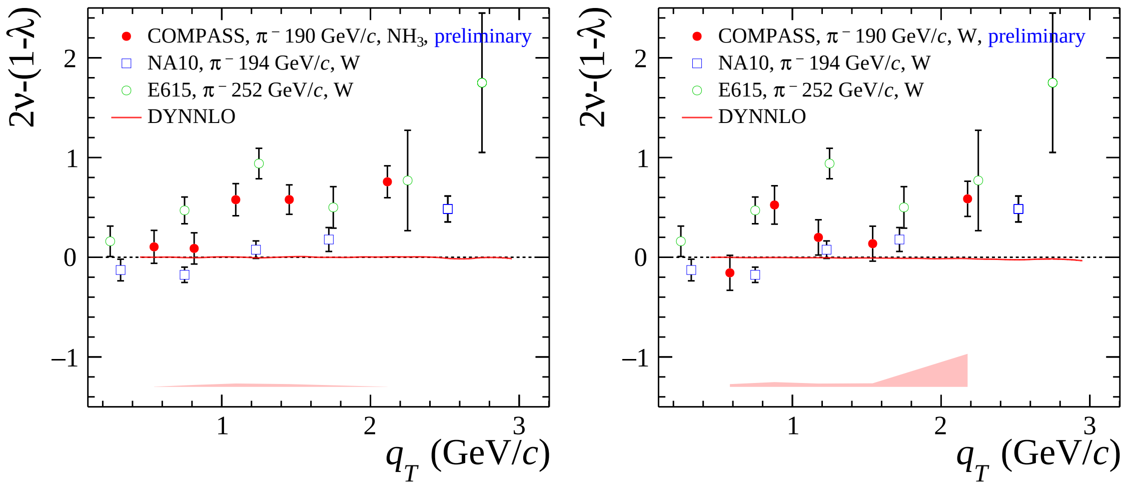

Figure 6.25: The Lam–Tung violation as a function of q_T from three pion-induced Drell–Yan experiments. Left panel: COMPASS NH_3 data, right panel: COMPASS W data.

6.6.1 Different Feynman-x Convention

The definition of x_F, x_π and x_N for the Drell–Yan unpolarized asymmetries from COMPASS in this Thesis follows the one from COMPASS-II proposal [13] (see Tab. 1.1):

$$x_\pi = \frac{q^2}{2P_\pi \cdot q} \tag{6.11}$$
$$x_N = \frac{q^2}{2P_N \cdot q}$$
$$x_F = x_\pi - x_N$$

However, this definition of x_F, x_π and x_N is not the conventional definition used for Drell–Yan kinematics [8], e.g. the one used by NA10 and E615 experiments:

$$x_F = \frac{2p_L^*}{\sqrt{s}} \tag{6.12}$$
$$x_\pi = \sqrt{\frac{M_{\mu\mu}^2}{s} + \frac{x_F^2}{4}} + \frac{x_F}{2}$$
$$x_N = \sqrt{\frac{M_{\mu\mu}^2}{s} + \frac{x_F^2}{4}} - \frac{x_F}{2}$$

where p_L^* represent the longitudinal momentum of virtual photon in the centre-of-mass frame.

The definition of x_F, x_π and x_N from COMPASS-II proposal is usually used in SIDIS kinematics, which have been explored by the COMPASS experiment in the past. The advantage to keep using this definition is to study the sign change of Boer–Mulders function between SIDIS and Drell–Yan process in the future. In order to perform a fair comparison between COMPASS result and the past experiments, Fig. 6.26 shows the Drell–Yan unpolarized asymmetries from COMPASS experiment by using Eq. (6.13) convention. The impact of the Drell–Yan unpolarized asymmetries between two convention are shown in Fig. 6.27.

The result shows visible difference for three unpolarized asymmetries as function of x_F, x_π and x_N, but within one sigma deviation.

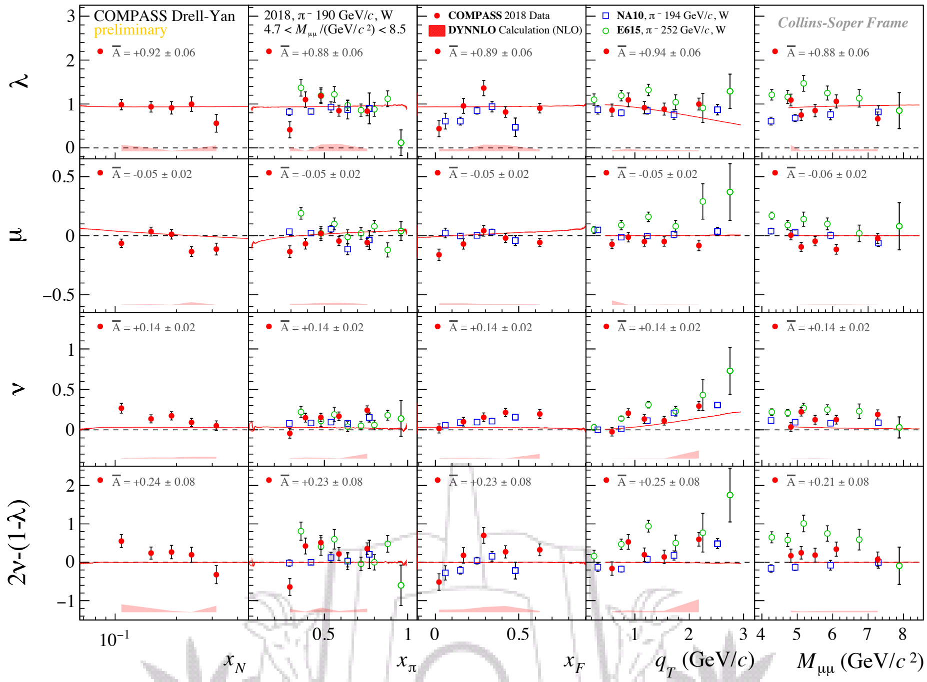

Figure 6.26: The comparison of extracted high-mass Drell–Yan unpolarized asymmetries from W target in Collins–Soper frame from COMPASS measurement (red close circle) by using the same definition of x_F, x_π and x_N with NA10 (blue open square), E615 (green open circle) experiments and also DYNNLO calculation (red line).

6.6.2 Unpolarized Asymmetries in Different Targets

The complete study of Drell–Yan unpolarized asymmetries from COMPASS in this Thesis is done for both NH_3 and W targets. The first preliminary result of Drell–Yan unpolarized asymmetries in W target from COMPASS measurement have been released at April 2021. In principle the asymmetries λ and ν between NH_3 and W target are consistent, but the ν asymmetries result from NH_3 target is observed a factor of two larger with respect to the result from W target. (see Fig. 6.14-6.16).

It's clear to see that the deviation of ν asymmetries are located in the large q_T region and in small x_F region, while there is no theoretical prediction of nuclear dependence on the ν asymmetries. Before the publication of Drell–Yan unpolarized asymmetries for both NH_3 and W targets, there is still a room of improvement for MC simulation chain such as complete period-by-period two-dimensional detectors efficiencies maps. Probably the puzzle of ν asymmetries difference between NH_3 and W targets will be answered after the improvement of acceptance estimation.

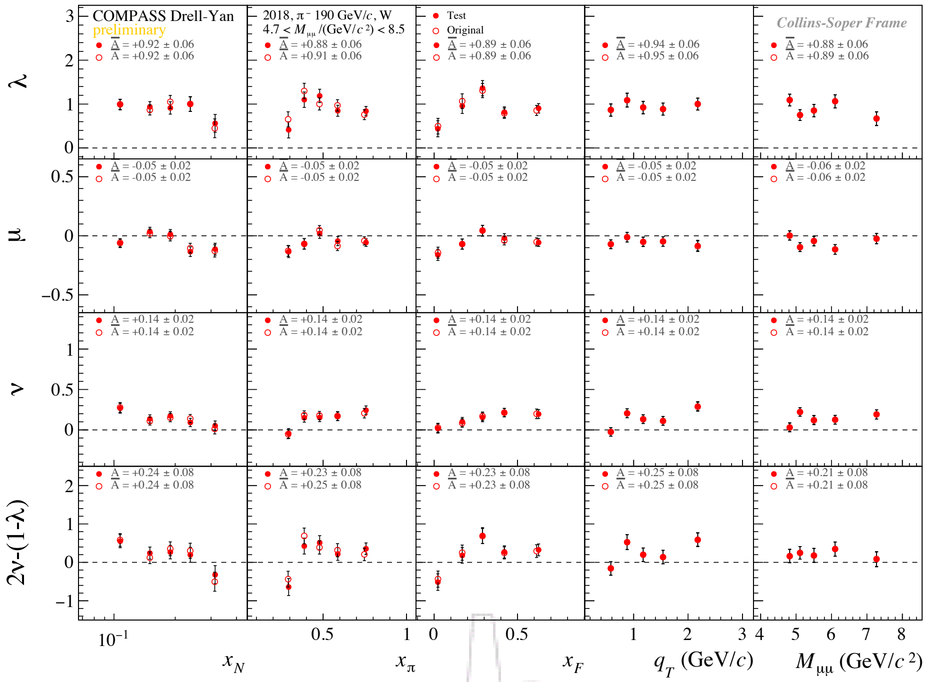

Figure 6.27: The impact of different definition of x_F, x_π and x_N in Collins–Soper frame on the extracted unpolarized asymmetries. The result with the convention in Eq. (6.12) are labelled as "Original", while the result with the Eq. (6.13) are labelled as "Test".

6.6.3 Rotational Invariant Quantities Check

The unpolarized asymmetries analysis from many past experiments (such as NA10 and E615, and also COMPASS) were done in the Collins–Soper frame, as it was demonstrated that this frame reflects an optimal average in approximating the hadronic to partonic frames when describing Drell–Yan process. But the unpolarized asymmetries being frame-dependent, this makes the comparisons and interpretation of results more difficult. Nevertheless, other more recent experiments have published their angular dependent studies of Drell–Yan-like processes (like Z^0 or J/ψ production) using other reference frames. One can demonstrate the existence of a number of independent rotational invariants describing the angular distribution of the Drell–Yan (and Drell–Yan like) dileptons [67, 68]. Using these quantities, the values of the unpolarized asymmetries become independent of the reference frame. Due to the property of frame-invariant, these quantities are particularly useful as a check for possible systematic effects. In particular the so-called $\tilde{\lambda}$ and $\mathcal{F}$ invariants, which are defined as

$$\tilde{\lambda} = \frac{2\lambda + 3\nu}{2 - \nu} \tag{6.13}$$

$$\mathcal{F} = \frac{1 + \lambda + \nu}{3 + \lambda} \tag{6.14}$$

Constraints apply to these "natural" invariants describing Drell–Yan process to be $-1 < \tilde{\lambda} < \infty$ and $0 < \mathcal{F} < 1$. The $\tilde{\lambda}$ and $\mathcal{F}$ invariants are calculated in the three reference frames (see Section 6.1) when analysing Drell–Yan. Results are shown in Fig. 6.28, for the two targets, NH_3 and W.

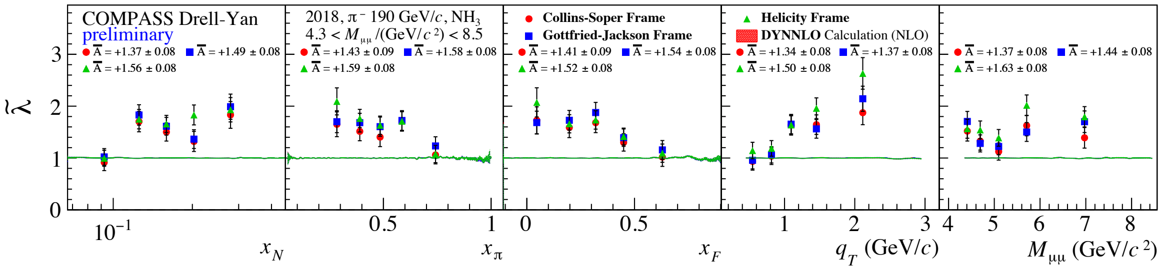

(a) NH_3 target

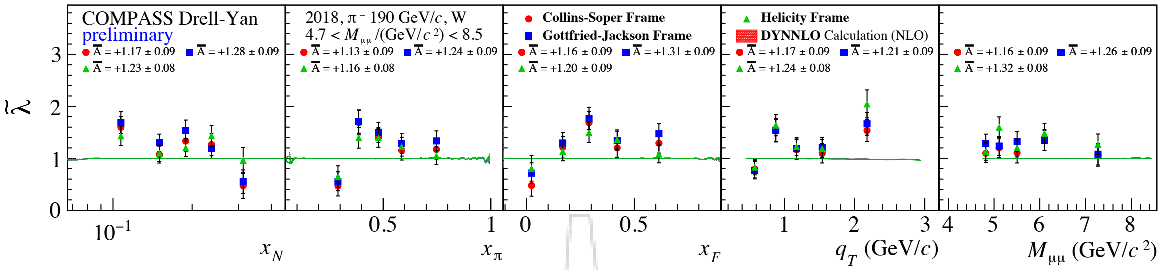

(b) W target

Figure 6.28: Rotational invariant $\tilde{\lambda}$ extracted in Collins–Soper, Gottfried–Jackson and Helicity frames, for the NH_3 target and the W target.

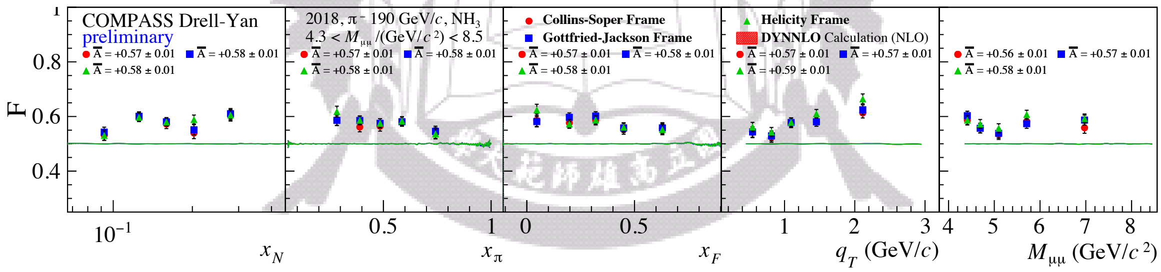

(a) NH_3 target

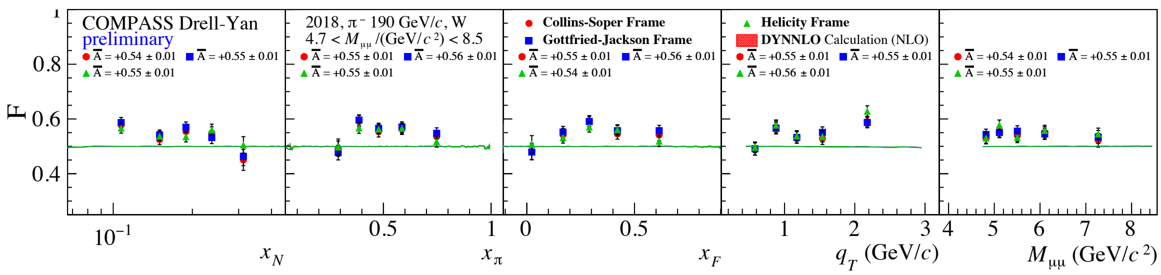

(b) W target

Figure 6.29: Rotational invariant $\mathcal{F}$ extracted in Collins–Soper, Gottfried–Jackson and Helicity frames, for the NH_3 target and the W target.

The agreement among the different frames gives a measure of systematic errors related to the acceptance correction. In the COMPASS data, $\tilde{\lambda}$ and $\mathcal{F}$ are compatible with 1 for the W target, and above unity for the NH_3 data. This result suggest the level of systematic uncertainties in this analysis are in a reasonable value. More detail systematic uncertainties checks are done and demonstrated in the Appendix C. The same type of analysis for the published E615 data [44] on W target also shows $\tilde{\lambda}$ above 1 (see Fig. 6.30a).

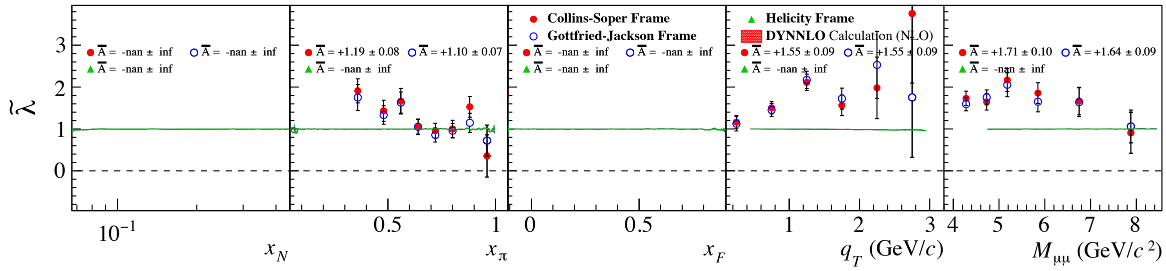

(a) E615

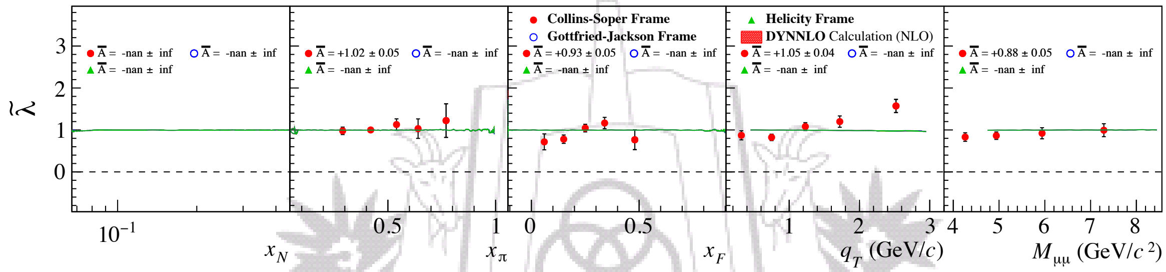

(b) NA10

Figure 6.30: Rotational invariant $\tilde{\lambda}$ extracted in Collins–Soper and Gottfried–Jackson frames, calculated from the E615 and NA10 published UAs results.

6.6.4 Estimation of Systematic Uncertainties

The study of overall systematic uncertainties of unpolarized asymmetries extraction have been done carefully. There are many points have been checked and validated, which are demonstrated in more detail at Appendix:

1. Compatibility of the results obtained from different periods.
2. Compatibility of the results obtained from different target cells (same material but different location).
3. Compatibility of the results obtained from different trigger priority.
4. Systematic of different q_T cut.
5. Systematic of different θ_{μ^-} cut.
6. Systematic of different bin size of two-dimensional angular histogram.
7. Systematic of different x_F cut.

8. Systematic of different dead zone cut.

9. Impact of different MC-generator settings.

Base on the result, only first of three items are found some remaining systematic effects so that they are included in the final systematic uncertainties. Three of relative systematic uncertainties with respect to statistics error $\sigma_{\text{Stat.},i}$ are extracted individually:

1. Relative systematic uncertainties of incompatibility from different periods $\frac{\sigma^{\text{Period}}_{\text{Syst.}}}{\sigma_{\text{Stat.}}}$

2. Relative systematic uncertainties of incompatibility from different target cells $\frac{\sigma^{\text{Target}}_{\text{Syst.}}}{\sigma_{\text{Stat.}}}$

3. Relative systematic uncertainties of incompatibility from different trigger priority $\frac{\sigma^{\text{Trigger}}_{\text{Syst.}}}{\sigma_{\text{Stat.}}}$

The total systematic uncertainties are summed up in quadrature in each kinematic bin i:

$$\frac{\sigma^{\text{Total}}_{\text{Syst.},i}}{\sigma_{\text{Stat.},i}} \equiv \frac{1}{\sigma_{\text{Stat.},i}} \sqrt{\left(\sigma^{\text{Period}}_{\text{Syst.}}\right)^2 + \left(\sigma^{\text{Target}}_{\text{Syst.},i}\right)^2 + \left(\sigma^{\text{Trigger}}_{\text{Syst.},i}\right)^2} \tag{6.15}$$

The result of total systematic uncertainties for unpolarized asymmetries extraction in Collins–Soper, Gottfried–Jackson and Helicity frame are summarized in Fig. 6.31.

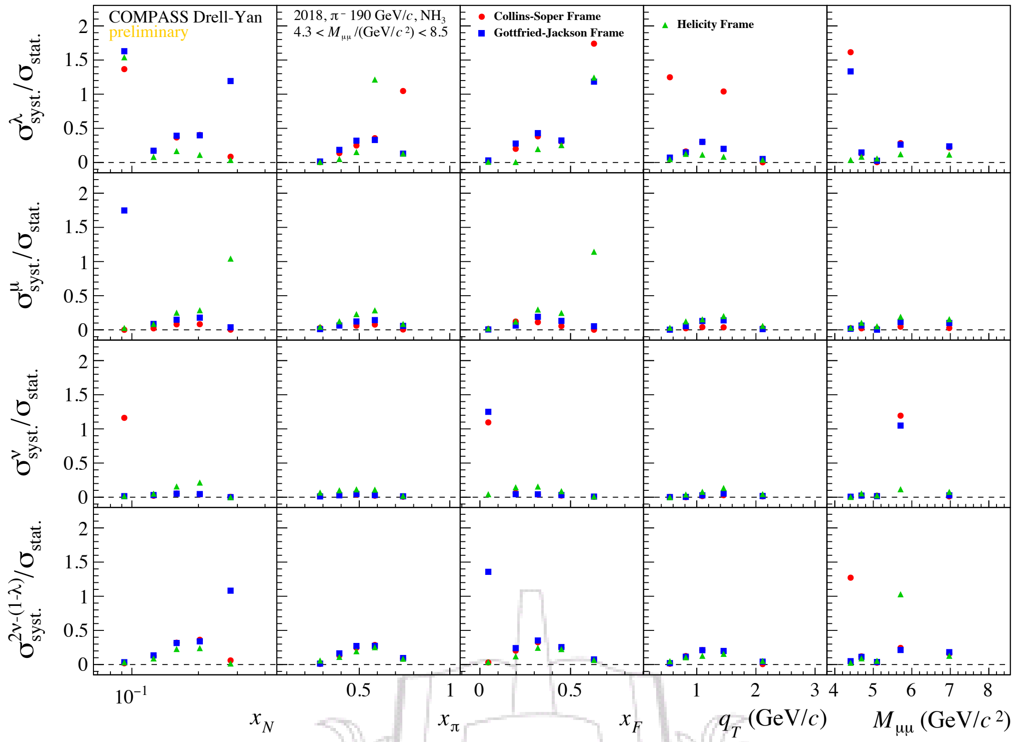

(a) NH_3 target

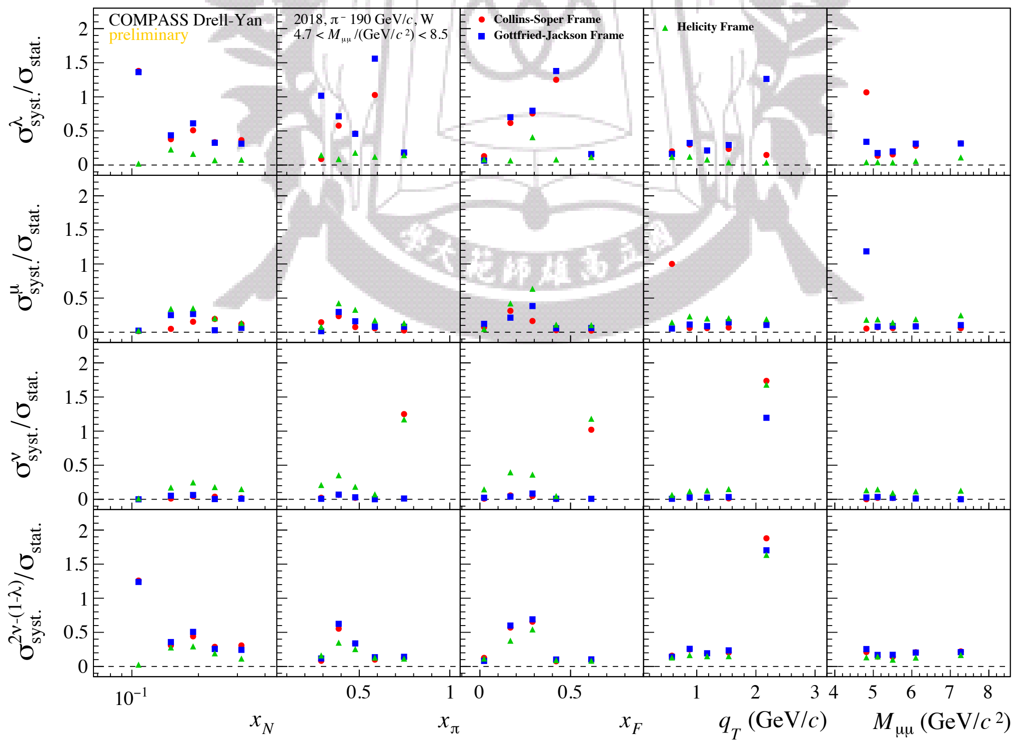

(b) W target

Figure 6.31: The estimated total systematic uncertainties for unpolarized asymmetries result in Collins–Soper, Gottfried–Jackson and Helicity frame.

CHAPTER 7

The Charmonium Production

7.1 J/ψ Production

The J/ψ meson, as a bound state of charm and anti-charm quark ($c\bar{c}$) from the charmonium production, have been discovered since 1974. The production of charmonium attracted people's attention until now since it's a good resource for understanding QCD framework in both perturbative and non-perturbative aspects. To investigate the non-perturbative aspects of QCD, one of the way is by studying the internal structure of pion, which is the lightest QCD bound state. Despite the fact that the pion is theoretically simpler than the proton in terms of partonic structure, the understanding of pion's parton distribution functions (PDFs) are not as plenty as proton due to experimental constrain. As a meson, too short lifetime made a difficulty to study the partonic structure of pion via scattering off a pion target. Building on that, the understanding of pion's PDFs relies on the pion-induced Drell–Yan data or charmonium production data. The pion-induced Drell–Yan data provide the valence quark distribution in the pion since Drell–Yan process are dominated by quark-antiquark annihilation, but cannot constrain the sea and the gluon distributions in the pion. The pion-induced charmonium production data has some advantages: first is the large cross-section compare with Drell–Yan process, second is detectable via dilepton decay channel as Drell–Yan process, also the domination of gluon-gluon fusion in charmonium production bring the constrain of gluon distribution in the pion. To constrain the remain component in pion PDFs, sea quark distribution, which can be accessed by performing the Drell–Yan measurement with π^+ and π^- beams on the isoscalar deuterium target.

Base on the global analysis with available pion-induced Drell–Yan data and J/ψ production data which carried out more than two decades ago, the calculations of pion PDFs determined by Sutton–Martin–Roberts–Stirling (SMRS) [69] and Gluck–Reya–Vogt (GRV) [70] are still widely used until now. Recently there are two global analysis have been performed by Jefferson lab Angular Momentum Collaboration (JAM) [71] and xFitter [72].

In general, the theoretical procedure for a heavy quarkonium production consists two steps: first is the production of heavy-quark pairs ($Q\bar{Q}$) at the parton level from the QCD description, second is the hadronization from $Q\bar{Q}$ into the quarkonium states. In case of the charmonium production from hadron collision, the $c\bar{c}$ pair is produced via the quark-antiquark annihilation ($q\bar{q}$), gluon-gluon fusion (gg) or quark-gluon scattering (qg) at first. Furthermore, the $c\bar{c}$ pair will be formed into a charmonium bound state via hadronization process, which is a non-perturbative process. Examples of heavy-quark pairs production from hadron collision are shown in Fig. 7.1.

In order to describe this non-perturbative hadronization process, several theoretical approaches have been proposed:

1. Color Evaporation Model (CEM) [73]

2. Color-Singlet Model (CSM) [74]

3. Non-Relativistic QCD (NRQCD) [75]

The CEM assumes a constant probability for a $c\bar{c}$ pair to hadronize into a given charmonium state (J/ψ, $\psi(2S)$, χ_{c0} ... and so on). The CSM assumes the production of charmonium state to be through the color-singlet $c\bar{c}$ channel of the same quantum numbers as charmonium state. The NRQCD expands the calculations by the powers of the average velocity of $c\bar{c}$

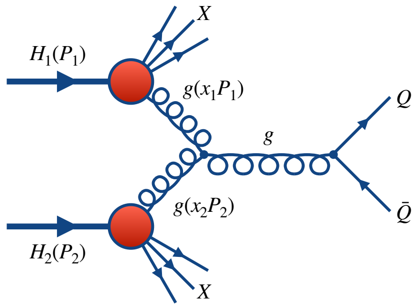

(a) gluon-gluon fusion

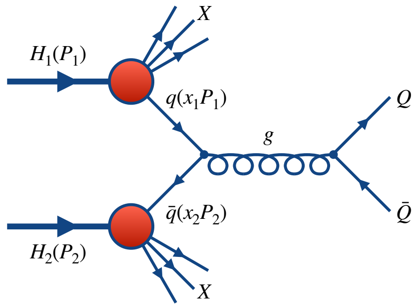

(b) quark-antiquark annihilation

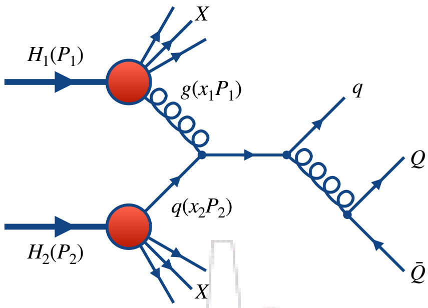

(c) quark-gluon scattering

Figure 7.1: Examples of heavy-quark pairs ($Q\bar{Q}$) production from hadron collision.

pairs in the charmonium state rest frame, where the hadronization probability of each $c\bar{c}$ pair depends on its color, spin state and angular momentum. Among three of theoretical approaches, the NRQCD is the mainstream approach since it provides a good description of experimental data taken at collider energies. But the failure of NRQCD approach in the measurement at fixed-target energies remains.

7.2 Non-Relativistic QCD

In the NRQCD approach, the cross-section of quarkonium production is expanded with the strong coupling constant α_s and the velocity of heavy quark pair $Q\bar{Q}$. The factorization of the $Q\bar{Q}$ pair proceeds through a short-distance partonic interaction is calculated perturbatively as a series of α_s in perturbative QCD. The probability of non-perturbative hadronization of a $Q\bar{Q}$ pair into the quarkonium bound state depends on its color, spin state and angular momentum, which is characterized by the so-called long-distance matrix elements (LDMEs) for each state with different color, spin and angular momentum. The LDMEs are extracted by a fit to the experimental data and assumed to be universal. The LDMEs can be divided into two categories: color-singlet LDMEs and color-octet LDMEs. In case of charmonium production, the color-singlet LDMEs can be extracted from the decay widths of charmonium state or model calculations, while the color-octet LDMEs are determined from fits to the cross-section and polarization of charmonium production data.

In the NRQCD, the general production cross-section for a quarkonium state H through two hadrons (A, B) colliding process $A + B \to H + X$ can be described as following:

$$\sigma_H = \sum_{i,j=q,\bar{q},g} \int_0^1 \mathrm{d}x_1 \mathrm{d}x_2 f_i^A(x_1) f_j^B(x_2) \hat{\sigma}(ij \to H) \tag{7.1}$$

where the index i and j in the first sum extends over all partons (quark q, anti-quark $\bar{q}$ and gluon G) in the colliding hadrons, $f_i^A(x_1)$ and $f_j^B(x_2)$ represent the corresponding PDFs in each hadrons as function of Bjorken-x x_1 and x_2. Here the production cross-section $\hat{\sigma}(ij \to H)$ is the sum of the products of the short-distance coefficients $C^{ij}_{Q\bar{Q}[n]}$ and LDMEs $\langle O_n^H \rangle$:

$$\hat{\sigma}(ij \to H) = \sum_n C^{ij}_{Q\bar{Q}[n]} \langle O_n^H \rangle \tag{7.2}$$

The short-distance coefficients $C^{ij}_{Q\bar{Q}[n]}$ describe the production of a quark-antiquark pair $Q\bar{Q}$ in a specific color state $[n]$ and calculated perturbatively in powers of $\alpha_s(2m_Q)$. The non-perturbative parameters LDMEs $\langle O_n^H \rangle$ describe the hadronization of the $Q\bar{Q}$ pair into a quarkonium state H. Because the LDMEs are non-perturbative parameters so that it can be only determined by a fit to data, which assumed to be universal[1].

In general, the leading-order $O(\alpha_s^2)$ calculation of $\hat{\sigma}(ij \to H)$ consists the quark-antiquark annihilation and the gluon-gluon fusion diagrams:

$$\begin{aligned} q + \bar{q} &\to Q + \bar{Q} \\ g + g &\to Q + \bar{Q} \end{aligned} \tag{7.3}$$

The next-to-leading-order $O(\alpha_s^3)$ calculation includes additional quark-gluon scattering and virtual gluon correction diagrams:

$$\begin{aligned} q + \bar{q} &\to Q + \bar{Q} + g \\ g + g &\to Q + \bar{Q} + g \\ q + g &\to Q + \bar{Q} + q \end{aligned} \tag{7.4}$$

7.3 Charmonium Production in NRQCD Approach

In case of charmonium production, base on Eq. (7.1), the differential cross-section as a function of Feynman-x (x_F) for a charmonium state H through the collision of hadron h and nucleon N: $hN \to H + X$ with the interpretation of NRQCD approach can be expressed as following:

$$\frac{\mathrm{d}\sigma_H}{\mathrm{d}x_F} = \sum_{i,j=q,\bar{q},g} \int_0^1 \mathrm{d}x_1 \mathrm{d}x_2 f_i^h(x_1, \mu_F) f_j^N(x_2, \mu_F) \hat{\sigma}(ij \to H) \tag{7.5}$$

where the index i and j in the first sum extends over all partons in the colliding hadrons, μ_F is the factorization scale and μ_R is the renormalization scales, $f_i^h(x_1, \mu_F)$ and $f_j^N(x_2, \mu_F)$

[1] independent of beam or target hadrons and the energy scale

represent the corresponding PDFs in beam hadron and target nucleon as function of μ_F and Bjorken-x x_1 and x_2. Here the charmonium production cross-section $\hat{\sigma}(ij \to H)$ is the sum of the products of the short-distance coefficients $C^{ij}_{c\bar{c}[n]}$ and LDMEs $\langle O^H_n \rangle$:

$$\hat{\sigma}(ij \to H) = \sum_n C^{ij}_{c\bar{c}[n]}(x_1 p_h, x_2 p_N, \mu_F, \mu_R, m_c)\langle O^H_n(^{2S+1}L_J)\rangle \tag{7.6}$$

The short-distance coefficients $C^{ij}_{c\bar{c}[n]}$ describe the production of a $c\bar{c}$ pair in a specific color state $[n]$ ($n = 8$ represent color-octet state, while $n = 1$ represent color-singlet state) and calculated perturbatively in powers of $\alpha_s(2m_c)$. The non-perturbative parameters LDMEs $\langle O^H_n(^{2S+1}L_J)\rangle$ describe the hadronization of the $c\bar{c}$ pair into a charmonium state H (J/ψ, $\psi(2S)$, χ_{c0}...) with specific color n, spin S, orbital angular momentum L and total angular momentum J.

In the charmonium production, the calculation of production cross-section up to the next-to-leading-order $O(\alpha_s^3)$ should considered $q\bar{q}$, gg and qg processes, which shown in Eq. (7.3) and Eq. (7.4). The processes in $O(\alpha_s^2)$ calculation will produce $c\bar{c}$ pair in an S-wave color-octet state or P-wave color-singlet state, while in $O(\alpha_s^3)$ calculation will produce $c\bar{c}$ pair in an S-wave or P-wave color-singlet state. The possible LDMEs in the different processes for each charmonium state are summarized in Tab. 7.1.

H	$q\bar{q}$	gg	qg
$J/\psi, \psi(2S)$	$\langle O^H_8(^3S_1)\rangle$ $(O(\alpha_s^2))$	Δ^H_8 $(O(\alpha_s^2))$ $\langle O^H_1(^3S_1)\rangle$ $(O(\alpha_s^3))$	
χ_{c0}	$\langle O^H_8(^3S_1)\rangle$ $(O(\alpha_s^2))$	$\langle O^H_1(^3P_0)\rangle$ $(O(\alpha_s^2))$	
χ_{c1}	$\langle O^H_8(^3S_1)\rangle$ $(O(\alpha_s^2))$	$\langle O^H_1(^3P_1)\rangle$ $(O(\alpha_s^3))$	$\langle O^H_1(^3P_1)\rangle$ $(O(\alpha_s^3))$
χ_{c2}	$\langle O^H_8(^3S_1)\rangle$ $(O(\alpha_s^2))$	$\langle O^H_1(^3P_2)\rangle$ $(O(\alpha_s^2))$	

Table 7.1: Relationship of LDMEs and the associated orders of α_s to different processes for various charmonium states in the NRQCD framework of Ref. [76].

There are five kinds of charmonium state: J/ψ, $\psi(2S)$, χ_{c0}, χ_{c1} and χ_{c2}. It's clear to see that the $c\bar{c}$ pair at $O(\alpha_s^2)$ in color-octet state can only hadronize into various charmonium states with the LDMEs $\langle O^H_8(^3S_1)\rangle$ in $q + \bar{q} \to c + \bar{c}$ process. The $c\bar{c}$ pair at $O(\alpha_s^3)$ in color-singlet state can only hadronize into χ_{c1} with the LDME $\langle O^H_1(^3P_1)\rangle/m_c^2$ in $q+g \to c+\bar{c}+q$ process. In $g + g \to c + \bar{c}$ (at $O(\alpha_s^2)$) process, the $c\bar{c}$ pair in color-octet state can hadronize into J/ψ and $\psi(2S)$ with the corresponding LDMEs Δ^H_8[2], while the $c\bar{c}$ pair in color-singlet state can hadronize into χ_{c0} and χ_{c2} with the LDMEs $\langle O^H_1(^3P_0)\rangle/m_c^2$ and $\langle O^H_1(^3P_2)\rangle/m_c^2$, respectively. Finally, in $g+g \to c+\bar{c}+g$ (at $O(\alpha_s^3)$) process, the $c\bar{c}$ pair in color-singlet state can hadronize into J/ψ, $\psi(2S)$ and χ_{c1} with the LDMEs $\langle O^H_1(^3S_1)\rangle/m_c^2$ and $\langle O^H_1(^3P_1)\rangle/m_c^2$, respectively. Base on the spin symmetry relation, the total number of LDMEs listed in Tab. 7.1 can be

[2] $\Delta^H_8 = \langle O^H_8(^1S_0)\rangle + \frac{3}{m_c^2}\langle O^H_8(^3P_0)\rangle + \frac{4}{5m_c^2}\langle O^H_8(^3P_2)\rangle$

further reduced:

$$
\begin{aligned}
\langle \mathcal{O}_8^{J/\psi,\psi(2S)}(^3P_J)\rangle &= (2J+1)\langle \mathcal{O}_8^{J/\psi,\psi(2S)}(^3P_0)\rangle \text{ for } J=2 \\
\langle \mathcal{O}_8^{\chi_{cJ}}(^3S_1)\rangle &= (2J+1)\langle \mathcal{O}_8^{\chi_{c0}}(^3S_1)\rangle \text{ for } J=1,2 \\
\langle \mathcal{O}_1^{\chi_{cJ}}(^3P_J)\rangle &= (2J+1)\langle \mathcal{O}_1^{\chi_{c0}}(^3P_0)\rangle \text{ for } J=1,2.
\end{aligned}
\tag{7.7}
$$

With the information of LDMEs, the charmonium production cross-section can be calculated as shown in Eq. (7.5). In case of J/ψ production cross-section calculation, one should take into account not only the contribution of direct production of J/ψ itself, but also feed-down J/ψ contribution from the hadronic decay of $\psi(2S)$ and radiative decays of χ_{c0}, χ_{c1} and χ_{c2} states. Therefore, the total J/ψ production cross-section should be estimated as following:

$$
\sigma_{J/\psi} = \sigma_{J/\psi}^{\text{direct}} + Br(\psi(2S) \to J/\psi + X)\sigma_{\psi(2S)} + \sum_{J=0}^{2} Br(\chi_{cJ} \to J/\psi + \gamma)\sigma_{\chi_{cJ}} \tag{7.8}
$$

where the $Br(*)$ represent the branching ratios of different decay channels related to J/ψ product, these values from PDG 2020 [77] is shown as following:

$$
\begin{aligned}
Br(\psi(2S) \to J/\psi + X) &= 61.4\% \\
Br(\chi_{c0} \to J/\psi + \gamma) &= 1.4\% \\
Br(\chi_{c1} \to J/\psi + \gamma) &= 34.3\% \\
Br(\chi_{c2} \to J/\psi + \gamma) &= 19.0\%
\end{aligned}
\tag{7.9}
$$

7.4 Long-Distance Matrix Elements Setting

By introducing the LDMEs in the NRQCD approach and its universality, the assumption of the factorization should be holds [75]. In order to test this point, analysing the low p_T cross-section from fixed-target data is necessary. Some articles have performed such study, which focusing exclusively on charmonium production from fixed-target experiments. One is reported by Beneke and Rothstein [76], another is reported by Maltoni *et al.* [78].

In Ref. [76], the partial next-to-leading order (up to $\mathcal{O}(\alpha_s^3)$) calculation in the NRQCD approach is performed. The color-singlet LDMEs $\langle \mathcal{O}_1^H(^3S_1)\rangle$ for J/ψ and $\psi(2S)$, and $\langle \mathcal{O}_1^H(^3P_0)\rangle$ for χ_{c0} are taken from the potential model calculation [79]. The color-octet LDMEs $\langle \mathcal{O}_8^H(^3S_1)\rangle$ for J/ψ, $\psi(2S)$ and χ_c are taken from the fits to the p_T differential cross-sections of charmonium production in Tevatron collider data [80]. The Δ_8^H LDMEs for J/ψ and $\psi(2S)$ were determined by a fit of the NRQCD calculation to the proton-induced data. The obtained LDMEs from Ref. [76] are summarized in Tab. 7.2.

After obtaining all of LDMEs, the proton- and pion-induced charmonium production cross-section are both calculated and compared with experimental data. Fig. 7.2 shows the J/ψ and $\psi(2S)$ production cross-sections from proton-induced data and compare with calculation for $x_F > 0$ region which using the LDMEs setting in Tab. 7.2. Same exercise has been done for pion-induced data and shown in Fig. 7.3. The comparison result of proton-induced J/ψ and $\psi(2S)$ production cross-sections shows a good agreement between

H	$\langle O_1^H(^3S_1)\rangle$	$\langle O_1^H(^3P_0)\rangle/m_c{}^2$	$\langle O_8^H(^3S_1)\rangle$	Δ_8^H
J/ψ	1.16		6.6×10^{-3}	3×10^{-2}
$\psi(2S)$	0.76		4.6×10^{-3}	5.2×10^{-3}
χ_{c0}		0.044	3.2×10^{-3}	

Table 7.2: NRQCD LDMEs for the charmonium production obtained in Ref. [76], all in units of GeV^3.

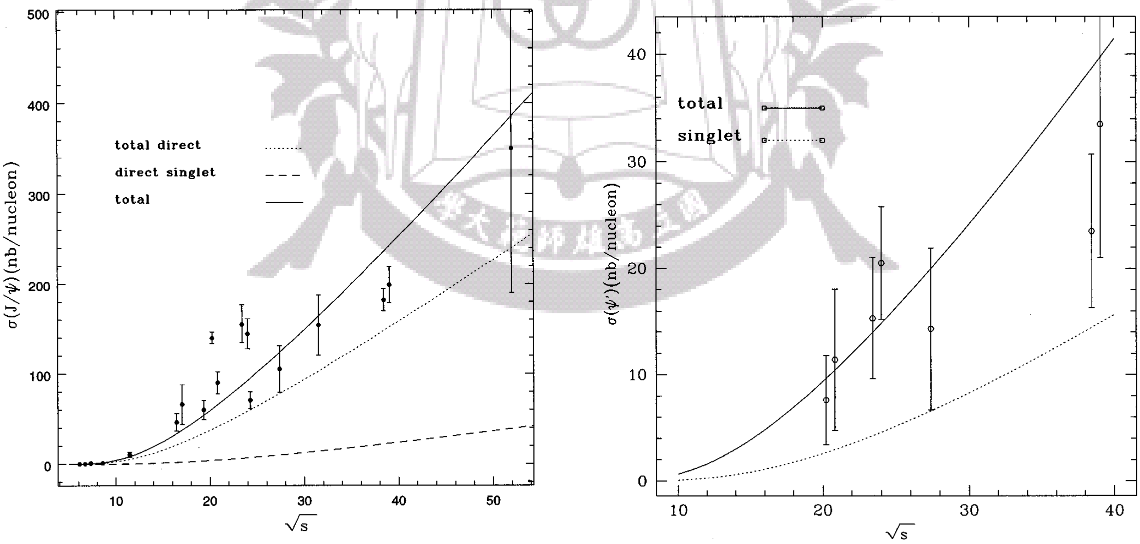

(a) J/ψ production cross-section

(b) $\psi(2S)$ production cross-section

Figure 7.2: The J/ψ and $\psi(2S)$ production cross-sections from proton-induced data and compare with calculation for $x_F > 0$ region. (Adopted from [76])

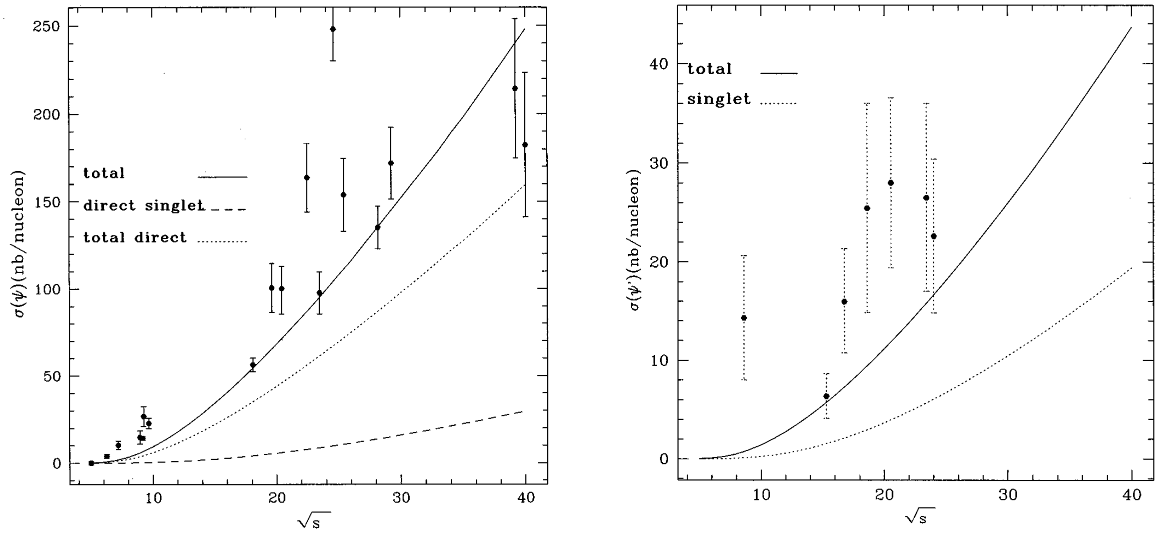

(a) J/ψ production cross-section

(b) $\psi(2S)$ production cross-section

Figure 7.3: The J/ψ and $\psi(2S)$ production cross-sections from pion-induced data and compare with calculation for $x_F > 0$ region. (Adopted from [76])

experimental data and calculation, while the calculation for both J/ψ and $\psi(2S)$ production cross-section were found to be systematically below the experimental data.

In Ref. [78], the complete next-to-leading order (up to $O(\alpha_s^3)$) calculation [81] in the NRQCD approach is performed. The S-wave color-octet LDMEs for J/ψ and $\psi(2S)$ were obtained by fitting to the proton-induced charmonium production cross-section from fixed-target data, while the rest of color-octet LDMEs were taken from the Tevatron data [82, 83]. The obtained LDMEs from Ref. [78] are summarized in Tab. 7.3.

H	$\langle O_1^H(^3S_1)\rangle$	$\langle O_1^H(^3P_0)\rangle/m_c{}^2$	$\langle O_8^H(^3S_1)\rangle$	Δ_8^H
J/ψ	1.16		1.19×10^{-2}	1.0×10^{-2}
$\psi(2S)$	0.76		5.0×10^{-3}	0.42×10^{-3}
χ_{c0}		0.11	3.1×10^{-3}	

Table 7.3: NRQCD LDMEs for the charmonium production adopted in Ref. [78], all in units of GeV^3.

The proton-induced J/ψ and $\psi(2S)$ production cross-sections are calculated and found to be agree with fixed-target experimental data. Fig. 7.4 shows the J/ψ and $\psi(2S)$ production cross-sections and also the cross-section ratio of $\sigma_{\psi(2S)}/\sigma_{J/\psi}$ from proton-induced data, which compare with the complete next-to-leading order NRQCD calculation by using the LDMEs setting in Tab. 7.3. The comparison result of proton-induced J/ψ and $\psi(2S)$ production cross-sections shows a good agreement between experimental data and calculation, but the comparison with pion-induced J/ψ and $\psi(2S)$ production were not tested.

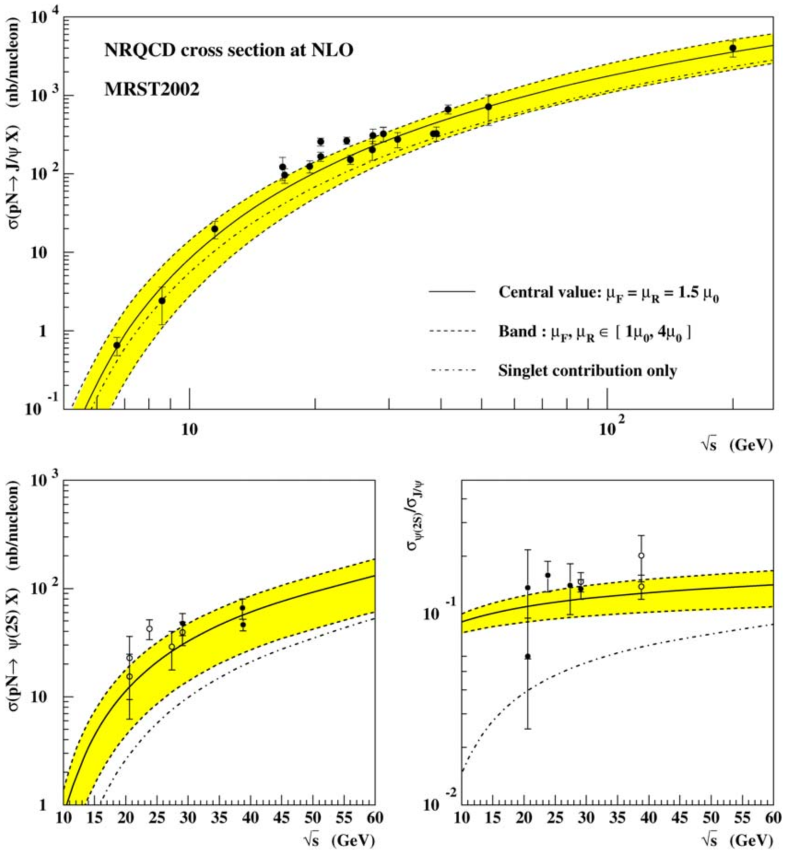

Figure 7.4: The J/ψ and $\psi(2S)$ production cross-sections and also the cross-section ratio of $\sigma_{\psi(2S)}/\sigma_{J/\psi}$ from proton-induced data, which compare with the complete next-to-leading order NRQCD calculation. (Adopted from [78])

7.5 Proton- and Pion-induced Charmonium Production

Although the failure of describing the pion-induced charmonium production from the fixed-target data by the set of LDMEs obtained from Ref. [76, 78] is contradict the universality of LDMEs between pion- and proton-induced processes, some improvements are suggested and to be tested.

To explore the possibility of a set of LDMEs can be identified to achieve a good description for both proton- and pion-induced data in charmonium production, a global analysis with several fixed-target experimental data from both proton- and pion-induced processes in the NRQCD framework is performed. Following the NRQCD framework in Ref. [76], the same exercise can be repeated. But a possible new set of LDMEs from a global fit can be re-evaluated by including the cross-section for J/ψ, $\psi(2S)$ and their ratios $R_\psi = \sigma_{\psi(2S)}/\sigma_{J/\psi}$ from both proton-induced data [78, 86, 87] and pion-induced data [84, 85, 88, 89] in the same time. Furthermore, the color-octet LDMEs $\langle O_8^H(^3S_1)\rangle$ should allowed to vary in the global fit.

The partial next-to-leading order NRQCD calculation is done base on the usage of the nucleon CT14nlo PDFs [90] and the pion GRV NLO PDFs [70] under the LHAPDF framework [91, 92] and also the necessary parameters setting: a charm quark mass $m_c = 1.5$ GeV/$c^2$and renormalization and factorization scale $\mu_R = \mu_F = 2m_c$.

Fig. 7.5 shows the comparison of J/ψ and $\psi(2S)$ production cross-sections in both proton- and pion-induced processes and also the cross-section ratio of $\sigma_{\psi(2S)}/\sigma_{J/\psi}$ from proton-induced data with the NRQCD calculation. The data in Fig. 7.5 are compared with the NRQCD calculation by using the different set of LDMEs, which obtained in three different approaches and labelled as: "Fit-R", "Fit-1" and "Fit-2", respectively. The definition of three different global fit approaches are defined as following:

1. **Fit-R**: (Reference fit)
   Fixed the LDMEs values which determined in Ref. [76] (see Tab. 7.2) in the global fit. By using the same set of LDMEs as Ref. [76], the whole global fit framework can be validated.

2. **Fit-1**: (Fit of proton-induced data)
   Leaving $\langle O_8^H(^3S_1)\rangle$ and Δ_8^H for both J/ψ and $\psi(2S)$ as free parameters, while the color-octet LDME for χ_{c0} is fixed as shown is Tab. 7.2 in the global fit and only fit with the proton-induced data. The $\langle O_8^H(^3S_1)\rangle$ LDMEs are responsible for the $q\bar{q}$ process, which plays an important role in pion-induced J/ψ production near threshold because the parton density at large x region is dominated by the valence antiquarks in pions. The observed underestimation of low-energy pion-induced data in "Fit-R" approach could caused by the too small value of $\langle O_8^H(^3S_1)\rangle$ LDMEs.

3. **Fit-2**: (Fit of proton- and pion-induced data)
   Leaving $\langle O_8^H(^3S_1)\rangle$ and Δ_8^H for both J/ψ and $\psi(2S)$ as free parameters, while the color-octet LDME for χ_{c0} is fixed as shown is Tab. 7.2 in the global fit and fit with both proton- and pion-induced data. The "Fit-2" approach is quite similar with "Fit-1" approach, only the data is different by including also pion-induced data. The combination of including both proton- and pion-induced data in the global fit should further constrain[3]

[3]Under the assumption that higher-twist effects are negligible

color-octet LDMEs because of the different nature of valence quarks in the protons and pions, which lead to the different energy dependence of the relative contributions of $q\bar{q}$ and gg processes for J/ψ and $\psi(2S)$ production.

The reduced χ^2/ndf of the whole data sets and the χ^2 divided by the number of data point (ndp) for each single data set in "Fit-R", "Fit-1" and "Fit-2" approaches for NRQCD calculations and the best-fit result of LDMEs are summarized in Tab. 7.4. Compare to the production cross-section result in "Fit-R" approach, the result in "Fit-1" approach for both proton- and pion-induced data are significantly enhanced (the overall χ^2/ndf is reduced from 16.8 to 6.0). The improvement of the global fit from "Fit-1" approach is due to the new values of LDMEs $\langle O_8^H(^3S_1)\rangle$ for J/ψ and $\psi(2S)$ are increased from 6.6×10^{-3} and 4.6×10^{-3} to $(1.47\pm0.07)\times10^{-1}$ and $(2.5\pm0.2)\times10^{-2}$, respectively. Despite an improved description of data in "Fit-1" approach, the color-octet LDME Δ_8^H for both J/ψ and $\psi(2S)$ are found to be vanished from the global fit. This fitting result suggest that these LDMEs cannot be determined from the proton-induced J/ψ and $\psi(2S)$ production data alone, the "Fit-2" approach might necessary by including pion-induced J/ψ and $\psi(2S)$ production data as well.

After including the pion-induced J/ψ and $\psi(2S)$ production data in the global fit, "Fit-2" approach shows better agreement between experimental measurement and calculation. The color-octet LDMEs Δ_8^H for both J/ψ and $\psi(2S)$ are also better constrained in "Fit-2" approach, which are found to be $(1.8\pm0.2)\times10^{-2}$ and $(4\pm6)\times10^{-4}$, respectively. The new value of color-octet LDMEs Δ_8^H for both J/ψ and $\psi(2S)$ with respect to the one determined from collider data are reduced by a factor of 2 and 10, which might indicate that the $q\bar{q}$ contribution determined by the fixed-target data is much larger than the contribution at collider energies.

Table 7.4: The reduced χ^2/ndf of the whole data sets and the χ^2 divided by the number of data point (ndp) for each data set in "Fit-R", "Fit-1" and "Fit-2" NRQCD calculations and the corresponding input or best-fit LDMEs. All of LDMEs are in units of GeV^3.

	Fit-R	Fit-1	Fit-2
χ^2_{total}/ndf	16.8	6.0	3.3
$\chi^2/ndp\vert^p_{\sigma(J/\psi)}$	9.2	4.1	5.4
$\chi^2/ndp\vert^p_{\sigma(\psi(2S))}$	2.2	1.4	1.7
$\chi^2/ndp\vert^p_{R(\psi(2S))}$	1.1	0.7	1.0
$\chi^2/ndp\vert^{\pi^-}_{\sigma(J/\psi)}$	46.8	15.3	3.7
$\chi^2/ndp\vert^{\pi^-}_{\sigma(\psi(2S))}$	2.8	0.9	0.7
$\langle O_8^{J/\psi}(^3S_1)\rangle$	6.6×10^{-3}	$(1.47\pm0.07)\times10^{-1}$	$(9.5\pm0.4)\times10^{-2}$
$\Delta_8^{J/\psi}$	3×10^{-2}	$(0\pm8)\times10^{-4}$	$(1.8\pm0.2)\times10^{-2}$
$\langle O_8^{\psi(2S)}(^3S_1)\rangle$	4.6×10^{-3}	$(2.5\pm0.2)\times10^{-2}$	$(2.6\pm0.2)\times10^{-2}$
$\Delta_8^{\psi(2S)}$	5.2×10^{-3}	$(0\pm8)\times10^{-4}$	$(4\pm6)\times10^{-4}$

Some of possible systematic effects in the global fit analysis are the initial setting value of charm quark mass m_c and the normalization scale $\mu=\mu_R=\mu_F$. An systematic uncertainties

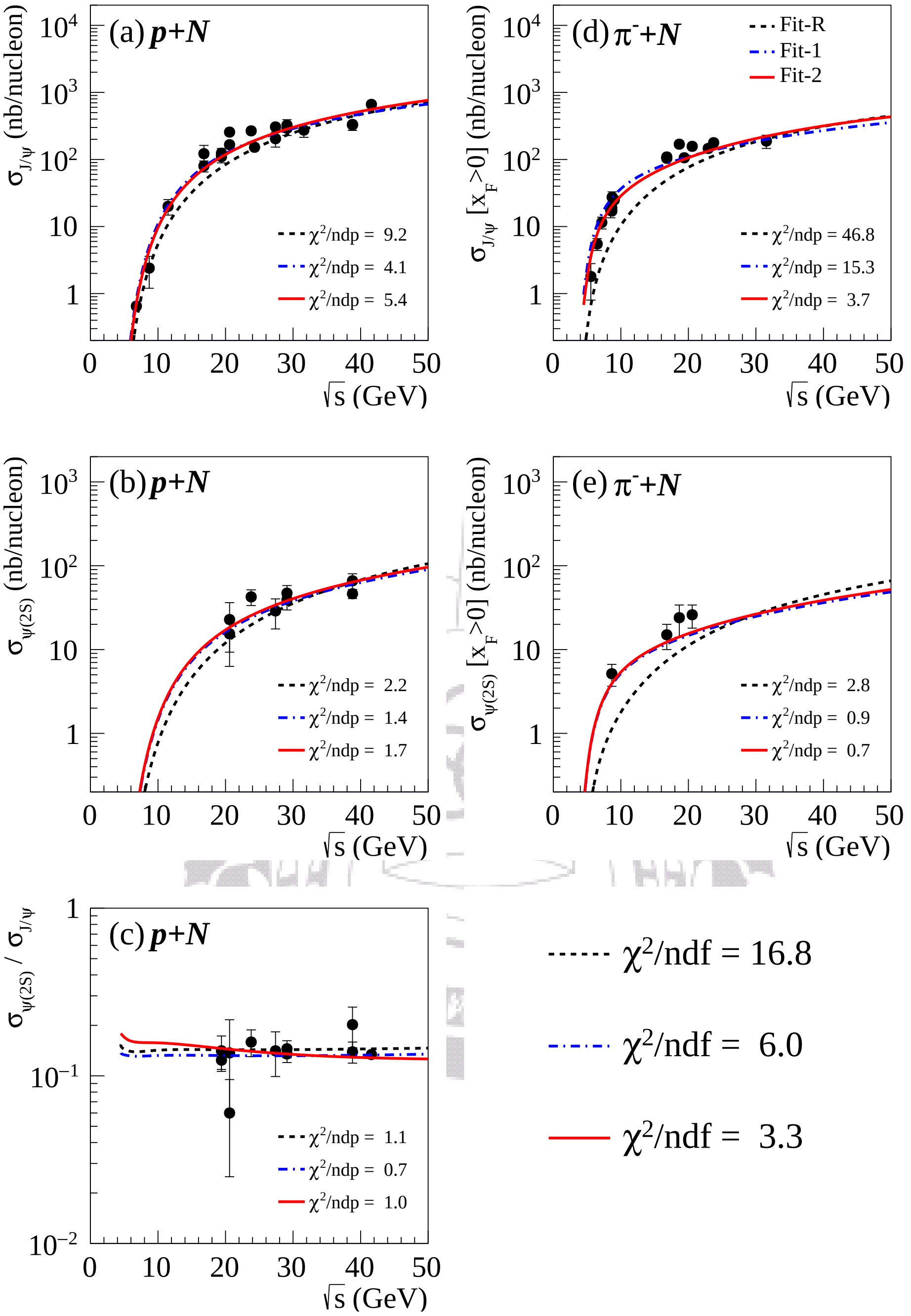

Figure 7.5: The J/ψ and $\psi(2S)$ production cross-sections in both proton- and pion-induced processes and also the cross-section ratio of $R_\psi = \sigma_{\psi(2S)}/\sigma_{J/\psi}$ from proton-induced data. The dashed (black), dot-dashed (blue) and solid (red) curves represent the NRQCD calculation by using LDMEs obtained in "Fit-R", "Fit-1" and "Fit-2" approaches, respectively. The reduced χ^2/ndf for all data are displayed in the bottom-right. The values of χ^2 divided by the number of data point (ndp) for each data set are also shown.

study for the J/ψ production cross-section in different m_c and μ setting are shown in Fig. 7.6. It's clear to see that the initial setting of charm quark mass m_c plays a significant role in the global fit analysis of the NRQCD calculation. The gg contribution is enhanced to much with m_c reduced to 1.2 GeV/c^2, which means the color-octet LDMEs as free parameters cannot not well constrained. In the m_c set to 1.5 GeV/c^2, the global fits are stable in different set of normalization scale μ among m_c, $2m_c$ and $3m_c$.

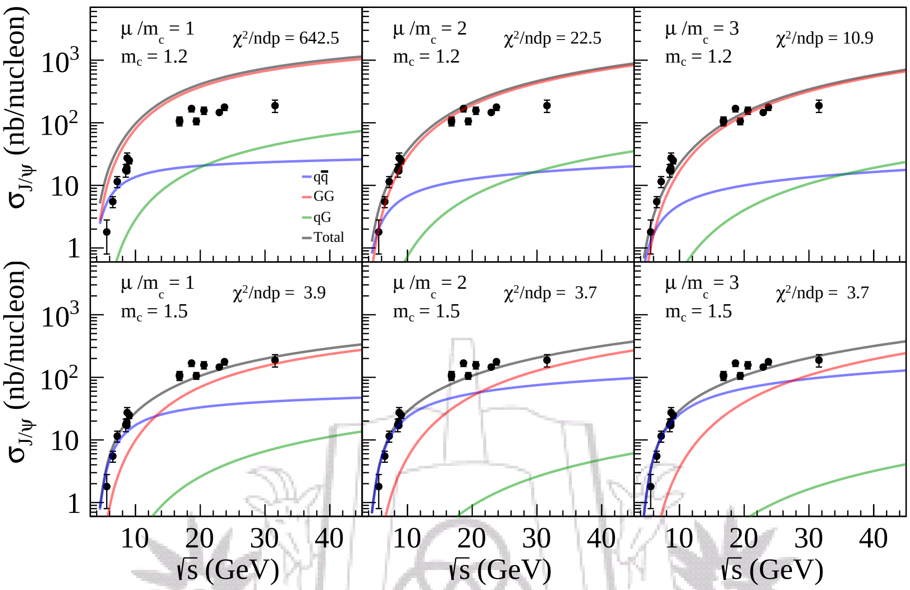

Figure 7.6: The J/ψ production cross-sections as a function of $\sqrt{s}$ in pion-induced data compare with the NRQCD calculation under variation of charm quark mass m_c, renormalization scale μ_R and factorization scale μ_F. The total cross sections in $q\bar{q}$, gg, qg and total contributions are denoted as blue, red, green and black lines, respectively. The values of m_c, $\mu = \mu_R = \mu_F$ in the NRQCD calculation as well as the best-fit χ^2/ndp are displayed in each plot.

7.6 Individual Contributions in Charmonium Production

In order to better understand the reasons for the improvement of the J/ψ and $\psi(2S)$ production cross-sections consistency between measurement and calculation, the decomposition of the J/ψ production cross-sections into individual contributions is a good start point. The individual contributions can be described in three fashions:

1. **Different sub-processes**: $q\bar{q}$, gg and qg sub-processes.

2. **Different color state**: color-singlet and color-octet states.

3. **Different charmonium state**: direct production of J/ψ and feed-down J/ψ from $\psi(2S)$ or χ_c

Fig. 7.7 shows the decomposition of J/ψ production cross-sections for both proton- and pion-induced interactions into the $q\bar{q}$, gg and qg sub-processes. The qg contributions remain unchanged in the "Fit-2" approach since the LDMEs for χ_{c0} are identical between "Fit-R" and "Fit-2". It's clear to see that the gg contribution is dominant in the J/ψ production with proton-induced data at all energies, except near the threshold. Additionally, the $q\bar{q}$ contribution for pion-induced data is significantly increased due to the enhancement of antiquark contribution in pion's valence region, which proof that the global fit will provides additional constraints on those $q\bar{q}$ contribution related LDMEs by including the pion-induced data. In particular, the low-energy fixed-target pion-induced data are very important for the determination of the color-octet LDMEs $\langle O_8^H(^3S_1)\rangle$.

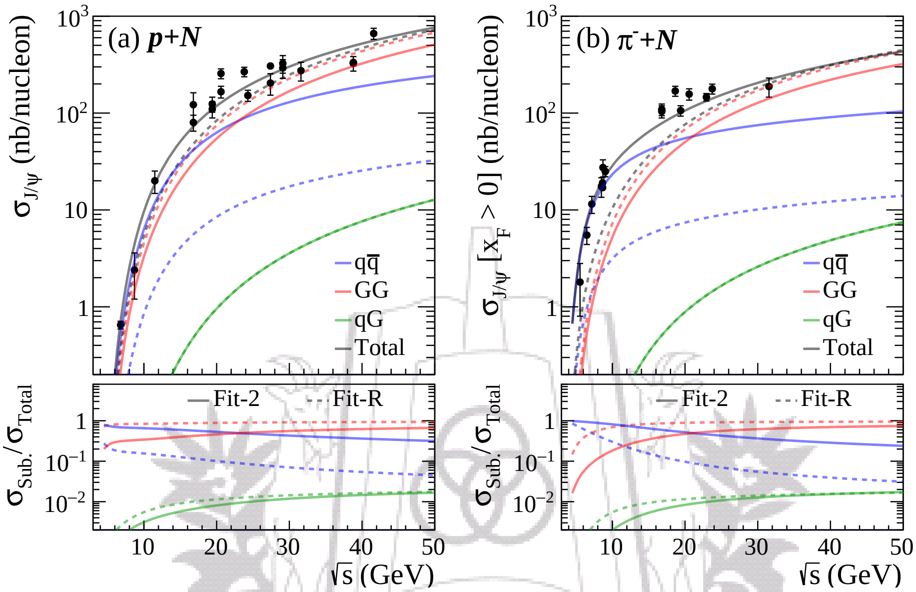

Figure 7.7: The total J/ψ production cross-sections (black) and contributions from $q\bar{q}$ (blue), gg (red) and qg (green) processes as a function of $\sqrt{s}$ in (a) proton- and (b) pion-induced interactions. The dashed and solid curves represent the "Fit-R" and "Fit-2" results. The bottom of each plot displayed the fractions of each sub-process cross-section to the total cross-section.

Fig. 7.8 shows the decomposition of J/ψ production cross-sections for both proton- and pion-induced interactions into the color-singlet and color-octet states. The color-singlet state contributions remain unchanged in the "Fit-2" approach since the LDMEs for color-singlet state are identical between "Fit-R" and "Fit-2". It's clear to see that the color-octet state contribution is increased at low energies but decreased at high energies, which are caused by the enlarged LDMEs $\langle O_8^H(^3S_1)\rangle$ and reduced LDMEs Δ_8^H in "Fit-2" approach, respectively.

Fig. 7.9 shows the decomposition of J/ψ production cross-sections for both proton- and pion-induced interactions into the contributions from direct production of J/ψ or feed-down from $\psi(2S)$ or χ_c states. The feed-down contributions from χ_c states remain unchanged in the "Fit-2" approach since the LDMEs for χ_{c0} are identical between "Fit-R" and "Fit-2". The most significant changes between the calculations with "Fit-R" and "Fit-2" approaches is the enhancement of the direct J/ψ production in pion-induced data at low energies, which caused by the enlarged LDMEs $\langle O_8^H(^3S_1)\rangle$.

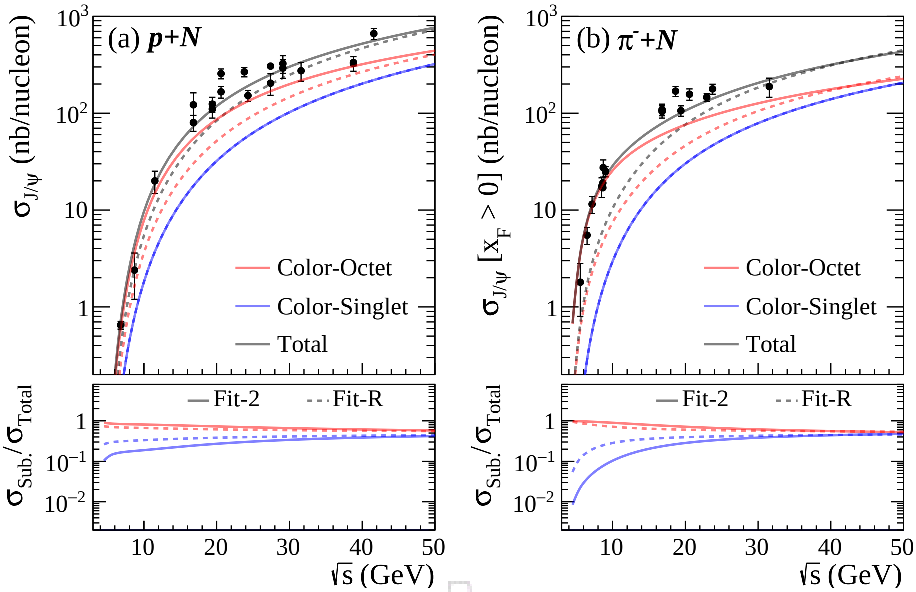

Figure 7.8: The total J/ψ production cross-sections (black) and contributions from color-singlet (blue) and color-octet (red) states as a function of $\sqrt{s}$ in (a) proton- and (b) pion-induced interactions. The dashed and solid curves represent the "Fit-R" and "Fit-2" results. The bottom of each plot displayed the fractions of each sub-process cross-section to the total cross-section.

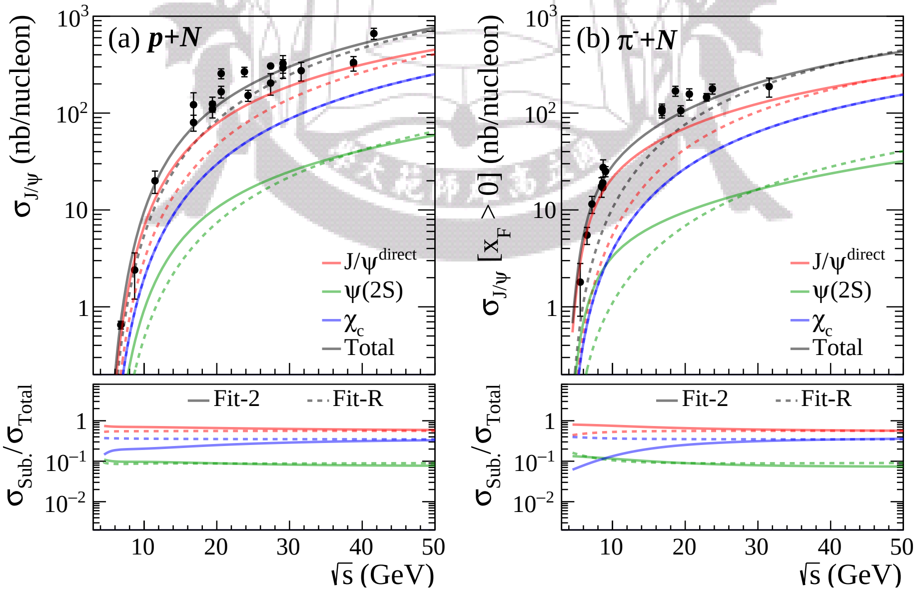

Figure 7.9: The total J/ψ production cross-sections (black) and contributions from direct production of J/ψ (red) and feed-down from $\psi(2S)$ (green) or all χ_c states (blue) as a function of $\sqrt{s}$ in (a) proton- and (b) pion-induced interactions. The dashed and solid curves represent the "Fit-R" and "Fit-2" results. The bottom of each plot displayed the fractions of each sub-process cross-section to the total cross-section.

7.7 Sensitivity to the Pion PDFs in the NRQCD Calculation

Using the new set of LDMEs from the improved global fit in "Fit-2" approach, the sensitivity of the J/ψ production cross-section to the pion PDFs in the NRQCD calculation can be reviewed.

Fig. 7.10 shows the J/ψ production cross-section in pion-induced data compare with the NRQCD calculation by using four different pion PDFs: SMRS [69], GRV [70], JAM [71] and xFitter [72]. In general, the total J/ψ production cross-section in pion-induced interaction for the four different pion PDFs shows similar result as a function of $\sqrt{s}$. However, the individual terms contribution are quite different. In case of SMRS and GRV pion PDFs, the gg contribution starts to dominate the total J/ψ cross-section around $\sqrt{s}$ = 20 GeV, while in case of JAM and xFitter pion PDFs, the gg contribution starts to dominate the total J/ψ cross-section around $\sqrt{s}$ = 35 GeV. This is cause by the relatively reduced gluon strength in the valence region in JAM and xFitter pion PDFs with respect to SMRS and GRV. The gg contributions are similar for GRV and SMRS, while those for xFitter and JAM are 50-80% smaller due to their weaker gluon density, which lead to an underestimation of the NRQCD calculations by using JAM and xFitter pion PDFs.

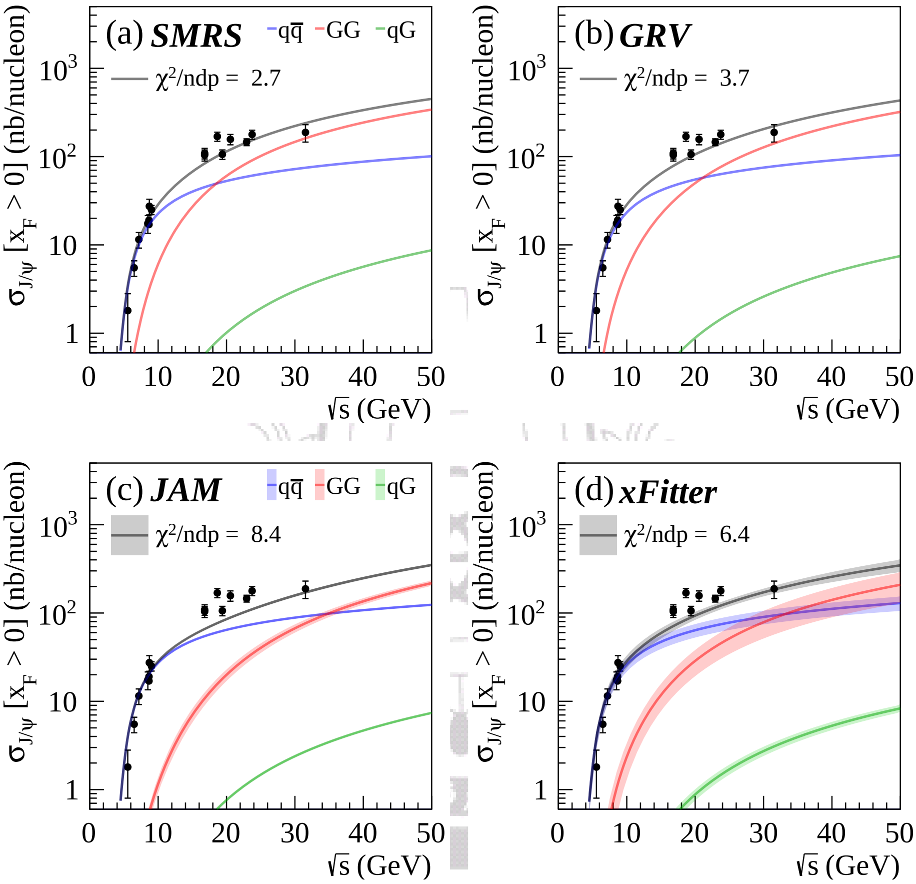

Figure 7.10: The J/ψ production cross-sections at $x_F > 0$ for the pion-induced data compare with the NRQCD calculation, which calculated form four different pion PDFs (SMRS, GRV, JAM and xFitter) using LDMEs of "Fit-2". The black, blue, red and green curves represent the calculated total cross-sections, and the $q\bar{q}$, gg, and qg contributions, respectively. The shaded bands on the JAM and xFitter calculations come from the uncertainties of the corresponding PDF sets. The SMRS and GRV PDFs contain no information on uncertainties.

CHAPTER 8

Conclusion and Future Prospect

COMPASS is a high-energy physics fixed-target experiment at the CERN M2 beam line. The exploration of the transverse spin structure of the nucleon is one of the main topics of the COMPASS phase-II experiment. In 2015 and 2018 COMPASS performed Drell–Yan measurements using a 190 GeV π^- beam interacting with a transversely polarized NH_3 target and unpolarized W target. Preliminary results on the Sivers asymmetry are consistent with the QCD prediction for a sign-change of Sivers functions in Drell–Yan process. The angular coefficients λ, μ and ν that describe the unpolarized part of the Drell–Yan cross-section have been extracted from the data collected with W target. The preliminary results on the angular coefficients indicate the violation of the Lam–Tung relation, consistent with the observation in earlier Drell–Yan experiments with pion beams. A comparison between the COMPASS preliminary results on the ν coefficient with perturbative QCD calculation suggests possible contributions from other non-perturbative QCD sources, such as the Boer–Mulders functions.

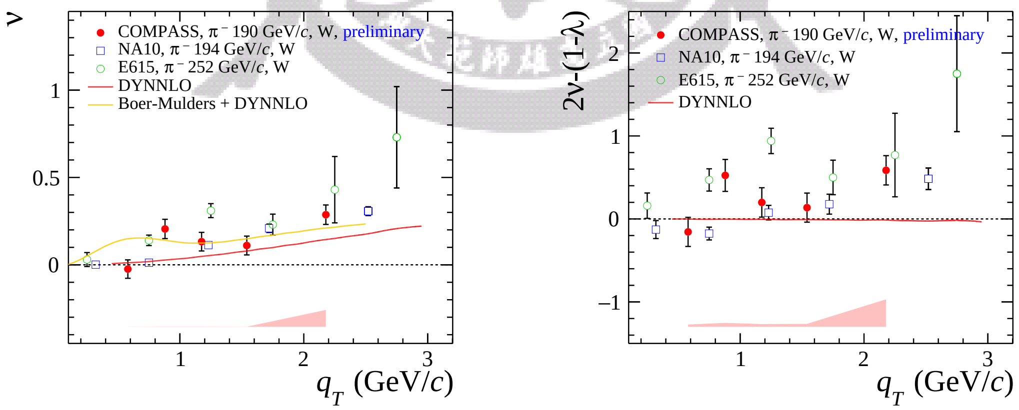

This thesis performs a complete study of Drell–Yan unpolarized asymmetries measured by COMPASS for both NH_3 and W targets. The first preliminary result of Drell–Yan unpolarized asymmetries in W target from COMPASS measurement have been released at April 2021. But the result from NH_3 target is not released yet because of the observation of a factor of two difference in the ν asymmetries. Before the publication of Drell–Yan unpolarized asymmetries for both NH_3 and W targets, there is still a room of improvement for MC simulation chain such as complete period-by-period two-dimensional detectors efficiencies maps. Probably the puzzle of ν asymmetries difference between NH_3 and W targets will be answered after the improvement of acceptance estimation. Furthermore, this analysis framework can be extended for the study of J/ψ unpolarized angular coefficients.

Appendices

APPENDIX A

Estimation of Hodoscopes Efficiencies

The smoothed two-dimensional hodoscope efficiencies from all of periods in 2018 are shown in Fig. A.1-A.10.

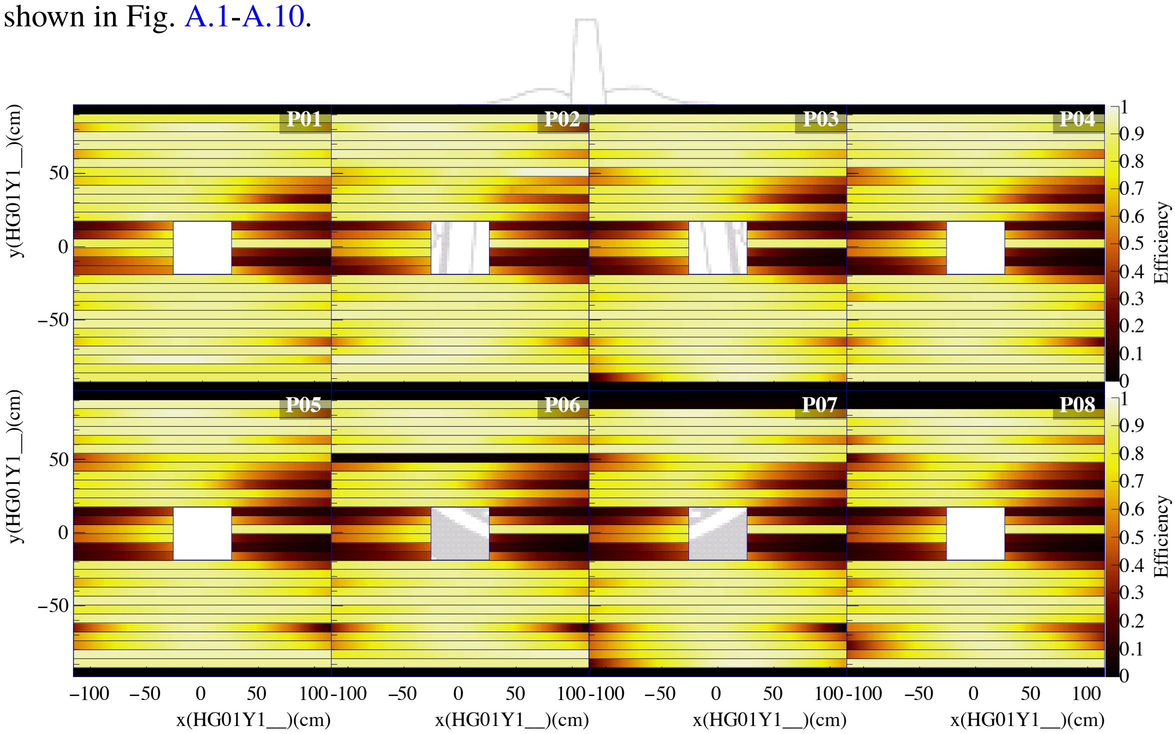

Figure A.1: The HG01Y1 hodoscope efficiencies during 2018 data taking.

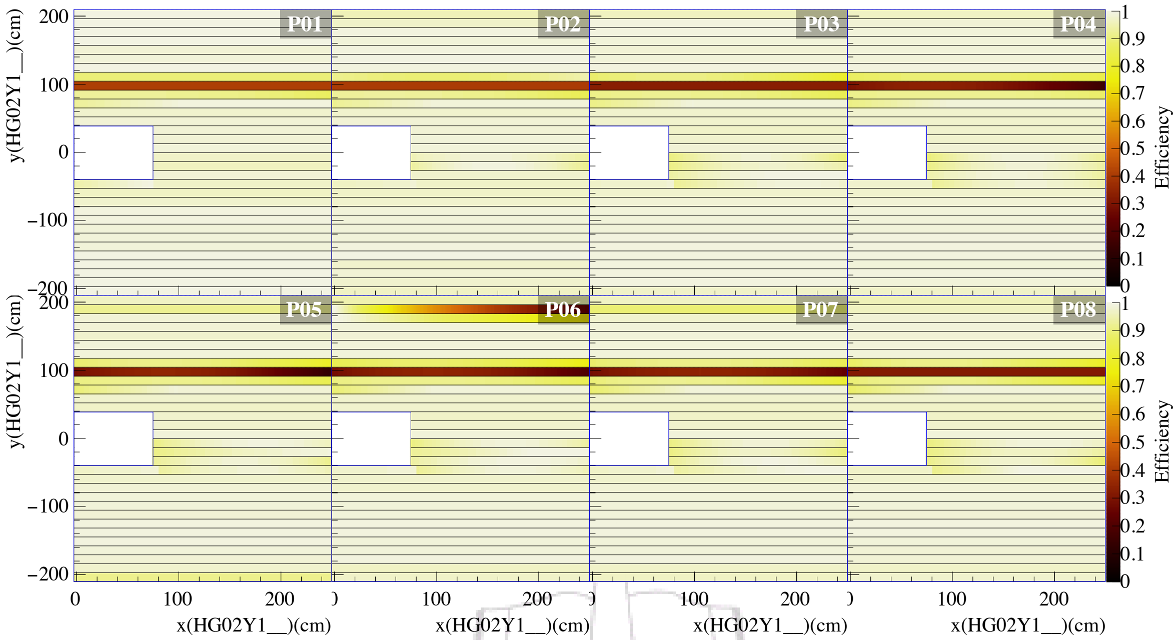

Figure A.2: The HG02Y1 hodoscope efficiencies during 2018 data taking.

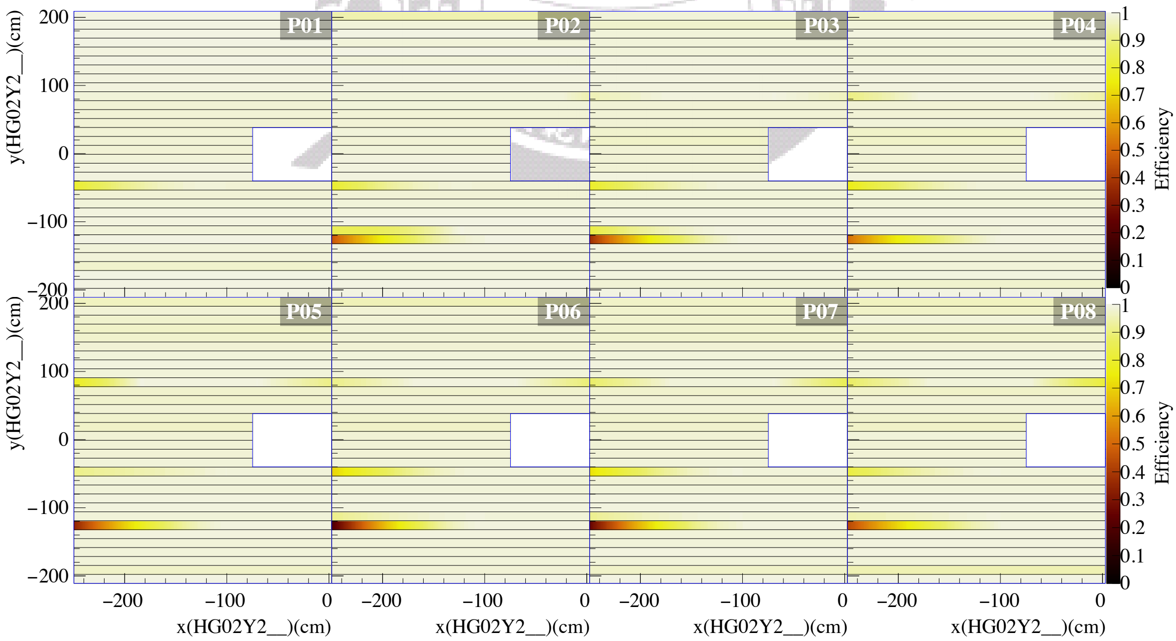

Figure A.3: The HG02Y2 hodoscope efficiencies during 2018 data taking.

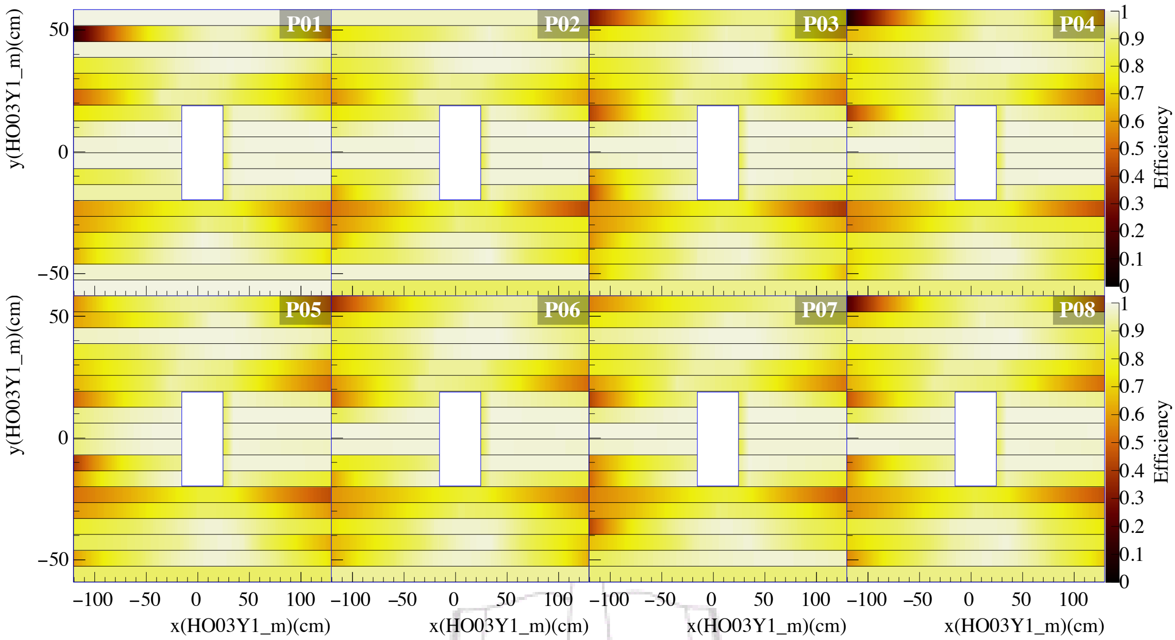

Figure A.4: The HO03Y1 hodoscope efficiencies during 2018 data taking.

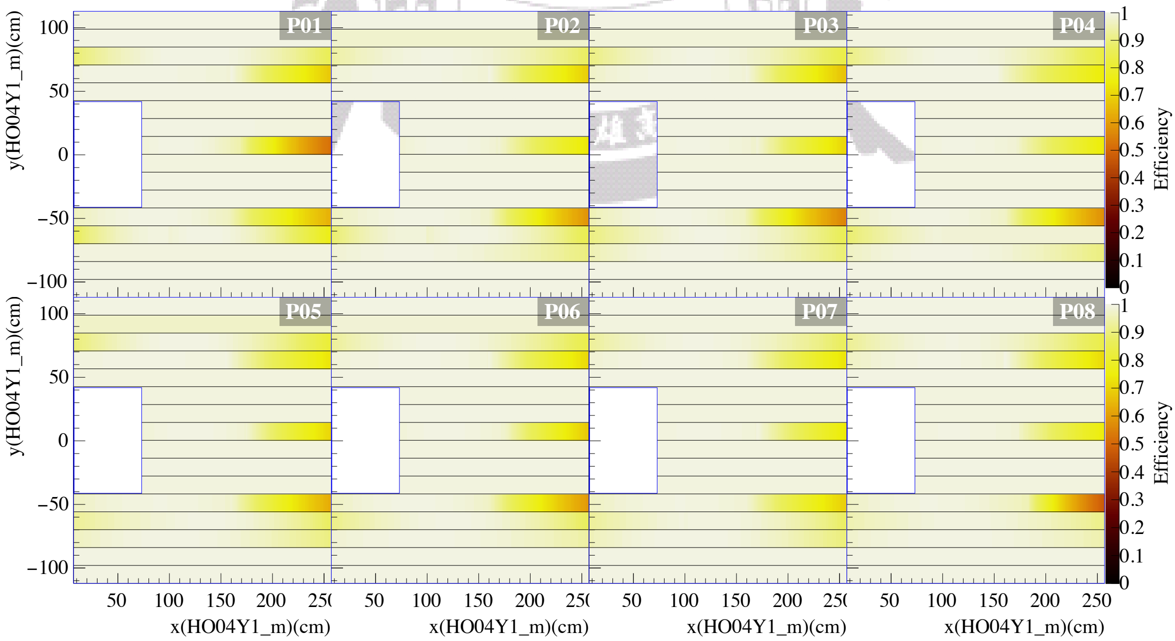

Figure A.5: The HO04Y1 hodoscope efficiencies during 2018 data taking.

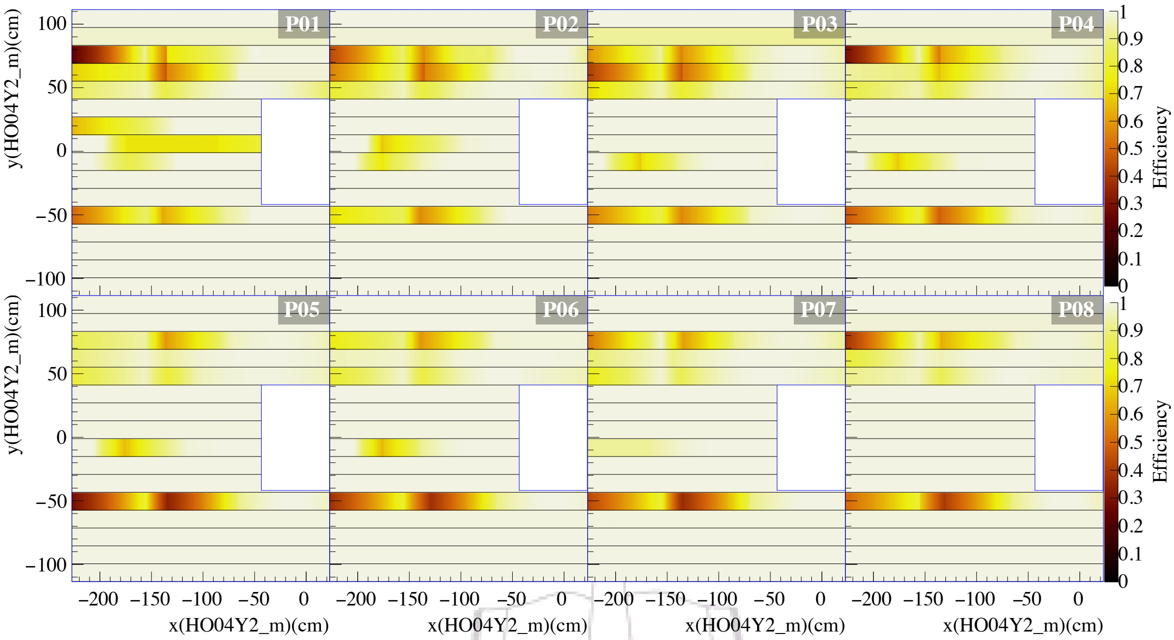

Figure A.6: The HO04Y2 hodoscope efficiencies during 2018 data taking.

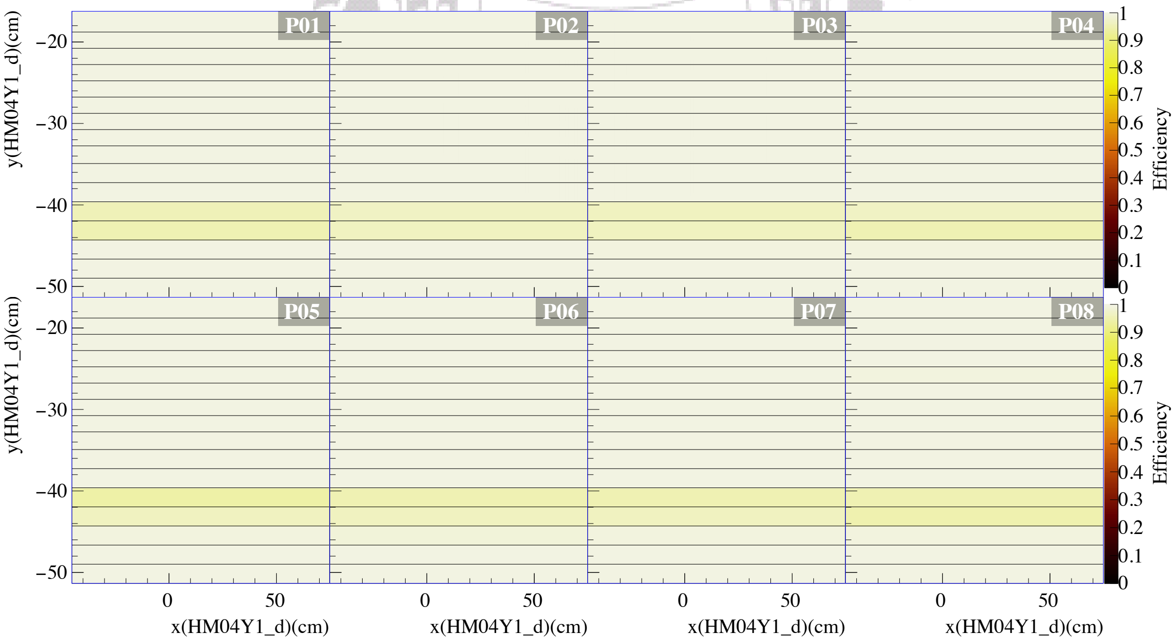

Figure A.7: The HM04Yd hodoscope efficiencies during 2018 data taking.

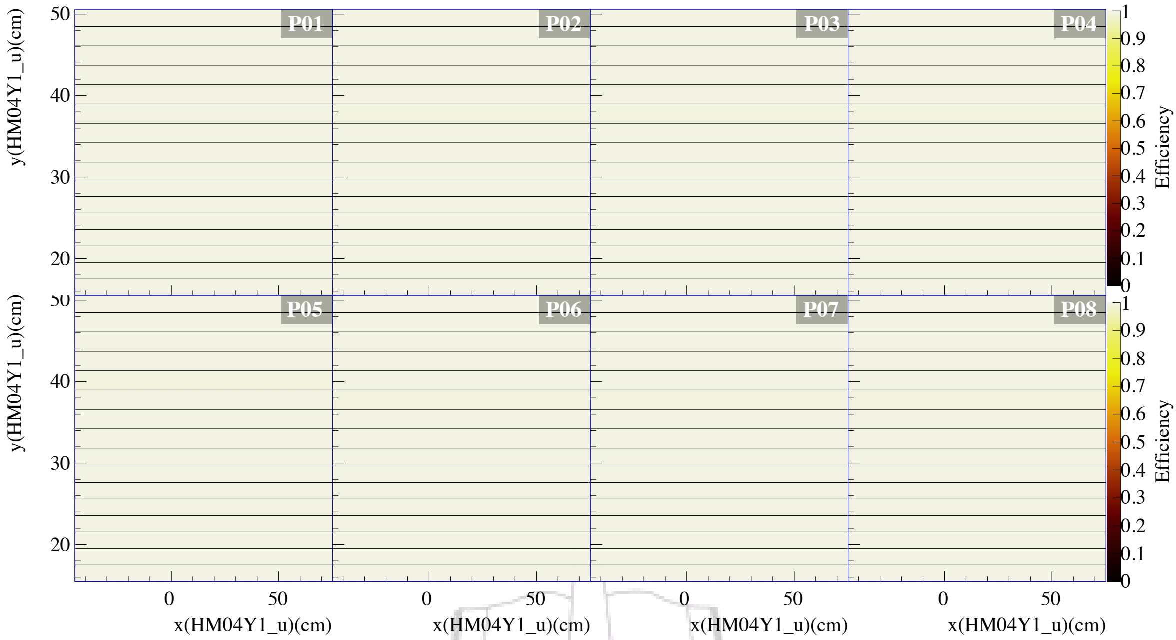

Figure A.8: The HM04Yu hodoscope efficiencies during 2018 data taking.

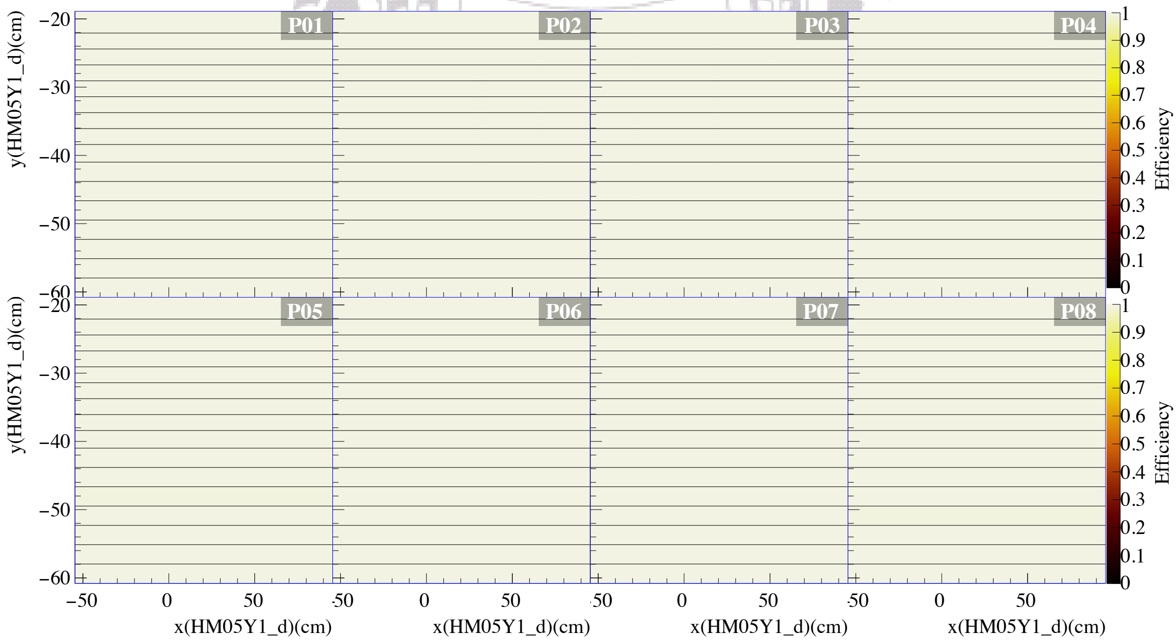

Figure A.9: The HM05Yd hodoscope efficiencies during 2018 data taking.

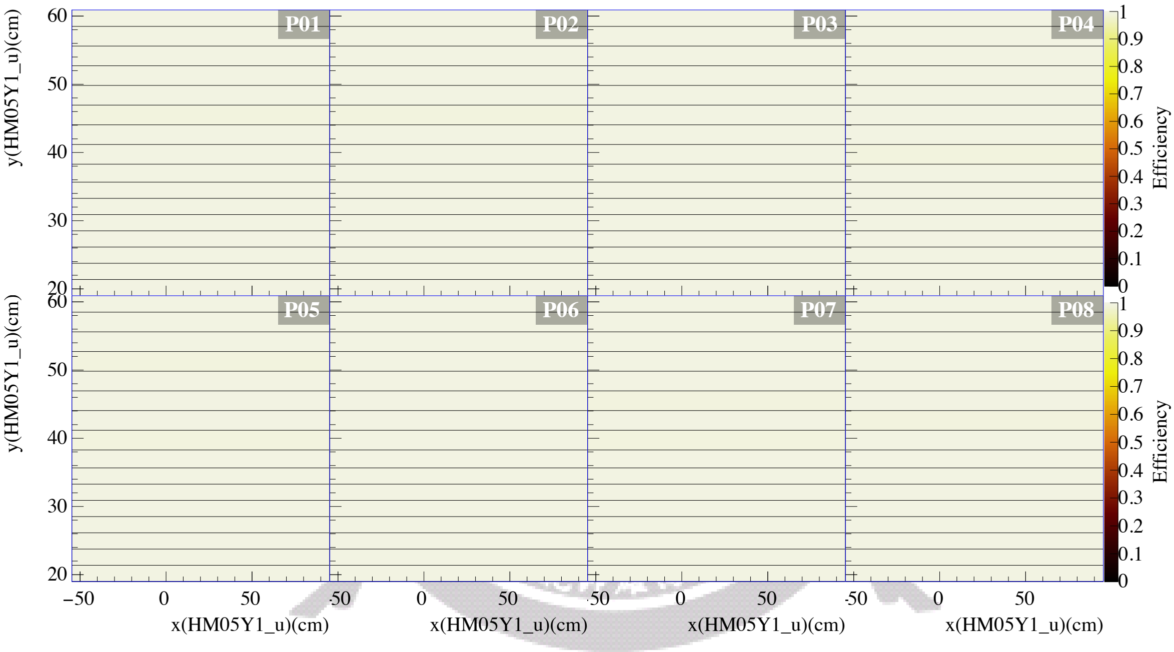

Figure A.10: The HM05Yu hodoscope efficiencies during 2018 data taking.

APPENDIX B

Estimation of Coincidence Matrix Efficiencies

The coincidence matrix efficiencies from all of periods during 2018 data taking are shown in Fig. B.1-B.4.

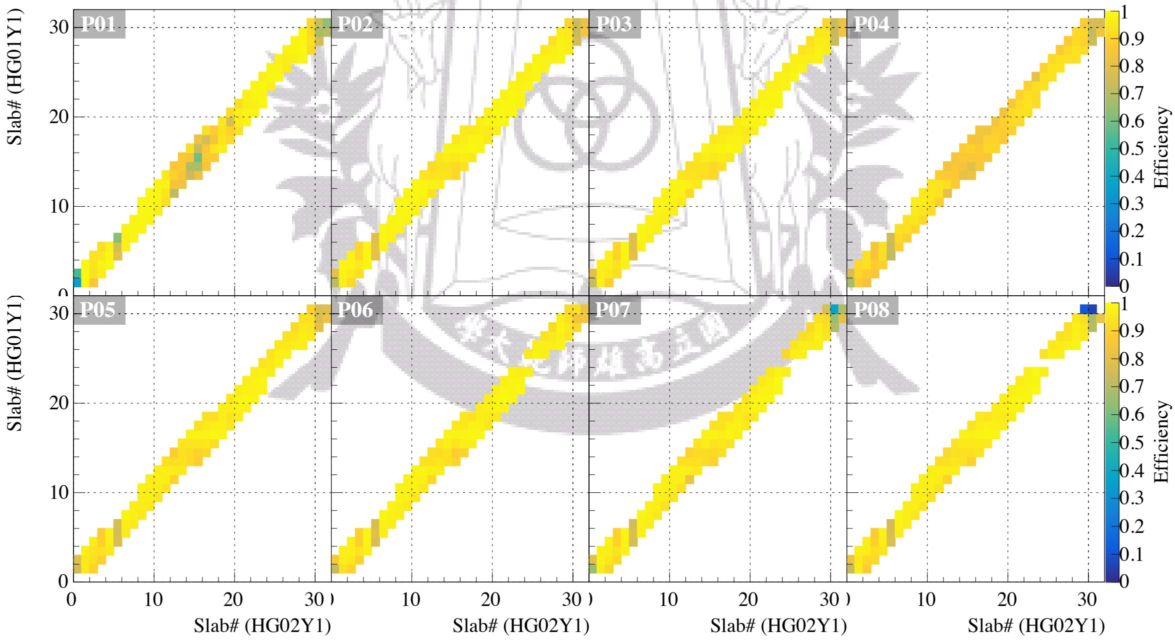

Figure B.1: The efficiencies of LAST1 coincidence matrices during 2018 data taking.

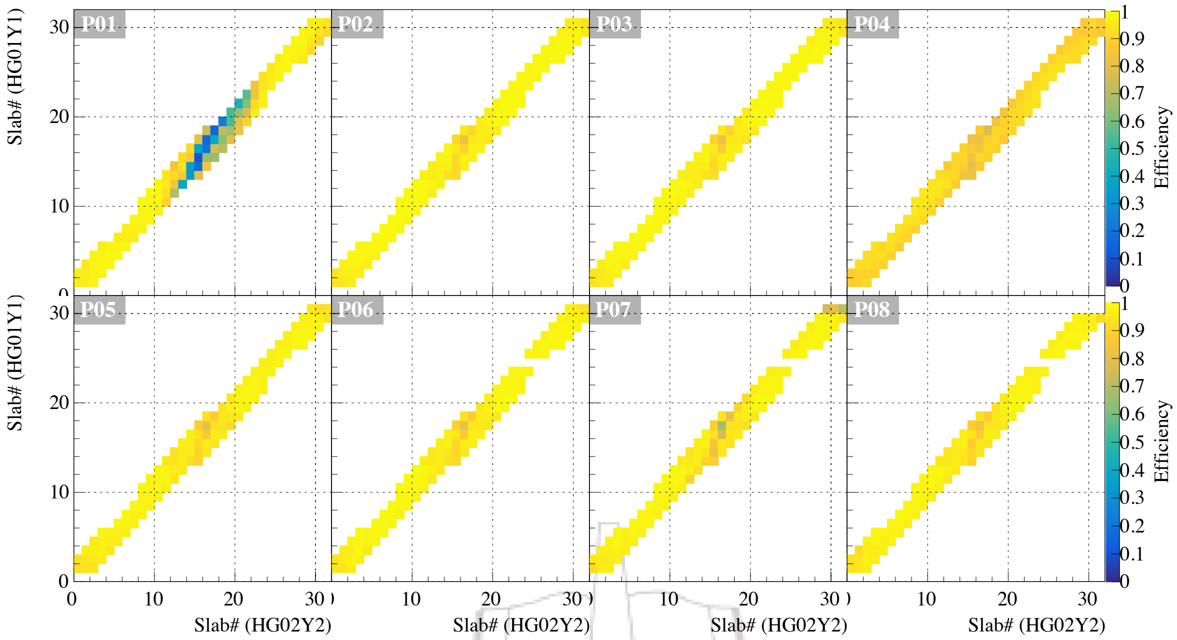

Figure B.2: The efficiencies of LAST2 coincidence matrices during 2018 data taking.

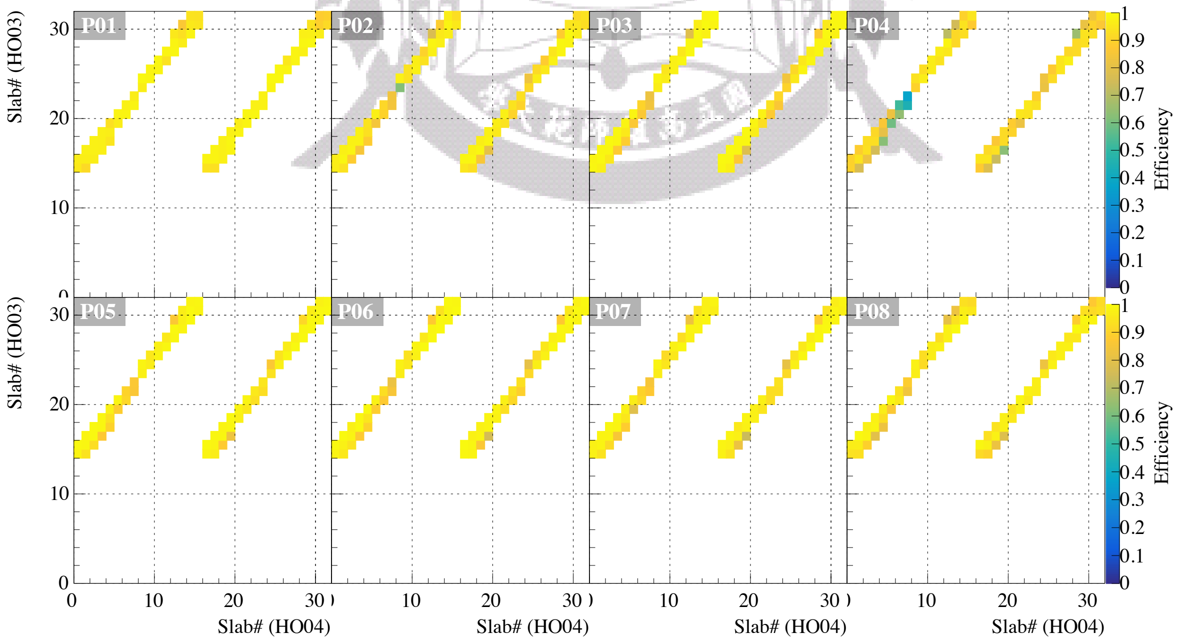

Figure B.3: The efficiencies of OT coincidence matrices during 2018 data taking.

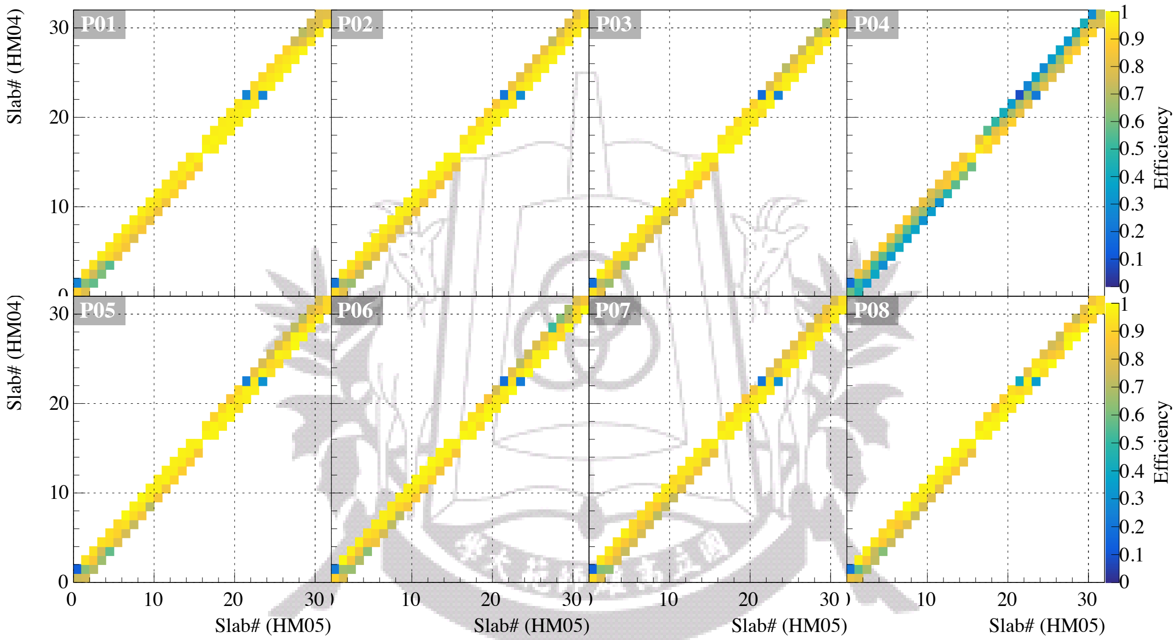

Figure B.4: The efficiencies of MT coincidence matrices during 2018 data taking.

APPENDIX C

Estimation of Systematic Uncertainties

In this chapter, the possible systematic uncertainties on the extraction of Drell–Yan unpolarized asymmetries will be demonstrated, as their are assessed up to now. Certain aspects of the data analysis (including the evaluation of systematic uncertainties) require considerable computing resources and processing time and are not fully accomplished yet.

C.1 Compatibility of the results obtained from different periods

For *test-8* production data the compatibility of the results from different periods is checked using period-by-period MC samples for acceptance evaluation to correct each of periods individually. This study is meant to account not only for detector and trigger performances that change from period to period, but also for the variations of beam properties, detectors alignment etc. The definition of pull distribution for the compatibility of the unpolarized asymmetries results obtained from different periods and different kinematics bins are:

$$\text{Pull} = \frac{(A_i - \bar{A})}{\sqrt{\sigma^2_{A,i} - \sigma^2_{\bar{A}}}} \tag{C.1}$$

where A represent each unpolarized asymmetries value and the index i represent the period and kinematics bin. To include also different kinematics bin is because only 8 out of 9 periods (P01,P02, P03, P04, P05, P06, P07 and P08) are considered in this study which is too limited to perform a pull distribution. The definition of *overall* systematic uncertainties over statistical uncertainties by the pull method is:

$$\frac{\sigma^{\text{Period}}_{\text{Syst.}}}{\sigma_{\text{Stat.}}} \equiv \sqrt{\left[\text{Max}(1, \sigma_{\text{pull}}) + \text{d}\sigma_{\text{pull}}\right]^2 - 1} \tag{C.2}$$

where p_{pull} represent the mean value of pull distribution, σ_{pull} represent the sigma width of pull distribution, $\text{d}\sigma_{\text{pull}}$ represent the uncertainty of sigma width of pull distribution given by the Gaussian fit. The results of pull distribution form NH_3 and W targets are shown in Figure C.1a and Figure C.1b, respectively.

However, the pull method for the estimation of systematic uncertainties remains some difficulties and doubts. For instance, how to deal with the additional systematic effect caused by the bin size of pull distribution and also the lack of entries? How to properly define the expected true value for the pull distribution? Is it true that the overall systematic uncertainties are equally contributed to each kinematics bins? Building on that, a new method, *unconstrained averaging*, for the estimation of systematic uncertainties from period variation is proposed.

As mention in Eq 6.9, the final reported asymmetries from different periods are merged by weighting average method. An example of measured λ in certain kinematics bin, in NH_3 target and in Collins–Soper, Gottfried–Jackson and Helicity frame from each period is shown in Figure C.2.

The propagated error from the weighting averaged method is defined as following:

$$\delta\bar{A} = \frac{1}{\sqrt{\sum_i w_i}} \tag{C.3}$$

The compatibility of each measurement i can be tested and calculated by χ^2 test:

$$\chi^2/(N-1) = \frac{\sum_i w_i(\bar{A} - A_i)^2}{N-1} \tag{C.4}$$

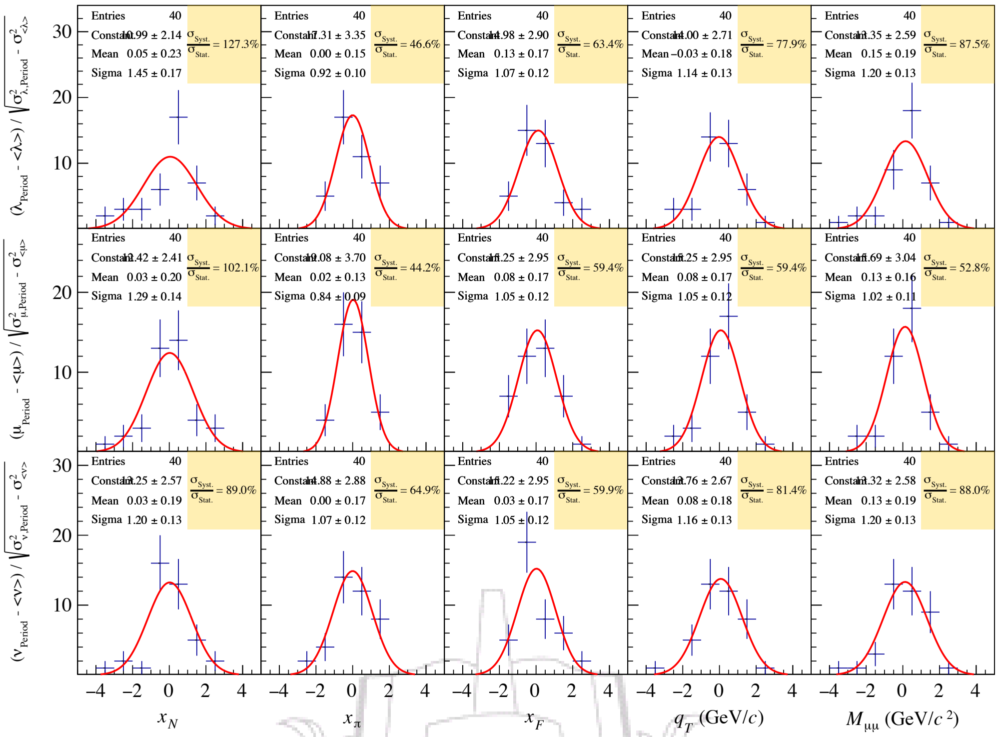

(a) NH_3 target

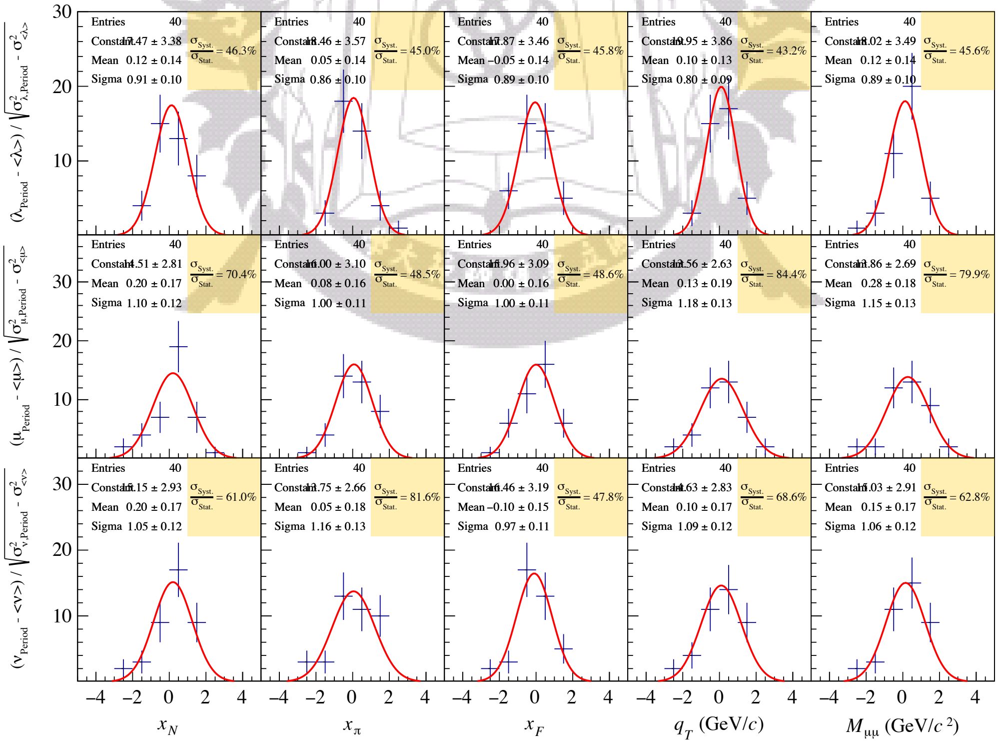

(b) W target

Figure C.1: The pull distribution and estimated systematic uncertainties for λ, μ and ν extraction in Collins–Soper, Gottfried–Jackson and Helicity frame from period compatibility.

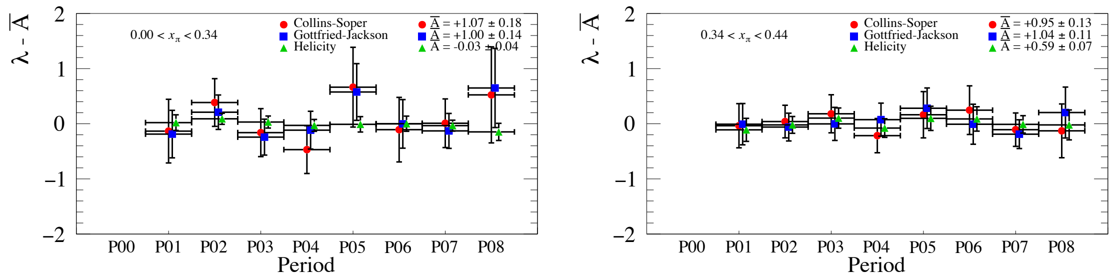

(a) $0.00 < x_\pi < 0.34$ (b) $0.34 < x_\pi < 0.44$

Figure C.2: An example of measured λ in NH_3 target and in Collins–Soper, Gottfried–Jackson and Helicity frame from each period.

where N is the total number of measurement, which in this case is number of periods ($N = 8$). The value $\chi^2/(N-1)$ represents the expectation value of χ^2 from N measurements if the measurements are from a Gaussian distribution.

If $\chi^2/(N-1) <= 1$, the result are merged as no known problem existed, so there is NO systematics effect should be reported. If $\chi^2/(N-1) \gg 1$, some serious problems existed and it's better to understand the caused instead of merging the result. If $\chi^2/(N-1) > 1$, some systematic effect existed but not so serious, in this case the systematic uncertainties can be estimated by a scale factor S defined as following:

$$S \equiv \frac{\sigma_{\text{Syst.}}}{\sigma_{\text{Stat.}}} = \sqrt{\chi^2/(N-1)} \tag{C.5}$$

This scale factor S will correct the original statistics error δx_i in case of underestimation ($\chi^2/(N-1) > 1$). If one scale up all the input statistics errors by this scale factor$S$, the propagated total average error scales up by the same factor so that $\chi^2/(N-1) = 1$.

The estimated systematic uncertainties for unpolarized asymmetries result in Collins–Soper, Gottfried–Jackson and Helicity frame from periods compatibility in NH_3 and W targets are summarized in Figure C.3a and Figure C.3b, respectively. The estimated systematic uncertainties are extracted frame-by-frame and bin-by-bin for each angular coefficient, where 8 out of 9 periods are considered in this study. The result shows that the overall systematic effect from period compatibility is quite small, only certain kinematics bins are visible. This result is adopted and included as the one of contribution of systematic uncertainties.

C.2 Compatibility of the results obtained from different target cells

Providing that the experimental apparatus is satisfactorily well described in MC and assuming that acceptance corrections are done properly, the asymmetries extracted separately for the upstream and downstream cells are expected to be the same. (In the case of W target, the upstream cell refer to the first 10 cm, while the downstream cell refer to the second 10 cm.) Thus, comparing these asymmetries allows to determine if there are biases due to an improper description of the acceptance of the spectrometer in the MC. The result of unpolarized asymmetries for NH_3 and W target in Collins–Soper frame are shown in Figure C.4a and Figure C.4b, respectively.

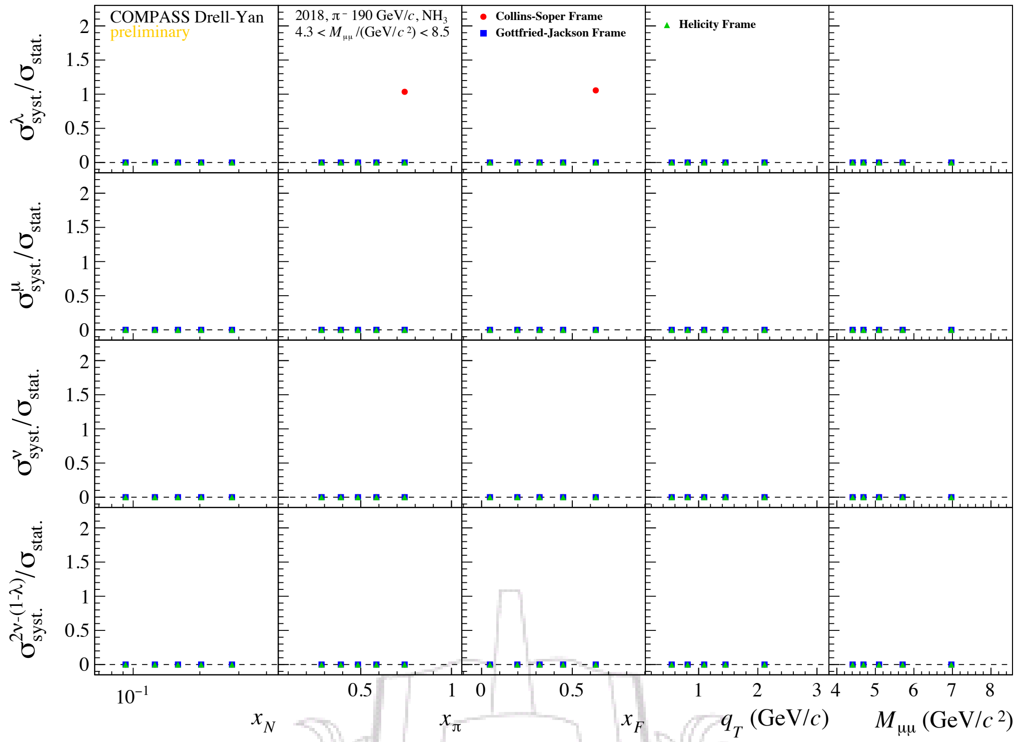

(a) NH_3 target

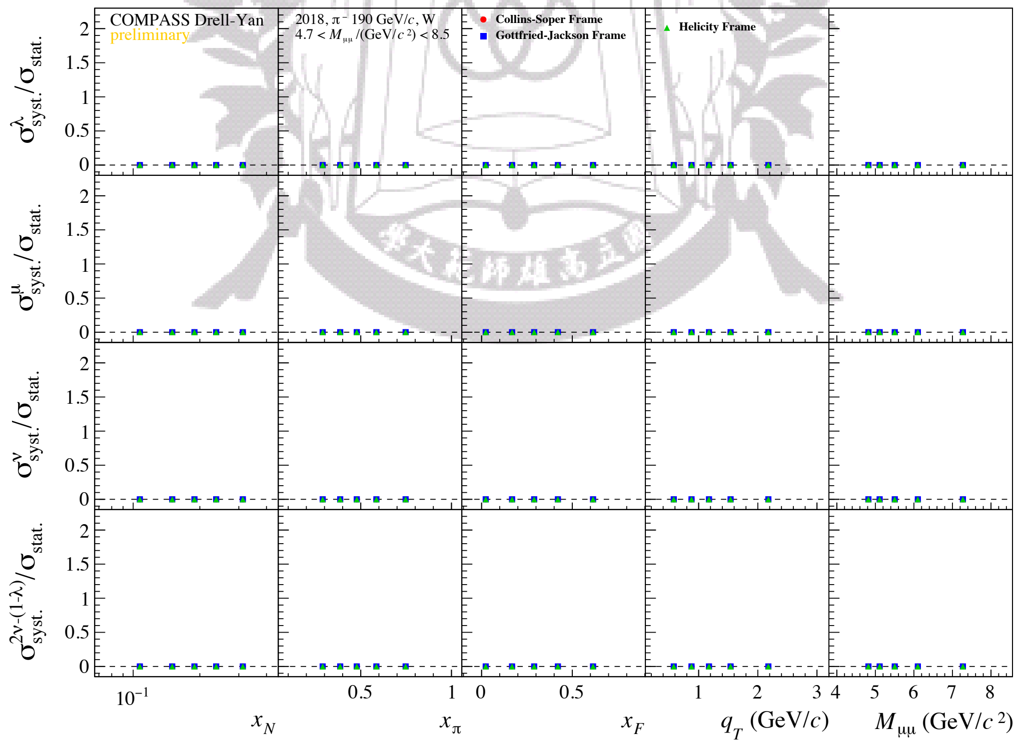

(b) W target

Figure C.3: The estimated systematic uncertainties for unpolarized asymmetries result in Collins–Soper, Gottfried–Jackson and Helicity frame from periods compatibility.

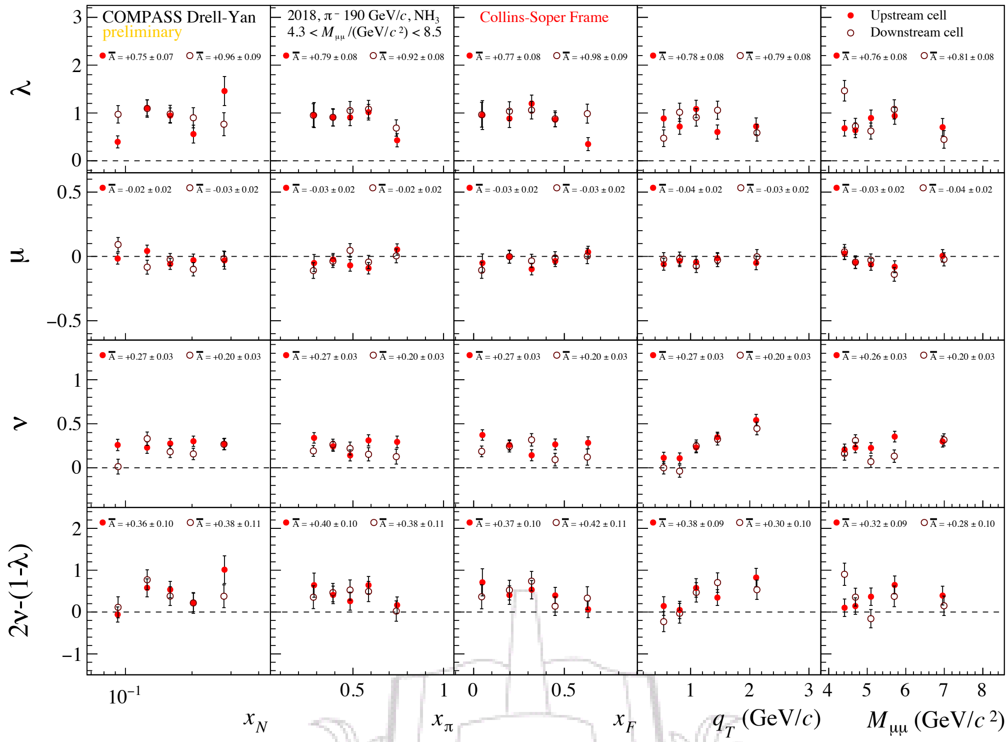

(a) NH$_3$ target

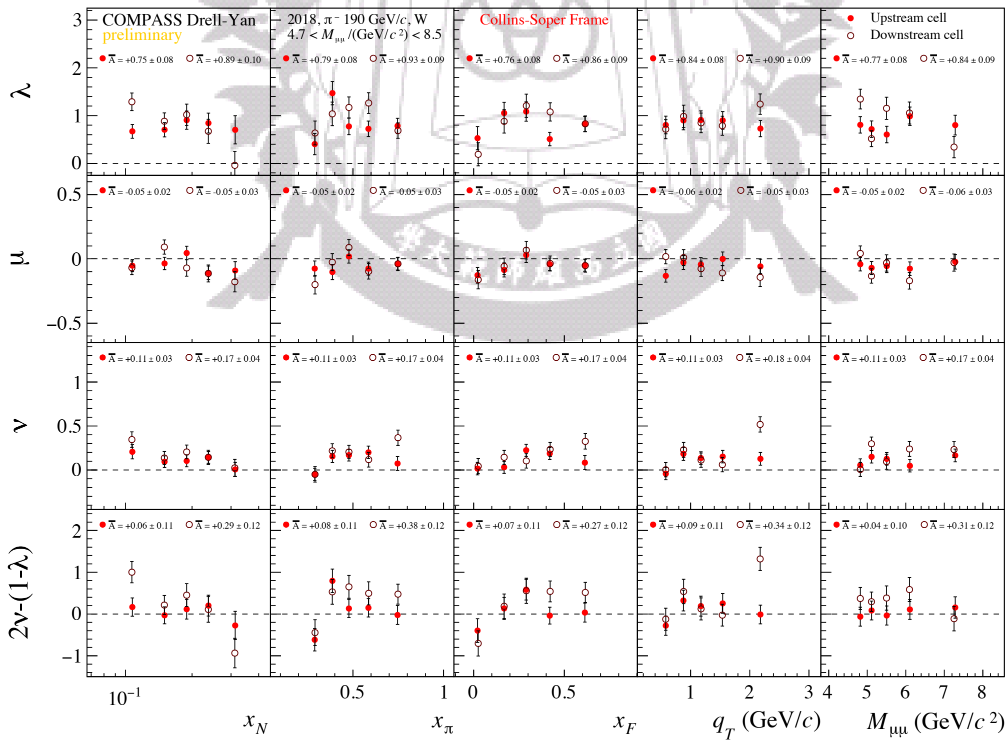

(b) W target

Figure C.4: The result of unpolarized asymmetries for λ, μ and ν extraction in Collins–Soper frame from target cells compatibility.

Due to the significant deviation of λ result between two target cells at some certain kinematics bins, the systematic effect form the incompatibility of different target cells should be taken into account in the final systematic uncertainties. The estimation of systematic uncertainties form the incompatibility of unpolarized asymmetries results obtained from different target cells is following the same approach as period compatibility, namely unconstrained averaging test (see Eq. C.5).

The estimated systematic uncertainties for NH_3 and W target are summarised in Figure C.5a and Figure C.5b, respectively.

C.3 Compatibility of the results obtained from different trigger priority

Providing that the experimental apparatus, especially trigger system, is satisfactorily well described in MC and assuming that acceptance corrections are done properly. Base on the extended histogram binned likelihood extraction method (see Section 6.4), the events from two triggers are separately filled into different $\cos\theta$ region. If an event satisfied both triggers criteria (both triggers fired), it will filled into only one of $\cos\theta$ region base on trigger priority setting. The asymmetries extracted separately for the different trigger priority setting are expected to be the same. The result of unpolarized asymmetries for NH_3 and W target in Collins–Soper frame from different trigger priority setting are shown in Figure C.4a and Figure C.4b, respectively.

Due to the visible deviation of λ result between two trigger priority approach in W target, the systematic effect form the incompatibility of different trigger priority should be taken into account in the final systematic uncertainties. The definition of relative systematic uncertainties form the incompatibility of unpolarized asymmetries results obtained from different trigger priority is:

$$\frac{\sigma^{\text{Trigger}}_{\text{Syst.}}}{\sigma_{\text{Stat.}}} \equiv \frac{\left|a_{\text{LAST-LAST},i} - a_{\text{OT-LAST},i}\right|}{\sigma_{\text{LAST-LAST},i}} \tag{C.6}$$

where index i represent kinematics bin, $a_{\text{LAST-LAST},i}$ and $a_{\text{OT-LAST},i}$ represent the mean value of unpolarized asymmetries from LAST–LAST trigger priority and OT–LAST trigger priority, $\sigma_{\text{LAST-LAST},i}$ and $\sigma_{\text{OT-LAST},i}$ represent the statistical error of unpolarized asymmetries from LAST–LAST trigger priority and OT–LAST trigger priority.

The estimated relative systematic uncertainties for NH_3 and W target are summarised in Figure C.7a and Figure C.7b, respectively.

C.4 Systematic of different q_T cut

As mention in Chapter 5, the dimuon q_T have been applied a maximum cut: 3 GeV/$c$in order to keep a good agreement between real data and MC. Compare the final unpolarized asymmetries extraction result with applying lower q_T cut: 2.5 GeV/c, the comparison plots are shown in Figure C.8a for NH_3 target and Figure C.8b for W target. The comparison plot shows the result are stable with lower q_T limit for both targets. In conclusion, there is no systematic uncertainties from this test.

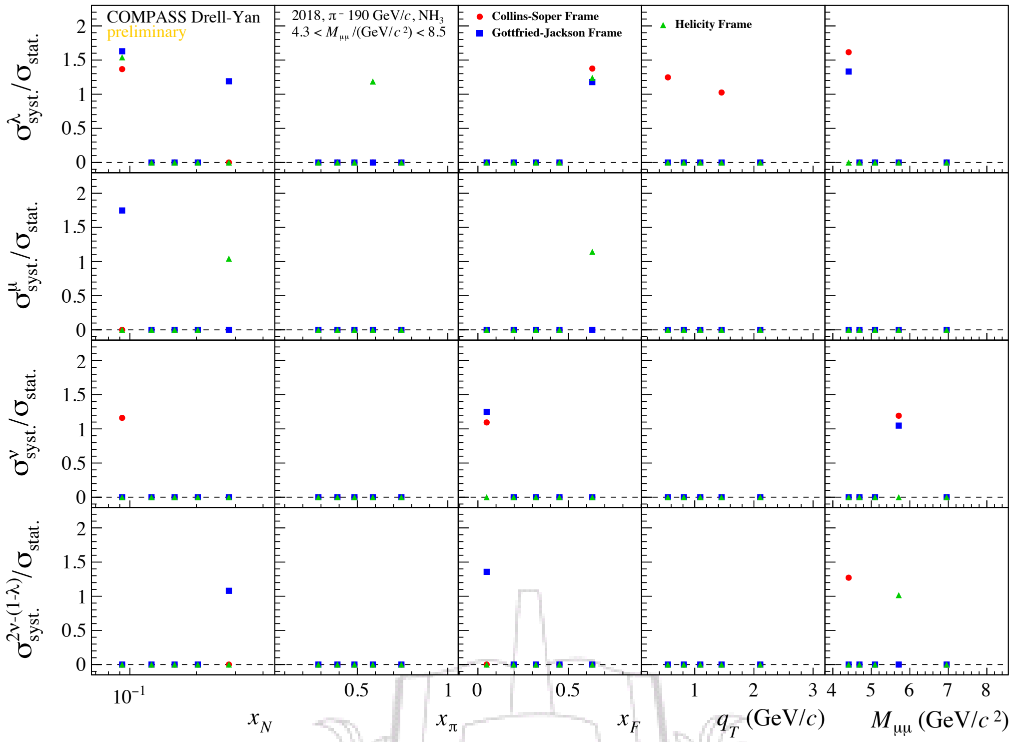

(a) NH_3 target

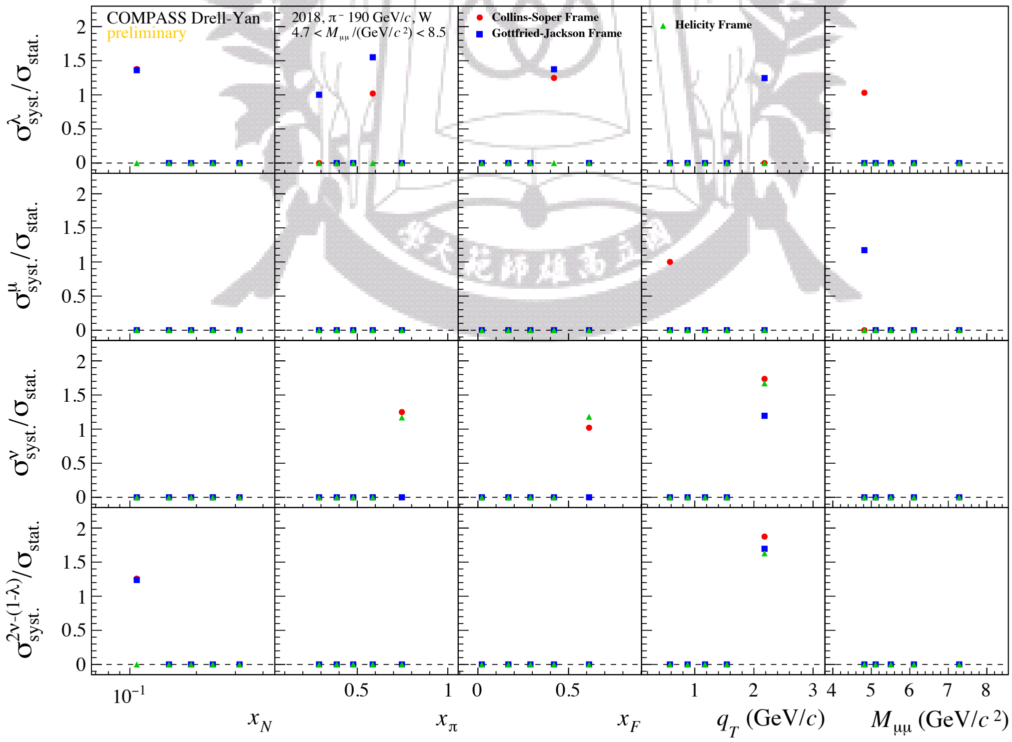

(b) W target

Figure C.5: The estimated systematic uncertainties for unpolarized asymmetries result in Collins–Soper, Gottfried–Jackson and Helicity frame from target cells compatibility.

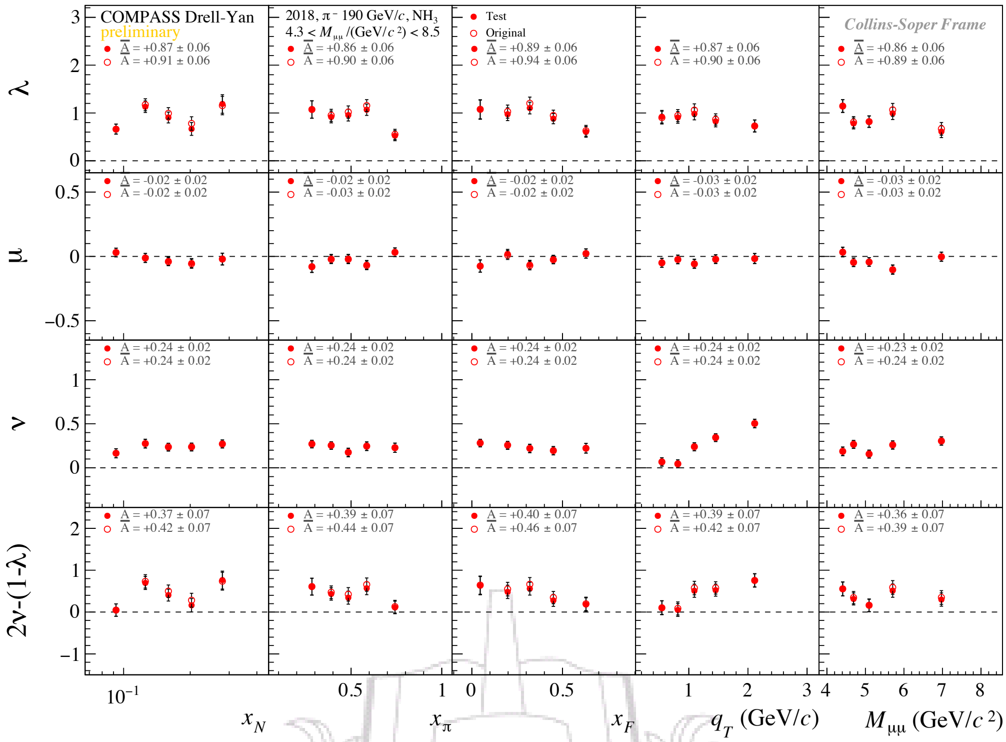

(a) NH_3 target

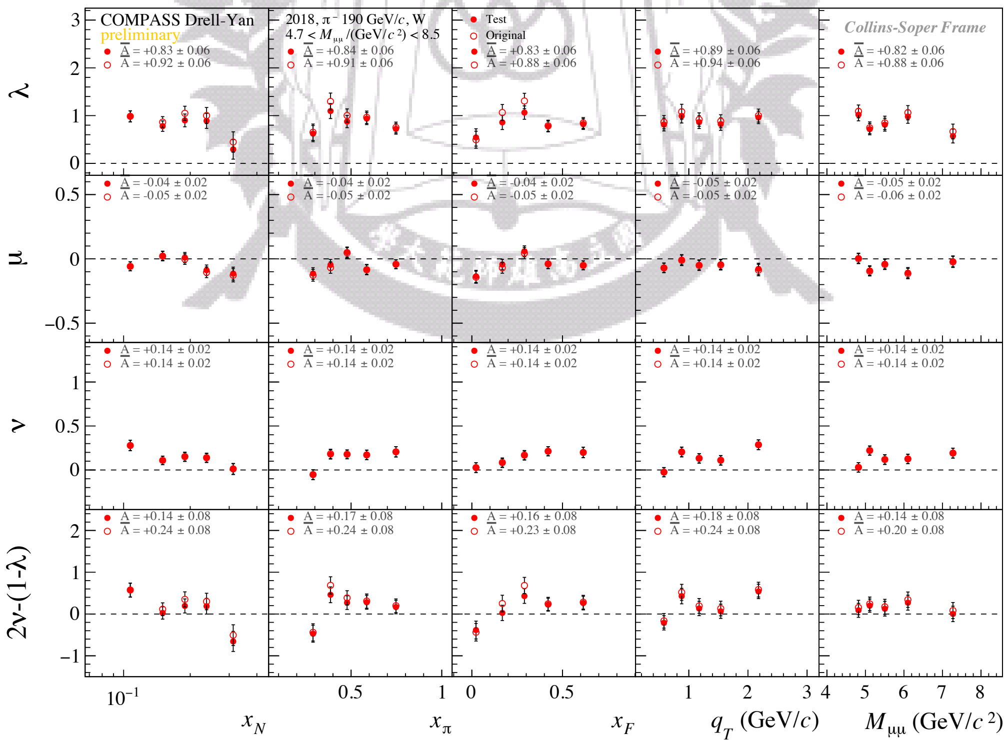

(b) W target

Figure C.6: The comparison of unpolarized asymmetries between LAST–LAST priority (labelled as "Original") and OT–LAST priority (labelled as "Test") in Collins–Soper frame.

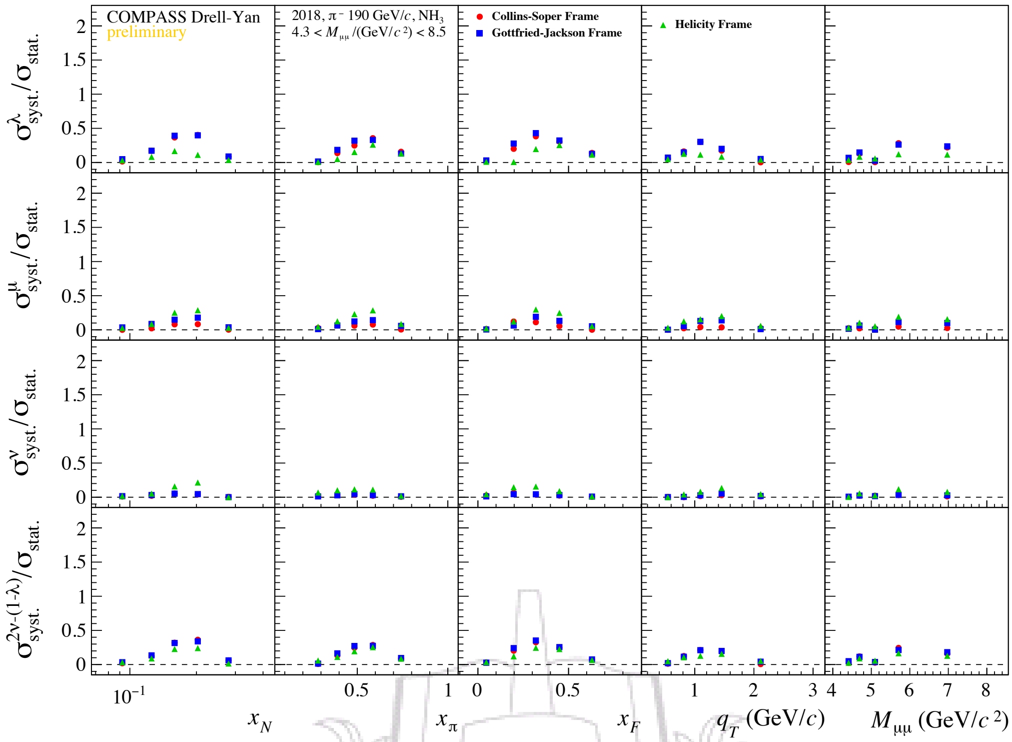

(a) NH_3 target

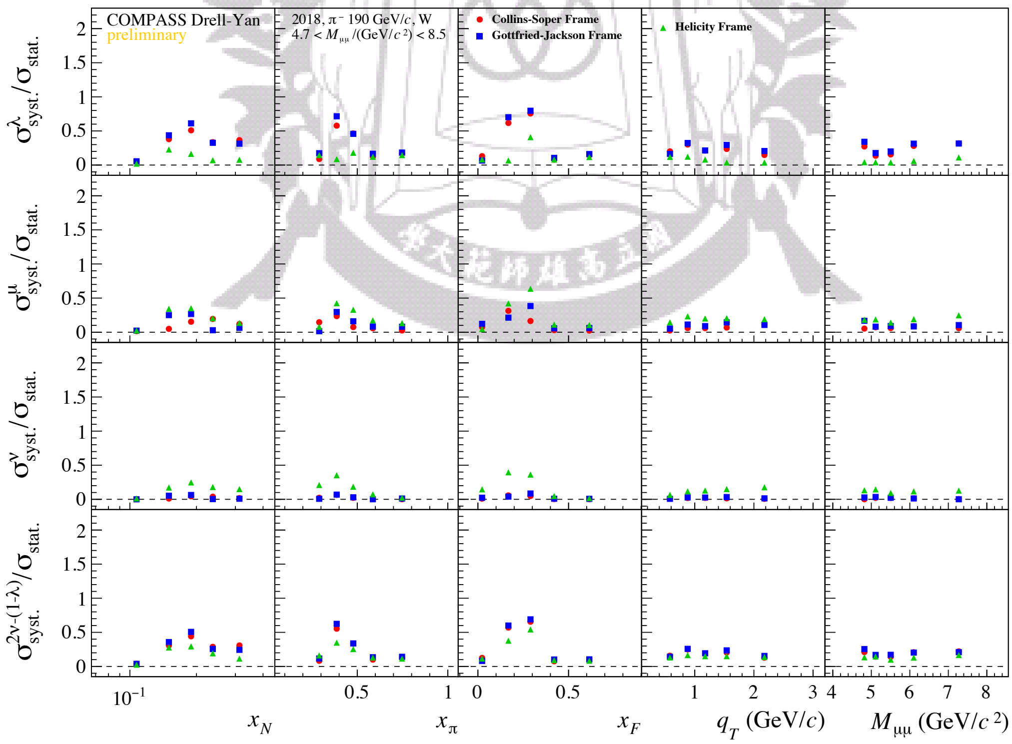

(b) W target

Figure C.7: The estimated systematic uncertainties for unpolarized asymmetries result in Collins–Soper, Gottfried–Jackson and Helicity frame from trigger priority compatibility.

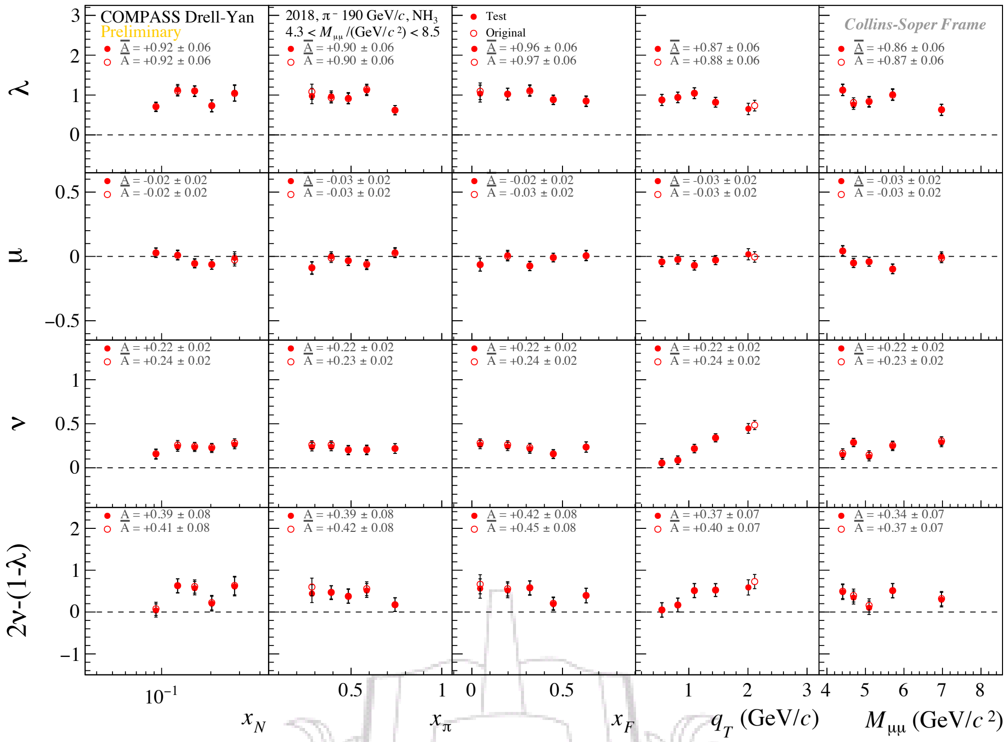

(a) NH_3 target

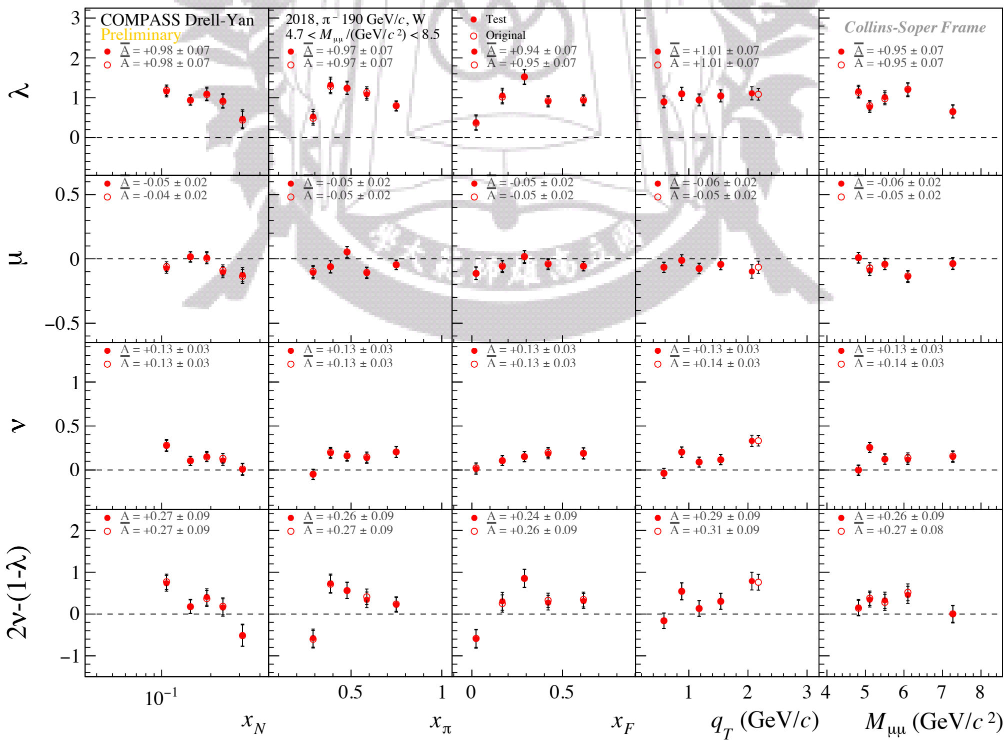

(b) W target

Figure C.8: The comparison of UAs extraction between original selection cut (labeled as "Original") and lower q_T limit cut (labeled as "Test").

C.5 Systematic of different θ_{μ^-} cut

As mention in Chapter 5, the polar angle of muon with negative charged θ_{μ^-} have been applied a lower cut: 0.02 rad for NH_3 in order to keep a good agreement between real data and MC. Compare the final unpolarized asymmetries extraction result with applying larger θ_{μ^-} cut: 0.03 rad, the comparison plots are shown in Figure C.9 for NH_3 target. The comparison plot shows the result are stable with larger θ_{μ^-} limit for NH_3 target. In conclusion, there is no systematic uncertainties from this test.

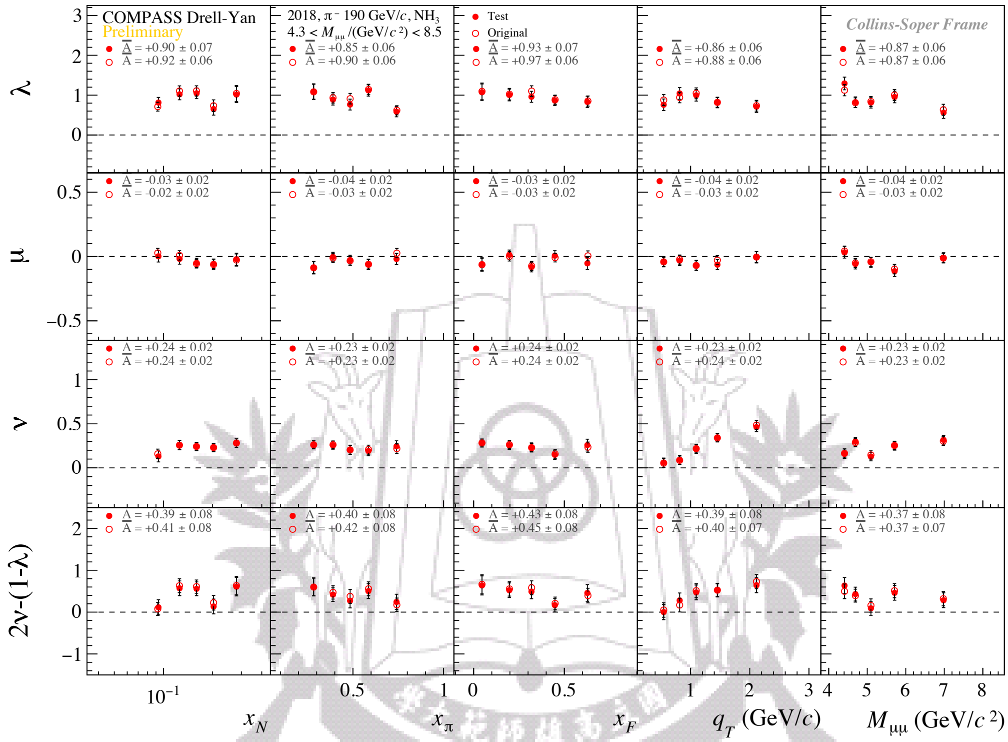

Figure C.9: The comparison of unpolarized asymmetries extraction between original selection cut (labeled as "Original") and larger θ_{μ^-} limit cut (labeled as "Test").

C.6 Systematic of different bin size of two-dimensional angular histogram

In the current unpolarized asymmetries extraction adopted 16 bins for extended $\cos\theta$ and 8 bins φ to perform two-dimensional angular histogram. Compare the final unpolarized asymmetries extraction result with using larger binning (20 bins for extended $\cos\theta$ and 10 bins φ), the comparison plots are shown in Figure C.10a and Figure C.10b for both NH_3 and W targets. The comparison plot shows the result are stable with smaller bin size for both targets. In conclusion, there is no systematic uncertainties from this test.

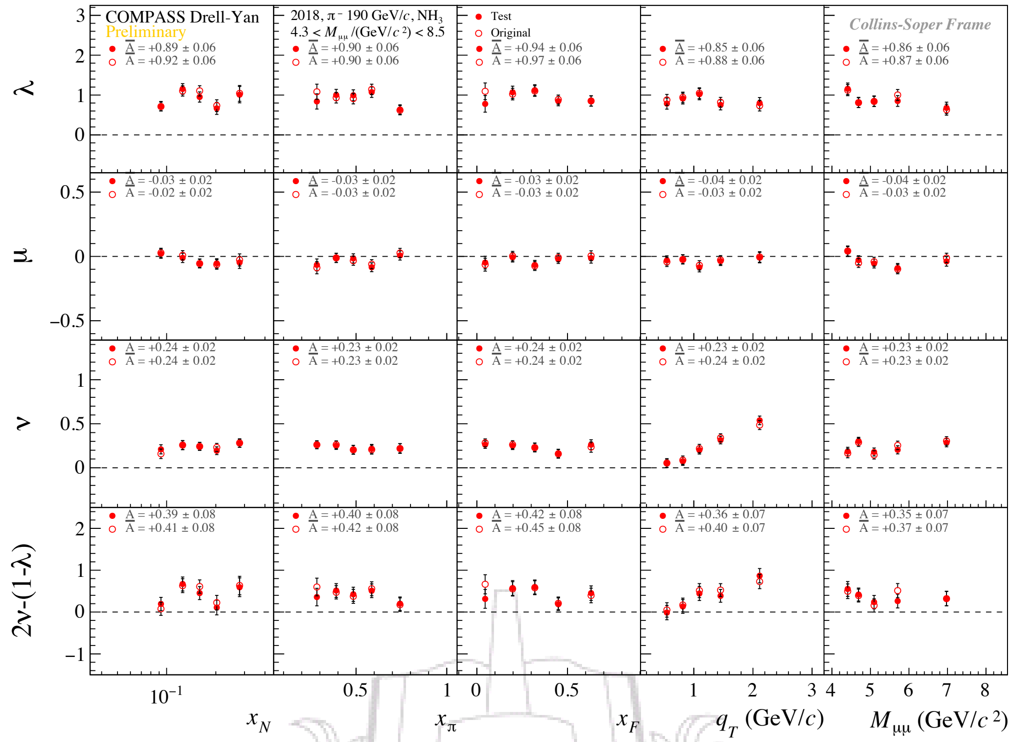

(a) NH_3 target

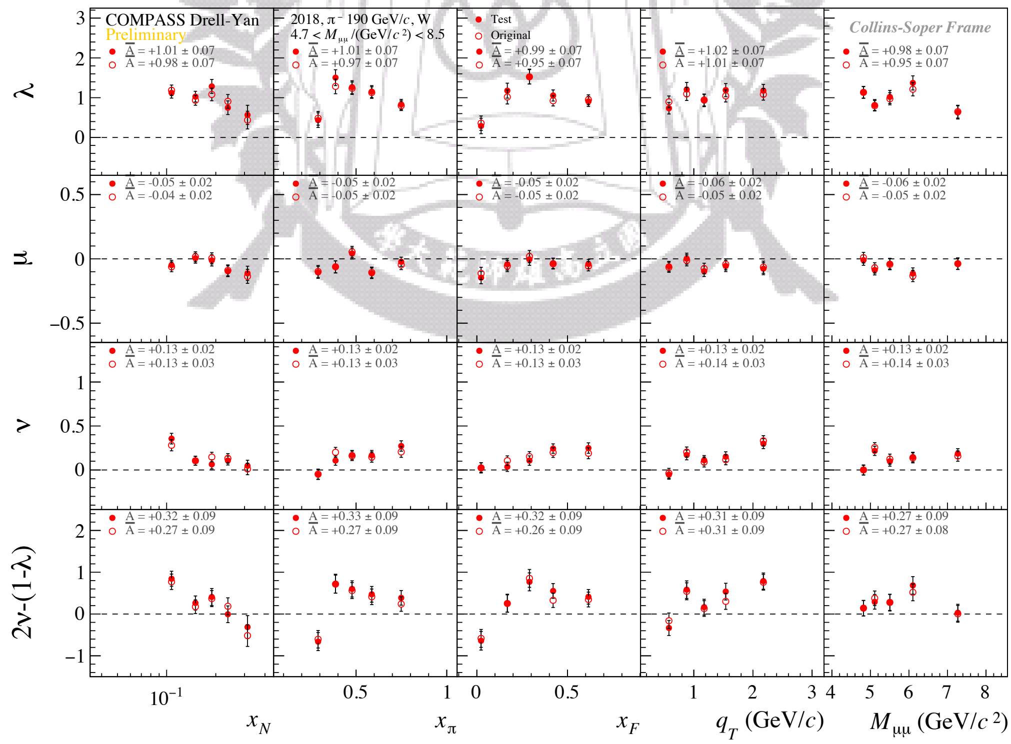

(b) W target

Figure C.10: The comparison of unpolarized asymmetries extraction between original binning: 16x8 (labeled as "Original") and larger binning: 20x10 (labeled as "Test").

C.7 Systematic of different x_F cut

As mention in Chapter 5, the lower limit cut of $x_F > -0.1$ have been applied in order to remove too low acceptance region. Compare the final unpolarized asymmetries extraction result with using larger limit: $x_F > 0$ which is only select positive x_F events, the comparison plots are shown in Figure C.10a and Figure C.10b for both NH_3 and W targets. The comparison plot shows the result are stable with tighter cut. In conclusion, there is no systematic uncertainties from this test.

C.8 Systematic of different dead zone cut

The enlargement of dead zone size by 2.5 cm in each side of dead zone edge and both XY direction have been applied for all of HG and HO hodoscopes in order to remove the region that cannot properly described in MC simulation. Compare the final unpolarized asymmetries extraction result with using larger limit cut: 3 cm. The comparison plots are shown in Figure C.10a and Figure C.10b for both NH_3 and W targets. The comparison plot shows the result are stable with larger dead zone size. In conclusion, there is no systematic uncertainties from this test.

C.9 Impact of different MC-generator settings

In first approximation, extracted asymmetries should not depend on the shape of the generated kinematic and angular distributions[1], since the information of the generator cancels out in the definition of the acceptance. But this approximation is only valid when we extracted the result in multi-dimensional method. Nevertheless, possible acceptance and phase-space edge effects can be convoluted in a complicated manner with the experimental resolutions and may introduce some correlations between the properties of generated distributions and evaluated angular acceptances. Different MC samples are being generated to study eventual correlations between evaluated angular acceptance distributions and event generator options and settings.

Produce one test MC sample where the generated events only include higher-order Drell–Yan process (Compton-scattering, $qG \to \gamma^* q$) and compared with the original high-mass Drell–Yan MC with leading-order Drell–Yan process. The kinematics mean values comparison between this test MC and real data (P02) in both targets is shown in Figure C.13. The test MC shows a large mean of q_T and x_F, from which a big impact on angular acceptance estimation is expected. The comparison of unpolarized asymmetries extraction between using original MC and test MC is shown in Figure C.14. The impact of extremely different model on unpolarized asymmetries extraction is visible in λ and μ but not in ν. But this impact is expected since the kinematics variables are too deviated from our measurement. The extraction of $\tilde{\lambda}$ by using this test MC which shown in Figure C.15 also suggest a large systematic uncertainties with this angular acceptance. Here the main message is that even in such extreme case, the extraction of ν is still quite stable in both targets. In conclusion,

[1]Assuming that generated distributions cover the same phase space as the experimental data.

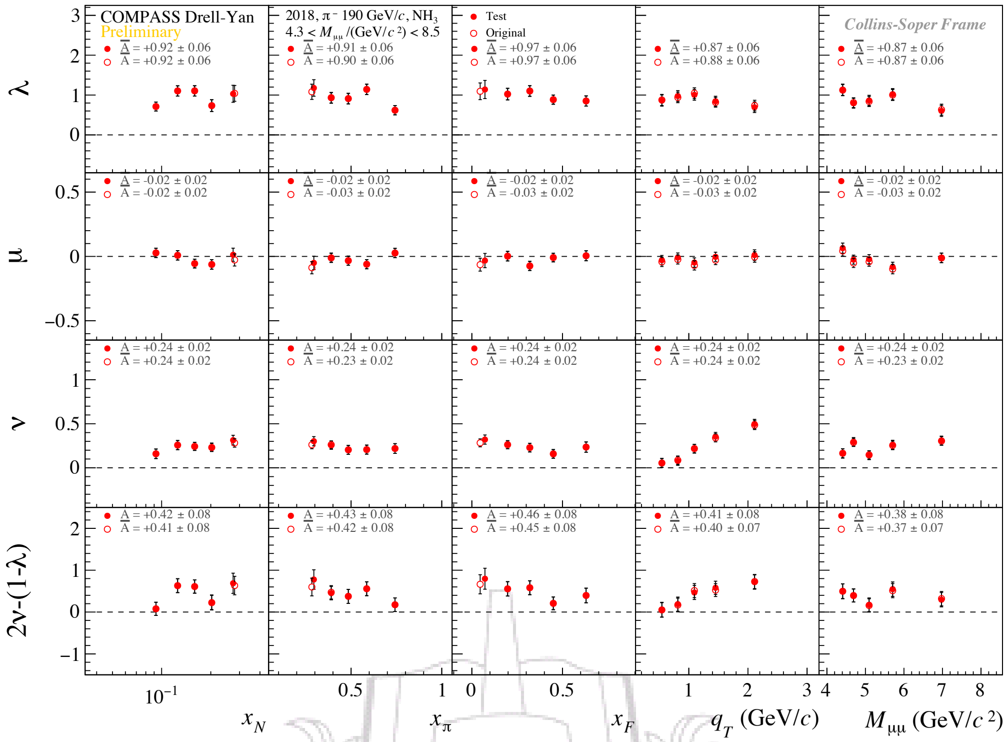

(a) NH_3 target

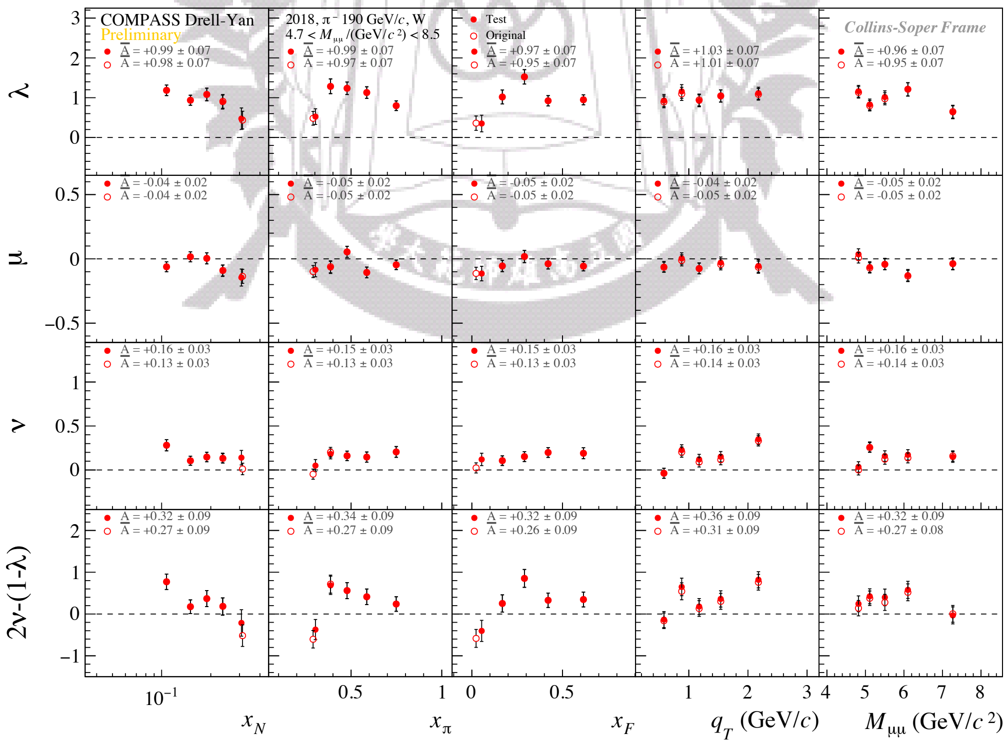

(b) W target

Figure C.11: The comparison of unpolarized asymmetries extraction between original x_F cut: $x_F > -0.1$ (labeled as "Original") and larger x_F cut: $x_F > 0$ (labeled as "Test").

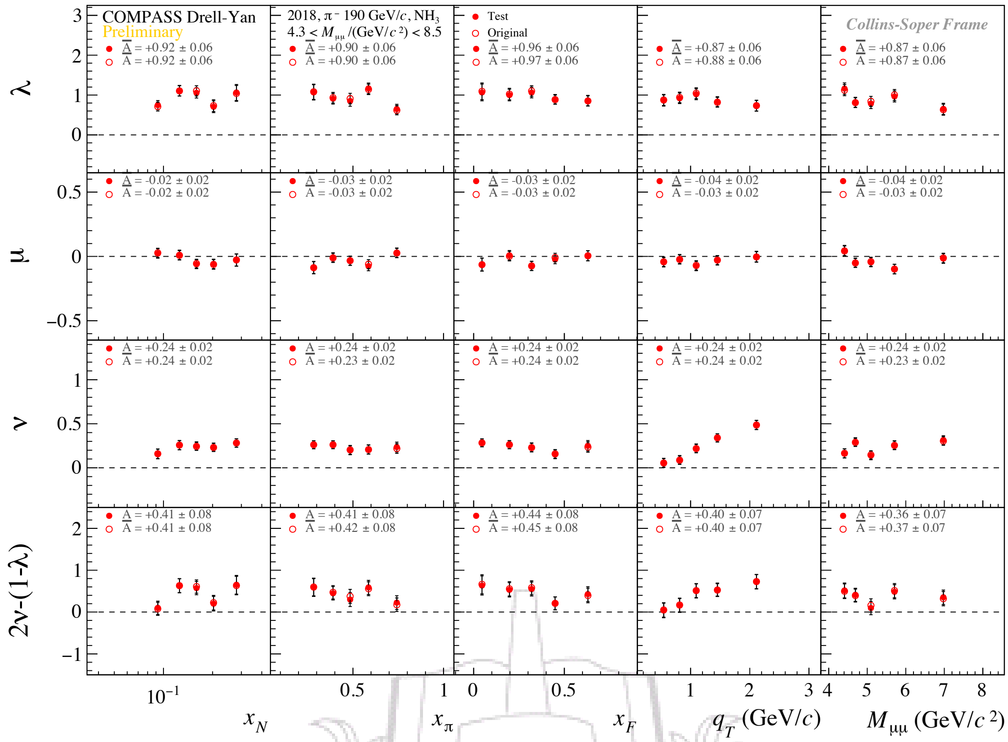

(a) NH_3 target

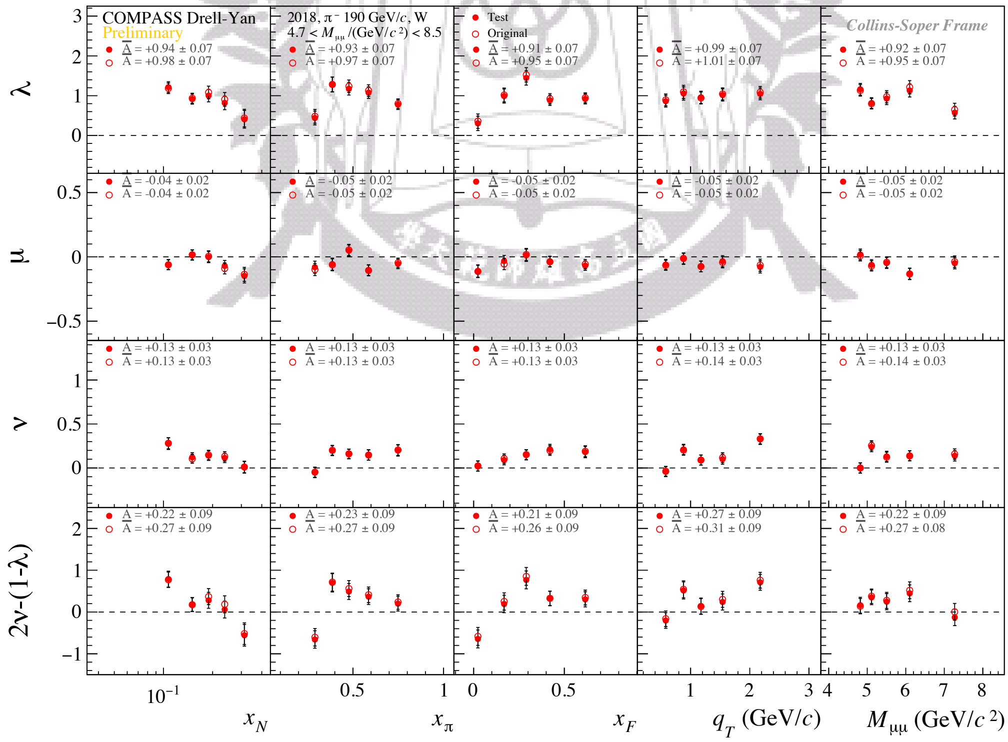

(b) W target

Figure C.12: The comparison of unpolarized asymmetries extraction between original dead zone cut: 2.5 cm (labeled as "Original") and larger dead zone cut: 3 cm (labeled as "Test").

the systematic uncertainties due to not proper angular acceptance correction which was introduced by the input model is taken care by $\tilde{\lambda}$, so in the end this is not included in the final systematic uncertainties.

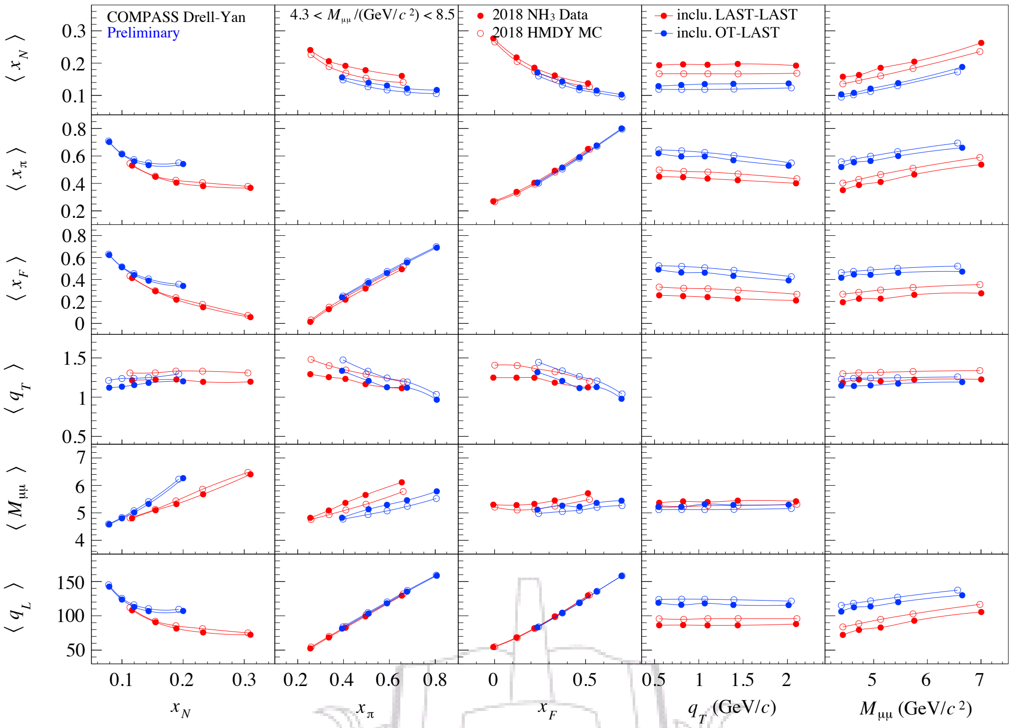

(a) NH_3 target

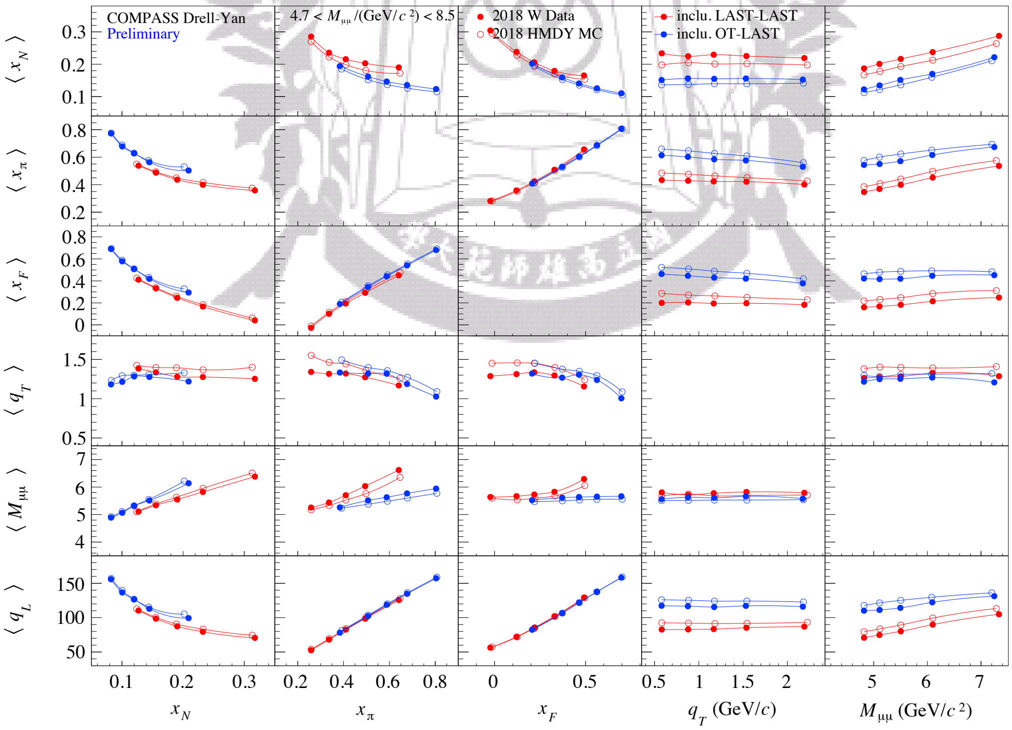

(b) W target

Figure C.13: The kinematics mean value comparison between the test MC and real data (P02).

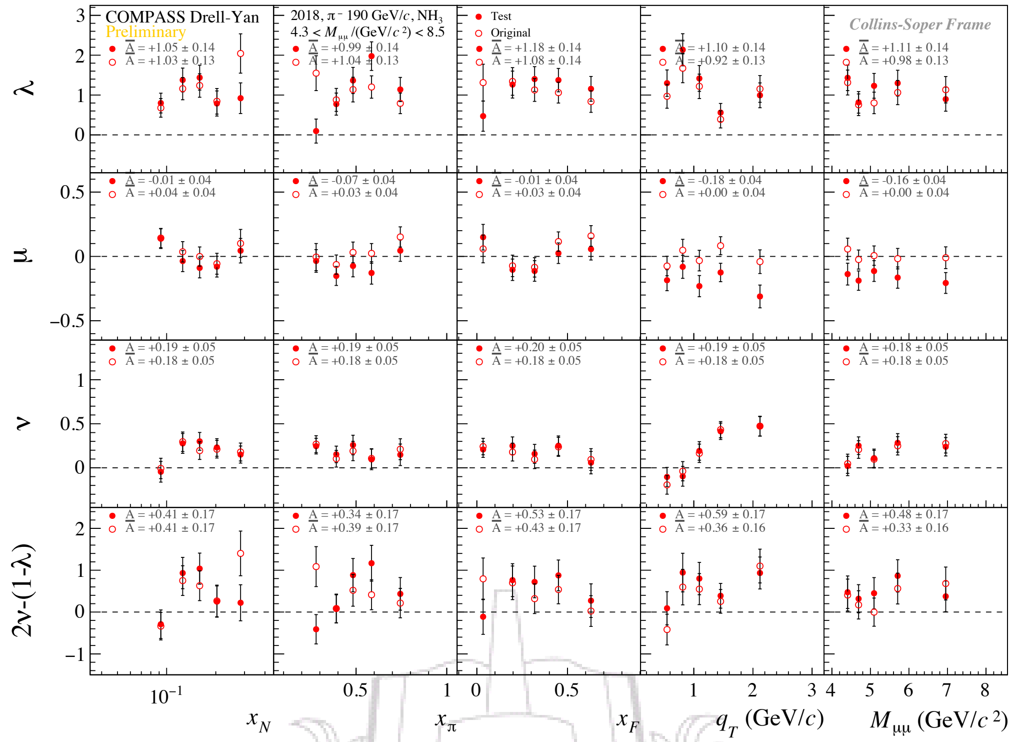

(a) NH_3 target

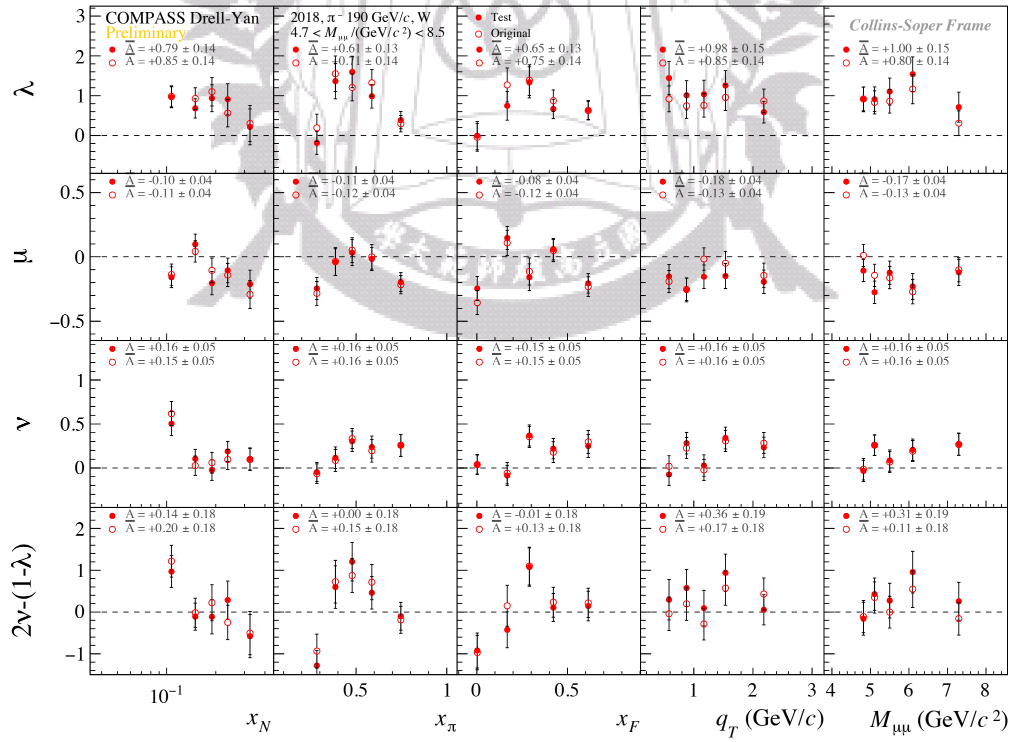

(b) W target

Figure C.14: The comparison of UAs extraction between test MC (higher-order Drell–Yan) and original MC.

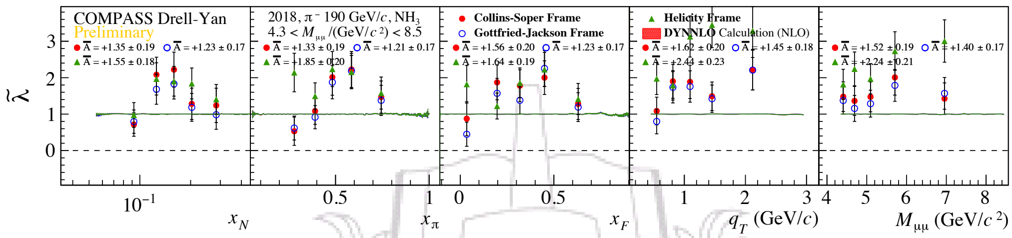

(a) NH_3 target

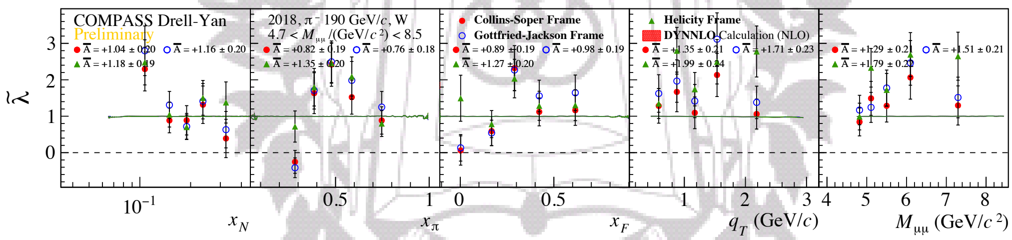

(b) W target

Figure C.15: Rotation invariant $\tilde{\lambda}$ extracted in Collins–Soper, Gottfried–Jackson and Helicity frames with the MC test and real data (P02).

Bibliography

[1] Richard P. Feynman, *Very high-energy collisions of hadrons*, Phys. Rev. Lett. **23**, 1415 (1969), doi:10.1103/PhysRevLett.23.1415.

[2] M. Diehl, *Transverse Spin Structure of the Nucleon*, Phys. Rep. **388**, 41 (2002), doi:10.1016/j.physrep.2003.08.002.

[3] M. G. Perdekamp and F. Yuan, *Transverse Spin Structure of the Nucleon*, Annu. Rev. Nucl. Part. Sci. **65**, 429 (2015), doi:10.1146/annurev-nucl-102014-021948.

[4] J. Ashman *et al.* [EMC Collaboration], *A measurement of the spin asymmetry and determination of the structure function g_1 in deep inelastic muon-proton scattering*, Phys. Lett. B **206**, 364 (1988), doi:10.1016/0370-2693(88)91523-7.

[5] A. Kotzinian, *New quark distributions and semi-inclusive electroproduction on polarized nucleons*, Nucl. Phys. B **441**, 234 (1995), doi:10.1016/0550-3213(95)00098-D.

[6] J. H. Christenson *et al.*, *Observation of Massive Muon Pairs in Hadron Collisions*, Phys. Rev. Lett. **25**, 1523 (1970), doi:10.1103/PhysRevLett.25.1523.

[7] Sidney D. Drell and Tung-Mow Yan, *Massive Lepton-Pair Production in Hadron-Hadron Collisions at High Energies*, Phys. Rev. Lett. **25**, 316 (1970), doi:10.1103/PhysRevLett.25.316.

[8] I. R. Kenyon, *The Drell–Yan Process*, Rep. Prog. Phys. **45**, 1261 (1982), doi:10.1088/0034-4885/45/11/002.

[9] J. C. Collins, D. E. Soper and G. F. Sterman, *Factorization of Hard Processes in QCD*, Adv. Ser. Direct. High Energy Phys. **5**, 1 (1989), doi:10.1142/9789814503266-0001.

[10] J.-W. Qiu and G. F. Sterman, *Power corrections in hadronic scattering. 1. Leading $1/Q^2$ corrections to the Drell–Yan cross-section*, Nucl. Phys. B **353** (1991) 105, doi:10.1016/0550-3213(91)90503-P.

[11] F. T. Brandt, J. Frenkel and J. C. Taylor, *Cancellation of soft interactions with spectators in the Drell-Yan process*, Nucl. Phys. B **312** (1989) 589, doi:10.1016/0550-3213(89)90573-7.

[12] S. Arnold, A. Metz and M. Schlegel, *Dilepton production from polarized hadron hadron collisions*, Phys. Rev. D **79** (2009) 034005, doi:10.1103/PhysRevD.79.034005.

[13] F. Gautheron *et al.* [COMPASS Collaboration], *COMPASS-II Proposal*, SPSC-P-340, CERN-SPSC-2010-014, `http://cds.cern.ch/record/1265628/files/SPSC-P-340.pdf`.

[14] D. Sivers, *Single-spin production asymmetries from the hard scattering of pointlike constituents*, Phys. Rev. D **41**, 83 (1990), doi:10.1103/PhysRevD.41.83.

[15] A. Airapetian *et al.* [HERMES Collaboration], *Observation of the Naive-T-Odd Sivers Effect in Deep-Inelastic Scattering*, Phys. Rev. Lett. **103**, 152002 (2009), doi:10.1103/PhysRevLett.103.152002.

[16] E. S. Ageev *et al.* [COMPASS Collaboration], *A new measurement of the Collins and Sivers asymmetries on a transversely polarised deuteron target*, Nucl. Phys. B **765**, 31 (2007), doi:10.1016/j.nuclphysb.2006.10.027.

[17] M. Alekseev *et al.* [COMPASS Collaboration], *Collins and Sivers asymmetries for pions and kaons in muon–deuteron DIS*, Phys. Lett. B **673**, 127 (2009), doi:10.1016/j.physletb.2009.01.060.

[18] C. Adolph *et al.* [COMPASS Collaboration], *Experimental investigation of transverse spin asymmetries in μ-p SIDIS processes: Sivers asymmetries*, Phys. Lett. B **717**, 383 (2012), doi:10.1016/j.physletb.2012.09.056.

[19] C. Adolph *et al.* [COMPASS Collaboration], *Collins and Sivers asymmetries in muon-production of pions and kaons off transversely polarised protons*, Phys. Lett. B **744**, 250 (2015), doi:10.1016/j.physletb.2015.03.056.

[20] X. Qian *et al.* [Jefferson Lab Hall A Collaboration], *Single Spin Asymmetries in Charged Pion Production from Semi-Inclusive Deep Inelastic Scattering on a Transversely Polarized ^3He Target at $Q^2 = 1.4 - 2.7\ GeV^2$*, Phys. Rev. Lett. **107**, 072003 (2011), doi:10.1103/PhysRevLett.107.072003.

[21] M. Anselmino *et al.*, *Sivers Effect for Pion and Kaon Production in Semi-Inclusive Deep Inelastic Scattering*, Eur. Phys. J. A **39**, 89 (2009), doi:10.1140/epja/i2008-10697-y.

[22] P. Sun and F. Yuan, *Energy evolution for the Sivers asymmetries in hard processes*, Phys. Rev. D **88**, 034016 (2013), doi:10.1103/PhysRevD.88.034016.

[23] L. Adamczyk *et al.* [STAR Collaboration], *Measurement of the Transverse Single-Spin Asymmetry in $p^\uparrow + p \to W^\pm/Z^0$ at RHIC*, Phys. Rev. Lett. **116**, 132301 (2016), doi:10.1103/PhysRevLett.116.132301.

[24] M. Aghasyan *et al.* [COMPASS Collaboration], *First Measurement of Transverse-Spin-Dependent Azimuthal Asymmetries in the Drell–Yan Process*, Phys. Rev. Lett. **119**, 112002 (2017), doi:10.1103/PhysRevLett.119.112002.

[25] M. Anselmino, M. Boglione, U. D'Alesio, F. Murgia, and A. Prokudin, *Study of the sign change of the Sivers function from STAR collaboration W/Z production data*, J. High Energy Phys. **04** (2017) 046, doi:10.1007/JHEP04(2017)046.

[26] M. G. Echevarria, A. Idilbi, Z.-B. Kang, and I. Vitev, *QCD evolution of the Sivers asymmetry*, Phys. Rev. D **89**, 074013 (2014), doi:10.1103/PhysRevD.89.074013.

[27] D. Boer and P. J. Mulders, *Time-reversal odd distribution functions in leptoproduction*, Phys. Rev. D **57**, 5780 (1998), doi:10.1103/PhysRevD.57.5780.

[28] Leonard P. Gamberg, Gary R. Goldstein, and Marc Schlegel, *Transverse quark spin effects and the flavor dependence of the Boer–Mulders function*, Phys. Rev. D **77**, 094016 (2008), doi:10.1103/PhysRevD.77.094016.

[29] B. Pasquini, M. Pincetti, and S. Boffi, *Drell–Yan processes, transversity, and light-cone wave functions*, Phys. Rev. D **76**, 034020 (2007), doi:10.1103/PhysRevD.76.034020.

[30] M. Göckeler *et al.*, *Transverse Spin Structure of the Nucleon from Lattice-QCD Simulations*, Phys. Rev. Lett. **98**, 222001 (2007), doi:10.1103/PhysRevLett.98.222001.

[31] Z. Lu and B.-Q. Ma, *The* $\cos 2\varphi$ *asymmetry of Drell–Yan and* J/ψ *production in unpolarized* $p\bar{p}$ *scattering*, Phys. Lett. B **615**, 200 (2005), doi:10.1140/epjc/s10052-006-0174-6.

[32] M. Burkardt and B. Hannafious, *Are all Boer–Mulders functions alike?*, Phys. Lett. B **658**, 130 (2008), doi:10.1016/j.physletb.2007.09.064

[33] Z. Lu, B.-Q. Ma and I. Schmidt, *Flavor separation of the Boer–Mulders function from unpolarized* $\pi^- p$ *and* $\pi^- D$ *Drell–Yan processes*, Phys. Lett. B **639**, 494 (2006), doi:10.1016/j.physletb.2006.06.053.

[34] M. Lambertsen, W. Vogelsang, *Drell-Yan lepton angular distributions in perturbative QCD*, Phys. Rev. D **93**, 114013 (2016), doi:10.1103/PhysRevD.93.114013.

[35] C. S. Lam and W. K. Tung, *Parton-model relation without quantum-chromodynamic modifications in lepton pair production*, Phys. Rev. D **21**, 2712 (1980), doi:10.1103/PhysRevD.21.2712.

[36] L. Y. Zhu *et al.* [FNAL E866/NuSea Collaboration], *Measurement of Angular Distributions of Drell-Yan Dimuons in* $p + p$ *Interactions at 800 GeV/c*, Phys. Rev. Lett. **102**, 182001 (2009), doi:10.1103/PhysRevLett.102.182001.

[37] A. Brandenburg, O. Nachtmann and E. Mirkes, *Spin effects and factorization in the Drell–Yan process*, Z. Phys. C **60**, 697 (1993), doi:10.1007/BF01558400.

[38] V. Khachatryan *et al.*, *Angular coefficients of Z bosons produced in pp collisions at* $\sqrt{s} = 8$ *TeV and decaying to* $\mu^+\mu^-$ *as a function of transverse momentum and rapidity*, Phys. Lett. B **750**, 154 (2015), doi:10.1016/j.physletb.2015.08.061.

[39] T. Aaltonen *et al.*, *First Measurement of the Angular Coefficients of Drell–Yan* e^+e^- *pairs in the Z Mass Region from* $p\bar{p}$ *collisions at* $\sqrt{s} = 1.96$ *TeV*, Phys. Rev. Lett. **106**, 241801 (2011), doi:10.1103/PhysRevLett.106.241801.

[40] W.-C. Chang, R. E. McClellan, J.-C. Peng and O. Teryaev, *Lepton angular distributions of fixed-target Drell–Yan experiments in perturbative QCD and a geometric approach*, Phys. Rev. D **99**, 014032 (2019), doi:10.1103/PhysRevD.99.014032.

[41] S. Falciano *et al.* [NA10 Collaboration], *Angular Distributions of Muon Pairs Produced by 194-GeV/cNegative Pions*, Z. Phys. C **31** (1986) 513, doi:10.1007/BF01551072.

[42] L. Anderson *et al.* [NA10 Collaboration], *A High Resolution Spectrometer for the Study of High Mass Muon Pairs Produced by Intense Hadron Beams*, Nuclear Instruments and Methods in Physics Research **223** 1 (1984) 26, doi:10.1016/0167-5087(84)90243-6.

[43] M. Guanziroli *et al.* [NA10 Collaboration], *Angular Distributions of Muon Pairs Produced by Negative Pions on Deuterium and Tungsten*, Z. Phys. C **37** (1988) 545, doi:10.1007/BF01549713.

[44] J. S. Conway *et al.*, *Experimental Study of Muon Pairs Produced by 252-GeV Pions on Tungsten*, Phys. Rev. D **39** (1989) 92, doi:10.1103/PhysRevD.39.92.

[45] D. Boer, *Investigating the origins of transverse spin asymmetries at BNL RHIC*, Phys. Rev. D **60**, 014012 (1999), doi:10.1103/PhysRevD.60.014012.

[46] J. C. Peng, *Transverse Spin Effects in Future Drell–Yan Experiments*, Eur. Phys. J. Web Conf. **85**, 01009 (2015), doi:10.1051/epjconf/20158501009.

[47] L. Y. Zhu [E866/NuSea Collaboration], *Measurement of Angular Distributions of Drell-Yan Dimuons in $p + d$ Interactions at 800 GeV/c*, Phys. Rev. Lett. **99**, 082301 (2007), doi:10.1103/PhysRevLett.99.082301.

[48] Z. Lu and I. Schmidt, *Updating Boer–Mulders functions from unpolarized pd and pp Drell–Yan data*, Phys. Rev. D **81**, 034023 (2010), doi:10.1103/PhysRevD.81.034023.

[49] S. Bastami *et al.*, *The Drell–Yan process with pions and polarized nucleons*, JHEP **2021**, 166 (2021), doi:10.1007/JHEP02(2021)166.

[50] X. Wang, W. Mao and Z. Lu, *The Drell–Yan process with pions and polarized nucleons*, Eur. Phys. Jour. C **78**, 643 (2018), doi:10.1140/epjc/s10052-018-6114-4.

[51] P. Abbon *et al.* [COMPASS Collaboration], *The COMPASS setup for physics with hadron beams*, Nuclear Instruments and Methods in Physics Research A 779 (2015) 69-115, doi:10.1016/j.nima.2015.01.035.

[52] H. W. Atherton *et al.*, *Precise Measurements of Particle Production by 400-GeV/cProtons on Beryllium Targets*, Ph.D Thesis, 2018.

[53] P. Abbon *et al.* [COMPASS Collaboration], *The COMPASS experiment at CERN*, Nuclear Instruments and Methods in Physics Research A 577 (2007) 455–518, doi:10.1016/j.nima.2007.03.026.

[54] R. Longo, *Measurement of spin effects in the Drell-Yan process at the COMPASS experiment*, CERN, 1980. - 25 p, doi:10.5170/CERN-1980-007.

[55] A. Abragam, *The Principles of Nuclear Magnetism*, The Clarendon Press Oxford, 1961.

[56] M. C. Altunbas *et al.*, *Construction, test and commissioning of the triple-GEM tracking detector for COMPASS*, Nuclear Instruments and Methods in Physics Research A 490 (2002) 177–203, doi:10.1016/S0168-9002(02)00910-5.

[57] Marco Meyer-Conde, *Measurement of absolute Drell–Yan cross-sections using a 190-GeV π beam at the COMPASS-II experiment*, Nuclear Experiment [nucl-ex]. Université Paris-Saclay, 2019. English. NNT : 2019SACLS472 . tel-02459225.

[58] M. Bodlak *et al.*, *New data acquisition system for the compass experiment*, Journal of Instrumentation, 8(02):C02009, 2013.

[59] M. Bodlak *et al.*, *FPGA based data acquisition system for COMPASS experiment*, Journal of Physics: Conference Series, 513(1):012029, 2014, doi:10.1088/1742-6596/513/1/012029.

[60] R. Frühwirth, *Application of Kalman filtering to track and vertex fitting*, Nuclear Instruments and Methods in Physics, A262:444–450, 1987, doi:10.1016/0168-9002(87)90887-4.

[61] T. Sjostrand, S. Mrenna, P. Skands, *PYTHIA 6.4 Physics and Manual*, JHEP **0605** (2006) 026, doi:10.1088/1126-6708/2006/05/026

[62] T. Sjöstrand *et al.*, *An Introduction to PYTHIA 8.2*, arXiv:1410.3012, `http://home.thep.lu.se/~torbjorn/pdfdoc/pythia8200.pdf`.

[63] T. Szameitat, C. Regali *et al.*, `https://na58-project-tgeant.web.cern.ch/content/authors-and-contact`.

[64] S. Agostinelli *et al.* [GEANT4 Collaboration], *Geant4—a simulation toolkit*, Nucl. Inst. and Meth. in Phys. R. Sec. A **506** (2003) 250, doi:10.1016/S0168-9002(03)01368-8

[65] T. Szameitat, *New Geant4-based Monte Carlo software for the COMPASS-II experiment at CERN*, PhD Thesis, Physikalisches Institut Albert-Ludwigs-Universität Freiburg, December 2016.

[66] P. Faccioli, C. Lourenço, J. Seixas, and H. K. Wöhri, *Towards the experimental clarification of quarkonium polarization*, Eur. Phys. J. C **69** (2010) 657, doi:10.1140/epjc/s10052-010-1420-5.

[67] M. Gavrilova, O. Teryaev, *Rotation-invariant observables as density matrix invariants*, Phys. Rev. D **99** 076013 (2019), doi:10.1103/PhysRevD.99.076013.

[68] P. Faccioli, C. Lourenço, J. Seixas, and H. K. Wöhri, *Model-independent constraints on the shape parameters of dilepton angular distributions*, Phys. Rev. D **83** 056008 (2011), doi:10.1103/PhysRevD.83.056008.

[69] P. J. Sutton, A. D. Martin, R. G. Roberts, and W. J. Stirling, *Parton distributions for the pion extracted from Drell-Yan and prompt photon experiments*, Phys. Rev. D **45** (1992) 2349, doi:10.1103/PhysRevD.45.2349.

[70] M. Gluck, E. Reya, and A. Vogt, *Pionic parton distributions*, Z. Phys. C **53** (1992) 651, doi:10.1007/BF01559743.

[71] P. C. Barry, N. Sato, W. Melnitchouk, and C. R. Ji, *First Monte Carlo Global QCD Analysis of Pion Parton Distributions*, Phys. Rev. Lett. **121** (2018) 152001, doi:10.1103/PhysRevLett.121.152001.

[72] I. Novikov *et al.*, *Parton Distribution Functions of the Charged Pion Within The xFitter Framework*, Phys. Rev. D **102** (2020) 014040, doi:10.1103/PhysRevD.102.014040.

[73] M. B. Einhorn, S. D. Ellis, *Hadronic Production of the New Resonances: Probing Gluon Distributions*, Phys. Rev. D **12** (1975) 2007, doi:10.1103/PhysRevD.12.2007.

[74] C.-H. Chang, *Hadronic production of J/ψ associated with a gluon*, Nucl. Phys. B **172** (1980) 425, doi:10.1016/0550-3213(80)90175-3.

[75] G. T. Bodwin, E. Braaten, and G. P. Lepage, *Rigorous QCD analysis of inclusive annihilation and production of heavy quarkonium*, Phys. Rev. D **55** (1997) 5853(E), doi:10.1103/PhysRevD.55.5853.

[76] M. Beneke and I. Z. Rothstein, *Hadroproduction of quarkonia in fixed target experiments*, Phys. Rev. D **54** (1996) 2005, doi:10.1103/PhysRevD.54.2005.

[77] P. A. Zyla *et al.* (Particle Data Group), Prog. Theor. Exp. Phys. 2020 (2020) 083C01.

[78] F. Maltoni *et al.*, *Analysis of charmonium production at fixed-target experiments in the NRQCD approach*, Phys. Lett. B **638** (2006) 202, doi:10.1016/j.physletb.2006.05.010.

[79] E. J. Eichten and C. Quigg, *Quarkonium wave functions at the origin*, Phys. Rev. D **52** (1995) 1726, doi:10.1103/PhysRevD.52.1726.

[80] P. L. Cho and A. K. Leibovich, *Color octet quarkonia production. II*, Phys. Rev. D **53** (1996) 6203, doi:10.1103/PhysRevD.53.6203.

[81] A. Petrelli, M. Cacciari, M. Greco, F. Maltoni and M. L. Mangano, *NLO production and decay of quarkonium*, Nucl. Phys. B **514** (1998) 245, doi:10.1016/S0550-3213(97)00801-8.

[82] M. Beneke and M. Krämer, *Direct J/ψ and ψ' polarization and cross-sections at the Tevatron*, Phys. Rev. D **55** (1997) 5269, doi:10.1103/PhysRevD.55.R5269.

[83] P. Nason *et al.*, *Bottom production*, In Geneva 1999, Standard model physics (and more) at the LHC* 231-304

[84] G. A. Schuler, *Quarkonium production and decays*, arXiv:hep-ph/9403387.

[85] R. Vogt, *J/ψ production and suppression*, Phys. Rept. **310** (1999) 197, doi:10.1016/S0370-1573(98)00074-X.

[86] I. Abt *et al.* [HERA-B Collaboration], *A Measurement of the ψ' to J/ψ production ratio in 920-GeV proton-nleus interactions*, Eur. Phys. J. C **49** (2007) 545, doi:10.1140/epjc/s10052-006-0139-9.

[87] C. Baglin *et al.* [NA38 Collaboration], *psi-Prime and J/ψ production in p W, p U and S U interactions at 200-GeV/nucleon*, Phys. Lett. B **345** (1995) 617, doi:10.1016/0370-2693(94)01614-I.

[88] M. J. Corden *et al.*, *Experimental Results on J/ψ Production by $\pi^{\pm}$, $K^{\pm}$, p and $\bar{p}$ Beams at 39.5-GeV*, Phys. Lett. **96B** (1980) 411, doi:10.1016/0370-2693(80)90799-6.

[89] Y. Alexandrov *et al.* [BEATRICE Collaboration], *Inclusive J/ψ and ψ' production in π^{-} - nucleus interactions at $S^{(1/2)}$ approximately equals 26-GeV*, Nucl. Phys. B **557** (1999) 3, doi:10.1016/S0550-3213(99)00412-5.

[90] S. Dulat *et al.*, *New parton distribution functions from a global analysis of quantum chromodynamics*, Phys. Rev. D **93** (2016) 033006, doi:10.1103/PhysRevD.93.033006.

[91] M. R. Whalley, D. Bourilkov and R. C. Group, *The Les Houches accord PDFs (LHAPDF) and LHAGLUE*, arXiv:hep-ph/0508110, `https://lhapdf.hepforge.org/lhapdf5/`.

[92] A. Buckley, J. Ferrando, S. Lloyd, K. Nordström, B. Page, M. Rüfenacht, M. Schönherr and G. Watt, *LHAPDF6: parton density access in the LHC precision era*, Eur. Phys. J. C **75** (2015) 132, doi:10.1140/epjc/s10052-015-3318-8. `https://lhapdf.hepforge.org/`.